ENERGY TRANSFER IN ANISOTROPIC SYSTEMS: A. EXCITATION MIGRATION IN SUBSTITUTIONALLY DISORDERED ONE-DIMENSIONAL SOLIDS B. THE SPECTROSCOPY OF MOLECULES ADSORBED ON METAL SURFACES

Dirk Adrian Zwemer
(Ph. D. thesis)

November 1978

Prepared for the U. S. Department of Energy
under Contract W-7405-ENG-48

LBL-8332

ENERGY TRANSFER IN ANISOTROPIC SYSTEMS:

A. EXCITATION MIGRATION IN SUBSTITUTIONALLY DISORDERED ONE-DIMENSIONAL SOLIDS

B. THE SPECTROSCOPY OF MOLECULES ADSORBED ON METAL SURFACES

Dirk Adrian Zwemer

Materials and Molecular Research Division
Lawrence Berkeley Laboratory and Department of Chemistry
University of California, Berkeley, California

Table of Contents

ENERGY TRANSFER IN ANISOTROPIC SYSTEMS:

A. EXCITATION MIGRATION IN SUBSTITUTIONALLY DISORDERED ONE-DIMENSIONAL SOLIDS

B. THE SPECTROSCOPY OF MOLECULES ADSORBED ON METAL SURFACES

Dirk Adrian Zwemer

Materials and Molecular Research Division
Lawrence Berkeley Laboratory and Department of Chemistry
University of California, Berkeley, California

ABSTRACT

The energy and dynamics of excited states in a variety of anisotropic environments, including isotopically and chemically mixed crystals and molecular overlayers adsorbed on a nickel (111) surface, are investigated using laser excitation phosphorescence spectroscopy, optically-detected magnetic resonance, and spectroscopic ellipsometry. The relationship between local and long-range structure and spectroscopic properties is explored.

A theory for energy transfer in substitutionally disordered solids is presented that includes the effects of coherent and incoherent migration of the wave packet, the statistical distribution of fluctuations in the potential energy surface the wave packet encounters, and tunneling. Explicit expressions for the "diffusion" coefficients in these limits and the energy partitioning ratios in binary systems are derived. It is also shown that an activation energy dependent upon the composition of the binary systems can emerge from such a treatment and

is an indication that energy transfer between localized states is facilitated by concurrent tunnelling and thermal promotion.

Experimental results for triplet energy partitioning between mobile and stationary trap states as a function of mobile trap concentration in the ternary d_2-1,2,4,5-tetrachlorobenzene-h_2-1,2,4,5-tetrachlorobenzene-pyrazine system are analyzed with regard to the proposed models for one-dimensional energy transfer in substitutionally disordered solids. It is shown that both tunnelling and thermal detrapping contribute to triplet exciton mobility below 4.2 K. Singlet exciton migration makes an important contribution to trap equilibration before intersystem crossing to the triplet manifold.

Spin coherence experiments are used to determine the energy level structure, physical geometry, and exciton dynamics of a series of impurity-induced traps in 1,2,4,5-tetrachlorobenzene. The Y trap, a perturbed host molecule, is shown to be caused by an adjacent, translationally equivalent chemical impurity whose triplet energy may lie above or below the host exciton, but above the trap. The slow rate of thermal processes within the trap is interpreted as weak coupling between the lattice phonons and localized phonons induced at the trap by the impurity.

The optical properties of well-characterized surfaces are studied in an ultra-high vacuum chamber equipped with LEED and Auger. The UV spectra of pyrazine, pyridine, and naphthalene adsorbed on a nickel single crystal (111) surface are measured by spectroscopic ellipsometry at low temperatures. The excited electronic and vibronic energy levels measured are similar to bulk molecular crystal values, but pyrazine and

pyridine show small, but significant deviations. The ordering of molecular overlayers is observed spectroscopically and information about overlayer crystal structure is deduced.

The excited triplet-state lifetime of pyrazine near the nickel surface is measured from the optically-excited phosphorescence decay. Phosphorescence excitation spectra for singlet manifold excitation corroborate spectroscopic ellipsometry results. Experimental lifetime results indicate that the critical distance for dipole-surface nonradiative energy transfer is much smaller than predicted theoretically. An alternative model involving stochastic intermolecular energy transfer to the surface is outlined.

To my parents and grandparents

I. OVERVIEW

The work presented in this thesis grew out of a desire by the author to approach a variety of scientific problems in molecular spectroscopy and energy transfer from a common set of perspectives on the interaction of structure and energy. The result is not a body of work dedicated to a single problem, theory, and technique, but a record of the pursuit of scientific opportunities that opened up in the ongoing research of this laboratory. Opportunism is a dubious scientific virtue, but it has made for an active and exciting graduate career. The record is, to some extent, chronological. The first two years were spent studying energy transfer in molecular crystals and the second two on surface science. The nature of the projects has been very different. The early work was part of a continuing effort on coherent energy transfer in solids and its application of triplet excitons in molecular crystals, particularly inspired by the exciton trapping studies of Harris and co-workers[1,2] and the percolation studies of Kopelman and co-workers.[3,4,5] The optical properties of surfaces, on the other hand, is a very new field and we have progressed cautiously in an area with few established preconceptions to limit our hypotheses.

Despite the dissimilarity of the subjects and instrumentation in these projects, it is hoped that this thesis will communicate the identity of questions, insights, and goals that inform all these studies. Structure and the interplay of structures is the theme and measure of all this work. The molecular structure affects and is affected by the

bulk crystal structure or the ordering of a molecular overlayer on a metal surface, and both interact with an electronic excitation that has a dynamic structure as distinct and important as any static structure. In molecular crystals, we have studied energy transfer in materials in which the structure determines the dimensionality of the transfer. On the intrinsically anisotropic structure of surfaces, we have studied energy transfer across the interface. As a consequence, each project has had two stages, the elucidation of the structure, represented by the magnetic resonance studies of impurity-induced traps and the spectroscopy of adsorbed aromatic molecules on nickel surfaces, and measurement of the energy transfer determined by that structure, represented by energy partitioning in molecular crystals and the phosphorescent lifetimes of excited states on surfaces.

The first division of this dissertation describes the molecular crystals research, beginning with a chapter on exciton migration and coherence in an ideal crystal to lay the groundwork for study of exciton dynamics in disordered systems. The next two chapters apply random walk probability results to triplet excitons in one-dimensional energy bands and propose models that differentiate between mechanisms for energy transfer across substitutional barriers. The fifth chapter compares the predictions of these models with experimental results obtained by the author. The next details a separate study of the structure and dynamics of one particular substitutional defect by optically-detected magnetic resonance. Chapter seven, a short interlude, summarizes the molecular

crystals work, before the second half of the thesis introduces the optical properties of surface adlayers. The contents and organization of that division are described in the introduction to chapter eight.

A. Exciton Migration in Substitutionally Disordered One-Dimensional Solids

Questi organi del mondo così vanno,
come tu vedi omai, di grado in grado,
che di sù prendono e di sotto fanno.

- Dante

II. EXCITON MIGRATION AND COHERENCE IN IDEAL CRYSTALS

Periodicity is the property of crystalline solids that makes possible the propagation of electronic excitation in solids as coherent wavepackets in the limit of weak exciton-lattice interactions. The prediction of coherence in molecular solids dates back to the work of Frenkel in 1931. In his original paper on excitons,[6] Frenkel develops three important insights. First, he pointed out that the electronic excitation can be delocalized and as a result be described by a series of Bloch wave-functions in analogy to the lattice modes of the crystal. Second, as a consequence of delocalization the superposition of several of the modes will form a localized wave-packet which propagates through the lattice with a group velocity determined by the exciton dispersion and the nature of exciton-lattice interaction. Third, because the excitation is coupled to the lattice, it creates a lattice distortion that travels adiabatically with the electronic excitation. As a result of these principles, a proper description of the dynamics of exciton migration in the Frenkel limit requires that the time dependence of the delocalized states of a crystal be considered. Because of the explicit localization introduced into the stationary states by phonon-exciton scattering, the electronic states, the phonon states, and phonon-exciton coupling must all be explicitly considered in terms of the crystal states. Basically, the phonons modulate the intermolecular interaction which in turn mixes the delocalized $\vec{k}$ states of the crystal and results in a state that can be described as a linear combination of the delocalized states.

In the Frenkel limit, this results in a partial localization of the electronic excitation but still allows for the excitation to propagate coherently as a wave packet, provided the linear combination of $\vec{k}$ states remains unchanged for times exceeding the time associated with the nearest-neighbor electronic intermolecular exchange. Indeed, it is the average frequency at which the linear combination of $\vec{k}$ states changes relative to the intermolecular interaction time that determines the dominant mechanism responsible for electronic energy transfer in solids at both high and low temperatures.

The properties of one-dimensional excitons in the absence of lattice coupling are summarized in Figure 1. A finite linear array of N independent molecules has N degenerate electronic states. The energy, E_o, of this system corresponds to the excited state energy of a single molecule. If the molecules interact pairwise, the Hamiltonian of the system becomes[7]

$$\mathcal{H} = \sum_{n=1}^{N} E_o a_n^+ a_n + \sum_{n,m}^{N} \beta_{nm} a_n^+ a_m \qquad [\text{II-1}]$$

The stationary eigenstates of the Hamiltonian are the delocalized Bloch wavefunctions

$$|k\rangle = N^{-1/2} \sum_{N} e^{ik\cdot r_n} |n\rangle \qquad [\text{II-2}]$$

characterized by the exciton wave-vector $\underline{k}$.

In order to properly consider exciton migration in solids, one must introduce exciton-phonon coupling which modulates the intermolecular

COHERENT PROPERTIES OF EXCITONS

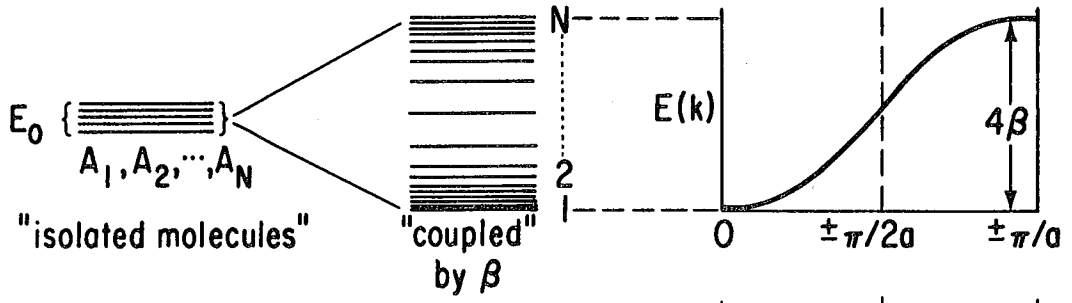

1. β generates a rate of energy transfer between molecules: $\nu_g(k)$.
2. Coherence lifetime, $\tau(k)$, generates a width to the state *and* a mean-free path for coherent energy migration

$$\ell(k) = \nu_g(k) \cdot \tau(k)$$

$$\tau(k)^{-1} \equiv \sum_{k'} (\tau_{kk'})^{-1} = \Gamma(k)$$

3. Distribution Function, D(k), determines the partition of energy between states of different velocities

$$D(k)_B \sim \rho(k) \exp[-E(k)/kT]$$

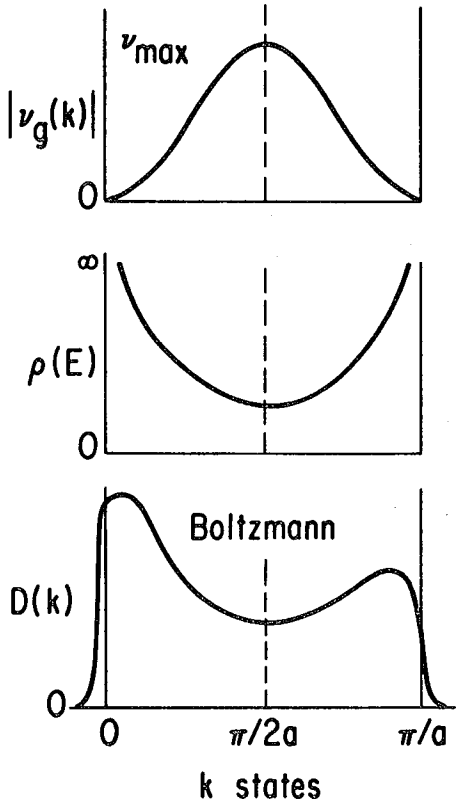

XBL 734-394

Figure 1. Properties of one-dimensional coherent excitons.

interaction and mixes the delocalized k-states. Phenomenologically, this partially localizes the exciton but still allows it to propagate coherently as a wave-packet, provided the explicit linear combination of k-states remains unchanged for times exceeding the time for nearest neighbor resonant transfer.[8] The complete Hamiltonian for an extended system[7] including coupling to the lattice is

$$\mathcal{H} = \sum_n E_o a_n^+ a_n + \sum_{n,m} V_{nm} a_n^+ a_m + \sum_{n,q} \omega_q \left(b_{qn}^+ b_{qn} + \frac{1}{2}\right) \qquad [II-3]$$

$$+ \sum_{n,q} g_{nq} a_n^+ a_n \left(b_{qn}^+ + b_{qn}\right) + \sum_{n,q} h_{nq} a_n^+ a_n \left(b_{qn}^+ + b_{qn}\right)^2$$

where ω_q is the energy of phonon q, and g_{nq} and h_{nq} represent the linear and quadratic exciton-phonon coupling constants, respectively. Theoretical studies of localization and coherent migration based on solutions to the above Hamiltonian have been given by a variety of workers and has been reviewed extensively and with great clarity by Silbey.[7]

It should be noted that each of the principal theoretical formulations, apart from Förster's study of incoherent transfer,[9] contain a coherent component in the transport equations that persists to relatively high temperatures. The Haken-Strobl-Reinecker[10-12] model requires no specific information on exciton-phonon coupling, but instead makes the site and interaction energies (E_o and β_{nm} in Eq. 1) time-dependent, fluctuating stochastically with delta function auto-correlation times (Markov limit). The expression they derive for the diffusion constant contains an incoherent term determined by the fluctuation amplitude and a coherent term which goes to infinity in the limit of zero fluctuation amplitude.

Grover and Silbey[13,14] begin with a dynamical model of the lattice coupling and transform to operators creating and destroying excitons with associated phonons. To obtain analytical expressions for exciton mobility, they also make the Markov scattering assumptions and get a diffusion constant similar to that of Haken and co-workers. Munn and Siebrand[15] have pointed out the importance of the quadratic coupling terms which were neglected by Grover and Silbey. Using generalized master equations, Kenkre and Knox[16-19] have derived the time evolution of an exciton system without the Markovian assumption, permitting the use of non-exponential coherence memory decays. These authors have also investigated the transition from coherent to Fermi golden rule intermolecular transfer rates that accompanies increased phonon scattering.

Although the number of different operational definitions of coherence is large, they may be broadly categorized into two groups. In the first, the stationary state of the excitation is a delocalized state or a wavepacket of states characterized by a constant wave-vector and group velocity. The wave-vector $\vec{k}$ is a good quantum number for times longer than the intermolecular transfer time. The extent of coherence determines the k-state lifetime and as a result, the homogeneous lineshape function for absorption to the exciton band edge. The implications of coherence in spectroscopy from this point of view have been developed and refined by a variety of people including Toyozawa,[20-23] Sumi,[24,25] Suna,[26] Harris[27,28] and others,[29-32] who have calculated optical absorption lineshapes for exciton transitions in various limits. This provides the rationale behind experimental lineshape studies, Toyozawa's

analysis[20] for alkali halide absorption spectra, and Thomas and Hopfield's demonstration of exciton coherence in CdS.[33] In addition, this description of coherence provides a means for easily relating the exciton's coherence time to the correlation time of a variety of other experimental techniques such as ESR and NMR. It was on this basis that coherent migration in triplet exciton bands in molecular solids was established by Harris and coworkers.[28,34-36]

A second and more empirical definition is that a coherent exciton has a mean free path greater than one lattice site but its motion is described by random walk processes on some time scale longer than the intermolecular transfer time. Studies of exciton dynamics based upon a statistical model for the probability of trapping excitons in the coherent and random walk limits rely on this definition. Implicit in these studies is a detailed consideration of the energy dispersion of the band, the number of k states comprising the band, and the partitioning of energy between the band and trap states when a Boltzmann distribution characterizes the ensemble. Exciton diffusion constants have been measured experimentally and used to infer properties of coherence based on this definition. The early work of Gallus and Wolf[37] in phenanthrene and Kepler and Switendick[38] and Avakian and Merrifield[39] can be interpreted in this context.

Exciton mean free path measurements have been less successful in demonstrating exciton coherence in many cases than lineshape interpretation. A coherent exciton has a mean free path greater than the intermolecular spacing and as such the extent of coherence determines the path

length. These measurements require the detection of exciton transfer between spectroscopically distinguishable initial and final states. A distinction between coherent and incoherent migration is often made in assessing whether or not a dynamical model provides a mechanism for achieving thermal equilibrium between these states within the lifetime of the state. Usually the experiment measures energy partitioning between an exciton band and traps, the time-dependence of emission build-up and decay in band or trap, or triplet-triplet exciton annihilation. In practice, these often require the introduction of isotopic, chemical, or structural traps or barriers outside the exciton band. Unfortunately, transfer processes associated with two or more component systems, such as trapping, tunneling, and thermal detrapping, are not well understood and the experimental demonstration of coherence is often ambiguous.

Fayer and Harris[40] have measured the experimental temperature dependence of the intensity of the intrinsic defect trap in 1,2,4,5-tetrachlorobenzene. If the migration is rapid, equilibration of the triplet state populations can be established among the exciton and trap states within the lifetime of the excited electronic state and the temperature dependence of the trap emission will obey Boltzmann statistics. If the migration is too slow, equilibrium is not reached and the qualitative behavior of the trap intensity is different. In this study, the experimental results could be fit to a Boltzmann curve with the best possible fit giving a trap concentration of one part in 90,000. This observation can only be interpreted in terms of a model which is dependent upon coherent migration in the TCB crystal at low temperatures.

Table I gives the ratio of the distances traveled by an exciton moving in the coherent limit versus random walk migration at 2.8 K for a narrow band-width excitation (the TCB triplet), a wide band dibromo-naphthalene triplet), and an intermediate band-width. The random walk migration is a factor of 10^4 to 10^6 slower than coherent migration. While a TCB exciton traveling completely coherently could sample approximately 10^9 lattice sites during its lifetime (10 msec), an exciton undergoing random walk migration will only sample about 10^4 lattice sites. The number of such excitons able to migrate longer distances falls off rapidly because one-dimensional random walk processes are describable by a Gaussian distribution of distances about the initial site. In the case of TCB, only three excitons out of 1000 traveling completely incoherently would be able to cover a distance of 5×10^4 lattice sites, which is half the average distance between traps. The conclusion drawn by the authors from the fact that the temperature dependence of the TCB trap intensity obeys Boltzmann statistics is that coherent migration is the principal mode of transport.

Table I. Ratio of the Coherent Migration Distance to the Random Walk Distance at 2.8 K.

Time	Band Width		
	$1.25\ cm^{-1}$	$15\ cm^{-1}$	$29.6\ cm^{-1}$
1 ms	3.7×10^4	7.8×10^4	7.8×10^4
10 ms	1.1×10^5	2.5×10^5	2.5×10^5
100 ms	3.7×10^5	7.8×10^5	7.8×10^5
1 s	1.1×10^6	2.5×10^6	2.5×10^6

III. EXCITON MIGRATION AND COHERENCE IN A PERIODIC ARRAY OF SCATTERERS

1. Introduction

Energy transfer in many solid state and biophysical systems is characterized by substitutional or structural disorder induced by chemical and ionic impurities, irregular bond conformation, or disordered site distribution. In multi-dimensional systems such as amorphous semiconductors, the concepts of amalgamation and percolation theory[22,41,42] have been applied with moderate success in explaining the behavior of electrical conduction. Although the percolation concept may be applied to problems where the solid can be considered two- or three dimensional[3-5,43] it is not applicable to one-dimensional systems, which may be of great importance in intra-molecular energy transfer in large biomolecules as well as the class of one-dimensional organic conductors. In addition, one-dimensional systems[44] are exemplified by electronic energy or Frenkel exciton migration[6] in molecular crystals. These crystals serve as effective model systems in which to investigate the effects of substitutional disorder since isotopic substitution provides a method of introducing well-characterized small perturbations into the periodic potential without disturbing the crystal structure.

In an unperturbed crystal, the localized degenerate excited states of the molecule interact to form delocalized band states. Exciton mobility within these bands is determined by the magnitude and dimensionality of the interactions, the strength of coupling with lattice phonons, and the lifetime of the excited state. Modes of exciton migration range from the propagation of coherent exciton wavepackets[36] over many molecular sites to short-range diffusive "hopping" between adjacent molecules. Isotopic substitution can reduce the delocalized bands to localized regions, making exciton mobility additionally dependent on the isotopic shift and the concentration of the substituent.

Theoreticians have considered coherence in substitutionally-disordered systems containing traps and barrier states in the chain. Pearlstein and collaborators[45,46] calculated the quenching kinetics in finite chains with energy traps, finding that fully coherent excitons have low probability amplitudes at the traps and are quenched more slowly than their group velocity along the chain would indicate. Greer,[47,48] on the other hand, investigated the exciton flux through a region of a linear chain containing N barriers to scatter the excitons. He found that transfer through this region is coherent, i.e., the flux is independent of N, only for a periodic distribution of barriers. Even for random barrier placement, however, the Frenkel exciton flux does not show pure diffusional behavior.

In this chapter, we present a theory that accounts for both the coherent nature of the wavepacket and the statistical distribution of fluctuations in the potential energy surface the wavepacket encounters.

It is based on tunneling through simple barriers whose heights are determined by differences in the zero point energy between isotopic substituents. The development proceeds from a simple but well defined model system in which only one distribution of the potential energy surface is available to the wavepacket. The effects of coherence are included in the model system and compared to the diffusive "random walk" limit. Expressions for "effective" diffusion coefficients in both limits are derived and compared to the uncorrelated migration model.

2. Exciton Diffusion: General Considerations

For our discussion, a simple disordered system may be defined by a series of identical barriers in the crystal potential field as shown in Figure 2. The barriers are formed by molecules of the higher energy isotopic species and the distribution of barriers is such that one barrier of unit molecular dimensions occur every S_1 lattice sites. The intermolecular spacing is taken as $\underset{\sim}{a}$ and the barrier spacing is given by $S_1 \underset{\sim}{a}$. Passage of a migrating exciton through a barrier may take place either by direct tunneling or by thermal promotion, but if all the barriers are identical, the exact nature of the process can be left unspecified and passage through the barrier is described by a constant transmission coefficient T^*. In a complex disordered system, differences in barrier heights and widths make the nature of the barrier transmission process critical to the exciton dynamics.

Within the interval between two barriers, the mode of exciton motion may be treated in two limits, the random walk "hopping" of a

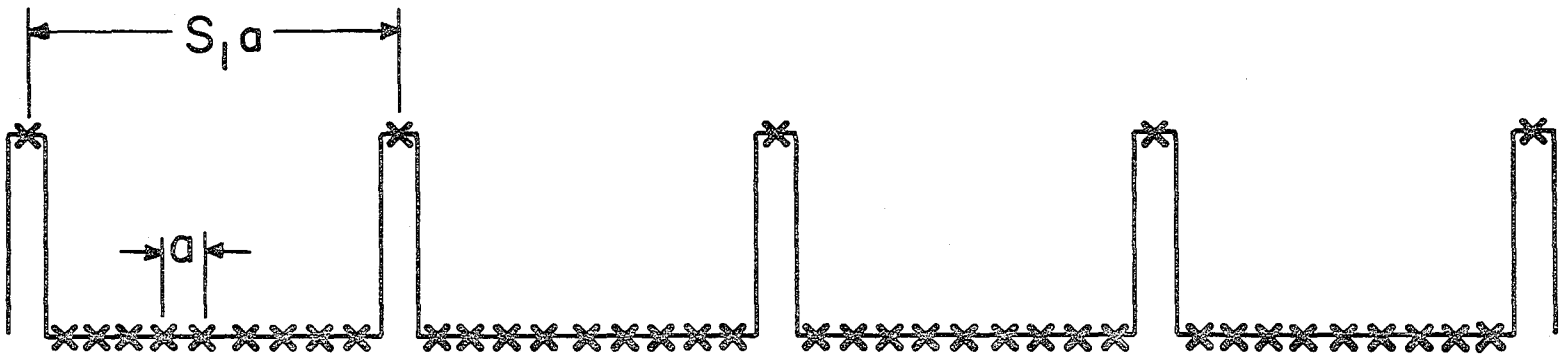

XBL 768-7373

Figure 2. Model of disordered system with periodic distribution of potential barriers. Crosses represent molecular sites along a one-dimensional crystal lattice axis.

localized excitation or the coherent propagation of an exciton wave-packet over a distance equal to $S_1 \underset{\sim}{a}$. The random "hopping" frequency between molecules is defined as ν_r, and is determined by the intermolecular interaction, β, and the correlation time, γ, associated with fluctuations in the site (diagonal) and exchange (off-diagonal) energies[7]

$$\nu_r = 8\pi^2 \beta^2 \gamma / h^2 \qquad [III-1]$$

The coherent exciton, on the other hand, is characterized by a wave vector k and a group velocity $V_g(k)$ which determine an intermolecular transfer frequency between adjacent molecules defined as ν_c. In the coherent limit, the group velocity is given by

$$V_g(k) = \frac{1}{\hbar} (\partial E(k)/\partial k) \qquad [III-2]$$

and hence the transfer frequency as a function of wave vector is given simply as

$$\nu_c(k) = V_g(k)/\underset{\sim}{a} \qquad [III-3]$$

For a Boltzmann distribution in the band, $V_g(k)$ should properly be thermally averaged[40] over the k states in the extended band in the interval $S_1 \underset{\sim}{a}$. In such a case the average group velocity $V_g(T)$ is given by

$$\langle V_g(T) \rangle = \sum_k \frac{1}{\hbar} \frac{\partial E(k)}{\partial k} e^{-E(k)/kT} / \sum_k e^{-(E(k)/kT)} \qquad [III-4]$$

where the sum over k extends over the S_1 sites in the interval $S_1 a$. Equation (4) rapidly converges for $S_1 > 20$ to a Bessel function form as

$$\langle V_g(T) \rangle = \frac{2\beta a}{\hbar} \left(\frac{2kT}{\pi\beta}\right)^{1/2} [I_{1/2}(Z)/I_o(Z)] \qquad \text{[III-5a]}$$

where

$$Z = 2\beta/kT \qquad \text{[III-5b]}$$

$$I_o(Z) = (1/\pi) \int_0^{\pi} Z \cos\theta \qquad \text{[III-5c]}$$

$$I_{1/2}(Z) = \left(\frac{1}{2} Z/\pi\right)^{1/2} \int_0^{\pi} e^{\pm Z \cos\theta} \sin\theta \, d\theta \qquad \text{[III-5d]}$$

Because of this fact there is little difference between the maximum value of $V_g(k)$ when k is discrete as in Eq. (4) or continuous as in Eq. (5). In both, the maximum occurs in the center of the bands at $|k| = \frac{\pi}{2a}$ and has a value for large S_1 of:

$$V_g^{max} = \frac{1}{\hbar} \left[\frac{\partial}{\partial k} (E_o + 2\beta \cos ka)\right]_{|k| = \pi/2a} = \frac{2\beta a}{\hbar} \qquad \text{[III-6]}$$

Long range exciton diffusion in the crystal depends on transfer between extended band states separated by intervening barriers. A critical parameter is the average time spent in an extended trap state between two barriers each a single site in width. This is equivalent to the effective tunneling time through a barrier and for a single barrier is defined as τ_1^c. This time strictly determines mean exciton dynamics in disordered systems and its calculation is of central importance in any question of one-dimensional energy transfer. Figure 3(a) illustrates the process. τ_1^c depends on the number of trap molecules over which the exciton may delocalize S_1, the barrier transmission coefficient T^*, and

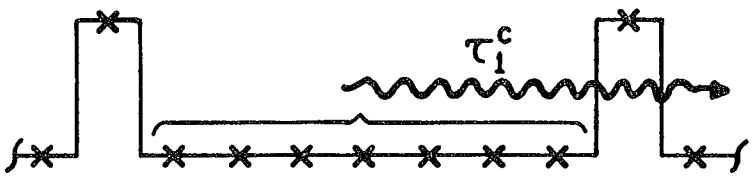

(a)

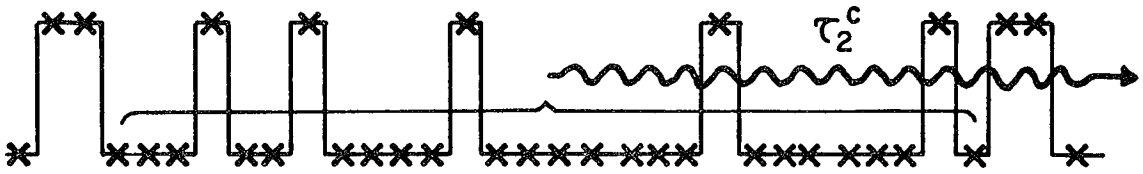

(b)

XBL 766-7117

Figure 3. (a) Escape process from interval bounded by monomer barriers. (b) Escape process from interval bounded by dimer barriers.

the intermolecular transfer frequency, $\nu=\nu_r$ or ν_c in the case of diffusive or coherent propagation, respectively.

The exciton begins its migration through the interval from a site adjacent to the barrier through which it has just passed. If the motion is completely coherent, the exciton is reflected back and forth with constant absolute momentum between the two barriers, colliding with a barrier every S_1 jumps. However, if the motion is random, probability theory predicts that the exciton, beginning from a site adjacent to a barrier, will still collide with some barrier every S_1 jumps.[49] This may be seen as the average of many collisions with the near barrier requiring only one or a few jumps and a few collisions with the far barrier requiring approximately S_1^2 jumps. In either the coherent or random walk limit, the average number of intermolecular jumps can be expressed as

$$\langle S \rangle = T^*(1-T^*)^{i-1}(iS_1)/\sum_{i=1} T^*(1-T^*)^{i-1} = \frac{S_1}{T^*} \qquad [III-7]$$

where iS_1 is the number of jumps completed after i collisions and $T^*(1-T^*)^{i-1}$ is the probability of transmission on the ith collision which is used to derive the weighted average of iS_1. The product of the average number of jumps before barrier transmission, $\langle S \rangle$, and the time per jump between band molecules, ν^{-1}, gives the effective jump time between intervals, τ_1^c:

$$\tau_1^c = \nu^{-1} \langle S \rangle = S_1/T^* \nu \qquad [III-8]$$

The physical significance of the expression is quite simple. $T^* \nu$ is the probability of transmission per unit time from a molecule adjacent to the barrier, but the effective tunneling time is increased by the S_1

molecules on which the exciton may sit. The exciton diffusion coefficient, which describes exciton dynamics, is

$$D = \frac{1}{2} (S_1 \underset{\sim}{a})^2 / \tau_1^c = \frac{1}{2} \underset{\sim}{a}^2 S_1 T^* \nu \qquad [III-9]$$

which differs for the random walk and coherent limits only so far as ν differs.

Equation (9) does not approach the correct limit as T goes to infinity (the barriers become infinitely far apart)

$$D = \frac{1}{2} a^2 \nu \qquad [III-10]$$

because the assumption that the probabilities of escaping through either barrier are equal is no longer true. A large transmission coefficient or large trap width allows a high probability of escape from a trap before a symmetric exciton population density in the trap is achieved, so the region of validity of (9) corresponds to $S_1 T^* << 1$. In this limit, a random walk treatment of a disordered one-dimensional system has been generalized by Dlott, Fayer, and Wieting[50] for a statistical distribution of trap widths to treat dilute barrier scattering. Our purpose, however, is to distinguish the effects of coherent and hopping migration <u>within</u> the trap on the random walk <u>between</u> traps. In the following two Sections, (9) is extended to the region $S_1 T^* \lesssim 1$ to reveal these effects.

3. Exciton Diffusion: Random Walk Limit

In the hopping limit, uniform population density in an interval S_1 molecules wide is effectively achieved in S_1^2 nearest-neighbor jumps. Figure 4 shows an example of a density function for $S_1 = 10$ for an

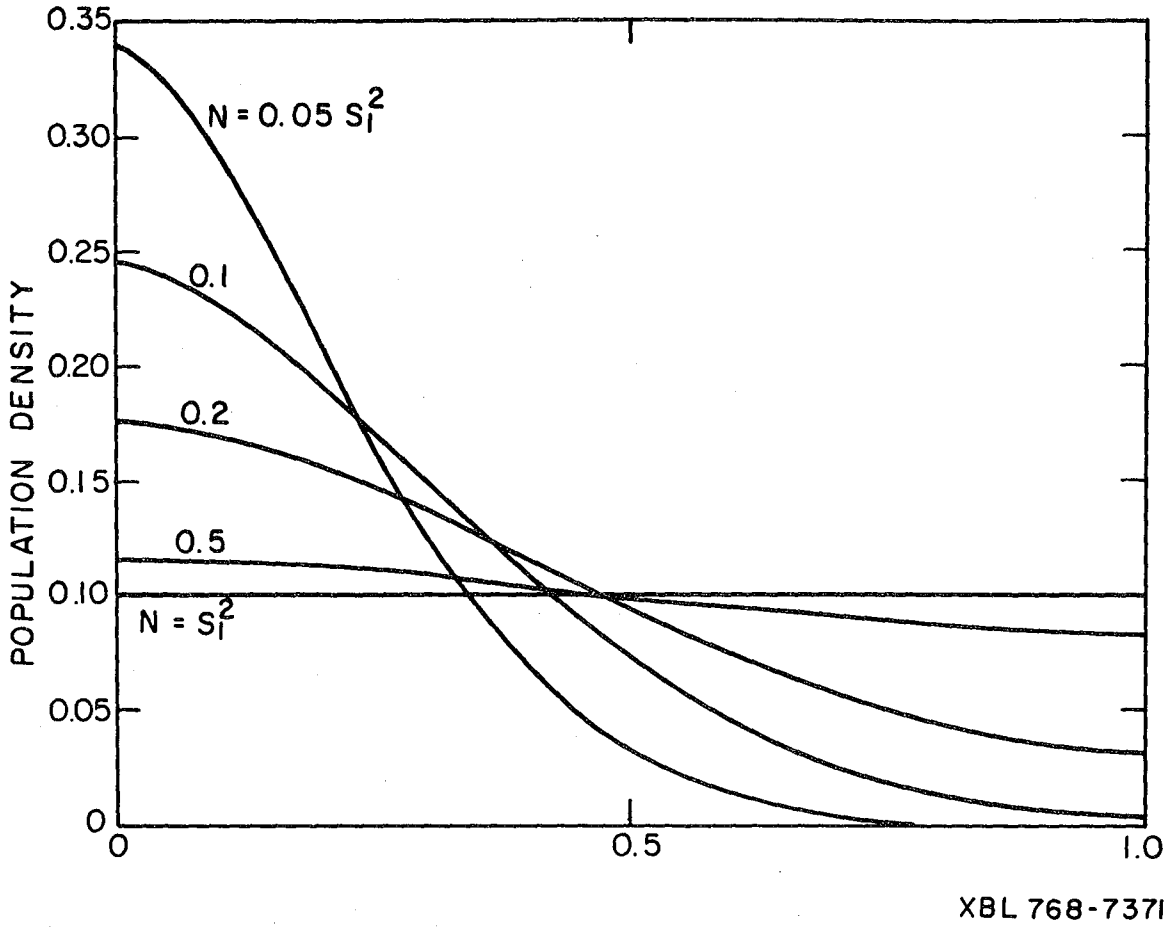

Figure 4. Population distribution for one-dimensional random walk with reflecting barriers. N equals number of jumps. Interval width (S_1 molecular sites) is 10 for purposes of illustration. Exciton position is 0 for N = 0.

exciton beginning at the left side of the interval. In the more rigorous language of probability theory, the mean first passage time to site S_1 from an origin at site 1, between two reflecting barriers, requires S_1^2 jumps.[51] The exciton begins its movement in the interval from a site adjacent to the barrier through which it has just passed from an adjacent interval. It will collide with this "near" barrier several times during the first S_1^2 jumps before it sees the "far" barrier, making the likelihood of passage back through the near barrier greater than for the far barrier. The resulting correlation between successive jumps[52] acts to keep the exciton in the vicinity of the near barrier.

The problem is treated by (i) calculating the number of collisions with the near barrier during the initial S_1^2 jumps and (ii) allowing successful escape during the period to decrease the overall frequency of migration between intervals, $1/\tau_1^c$, since a "correlated" jump which goes backwards will have the effect of cancelling out the previous jump. Part (i) corresponds to finding the number of returns to origin in S_1^2 jumps, $\langle n \rangle$, where the origin is site 1 adjacent to the near barrier.[51]

$$\langle n \rangle = \sqrt{2}\ (2S_1^2 + 1)!\,/2^{2S_1^2}(S_1^2!)^2 \qquad \text{[III-11]}$$

which may be simplified by Stirling's approximation

$$\langle n \rangle = S_1 \frac{2}{\pi}^{1/2} \left[1 + \frac{3}{8S_1^2} - \frac{7}{128S_1^4} + \cdots\right] \qquad \text{[III-12]}$$

The probability of escape from the interval before a symmetric population density (before S_1^2 jumps) is achieved is defined as P_e

$$P_e = \sum_{n=1}^{\langle n \rangle} (T^*(1-T^*)^{n-1}) = 1 - (1-T^*)^{\langle n \rangle + 1} \qquad \text{[III-13]}$$

The effective jump rate between intervals is

$$\left(\frac{1}{\tau_1^c}\right)_{\text{eff}} \cong \left(\frac{1}{\tau_1^c}\right) \sum_{i=0}^{\infty} \frac{(1-P_e)P_e^{2i}}{(2i+1)} \qquad \text{[III-14]}$$

The first term of the sum, $(1-P_e)$, is the contribution to the escape rate of an escape that is <u>not</u> followed by a "correlated" jump which cancels it out. The second term, $\frac{1}{3}(1-P_e)P_e^2$, is the contribution to the escape rate of an escape that is followed by <u>two</u> "correlated" jumps which cancel themselves out. Notice that it takes three jumps in all to move only one interval, so the contribution to the escape frequency is reduced to $\frac{1}{3}$. The stochastic "hopping" diffusion coefficient, D_r, calculated with the effective τ_1^c, is

$$D_r \cong \frac{1}{4} a^2 \nu \, S_1 T^* \left(\frac{1-P_e}{P_e}\right) \ell n \left(\frac{1+P_e}{1-P_e}\right) \qquad \text{[III-15]}$$

where an analytical expression is substituted for the sum in (14). Equation (15) approaches the barrier-less regime of (10) assymtotically through the region $S_1T^* \lesssim 1$, but begins to break down for $S_1T^* > 1$, because correlations between escape time and probability of making a correlated escape are not treated exactly in (14). In the opposite limit T^* approaches zero, the correlation factor goes to unity and (15) becomes the same as (9) as it should in the limit $S_1T^* << 1$.

4. Exciton Diffusion: Coherent Limit

In the perfect coherent limit, the delocalized wavepacket elastically scatters off the two barriers alternately. The probability of passing through the far barrier, P_f, which always undergoes the initial collision because of the wave vector momentum carried over from the last barrier transmission, will be greater than P_n, the probability of passing through the near barrier. The far barrier withstands the first, third, fifth, and succeeding alternate collisions with probability of transmission T* on the first collision, R^2T^* on the third, R^4T^* on the fifth, and so forth, where R is the reflection coefficient, $R \equiv 1 - T^*$. Likewise, the near barrier feels the second, fourth, sixth, etc. collisions with similar progression in transmission probabilities. Therefore,

$$P_f = T^* + R^2T^* + R^4T^* + \cdots = \frac{1}{2-T^*} \qquad \text{[III-16a]}$$

$$P_n = RT^* + R^3T^* + R^5T^* + \cdots = \frac{1-T^*}{2-T^*} \qquad \text{[III-16b]}$$

The effect on the diffusion coefficient of the correlated transfer between the intervals due to coherent transfer within intervals is to lengthen the effective jump distance, λ_{eff}.

$$\lambda_{eff} = (1 + (P_f - P_n) + (P_f - P_n)^2 + \cdots) S_1 a \qquad \text{[III-17a]}$$

$$= \frac{2-T^*}{2-2T^*} S_1 a$$

The term $P_f - P_n$ gives the probability of traveling a second interval coherently due to the correlated motion. $(P_f - P_n)^2$ and higher order terms allow for three or more intervals to be passed through coherently and these terms converge quickly for moderate T* to the value given, which

is greater than the length of a single interval. Equivalently, the effective jump time, $(\tau_1^c)_{eff}$, will be increased by the possibility of making two or more coherent jumps.

$$(\tau_1^c)_{eff} = \frac{2 - T^*}{2 - 2T^*} \qquad \text{[III-17b]}$$

The equivalent of a diffusion coefficient for coherent propagation in the interval may be defined as D_c

$$D_c = \frac{1}{2} a^2 \nu_c S_1 T^* \left(\frac{2 - T^*}{2 - 2T^*} \right) \qquad \text{[III-18]}$$

In the limit T* approaches zero, the correlation factor again goes to unity and (18) becomes (9) in the limit $S_1 T^* << 1$. In the opposite limit $T^* = 1$, D_c becomes infinite. This is the proper limit for a purely coherent exciton in an ordered lattice, for which no finite diffusion coefficient can be assigned because the propagation is not diffusive on any time scale.

The effects of coherent vs incoherent propagation in the interval on transfer between intervals show up in the region $S_1 T^* << 1$. Figure 5 illustrates the diffusion coefficients in (9), (15), and (18), normalized by the applicable intermolecular transfer frequency ν, versus the transmission coefficient. The limiting case for "hopping" transfer in the interval shows D_r increasing more slowly than linearly with T*, approaching the diffusion coefficient in (10) asymptotically, while D_c increases slightly faster than linearly in the region shown, diverging to infinity at T* = 1. The variation of D with T* is a function of

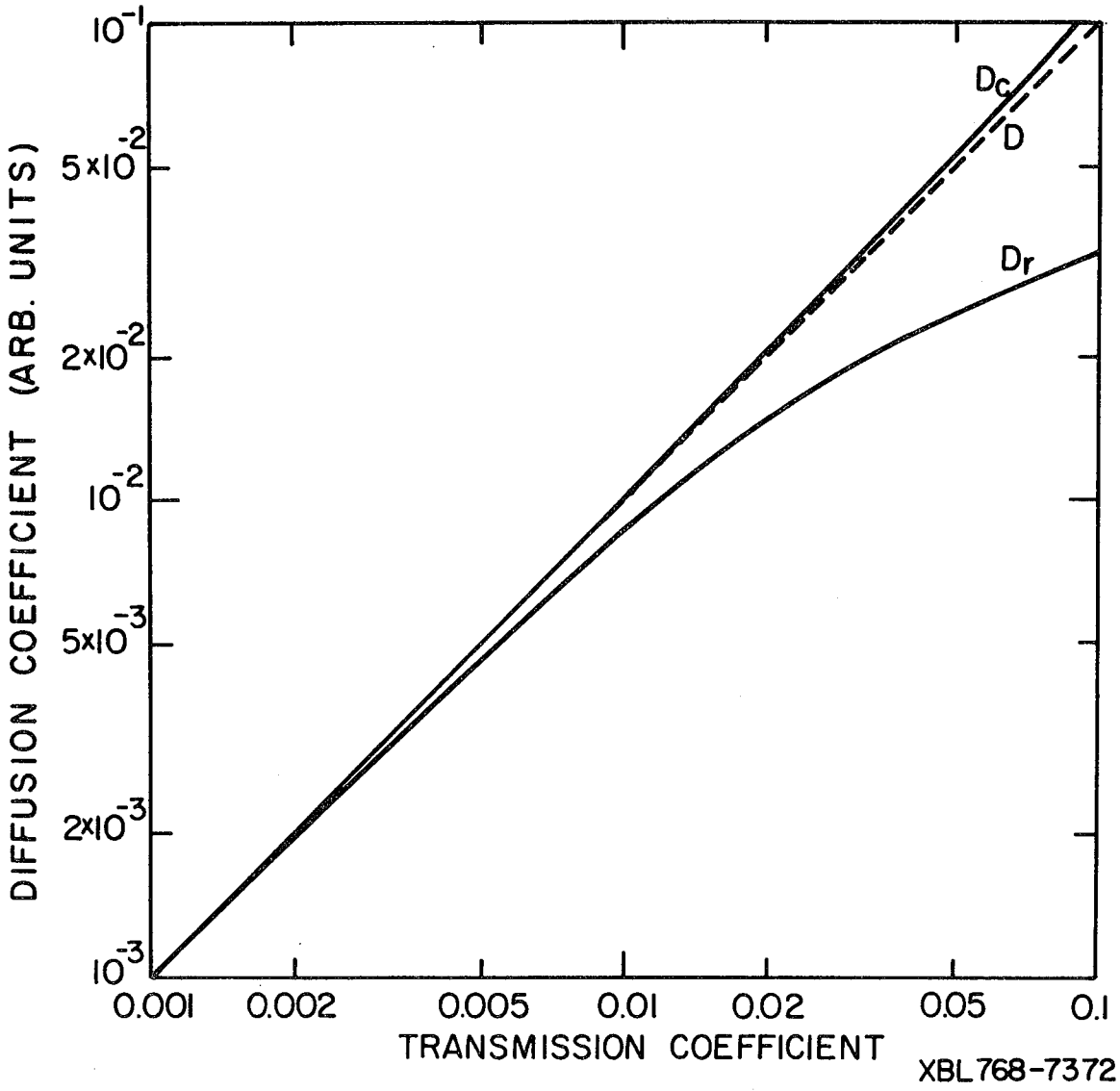

Figure 5. Diffusion coefficients vs. barrier transmission probability for one dimensional simple disordered system.

coherence length, ranging from a coherence length of $\underset{\sim}{a}$ for the hopping mode to an infinite coherence length for D_c. This variation will be particularly sensitive to coherence lengths less than $S_1\underset{\sim}{a}$, the interval width, which could be controlled by impurity concentration in a real system. An experiment where T* also could be varied, such as temperature variation where thermal promotion over barriers is important, should be a useful probe of the exciton coherence length.

IV. EXCITON MIGRATION AND COHERENCE IN RANDOM ARRAYS OF SCATTERERS

1. Introduction

As the mole fraction of a low energy isotopic trap is increased, one expects the potential surface along which the exciton travels to change from a delocalized host band interrupted by localized trap states to extended trap states interrupted by narrow barriers comprising the remaining host molecules. In such cases, the exciton mobility will be limited by the rate of transfer through or around the barrier sites. It is clear that percolation theory cannot be applied to substitutionally disordered systems when the intermolecular interaction responsible for energy transfer is principally between molecules related by translational symmetry along one axis of the crystal and vanishingly small along the others. In these cases, at least three distinct modes of transfer are available: (i) the exciton may tunnel through the higher energy host molecules;[2] (ii) it may be thermally promoted by a phonon to the host band states and make its way to another trap state at a rate dictated by its mobility in a pure band;[53] (iii) finally, if the bandwidth is large enough to mask a much smaller isotopic shift, this analysis is inappropriate and exciton migration will approach an unperturbed-crystal-type behavior termed amalgamation.[22]

In this chapter, we apply these insights to more complex disordered systems, differentiating between mechanisms of energy transfer within the context of the energy partitioning experiments which are the standard probes of such systems.[3] The limiting cases of tunneling and

thermal promotion (as well as a hybrid case) are illustrated for a range of physically realistic parameters.

2. Direct Transfer

Physically realistic and useful models of exciton transfer in a two-component substitutionally disordered system must hold over the entire concentration range. Increased barrier molecule concentration leads to the formation of a statistical distribution of aggregate barriers of two, three or more adjacent barrier molecules and the nature of the transmission process which sets the relative transmission coefficients for the different barriers becomes extremely important. At sufficiently low temperatures, exciton transfer between localized trap states is determined by resonant tunneling. Figure 6 illustrates this process for tunneling from single traps.

If the intermolecular interaction, β, is the same for both components, as in isotopic mixtures, the interaction energy between two traps separated by n barrier molecules[54,55] is

$$\beta_n = \beta^{n+1} \Delta^{-n} \qquad [IV-1]$$

where Δ is the trap depth. A simple quantum mechanical resonance model predicts a transfer time across the barrier.

$$\tau_n = h/4\beta_n \qquad [IV-2]$$

Because the width of the barriers is so critical to the transmission time, the system may be treated within the concept of a hierarchy of barriers. The interval between single barriers will contain S_1 unperturbed trap

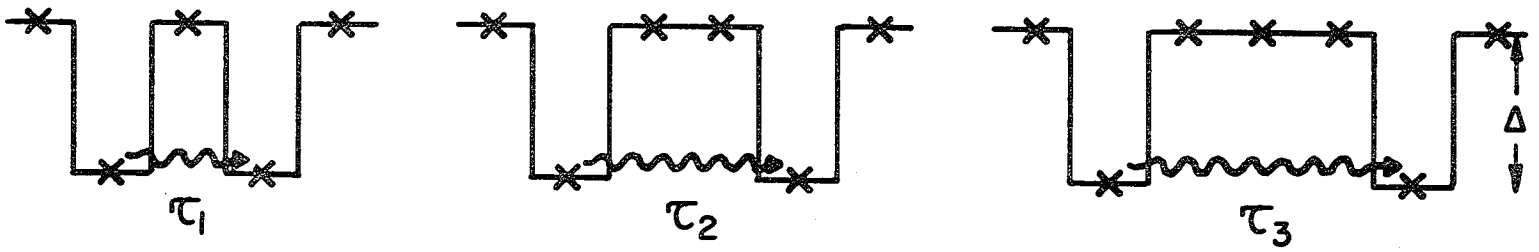

XBL766-7118

Figure 6. Resonant tunneling between traps separated by one, two, and three host molecules.

molecules,

$$S_1 = x^{-1} \qquad \text{[IV-3]}$$

where x is the barrier molecule mole fraction. A random isotopic distribution is assumed. On the next step of the hierarchy, the interval between double barriers contains S_1 intervals bounded by two single barriers or a single barrier and a double barrier, as in Figure 3(b). Likewise, the interval between triple barriers contains S_1 intervals bounded by double barriers and so forth. The important requirement in order to apply this framework to exciton dynamics is that the matrix element for tunneling through a barrier n molecules wide, β_n, is so much less than the matrix element for passing through a barrier n-1 molecules wide, that all smaller intervals within a larger interval will be visited by the exciton before it escapes from the larger interval. This is equivalent to the requirement that $T^* \ll 1$ where $T^* \cong \beta/\Delta$, so that no correlated motions need be considered and exciton transfer between intervals may be treated by simple random walk statistics.

In Chapter III-2, an expression for the effective tunneling time through a single barrier, τ_1^c, was derived. According to the hierarchy of barriers argument, the expression for a double barrier, τ_2^c, can be derived assuming that the basic unit between two double barriers is not a single trap molecule, but an extended trap state between two single barriers. In such cases:

$$\tau_2{}^c = \tau_1^c \langle S \rangle = \Delta^2/\beta^2 x^2 \nu \qquad \text{[IV-4]}$$

The higher terms are derived analogously, with the tunneling time across an n molecule wide barrier determined by a random walk between intervals surrounded by n-1 molecule wide barriers. The general term is given by

$$\tau_n^c = \left(\frac{\Delta}{\beta x}\right)^n \nu^{-1} \qquad \text{[IV-5]}$$

The tunneling model with its characteristic times can be applied to the problem of energy partitioning between "mobile" trap states, out of which the exciton may tunnel, and "stationary" trap states, in which the exciton is trapped over the excited state lifetime. Figure 7 shows schematically the potential surface of such a ternary system. The model proposes that excitons are unable to pass through barriers n+1 or more host molecules wide during the excited state lifetime. The excitons sample intervals between barriers of n hosts according to random walk statistics with a characteristic jump time τ_n^c, and a limiting excited state lifetime, T. The effect of smaller barriers is incorporated within τ_n^c. The fraction of exciton population reaching a stationary trap is a function of the number of sites visited and the site probability (or mole fraction) of the stationary trap, x_s.

Let c_n be the fraction of excitons which do not have access to a stationary trap unless they cross an n+1 molecule wide barrier and t_n be the concentration of barriers n+1 molecules wide or wider. c_n and t_n are given by:

$$t_n = x^{n+1}(1-x) \qquad \text{[IV-6]}$$

$$c_n = \left[(t_n'-1)/t_n'\right]^{x_s'} \qquad \text{[IV-7a]}$$

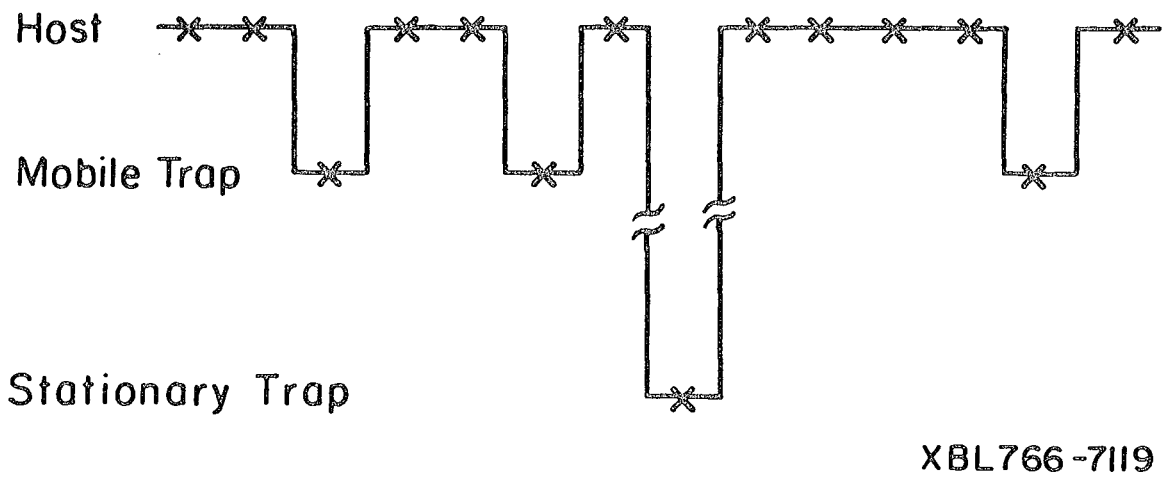

Figure 7. Model of potential surface for energy-partitioning studies. Depth of stationary trap is much greater than kT.

while,

$$x_s'/t_n' = x_s/t_n \qquad x_s',\ t_n' << 1, \qquad \text{[IV-7b]}$$

and c_n converges rapidly for large x_s' and t_n'. x_s' and t_n' are the number of stationary traps and impassable barriers, respectively, in an arbitrarily large volume of the system. t_n' is also the number of intervals between impassable barriers. The probability that one such interval in the arbitrarily large volume will not contain a stationary trap is the number of ways of distributing x_s' traps in all the other $t_n' - 1$ intervals, $(t_n' - 1)^{x_s'}$, divided by the number of ways of distributing these traps in all the intervals, $t_n'^{\,x_s'}$. If x_s', $t_n' >> 10^3$, c_n will be very close to the infinitely large volume result.

The average number of intervals between n-wide barriers sampled is[56] $1.60\ T/\tau_n^c$, so the number of sites sampled N is

$$N = 1.60\sqrt{T/\tau_n^c}\ \ x^{-n}(1-x)^{-1} \qquad \text{[IV-8a]}$$

The number of sites between the two impenetrable n+1-molecule wide barriers is given by N_2 (and represents) the maximum number of sites an exciton may sample within this model. This is given by

$$N_2 = t_n^{-1}, \qquad \text{[IV-8b]}$$

so the smaller of the two quantities N_{min} must be used to derive the percentage of population that reaches a stationary trap before decaying, $\frac{N_{stat}}{N_{total}}$. If unit trapping efficiency is assumed, then the normalized population "probe" (stationary site) is given as:

$$(N_{stat} / N_{total}) = (1 - c_n) \sum_{i=0}^{N_{min}} x_s (1 - x_s)^i \qquad [IV-9]$$

where $(1 - c_n)$ is a factor that accounts for those excitons which do not have a stationary trap accessible to them.

If the fractional population of the stationary trap is plotted against the guest mole fraction, the statistical treatment of the tunneling model is characterized by a sharp transition from low to high stationary trap population as shown in Figure 8. These curves are surprisingly similar to those for the onset of macroscopic[57] percolative conduction in two- and three-dimensional systems. Figure 8 shows that when the stationary trap population, x_s, is reduced, approaching a limit where the exciton must travel a macroscopic distance to reach a stationary trap, the transition threshold becomes more sharply defined. In percolation theory, a similar sharpening takes place as the size of the interconnected clusters increases. Variations of other parameters, such as excited state lifetime, T, or barrier size limits, n, does not qualitatively change the nature of the single sharp concentration threshold. This is illustrated in Figure 9.

3. Indirect Transfer

Thermal detrapping and migration along host band states is an important alternative mechanism for exciton transfer along a substitutionally disordered potential surface. Fayer and Harris[53] proposed a two-step model for thermal promotion where the trapped exciton is first promoted to a state degenerate with the host band and then decays into

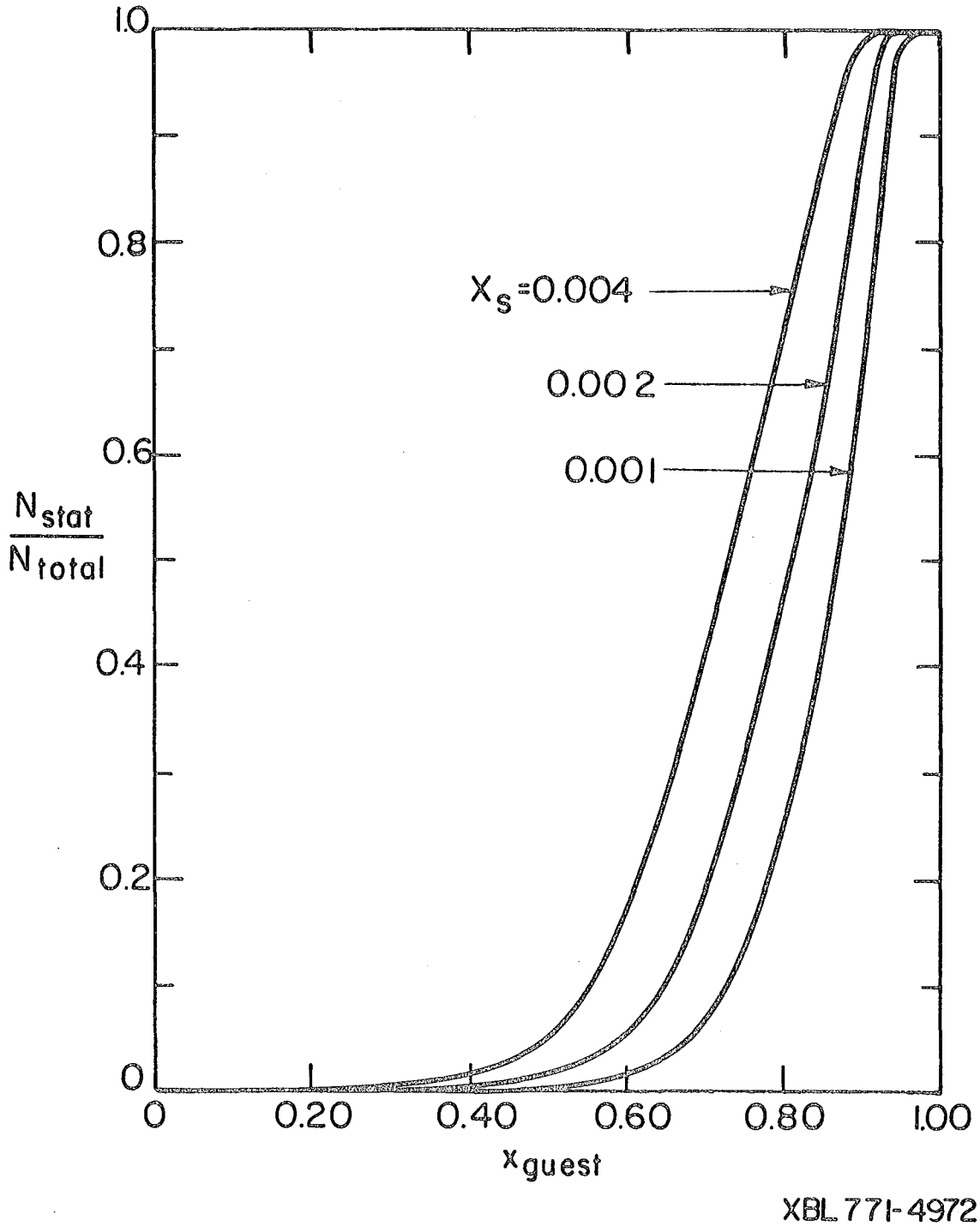

Figure 8. Resonant tunneling model: fraction of population reaching stationary trap vs. mobile fraction. Stationary trap concentration is varied. ($n = 4$, $\beta = 0.3$ cm^{-1}, $\Delta = 21$ cm^{-1}, $T = 25$ msec.)

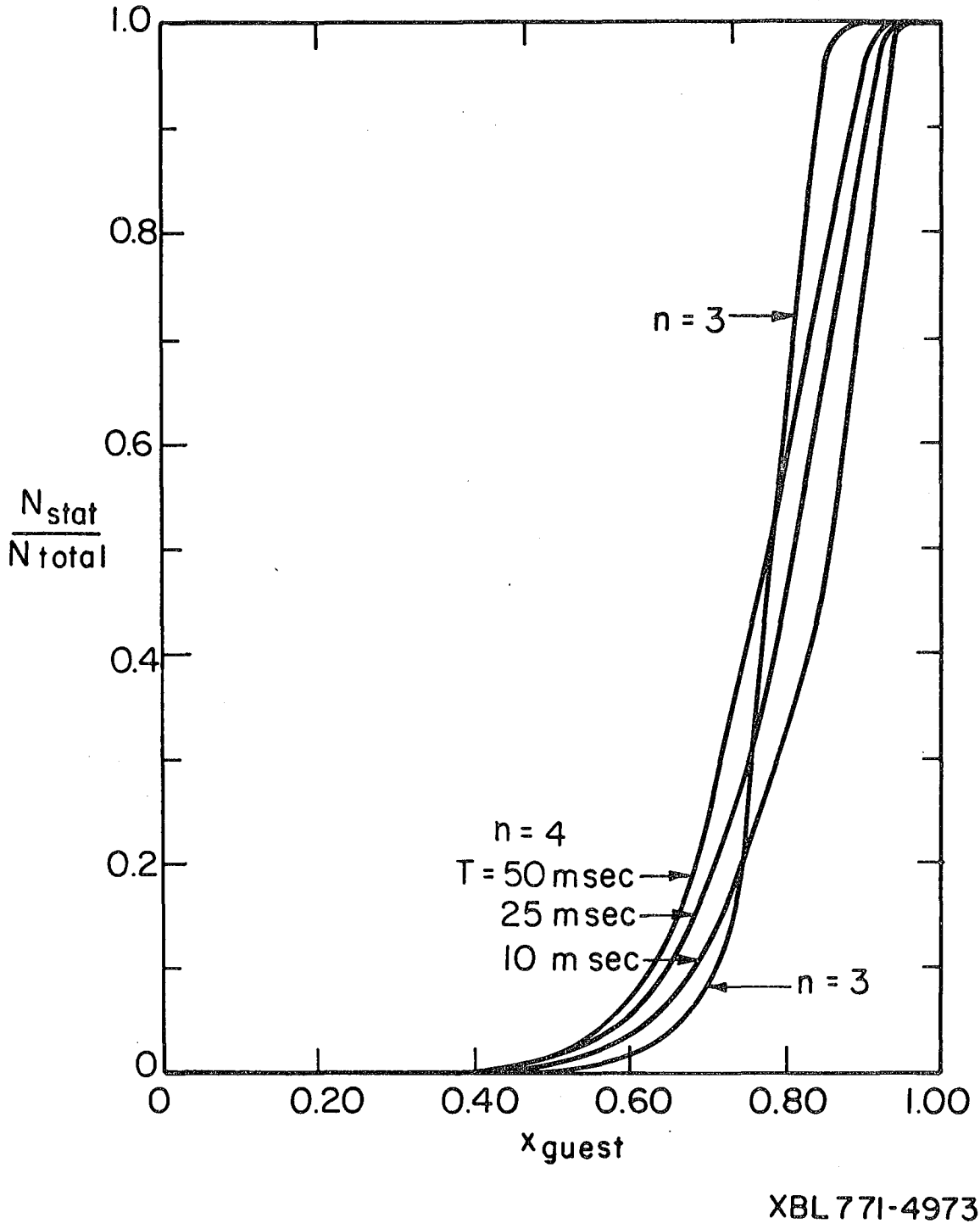

Figure 9. Resonant tunneling model; fraction of population reaching stationary trap vs. mobile trap mole fraction. Excited state lifetime and maximum penetrable barrier size are varied. ($x_s = 0.002$, $\beta = 0.3$ cm^{-1}. $\Delta = 21$ cm^{-1}; for n = 3, T = 25 msec.)

the manifold of band states, with the combined rate given by

$$K_{\varepsilon k} = \frac{2\pi}{h} \langle n(\varepsilon)\rangle_T \left| \langle \tau P(\varepsilon) \left| H_{TP} \right| \tau_i \; P(\varepsilon - E_i)\rangle \right|^2$$

$$\cdot \left| \langle \tau_i \; P(\varepsilon - E_i) \left| H_{TE} \right| kP(\varepsilon - E_i)\rangle \right|^2 \rho(E_i) \qquad \text{[IV-10]}$$

where the matrix elements represent coupling of exciton with phonon and exciton-phonon complex with band, respectively. τ is the trap state, τ_i is the exciton-phonon excited state, and k is a host band state.

The rate of thermal promotion to the band must be distinguished from the rate of exciton migration to another trap. Few experimental determinations of the ratio of these rates given by the migration efficiency α are available.[58] If the problem of migration through the real barrier band states is treated as a one-dimensional random walk with absorbing barriers i.e., the trap states, the efficiency α is given by,

$$\alpha = \frac{1}{n+1} \qquad \text{[IV-11]}$$

where n is the barrier width. One notes that α increases as the barrier width n decreases or as the exciton coherence length in the band increases. Since the coherence length is a strong function of exciton-phonon coupling and therefore of temperature, α is temperature dependent as well as concentration dependent. This effect will not be considered in detail here although it can be incorporated parametrically into the equations.

An energy partitioning model for transfer by thermal promotion can be proposed which is a one-dimensional random walk where the characteristic effective jump time across an <u>average</u> barrier is $\langle K_{\varepsilon k}^{-1} \; \alpha^{-1} \rangle$.

Certain assumptions are made. (i) $K_{\varepsilon k}$ is independent of barrier width and may be expressed as a constant times a Planck distribution function for the phonon density of states at the barrier height Δ: i.e.

$$K_{\varepsilon k} = He^{-\Delta/kT} \qquad \text{[IV-12]}$$

(ii) α is averaged over a statistical distribution of barrier widths;

$$\langle\alpha\rangle = \sum_{i=1}^{\infty} \left(\frac{1}{i+1}\right)x^i(1-x)^2 \Big/ \sum_{i=1}^{\infty} x^i(1-x)^2 \qquad \text{[IV-13a]}$$

$$\langle\alpha\rangle = \frac{1-x}{x^2}\left[\ln\left(\frac{1}{1-x}\right)-1\right] \qquad \text{[IV-13b]}$$

and (iii) unit trapping efficiency is assumed. As in the tunneling model, the number of jumps made is the exciton lifetime divided by the jump time $\langle K_{\varepsilon k}^{-1}\,\alpha^{-1}\rangle$. Finally, (iv) thermal promotion is the rate limiting step in exciton transfer, as opposed to diffusion within trap or band. The number of intervals sampled goes as the square root of the number of jumps, and the number of sites sampled, N, is

$$N = 1.60\sqrt{TK_{\varepsilon k}\langle\alpha\rangle}\;x^{-1}(1-x)^{-1}, \qquad \text{[IV-14]}$$

hence,

$$\frac{N_{stat}}{N_{total}} = \sum_{i=0}^{N} x_s(1-x_s)^i \qquad \text{[IV-15]}$$

Representative curves are shown in Figure 10. Note that N_{stat}/N_{total} is now temperature dependent with an activation energy of $\Delta/2$ because of the square root in N. In these cases the temperature dependence of the "probe" site would show a composition independent activation energy $\Delta/2$.

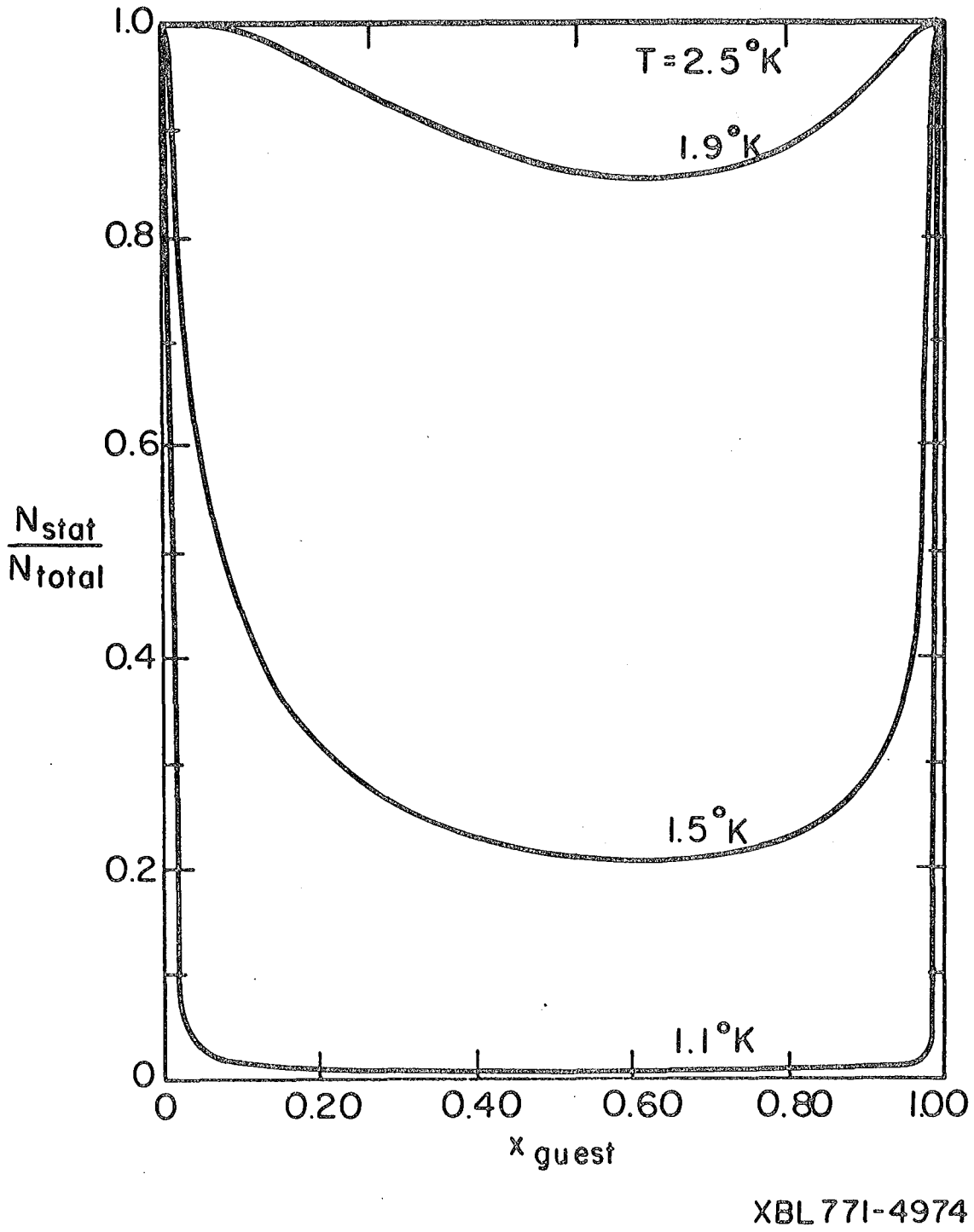

Figure 10. Thermal detrapping model; fraction of population reaching stationary trap vs. mobile trap mole fraction. Temperature is varied ($x_s = 0.002$, $H = 3 \times 10^{10} s^{-1}$, $\beta = 0.3$ cm^{-1}, $\Delta = 21$ cm^{-1}, $T = 25$ msec).

4. Hybrid Transfer

As we have shown resonant tunneling between exciton-phonon complexes across a barrier contributes significantly to the overall tunneling rate. However as the population of phonon states decreases with increasing energy, fewer states are promoted. The decrease in effective barrier height upon promotion results in an enhanced tunneling rate. This effect becomes more important as the barrier width increases. The quantum mechanical rate, $k(n,\varepsilon)$, from an energy ε above the original trap state (Figure 11), is given as the Boltzmann average over ε from 0 to $\Delta-\delta$, where $\Delta-\delta$ is some energy below the barrier band states. Equations (1) and (2) still hold in this case and hence the averaged rate is given by:

$$\langle k(n)\rangle_{\varepsilon} = \int_{o}^{\Delta-\delta} \left[\frac{h}{4\beta^{n+1}} (\Delta-\varepsilon)^{n}\right]^{-1} e^{-\varepsilon/kT} d\varepsilon \Big/ \int_{o}^{\Delta-\delta} e^{-\varepsilon/kT} d\varepsilon \qquad [IV-16]$$

The hierarchy of barriers argument used in Section IIIA must be invoked in the limit where $kT << \Delta$, if it is valid for the same parameters in the pure tunneling model. In the high temperature limit, the thermal promotion model of Chapter IV-3 is more appropriate and the escape time from an interval bounded by n- molecule wide barriers is given as

$$\tau_n^c = x^{-n}/\langle k(n)\rangle_{\varepsilon} \qquad [IV-17]$$

Equations (6) through (9) may be used to calculate the energy partitioning ratio incorporating equation τ_n^c of Equation (17). Representative curves are shown in Figure 12. An interesting result of this model is that the tunneling model now shows an activation energy and the value

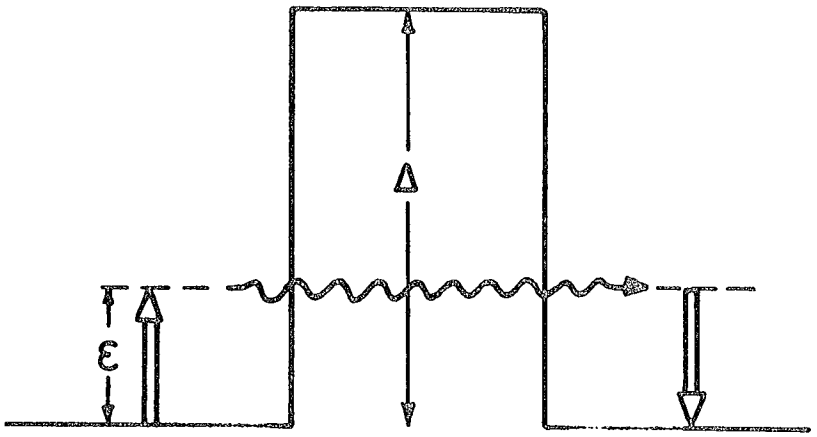

XBL771-4970

Figure 11. Model for hybrid tunneling.

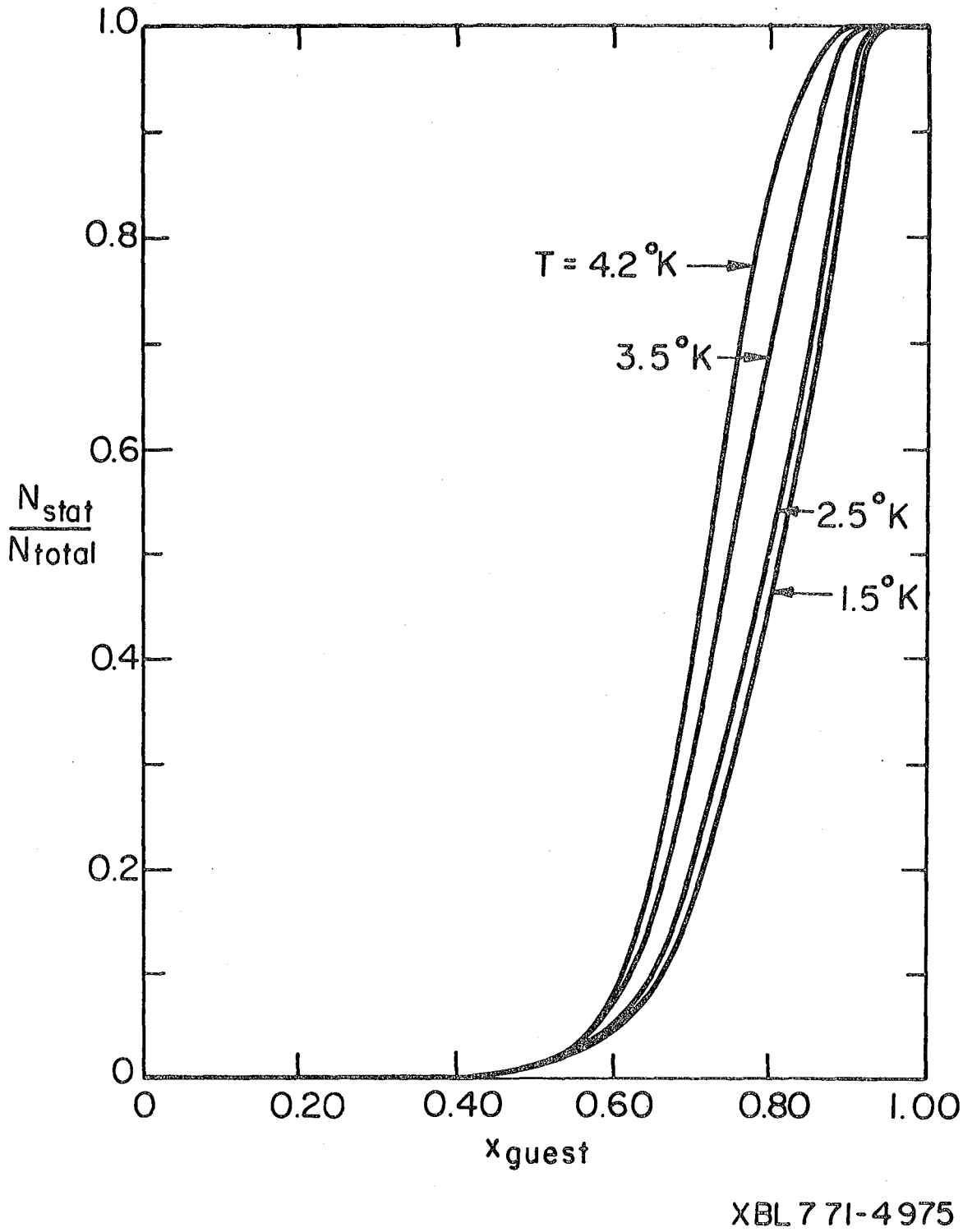

Figure 12. Hybrid tunneling model; fraction of population reaching stationary trap vs. mobile trap mole fraction temperature is varied (x_s = 0.002, β = 0.3 cm^{-1}, Δ = 21 cm^{-1}, T = 25 msec, n = 4).

experimentally measured will be a function of concentration (Figure 13). This may be seen physically as follows. A wide barrier will show a larger effective activation energy $\langle\varepsilon\rangle$ than a small barrier. Quantitatively, $\langle\varepsilon\rangle$ is given as:

$$\langle\varepsilon\rangle = \int_0^{\Delta-\delta} (\varepsilon)k(n,\varepsilon)\, e^{-\varepsilon/kT}\, d\varepsilon \Big/ \int_0^{\Delta-\delta} k(n,\varepsilon)\, e^{-\varepsilon/kT}\, d\varepsilon \qquad \text{[IV-18]}$$

because activated tunneling becomes more favorable as n increases. As the barrier molecule concentration, x, grows, the effective activation energy averaged over the statistical distribution of barriers, $\langle\langle\varepsilon\rangle\rangle_n$, grows

$$\langle\langle\varepsilon\rangle\rangle_n = \sum_{n=1}^{\infty} \langle\varepsilon\rangle\, x^n(1-x)^2 \Big/ \sum_{n=1}^{\infty} x^n(1-x)^2 \qquad \text{[IV-19]}$$

because the distribution shifts to larger n and more wide barriers. Similarly, Figure 13 shows that this expression for the average activation energy will be a strong function of temperature. Higher temperatures will increase transmission rates through wide, high activation energy barriers disproportionately, thus increasing the average activation energy. The net result is that the transfer of excitation proceeds via tunneling at the low barrier limit to thermal promotion at the other limit. This is the physical basis for the apparent activation energy being dependent on the composition of the crystal. This is an important prediction and will be dealt with in a more detailed fashion in the next chapter.

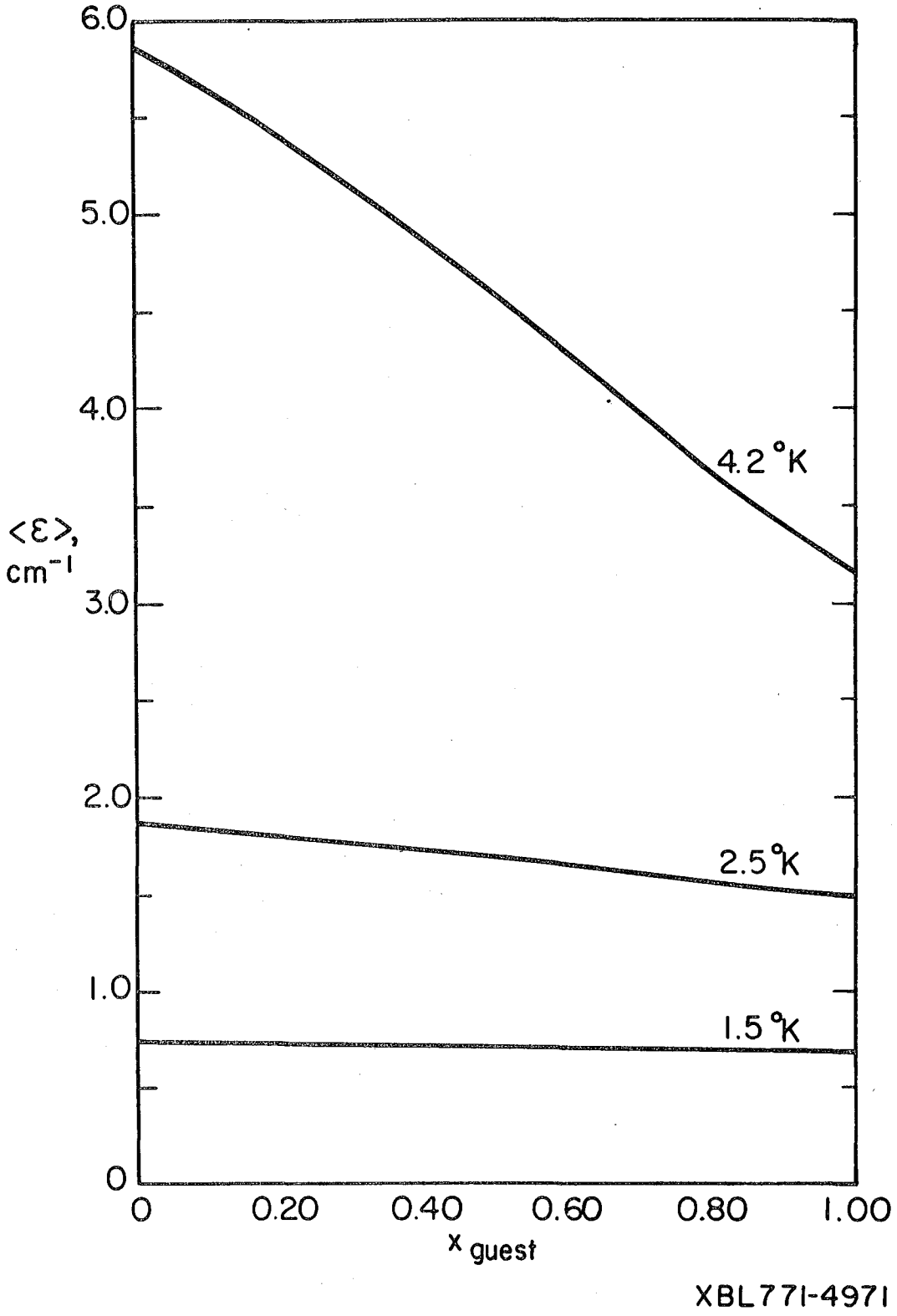

Figure 13. Calculated activation energy for hybrid tunneling. (parameters are the same as in Figure 11)

V. EXCITON MIGRATION AND COHERENCE IN ISOTOPICALLY MIXED 1,2,4,5-TETRACHLOROBENZENE

1. Introduction

The effect of substitutional disorder on energy transfer in molecular crystals has commanded much interest since El-Sayed, Wauk, and Robinson[59] observed the quenching of phosphorescence by chemical impurities. In particular, the mediation of trap-trap interactions by the crystal host, as is common in isotopic mixed crystals, has been investigated by observing triplet-triplet annihilation,[60] delayed fluorescence,[61] and energy partitioning between mobile and stationary traps.[3] Several models have been proposed and experimentally supported to explain long-range exciton transfer between localized trap states, such as quantum tunneling through virtual states of the host,[2] thermal detrapping and migration though real states of the host,[53] and percolation through a continuous trap sublattice in the system.[3-5]

One-dimensional propagation of Frenkel excitons is well established in several systems,[35,36,62] but the apparently simple theoretical tractability of the problem has not attracted many investigators. Hochstrasser and Whiteman[62] discussed qualitatively the quenching of defect phosphorescence in dibromonaphthalene with increased deuteration of the sample. More elegant theoretical treatments, such as that of Greer[47,48] for exciton propagation through a random array of scatterers, bear little relation to the experimental realities of exciton-phonon coupling and the detailed dynamics of exciton-barrier scattering.

The fourth chapter presented two semi-empirical models for exciton diffusion in a one-dimensional substitutionally disordered system: (i) pure and thermally-assisted tunneling between trap states and (ii) thermal promotion to the host band and migration to another trap state. Both mechanisms have been previously observed experimentally for short-range exciton transfer.[2] Chapter IV derived analytic expressions for long-range multi-event exciton transfer across a statistical distribution of one-dimensional trap and host clusters for both models, taking the energies and aggregation of the host and trap molecules, the dimensionality of intermolecular interactions, and exciton-phonon coupling into account phenomenologically.

In this chapter, we present experimental results for singlet and triplet exciton transfer in a one-dimensional exciton conductor, 1,2,4,5-tetrachlorobenzene, measured by phosphorescence-monitored energy partitioning between mobile trap states and stationary trap states. We will interpret the concentration and temperature dependence of the partitioning ratio in terms of the models presented. The difference between singlet and triplet exciton migration will be related to the limit of mixed crystal band structure amalgamation.[22,63]

The substitutionally disordered one-dimensional band is prepared by isotopic substitution. The perprotonated compound (h_2-TCB) acts as a trap 22 cm^{-1} below the perdeuterated host molecules (d_2-TCB), which may also be referred to as the barrier molecules in the limit of high trap mole fraction and low temperature. The energies of the lowest triplet state of the host d_2-TCB band and the h_2-TCB substituent are determined

spectroscopically. The energy of the $^3B_{1u}$ state of the isolated h_2-TCB molecule in the d_2-TCB host is also the energy of the center of the $^3B_{1u}$ h_2-TCB band in the neat h_2-TCB crystal. The same holds true for the deuterated compound.

The triplet manifold is populated directly by excitation with a high intensity pulsed dye laser source or by intersystem crossing from the singlet state after excitation into the singlet with a wideband source. The excitation is generally mobile, being transferred between h_2-TCB molecules along the one-dimensional chains via the d_2 band (ii) or directly via tunneling (i). h_2-TCB constitutes the mobile trap. In order to monitor the dynamics of transfer in the TCB manifold, a small amount of pyrazine is substituted in the lattice. The pyrazine $^3B_{2u}$ state is 148 cm^{-1} below the d_2-TCB band, sufficiently far below all TCB bands that excitation transferred from TCB to pyrazine remains at the pyrazine until decay to the ground state occurs. Pyrazine therefore constitutes the stationary trap. The important energy levels are shown schematically in Figure 14.

2. Experimental

a) Sample Preparation and Characterization

The h_2-TCB was from Aldrich Chemical and the deuterated compound was prepared as described elsewhere. A 97.5% deuteration was achieved. Both compounds were zone-refined for 150 passes. The pyrazine was Aldrich Gold Label, 99+%, and used without further purification.

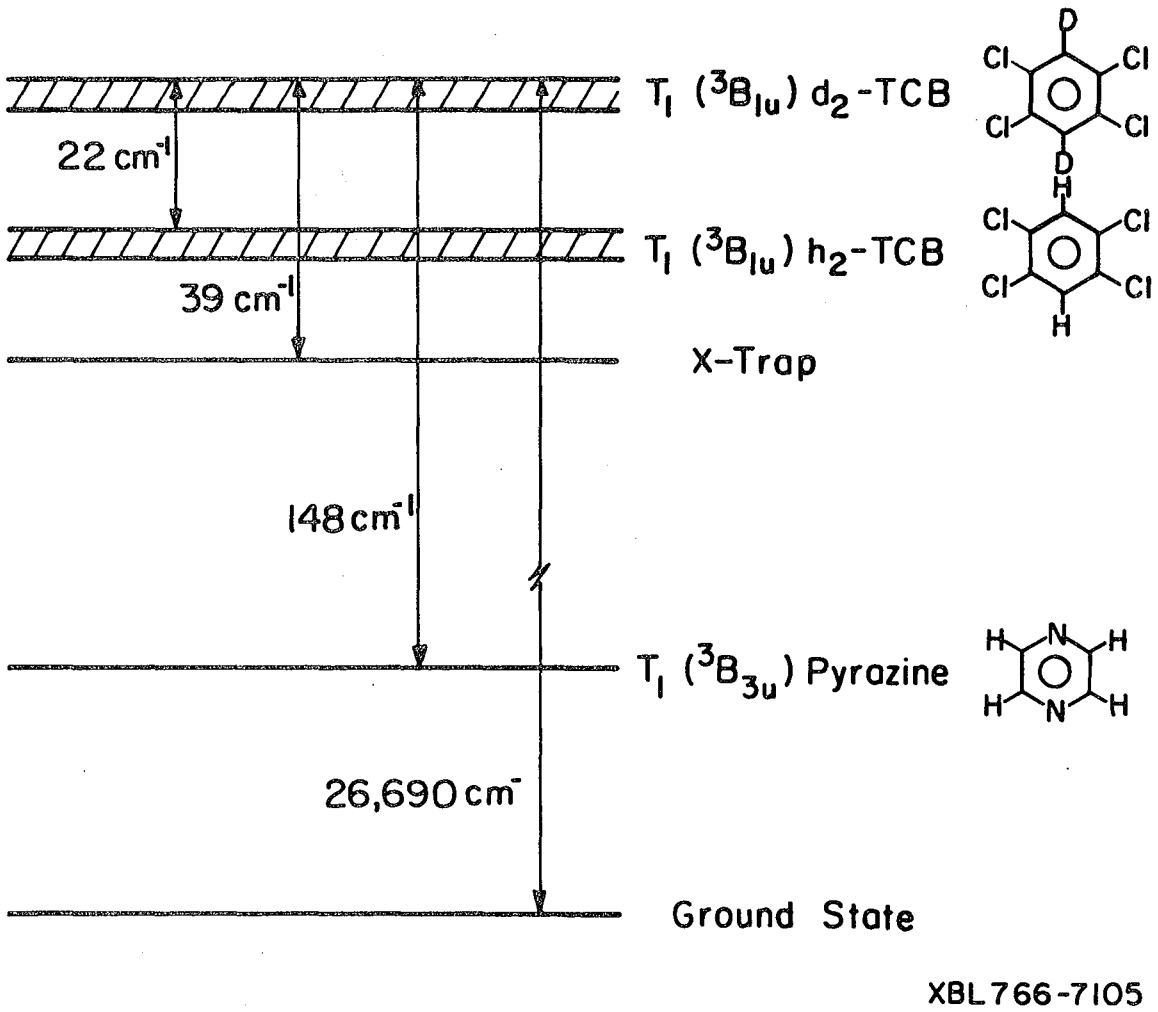

Figure 14. Energy levels of ternary TCB-pyrazine system.

Crystals were grown by standard Bridgeman techniques under carefully standardized crystallization conditions and annealed in their crystal-growing tubes for ten days at 135°C. The desired proportion of h_2- and d_2-TCB (m.p. 139.5-140.5°C) was doped with 5% pyrazine (m.p. 54°C), most of which was expelled from the TCB lattice during crystallization and formed a polycrystalline mass on the top of the boule which was discarded.

The relative concentration of h_2- and d_2-TCB was confirmed by low resolution mass spectra. The pyrazine concentration was below the sensitivity threshold of the mass spectrometer, giving an upper limit of 0.1 mole percent. Comparison of emission for a crystal with low known h_2-TCB fraction in the first series gives a pyrazine mole fraction of 0.0004. The quantity can remain, however, an adjustable parameter. The pyrazine emission is identified by its vibrational structure and the doublet site-splitting of the peaks due to hydrogen bonding onto a neighboring h_2- or d_2-TCB molecule.[64] The hd-TCB trap, although present in concentrations up to 4 mole percent, is rapidly depopulated by thermal promotion and is not observed. In pure h_2-TCB crystals, both h_2-TCB exciton emission and x-trap emission is observed. The x-trap is 40 cm^{-1} below the band and it can in all likelihood be ascribed to a mechanical defect in the lattice along a dislocation plane, although the exact nature of the state is unknown. The x-trap was treated as an additional stationary trap whose concentration remained a constant fraction of stationary emission.

b) Sample Excitation

The phosphorescent triplet state was excited directly with a Molectron UV1000/DL300 nitrogen-laser-pumped dye laser with PBD (Eastman Kodak, λ_{max} 380 nm) in dioxane undoubled. In these experiments, the h_2-TCB triplet vibronic origin was pumped, having been identified by a phosphorescence monitored excitation spectrum. The singlet state was excited with a broadband Hg lamp with Schott 2800 Å UV interference filter. The crystal samples were mounted in a cryogenic dewar in contact with liquid helium whose temperature could be maintained between 4.2 K and 1.4 K by pumping. Phosphorescence at right angles to the excitation source was focussed on the slits of a Spex 3/4 m spectrometer and detected with an EMI 6256 photomultiplier tube. All vibronic peaks for the first 200 angstroms beyond the triplet origins were measured from the original spectra by peak height and halfwidth.

Due to the pulsed nature of the dye laser triplet excitation, several experiments were repeated to confirm that different laser repetition rates and detector time constants did not effect the energy partitioning ratios. Experiments were also repeated with neutral density filters between laser and crystal, showing only linear changes in phosphorescence intensity. Non-linear effects were therefore presumed to be insignificant. Laser emission was not strongly polarized and crystals were mounted with the c axis perpendicular to both excitation and detection axes, so polarization effects were not considered.

c) One-Dimensional System

The system we have chosen for this investigation, 1,2,4,5-tetrachlorobenzene (TCB), has been shown from a variety of criteria [36,65] to be almost exclusively one-dimensional in its triplet band along a translationally equivalent axis in the tetrachlorobenzene crystal structure[66] is such that they stack along the c axis with the planes of the aromatic rings parallel to one another at an angle of 66° to the c axis. This is illustrated in Figure 15. The adjacent molecules are separated by 3.86 Å along the c axis although the distance between molecules along an axis normal to the planar benzene rings is only 3.53 Å. Translationally equivalent molecules along the other axis are separated by 9.6 Å and 10.5 Å. As a result of the structure, the largest intermolecular interaction, β_c, in the $^3B_{iu}$ triplet state is along c. It has been shown that the triplet band along c is ~ 1.25 cm^{-1} wide[67] while that associated with the translationally non-equivalent molecules is less than 10^{-5} cm^{-1}.[36] To a first approximation then, the ratio of the translationally equivalent to nonequivalent interactions is greater than 10^5 and one expects the system to be accurately described by a one dimensional band structure in the triplet manifold.

3. Results and Discussion: Triplet Excitation

The ratio of stationary trap phosphorescence to total phosphorescence for direct triplet excitation into the h_2-TCB band is plotted against h_2-TCB mole fraction in Figure 16. The x-trap comprises a constant percentage (± 5%) of the stationary trap phosphorescence.

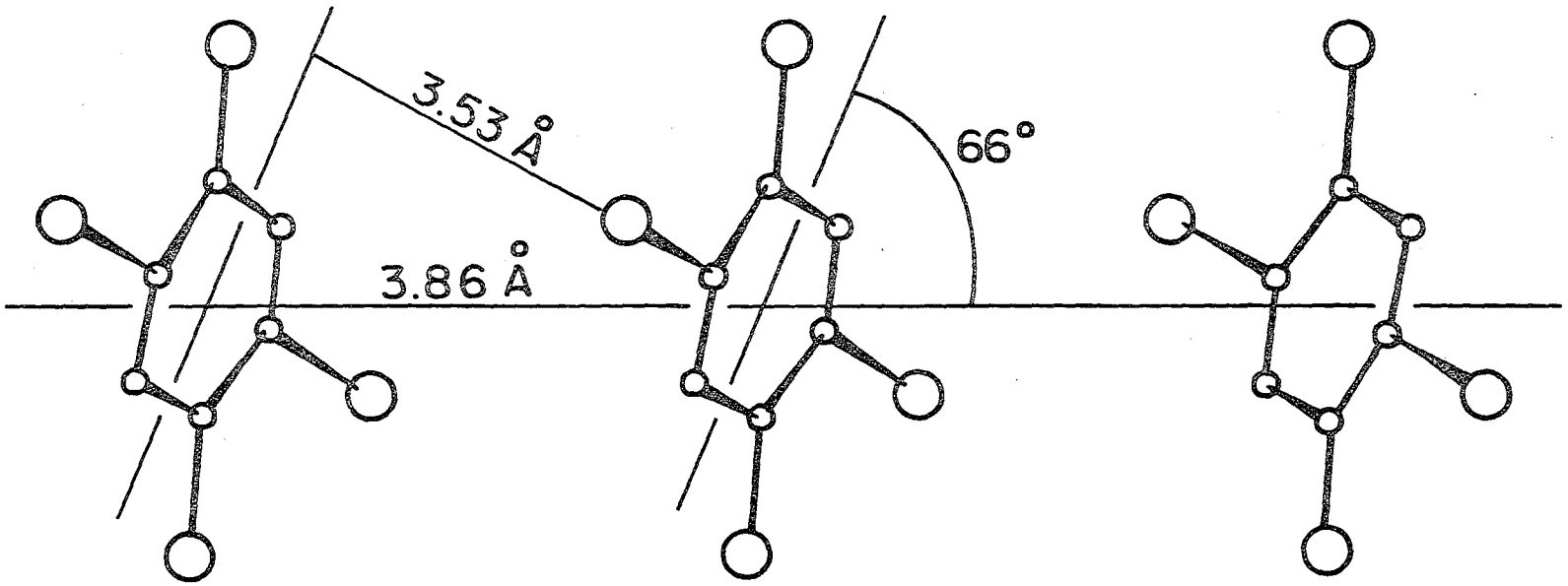

XBL 766-7104

Figure 15. Intermolecular separation of translationally equivalent molecules along c axis.

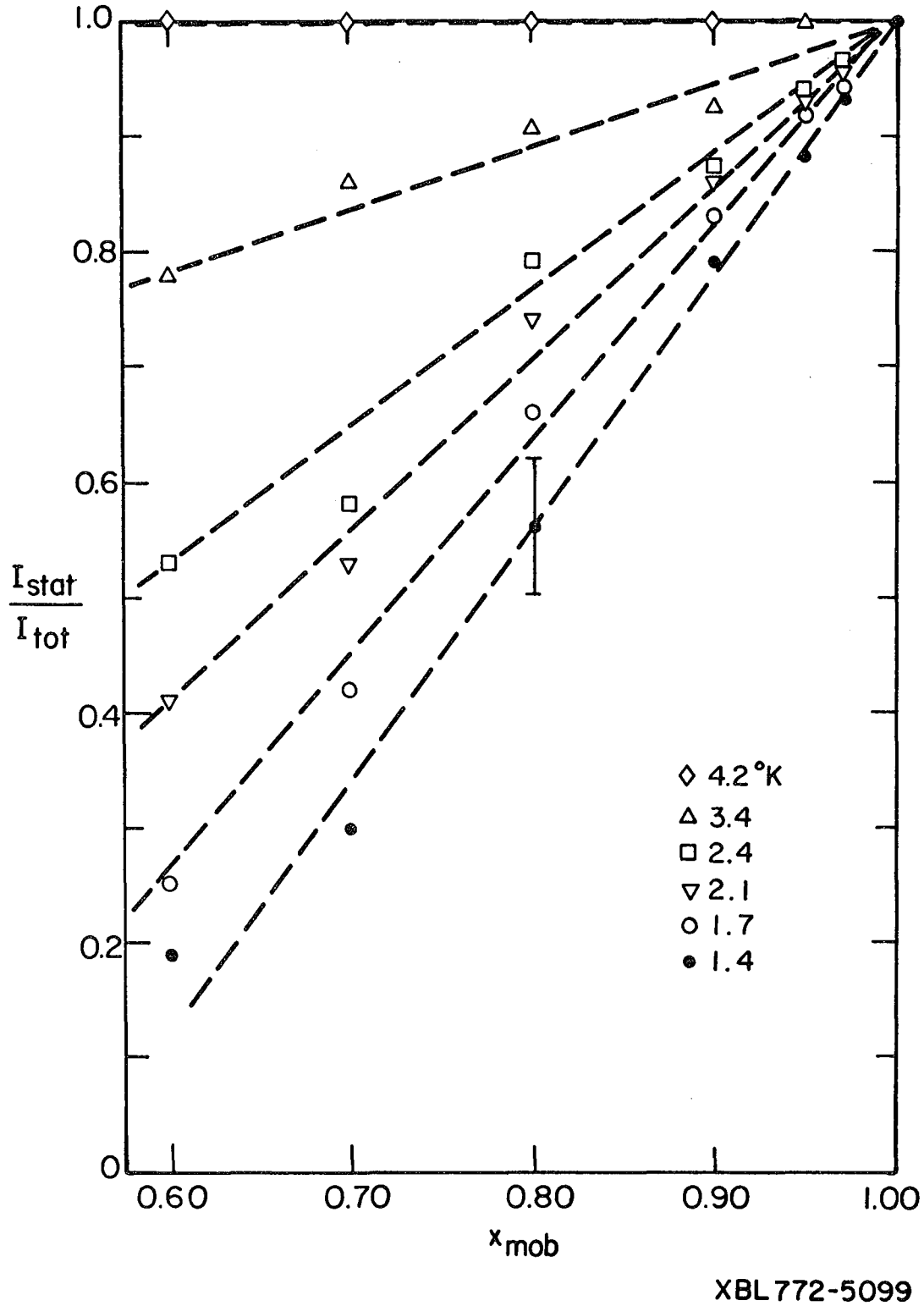

Figure 16. Ratio of stationary trap (pyrazine and x-trap) phosphorescence intensity to total phosphorescence intensity vs. x_{mob}, the mole fraction of the mobile trap. Dotted lines are linear least squares fit to experimental points.

Preliminary work at 1.4 K has shown an absence of stationary trap phosphorescence below $x_h = 0.50$ and a gradual increase to include all emission at $x_h = 1.0$. For the region above $x_h = 0.60$, Figure 16 shows that stationary trap phosphorescence increases regularly with mobile trap concentration and temperature. The temperature dependence for each crystal is plotted in an Arhennius-type plot in Figure 17, where it shows a linear dependence with a different activation energy at each concentration.

The delayed onset of pyrazine phosphorescence is strong confirmation of the one-dimensional nature of the intermolecular interaction. Percolation theory states that an unblocked site probability (corresponding to a mobile trap probability in this context) of 50% in a two-dimensional rectangular lattice and 25% in a cubic lattice will establish a complete network of adjacent trap states within a macroscopic sample.[42] The rapid communication between trap sites in such a network would enable the h_2-TCB trap to populate the stationary states within the triplet state lifetime. Such behavior has been observed in naphthalene, a two-dimensional exciton conductor, although the sharp transition between mobile trap and stationary trap emission occurs well below the predicted 50% threshold due to long-range tunneling between traps or a small intermolecular interaction along the third crystal axis.[3]

In Chapter IV, we proposed two models to describe exciton migration in a one-dimensional isotopically disordered system in the narrow bandwidth limit. We have attempted to fit the experimentally observed phosphorescence intensity distribution of Figure 16 to the trap population distributions calculated for the detrapping and tunneling models. Most

Figure 17. Relative stationary trap phosphorescence vs. reciprocal temperature. Solid lines are least squares fit for different crystals identified by h_2-TCB mole fraction. Activation energies are 2.4 cm^{-1} for $x_{mob} = 0.6$, 1.7 cm^{-1} for $x_{mob} = 0.7$, 0.84 cm^{-1} for $x_{mob} = 0.8$, 0.24 cm^{-1} for $x_{mob} = 0.9$, and 0.19 cm^{-1} for $x_{mob} = 0.95$.

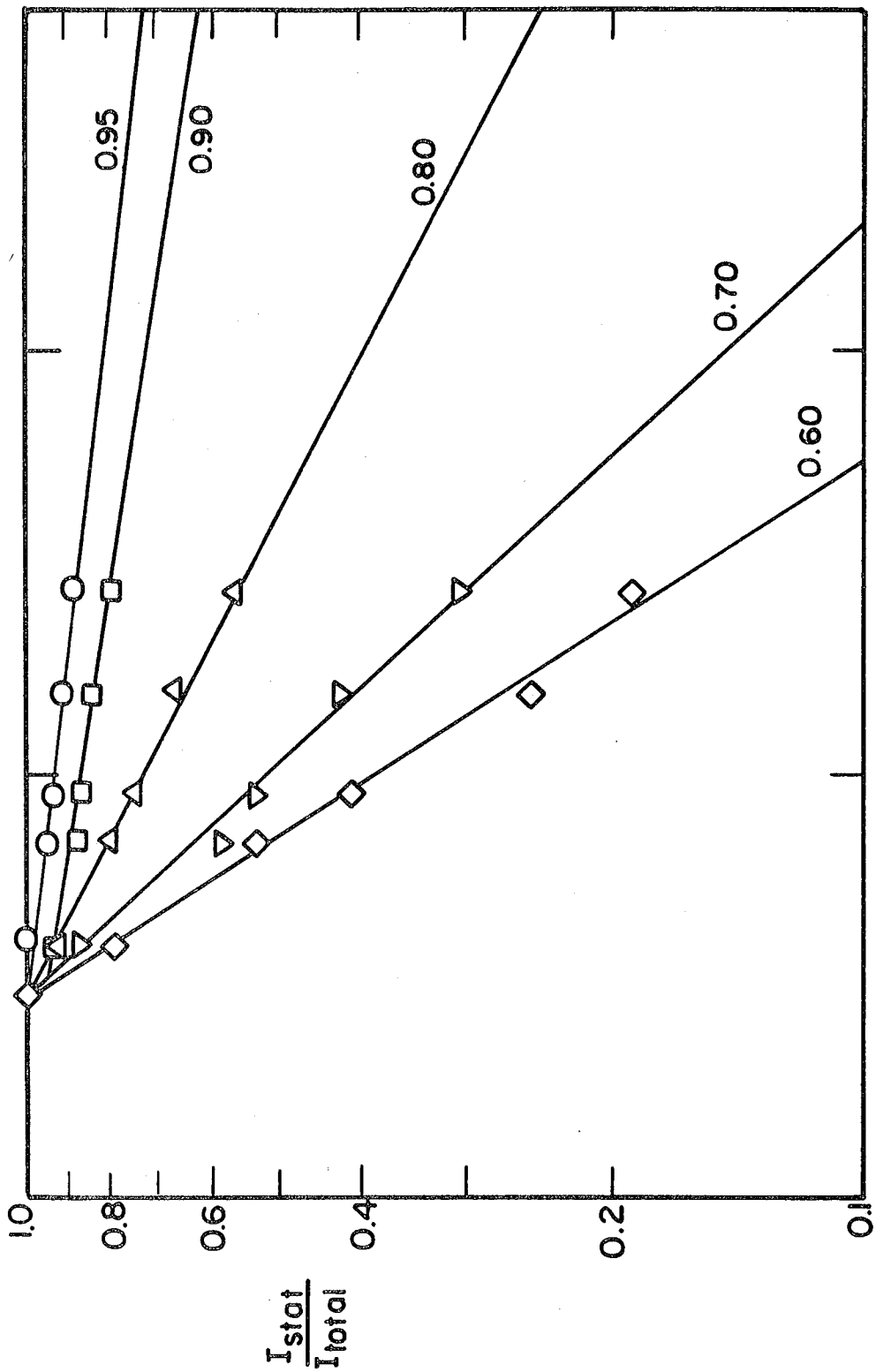

XBL 766-7111

Figure 17

model parameters, including triplet state lifetime T, intermolecular interaction β, isotopic splitting Δ, and pre-exponential detrapping frequency H, have been evaluated in previous work.[2,34,36] Only the stationary trap concentration x_s could not be accurately obtained.

The thermally-assisted tunneling model proposes that exciton transfer takes place exclusively along the one-dimensional chain in a random walk between mobile trap states by tunneling through host molecule barriers. The tunneling rate through a barrier n molecules wide, k(n), falls with increasing barrier width n and trap depth Δ

$$k(n) = 4\beta^{n+1}/\Delta^{n}\, h \qquad [V\text{-}1]$$

and above a certain width, the barriers may be treated as impenetrable during the excited state lifetime. Transmission is dependent on temperature because tunneling may take place from a state thermally promoted above the mobile trap origin. Because of the nth power dependence of the tunneling rate on Δ, a small decrease in Δ may greatly increase the average thermally-assisted tunneling rate

$$\langle k(n)\rangle_{\varepsilon} = \int_{o}^{\Delta-\delta} \left[\frac{h}{4\beta^{n+1}}\,(\Delta-\varepsilon)^{n}\right]^{-1} e^{-\varepsilon/kT}\, d\varepsilon \Big/ \int_{o}^{\Delta-\delta} e^{-\varepsilon/kT}\, d\varepsilon \qquad [V\text{-}2]$$

where ε is the energy of the phonon-exciton complex above the mobile trap origin and the constraint $\Delta >> \delta >> \beta$ insures that the average will not be carried over a region where Equation 1 breaks down. This formulation of the tunneling model holds only in the limit $kT << \Delta$. The population distributions in Figure 18 are calculated for a random walk over a statistical distribution of barriers. Salient features are a roughly linear

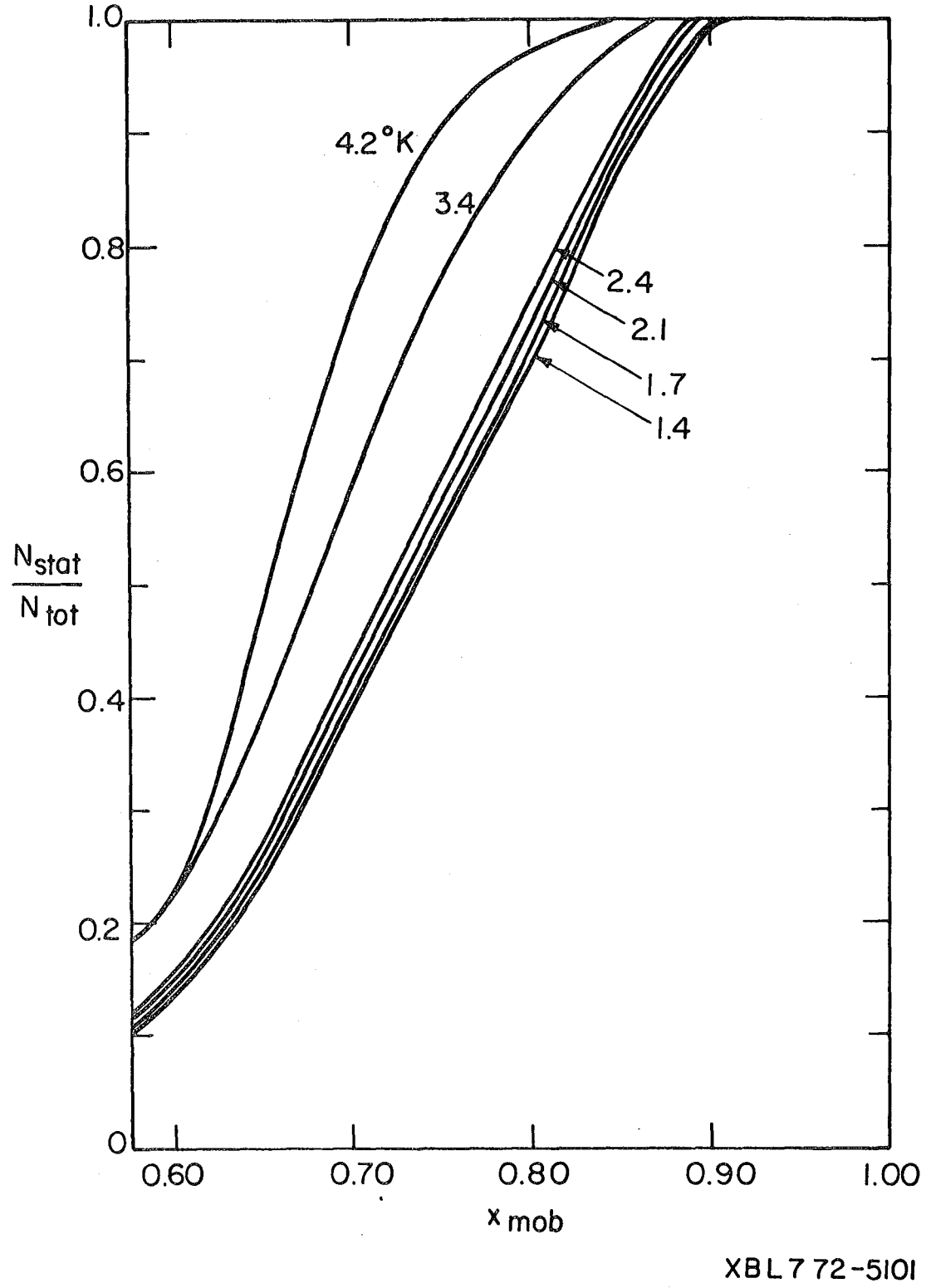

Figure 18. Calculated population partitioning ratio for thermally-assisted tunneling transfer vs. h_2-TCB mole fraction between 1.4 and 4.2 K. Parameters are T = 25 msec, β = 0.3 cm^{-1}, $\delta = 1/2\ \Delta$, and $x_s = 0.002$. Maximum penetrable barrier is 4 d_2-TCB molecules wide.

concentration dependence on x_{mob}, the mobile trap mole fraction, in the threshold region, a weak temperature dependence below 2.4 K, and a concentration dependent activation energy.

Figure 19 shows the corresponding curves generated for the thermal detrapping model, where barrier transmission occurs by thermal promotion of an exciton from a mobile trap state to the host barrier states and subsequent migration along the one-dimensional chain to another trap site. The probability of migration to a new site relative to retrapping at the original site is accounted for by the migration efficiency α. The barrier transmission rate is the product of the detrapping rate $K_{\varepsilon k}$ and the migration efficiency α averaged over the statistical distribution of barrier widths.

$$K_{\varepsilon k} = H\, e^{-\Delta/kT} \qquad [V-3]$$

$$\langle \alpha \rangle = \frac{1-x}{x^2} \left[\ln \left(\frac{1}{1-x} \right) - 1 \right] \qquad [V-4]$$

Exciton migration is again treated as a random walk with a barrier density set by the mobile trap density. The important features of Figure 19 are the strong temperature dependence and the weak concentration dependence over much of the range.

The most important observation to be drawn from Figures 18 and 19 is that both models predict significant exciton mobility under the experimental conditions studied. Neither mechanism is individually sufficient to predict the experimental results. At the lowest temperatures reached, tunneling is the predominant barrier transmission process and

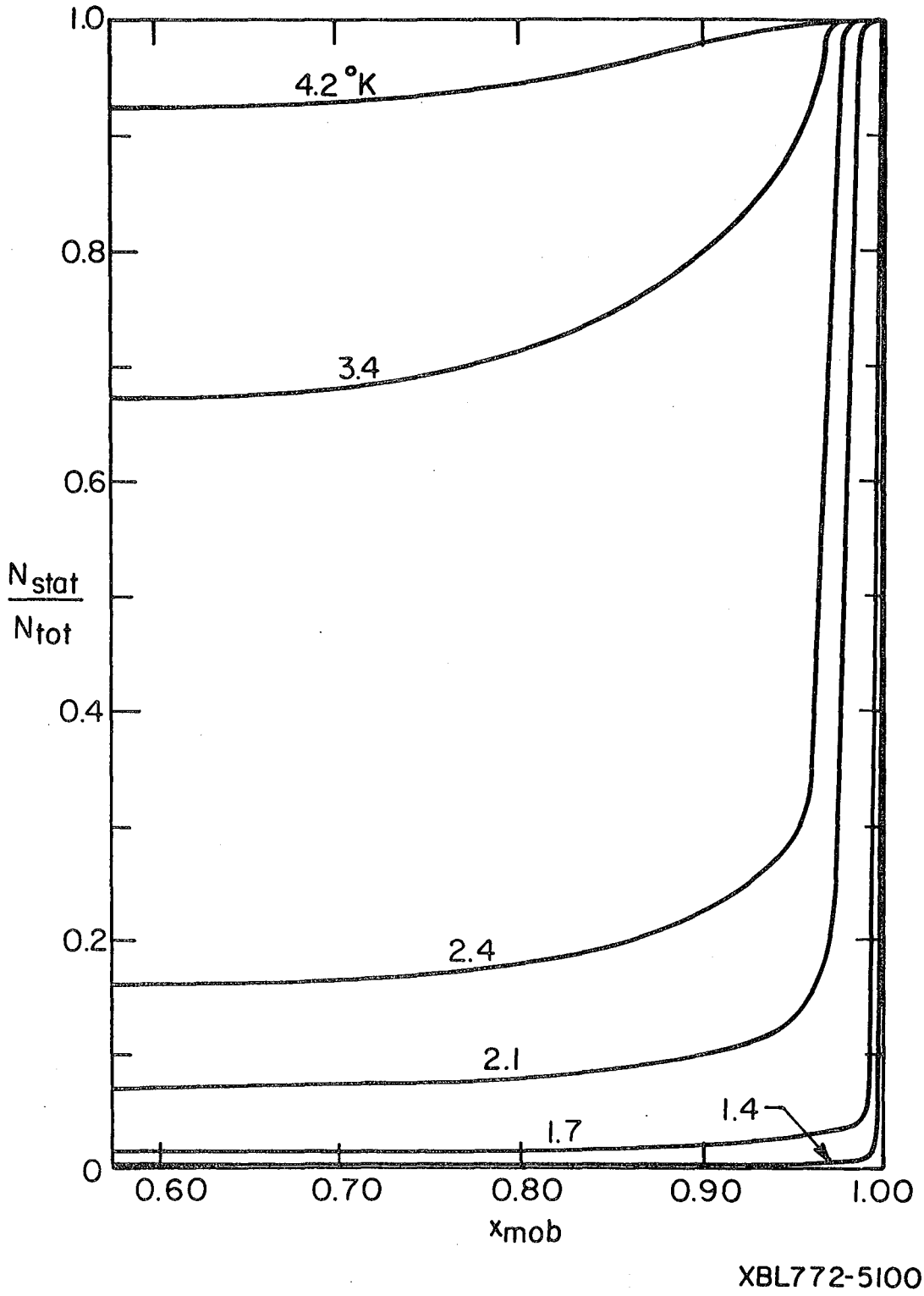

Figure 19. Calculated population partitioning ratio for thermal detrapping transfer vs. h_2-TCB mole fraction between 1.4 and 4.2 K. Parameters are T = 25 msec, $\beta = 0.3\ cm^{-1}$, $x_s = 0.002$, and $H = 3 \times 10^{10}\ sec^{-1}$.

experimental results in Figure 20 match the gradual onset of stationary trap phosphorescence starting about $x_{mob} = 0.50$ that is characteristic of the tunneling model. As the sample temperature increases, detrapping surpasses tunneling as the major transmission process. The detrapping model predicts almost complete Boltzmann thermalization at 4.2 K between stationary and mobile trap states, which is seen experimentally in Figure 21. A rigorous treatment of exciton dynamics in disordered systems must consider both mechanisms.

4. Results and Discussion: Singlet Excitation

The same system under singlet excitation shows important differences in behavior. Figure 22 shows the fraction of stationary trap phosphorescence for singlet excitation. The differences between this graph and Figure 16 shows that significant exciton migration and trapping occur in the singlet manifold before intersystem crossing into the triplet.

The bandwidth of singlet excited states is generally orders of magnitude larger than the triplet bandwidth, but these singlet state lifetimes are relatively so short that exciton migration is considered primarily a triplet state phenomenon in many systems. The singlet bandwidth may play a critical role, however, in substitutionally disordered crystals. The TCB triplet bandwidth, about 1.2 cm^{-1}, is much smaller than the 23 cm^{-1} isotope shift and the triplet bands are an example of the persistence limit. Neither the isotopic shift nor the bandwidth are known for the first excited singlet state, but phosphorescence monitored absorption spectroscopy performed by scanning the excitation source across

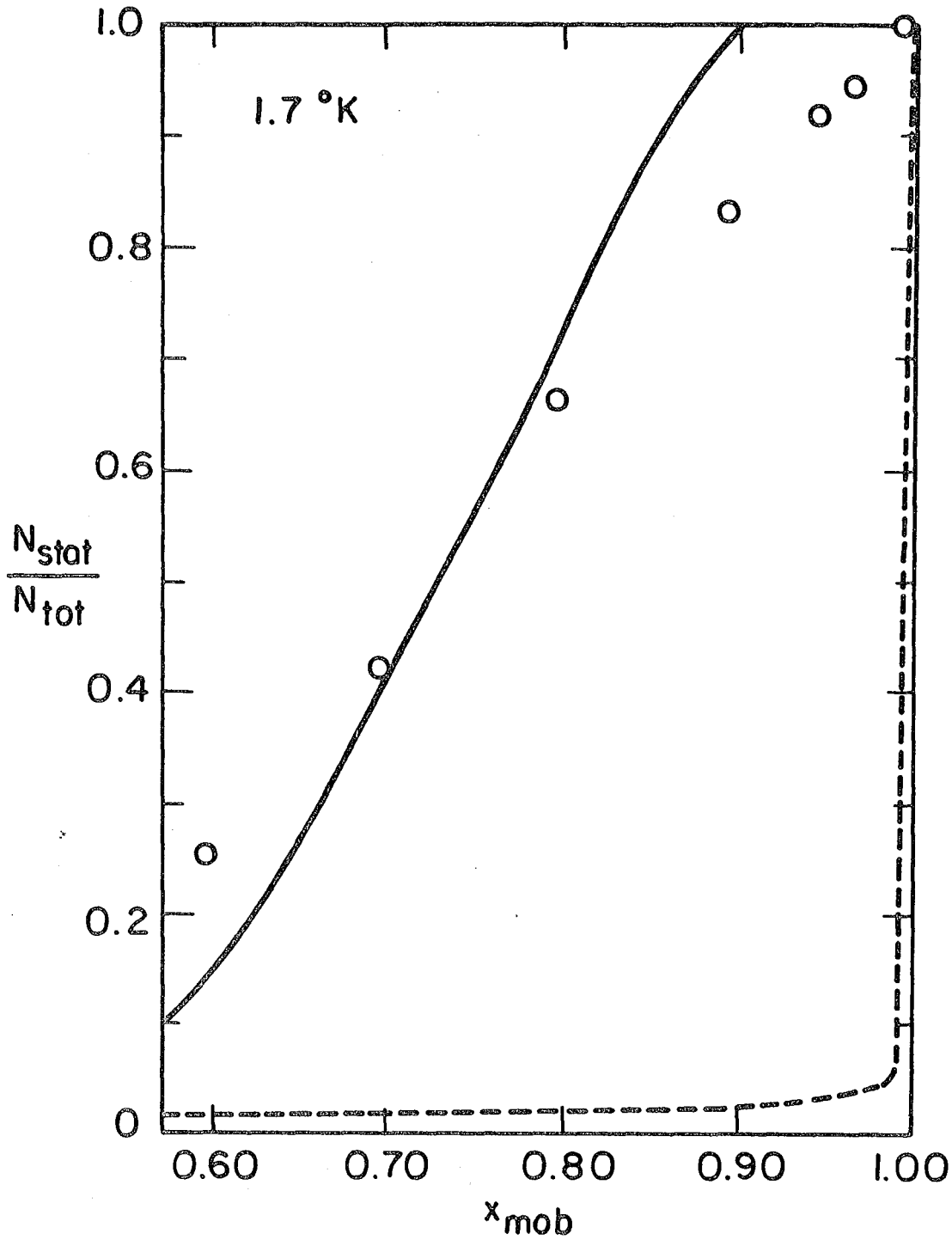

XBL784-4834

Figure 20. Comparison of experimental intensity partitioning ratio (open circles) with calculated population partitioning ratios for tunneling (solid line) and detrapping (dashed line) at 1.7 K. Curves are taken from Figures 17-19.

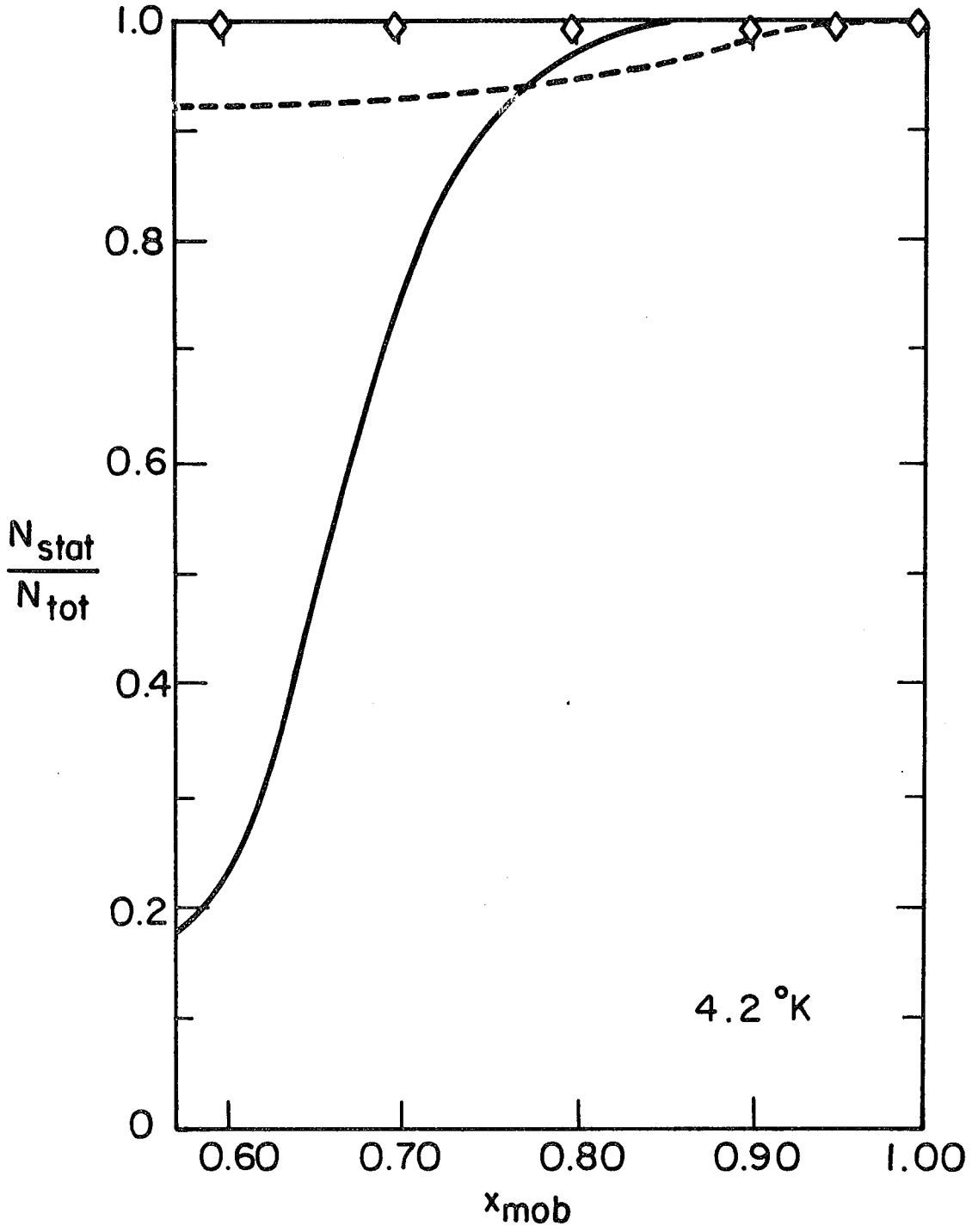

XBL784-4835

Figure 21. Comparison of experimental intensity partitioning ratio (open diamonds) with calculated population partitioning ratios for tunneling (solid line) and detrapping (dashed line) at 4.2 K. Curves are taken from Figures 17-19.

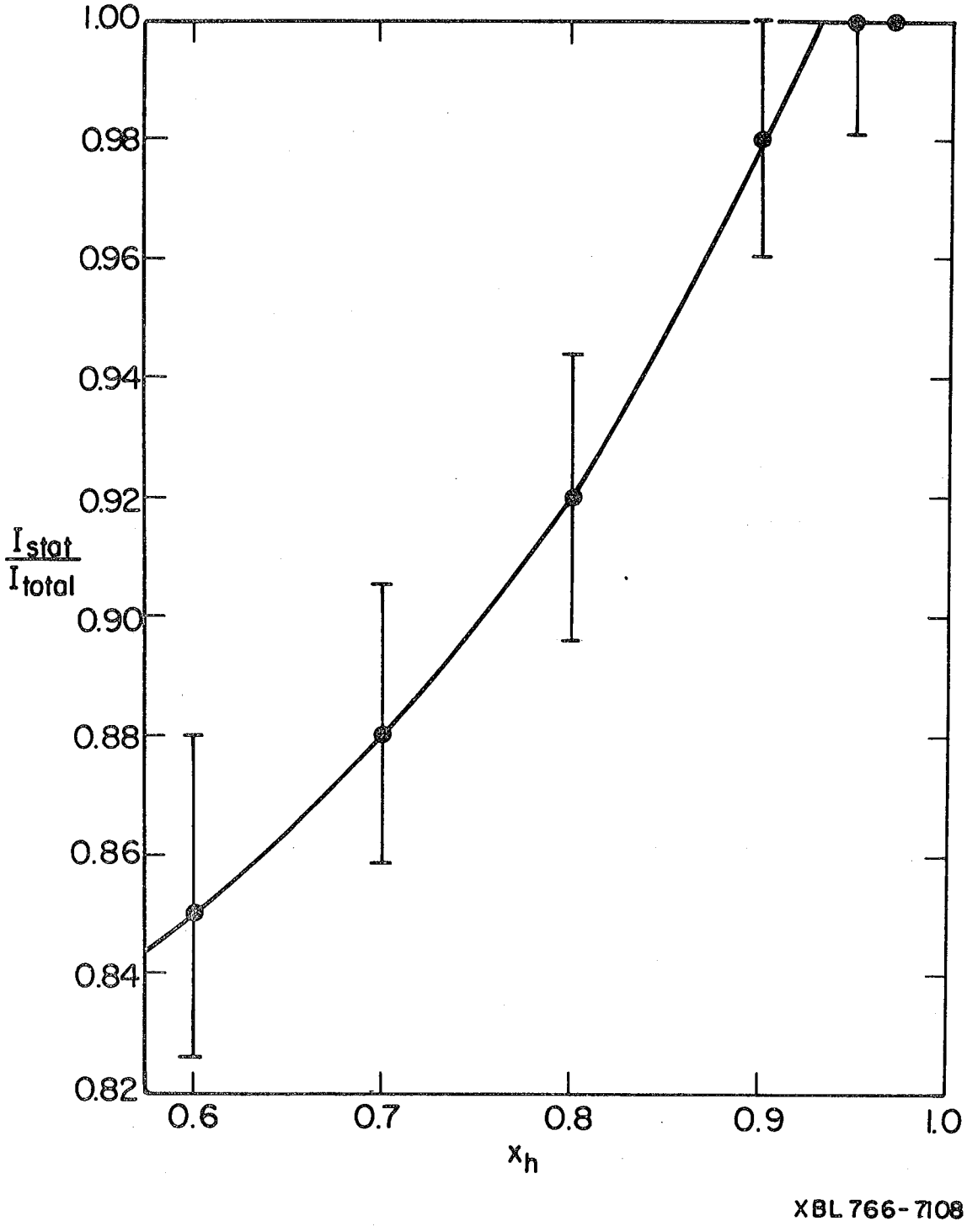

Figure 22. Ratio of stationary trap phosphorescence intensity to total phosphorescence intensity for singlet excitation vs. mobile trap mole fraction, x_h, at 1.4 K.

the singlet absorption near 2965 Å indicates a bandwidth greater than 100 cm^{-1} if transitions to the entire band are allowed by disorder induced mixing of k states. It is reasonable that the singlet isotope shift is comparable to the bandwidth and the d_2- and h_2-TCB singlet bands are amalgamated over the whole concentration range. The nearest pyrazine singlet state is 2700 cm^{-1} lower and does not take part.

The composition of the supertrap phosphorescence is significantly different between the singlet and triplet data. For triplet excitation, x-trap phosphorescence comprises ~ 55% of all supertrap emission, while in the singlet it accounts for only 5-10%. This may be explained if the x-trap does not act as a trap in the excited singlet state or is masked by the increased bandwidth. The x-trap phosphorescence then gives us a measure of how many excitons are trapped after intersystem crossing to the triplet and therefore how many are trapped in the singlet. By this measure, 75-80% of the total phosphorescence is due to trapping at a pyrazine from the singlet state and this quantity is independent of the composition of the crystal. In Figure 23 a constant 80% of the pyrazine phosphorescence at 1.7 K in Figure 8 has been subtracted out and the remainder normalized to 100%. The result is identical within experimental error to the triplet result. The important conclusions are that exciton migration in excited singlet states may be comparably efficient with that in much longer-lived triplet states in disordered crystals and that energy transfer through an amalgamated band is independent of the band composition.

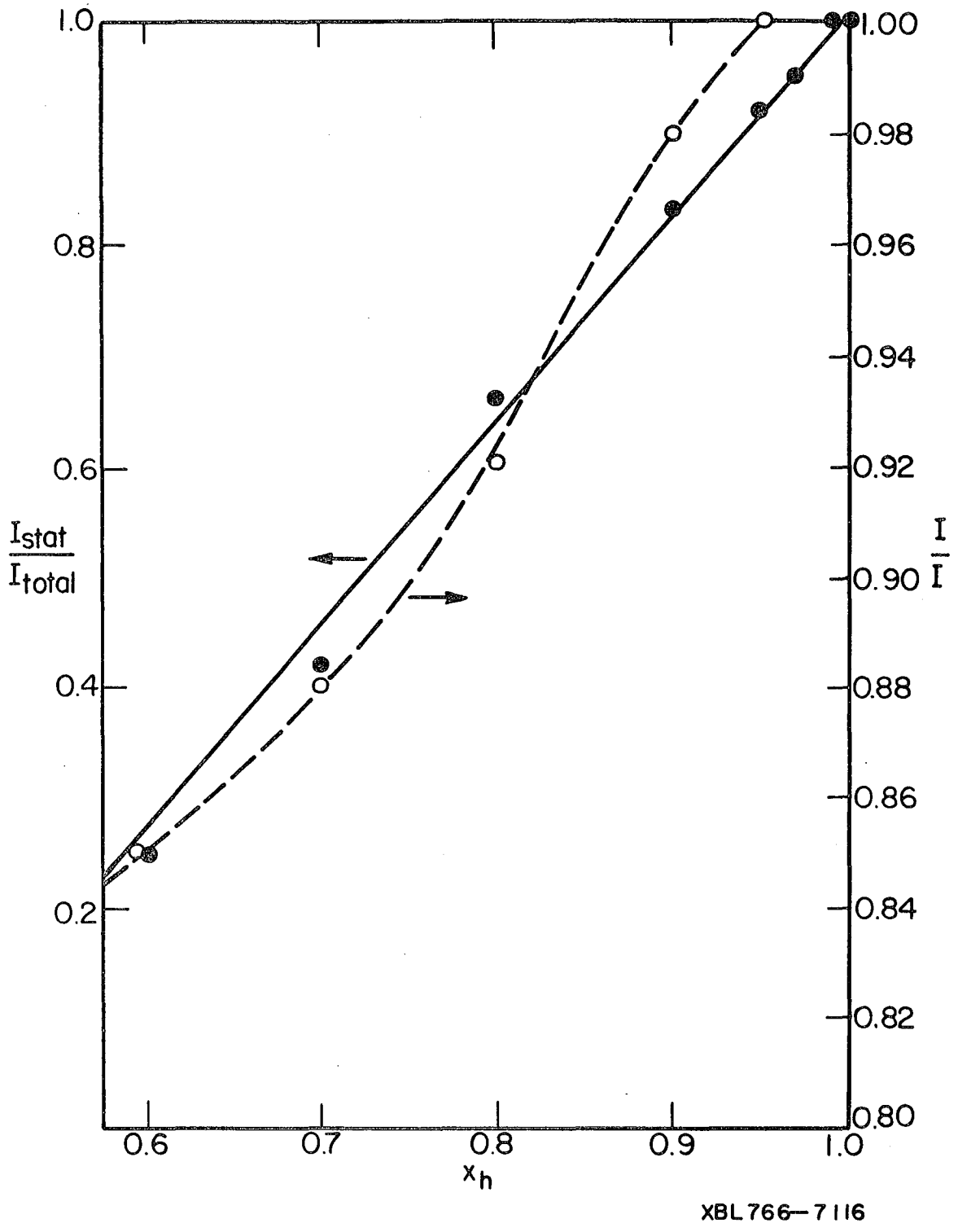

Figure 23. Comparison of triplet-excited phosphorescence ratio (dark circles, left hand scale) with singlet-excited phosphorescence ratio (open circles, right hand scale) vs. h_2-TCB mole fraction at 1.4 K.

5. Summary

Explicit expressions for energy-partitioning ratios in a quasi-binary (low stationary trap concentration) system derived in the previous section draw a sharp distinction between the thermal promotion model, on one hand, and the pure and hybrid tunneling models, on the other. The enhancement of communication between localized trap states by exciton tunneling through virtual states of the host is a strong function of the width of the intervening barriers and shows a relatively sharp concentration dependence. The detrapping model and its energy partitioning ratio depend primarily on the number of barriers, which is symmetric in the guest-host composition, and only secondarily on the barrier widths. The problem may be reduced to an average barrier width (and average trap width) much like the simple disordered system of Chapter III-2. Averaging procedures in all models require, of course, that the exciton visit many sites before decaying.

We have not dealt with the effects of coherence and incoherence in heavily disordered systems. Incoherent effects at barriers are expected to be extremely important in such cases, severely limiting long range exciton diffusion. The effect of coherent wavepacket propagation will be attenuated by the high concentration of scatterers resulting in a localization of k states even within the intervals of pure guest or host molecules.

In practice, both models of exciton migration may be simultaneously effective and should properly be treated as competing processes. Realistically, the tunneling model must include the occasional detrapping

event which does not behave within the hierarchy of barriers structures and the thermal promotion model should include the correlations induced by the remaining bias towards transmission through the smaller of two confining barriers. Additionally, both models lose validity as the amalgamation limit is approached closely. Here we have dealt implicitly with the region where $\beta << \Delta$, but extension to an intermediate bandwidth region requires only an additional averaging for promotion or tunneling rates convolved with a Boltzmann distribution of initial and final states. The flexibility of the models proposed here, which include the quantum mechanical wavepacket properties of energy transfer, allows treatment of ternary and more complex systems. The energy transfer properties of any one-dimensional substitutionally disordered system in which the interactions between low energy or conducting sites are known are accessible. We note also that some of the ideas presented here, when extended to random walks in two or three dimensions may be useful in understanding energy transfer in higher-dimensional systems where the mobile trap concentration is well below the percolation threshold and transfer between clusters is mediated by host barriers of varying width.

We have presented experimental energy-partitioning data between mobile and stationary trap states along a one-dimensional exciton conductor for both singlet and triplet excitation. The percentage of stationary trap phosphorescence increases with increasing mobile trap concentration, with increasing temperature, and is larger for singlet excitation than for triplet excitation.

Two simple models for (i) resonant tunneling transfer and (ii) thermal detrapping and migration, across a statistical distribution of barriers, do not accurately represent the experimental results for triplet excitation. Both mechanisms are important and contribute to exciton mobility over the temperature range studied.

Where competition between singlet and triplet manifolds for exciton migration occurs, the singlet may be much less efficient in the unperturbed crystal because of its short lifetime. In a substitutionally disordered crystal, the much wider bandwidth of the singlet may hide the perturbation of the potential surface and allow much more efficient exciton transfer than the triplet. The experimental data presented here shows that ~ 80% of the excitons reach a supertrap in the singlet state before intersystem crossing and that this percentage is independent of the band composition.

VI. SPIN DEPHASING IN IMPURITY-INDUCED STATES IN MOLECULAR SOLIDS

1. Introduction

In recent years, the demonstration of coherent exciton migration in one-dimensional molecular solids[35,36] has provoked great interest. In these systems, the coherence length can be limited by either exciton-defect scattering or by exciton-phonon scattering. For triplet states, the relatively narrow bandwidth of the Frenkel excitons makes them particularly sensitive to energy "traps" and "barriers" at temperatures where coherent propagation is achieved. Although triplet exciton dynamics have been investigated in neat and isotopically-mixed systems,[68] only a few studies have been made in chemically mixed systems because the methods have been hindered by the unknown nature of the perturbations in the crystal structure. These would include molecular site anisotropies and interaction energy differences introduced by chemical substitution. When the perturbation is sufficiently complex, the nature of the site and the associated energy transfer dynamics are not accessible by conventional spectroscopic techniques and more sophisticated probes are necessary for a full understanding of both the static and dynamic properties of the localized states.

In this chapter, we present the results of a systematic study of this problem using optically detected spin locking[53] in photo-excited triplet states in combination with zero field optically detected magnetic resonance. These techniques have been used to elucidate the different

structures and properties of a series of chemically-induced triplet traps in 1,2,4,5-tetrachlorobenzene (TCB). Introduction of certain chemical impurities gives rise to the appearance of a predominant trap in the phosphorescence spectrum below 4.2 K.[34] Similar traps in other systems have been interpreted as host molecule states split from the bottom of the exciton band by an adjacent chemical impurity whose triplet energy lies above the band.[69-71] We should like to suggest that the TCB Y-traps are of a similar nature, where the physical geometry of trap and impurity in the host is largely independent of the identity of the impurity, but the energy level structure is very dependent on the impurity.

We will also demonstrate the use of optically-detected spin coherence experiments in measuring the coupling of local[72,73] and delocalized phonon modes of a disordered solid through the effect it has on energy exchange in which exciton propagation from the impurity is governed by processes such as thermal detrapping and thermally-activated tunneling, which are in turn governed by the population of local phonon modes which provide the thermal energy. We have measured the rate of exciton promotion from the bottom of the trap to a phonon mode of the trap by the loss of spin coherence and we will show that the rate is slower when phonon modes are decoupled by an adjacent chemical impurity than when the phonon band is only slightly perturbed by isotopic substitution.

2. Experimental

Experiments were performed on five systems. 1,2,4,5-tetrachlorobenzene-h_2 (Aldrich Chemical, zone refined 200 passes) was doped with 5%, 1% and 0.05% 1,2,4,5-tetrabromobenzene, TBB (Eastman Organic, zone refined

50 passes), and crystals were grown by standard Bridgeman techniques. The final TBB concentrations in the crystals were confirmed by mass spectra. The TCB was also doped with 1% concentrations of 1,4-dichlorobenzene, DCB (Eastman), and 1,4-bromochlorobenzene, BCB (Aldrich), but mass spectra of the crystals showed that most of these dopants were removed during crystallization and dopant concentrations were less than 0.1 mol%.

The experimental arrangement for optically detected magnetic resonance and coherence experiments is identical to that described previously.[2,53,74-76] In the phosphorescence spectra, the Y-traps lie 44 cm^{-1} below the unperturbed TCB exciton band for DCB/TCB and TBB/TCB Y-traps and 48 cm^{-1} below the band for the BCB/TCB Y-trap. All three Y-traps show normal TCB vibrational structure.[34] Table II lists the zero-field ODMR parameters measured for the Y-traps with axes defined as in Ref. 34. In this table and throughout the chapter, the results given for the TBB/TCB Y-trap are for the 0.05% crystal. Both optical and microwave transitions are broadened by dimer and higher multimer trap interactions in the more concentrated crystal. Phosphorescence-microwave double resonance (PMDR)[74] and microwave-induced delayed phosphorescence (MIDP)[75] experiments established the similarity of relative radiative rate constants, and triplet sublevel lifetimes and population among the three systems.

For the coherence experiments, all systems were spin-locked on resonance at the Y-trap D $-|E|$ transition. The temperature-dependent components of the spin-locking decay time are plotted in Figure 24.

Table II. Y-trap zero field splittings.

	DCB	BCB	TBB	
D - E	3608.3	3607.6	3593.0	MHz
D + E	5437.2	5436.2	5517.8	MHz
2 E	1829.4	1806.0	1925.3	MHz

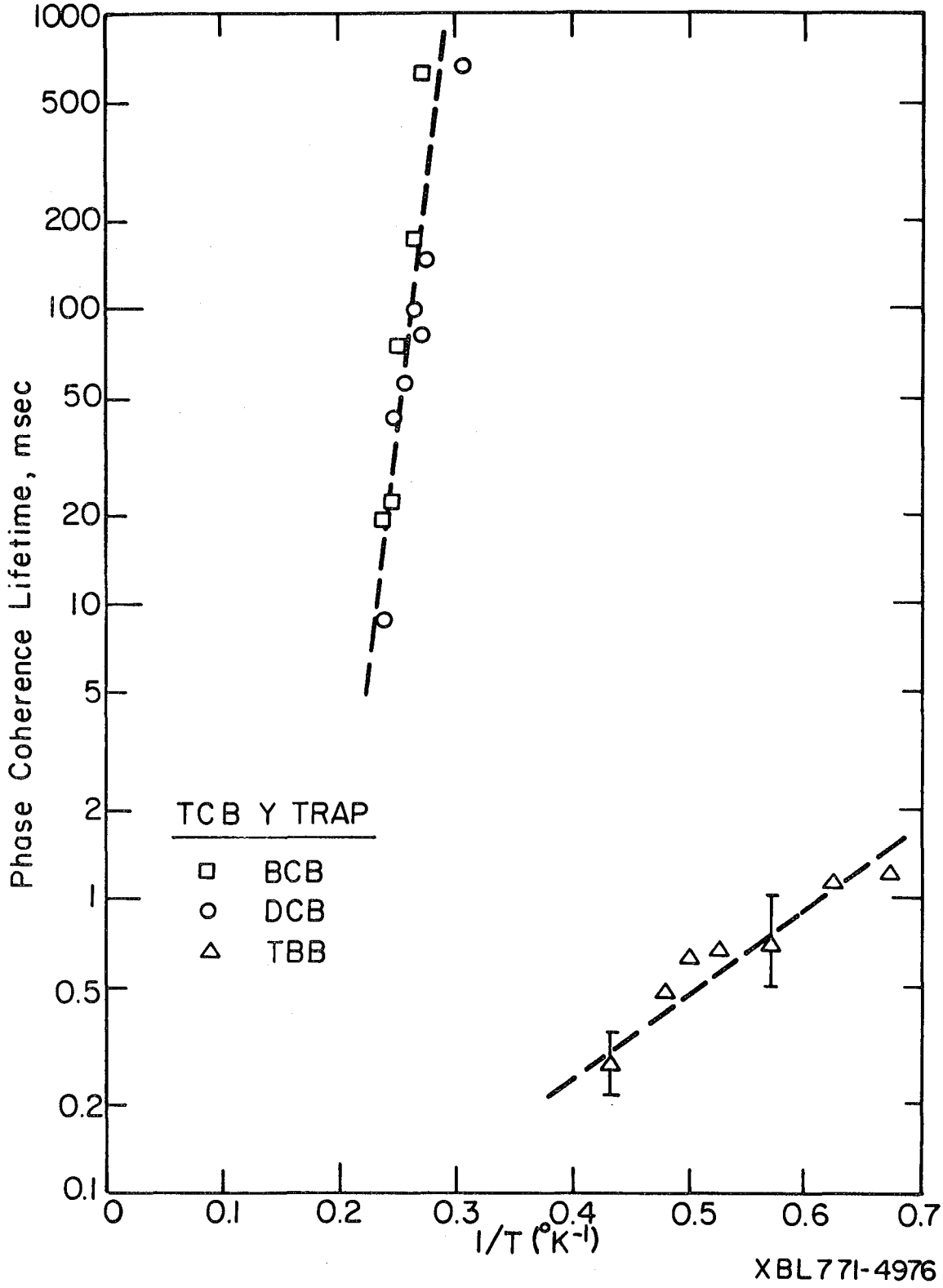

Figure 24. Phase coherence lifetimes for Y-trap systems calculated from temperature-dependent contribution to spin-locking decay rate. Data was taken at D - E transition of TCB Y-trap.

3. Y-Trap Geometry and Energy Level Structure

Several experimental parameters of the Y-trap systems are largely independent of the identity of the chemical impurity. These parameters are related to the static or equilibrium properties of the trap and impurity in the host. The trap depths measured in the phosphorescence spectra are very similar. The zero field splittings, listed in Table II, are within a percent of each other. The sublevel lifetimes, listed in Table III, were measured by microwave-induced delayed phosphorescence and only show significant variation in the τ_y lifetime. From the sublevel lifetimes and the phosphorescence-microwave double resonance spectra, unambiguous ordering of the sublevel populations N_n and the radiative rate constants k_n^R to the origin have been assigned to the DCB/TCB and BCB/TCB Y-traps.

$$N_x > N_y > N_z \qquad [VI-1]$$

$$k_y^R > k_z^R > k_x^R \qquad [VI-2]$$

The decrease in the τ_y sublevel lifetime for the TBB/TCB Y-trap revises the ordering of the populations,

$$N_x > N_z > N_y \qquad [VI-3]$$

while the ordering of radiative rate constants does not change. This variation is relatively minor and on the basis of the otherwise similar values, we propose that the physical geometries of all Y-traps are qualitatively the same.

Table III. Sublevel lifetimes.

	BCB	DCB	TBB	
z	21.5 ± 2	23 ± 1	21.6 ± 2	msec
y	21.5 ± 2	22.5 ± 1	14.3 ± 2	msec
x	835 ±	860 ± 15	815 ± 50	msec

Spin coherence experiments, such as optically detected spin locking, give the dynamic behavior of the Y-trap system directly and this will be considered in detail in the next section. The decay of the spin-locking signal is sensitive only to processes that remove the molecule from the spin-locked ensemble and, as a consequence, is a useful probe for studying detrapping, tunneling, vibrational excitation, or any transient exchange with a state having different zero field splittings. One static parameter of immediate importance to the question of energy level structure can, however, be extracted from the spin-locking decay. When the temperature-independent contributions of sublevel lifetime and relaxation against the microwave field are subtracted out, the spin coherence decays in Figure 24 show an activation energy of 4 cm^{-1} for the TBB/TCB Y-trap and 25 cm^{-1} for the DCB/TCB and BCB/TCB Y-traps.

We attribute the 4 cm^{-1} decay to detrapping from the TBB/TCB Y-trap to an adjacent, translationally equivalent TBB molecule as in Figure 25. Below 188 K the unperturbed TCB crystal is monoclinic with two molecules per unit cell.[66] The intermolecular spacing along the c axis is 3.5 Å and energy transfer is exclusively along this axis. The optically-detected ESR spectra of the TBB/TCB Y-trap shows two important effects. Bromine quadrupole satellites due to transferred hyperfine interaction from the nearby TBB impurity appear symmetrically at 291 and 245 MHz from the Y-trap transition frequencies. This phenomenon was also observed with the ODMR of quinoxaline in TCB and pyrazine in DCB host.[77] By itself, this evidence confirms proximity (i.e., positions A or B in Figure 25), not translational equivalence (i.e., position A). The ODMR spectra at 20

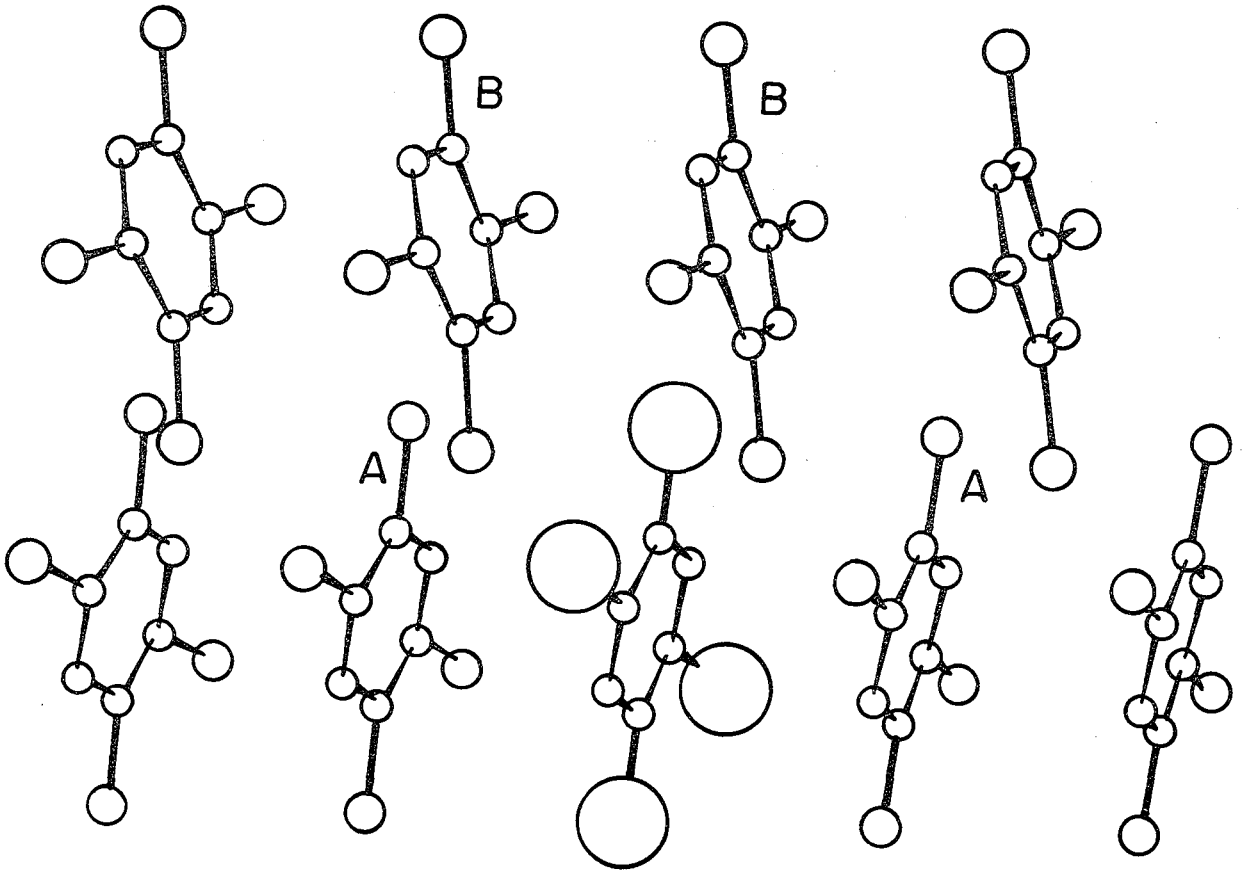

XBL 768-7476

Figure 25. Diagram of two translationally inequivalent chains in 1,2,4,5-tetrachlorobenzene. Exciton transfer occurs along close-packed axis running across page. Molecule in lower center represents chemical impurity and sites A and B represent nearest-neighbor translationally equivalent and second-nearest-neighbor translationally inequivalent sites, respectively.

W microwave power shows the D - | E | and D + | E| transitions of the TBB molecule[78] in the phosphorescence emission of the TBB/TCB Y-trap. In order to optically detect spin polarization induced by a microwave field in resonance with a TBB triplet transition, energy transfer between the TBB molecule and Y-trap must be extremely rapid, which requires that TBB and Y-trap lie adjacent along the c-axis. It has also been reported that the lowest triplet state origin in neat h_2-TBB triplet origin at 26,696 cm^{-1} (Ref. 79) is comparable to the h_2-TCB triplet origin at 26,676 cm^{-1}. It is plausible that the solvent shift of the TBB molecule in the TCB host could bring its energy close to that of the Y-trap.

We attribute the 25 cm^{-1} decay for DCB/TCB and BCD/TCB Y-traps to excitation to a vibronic level of the Y-trap molecule. The absorption spectrum of h_2-TCB shows a 26 cm^{-1} lattice vibration in the triplet excited state.[80] No ODMR transitions of DCB or BCB appear in the spectra of their respective Y-traps. There is no evidence of detrapping to the DCB or BCB impurities, which probably lie much higher than the TCB host band. Unlike TBB, the lowest triplet origins of DCB and BCB lie 1214 cm^{-1} and 1184 cm^{-1} (Ref. 79) above the triplet origin of TCB. Figure 26 summarizes our models for the Y-traps.

4. Excitation Exchange in Chemically-Mixed Systems

The decay of the spin-locking signal reflects the promotion of spin population to another state. The effectiveness of the cycle of promotion and subsequent relaxation in dephasing the spin coherence depends on τ, the lifetime in the upper state, and $\delta\omega$, the Larmor frequency difference of the two states.[81] In order to quantitatively correlate the

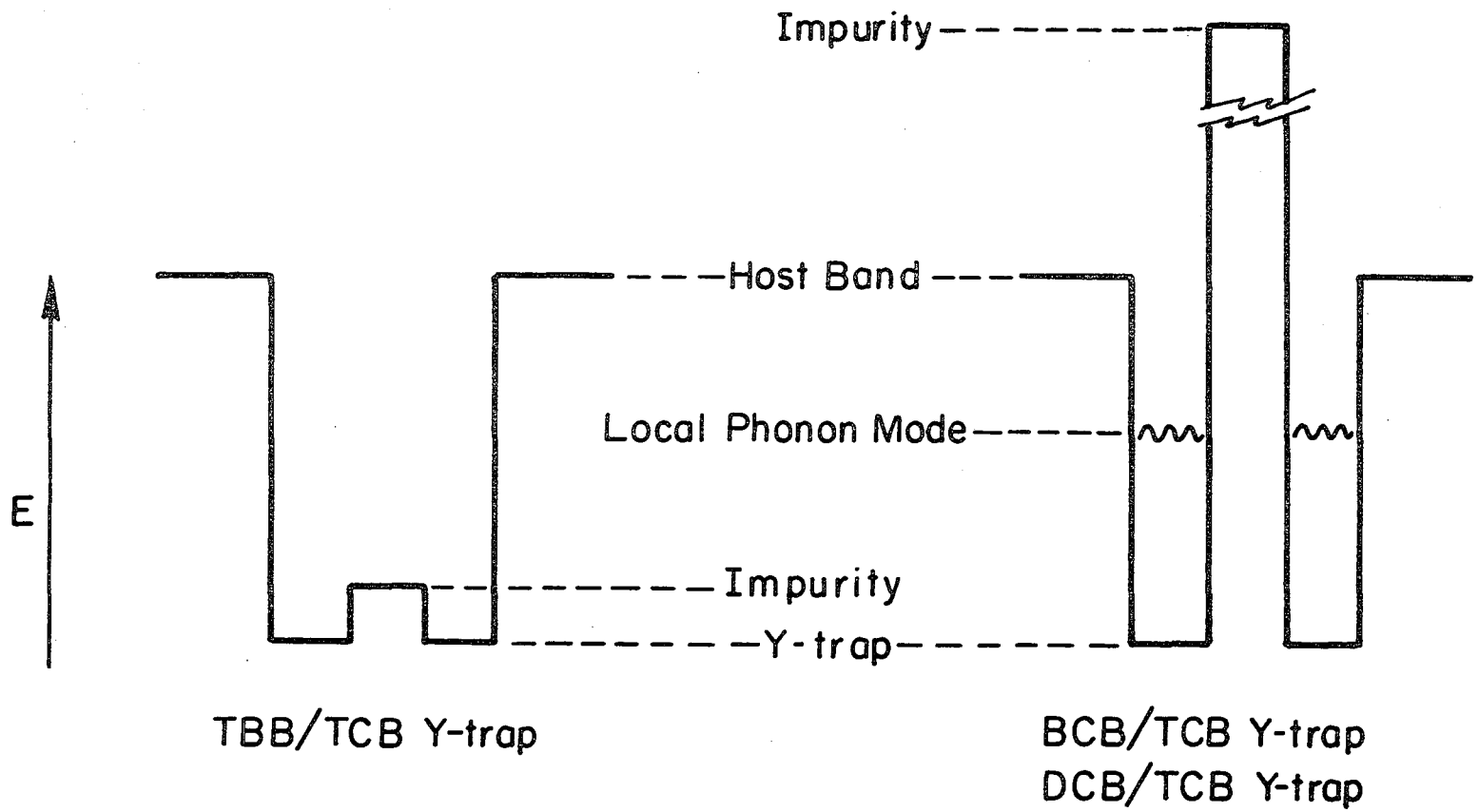

Figure 26. Schematic diagram of proposed Y-trap triplet energy levels.

spin dephasing rate with the promotion rate, W_+, it must be established whether the exchanging systems are in slow exchange, $\delta\omega \cdot \tau > 1$, where all spin memory is lost in promotion, or in fast exchange, $\delta\omega \cdot \tau < 1$, where significant spin memory is retained.[82] It has been shown that by observing both the linewidth of a transition, $T_{1\rho}^{-1}$, and its frequency shift, $\Delta\omega$, the type of exchange may be determined[27] in the optical case. The same is true for the magnetic case. Specifically, the value of

$$T_{1\rho}^{-1} / \Delta\omega = \delta\omega \cdot \tau \qquad \text{[VI-4]}$$

determines the exchange region. The promotion rate to the upper system, W_+, can be extracted from $T_{1\rho}^{-1}$ and, assuming Boltzmann equilibrium between promotion and relaxation, the upper state lifetime, τ, can be determined by

$$W_+ \tau = e^{-\Delta/kT} \qquad \text{[VI-5]}$$

where Δ is the measured activation energy.

On this basis, we propose that the population exchange between the trap origin and the 25 cm^{-1} local phonon state of the trap in the DCB/TCB and BCB/TCB systems is in slow or intermediate exchange, $\delta\omega \cdot \tau \approx 1$. The homogeneous linewidth, $(T_{1\rho})^{-1}$, can be extracted from a Fourier transform of the spin-locking decay and is about 30 Hz FWHM at 4.2 K. On the other hand, no frequency shift in the $D - |E|$ transitions could be observed between 1.4 and 4.2 K. Assuming, therefore, that $\Delta\omega \leq T_{1\rho}^{-1}$, we find that the system is in slow or intermediate exchange and we can estimate τ

$$3.6\ \mu\text{sec} \leq \tau \leq 7.2\ \mu\text{sec} \qquad \text{[IV-6]}$$

giving $\delta\omega \geq 0.28$ MHz. For the specific case of intermediate exchange, W_+ is plotted in Figure 27.

The important observation here is that τ is extremely long for a vibrational level, 10^{-5} - 10^{-6} sec, as opposed to the vibrational relaxation times 10^{-12}- 10^{-13} sec measured by picosecond laser and Raman linewidth studies.[83] Similarly, the promotion rate W_+ is relatively low. In comparison, promotion to an excited vibrational level 21 cm^{-1} above a para-benzoquinone trap in an isotopically-mixed crystal is 10^4 times faster.[68] This behavior suggests tha the rate limiting step for vibrational promotion or relaxation in the vicinity of a chemical impurity is the transfer of thermal energy between the lattice phonons and the localized phonon levels of the trap.

The TBB/TCB Y-trap system is somewhat unusual in spin coherence exchange studies in that both τ and $\delta\omega$ may be determined independently. τ is extracted from Eq. (5) giving $\tau \cong 30$ μsec. The $D - |E|$ transitions of both TBB and TBB/TCB Y-trap may be observed in the Y-trap phosphorescence, giving $\delta\omega \cong 2.5$ GHz. Therefore, $\delta\omega\tau \sim 7.5 \times 10^4 >> 1$, and the system is in slow exchange. This is corroborated by the lack of a frequency shift in the ODMR temperature dependence. The interaction matrix element between the Y-trap and TBB molecule is quite small. The preexponential factor of W_+ is on the order of 10^4 sec^{-1} as opposed to 10^{11} sec^{-1} for equivalent TCB molecules[36] in the host band.

The major contribution to the slowing of the transfer process could be due to be the promotion of the trapped exciton to a trap-phonon state equienergetic with the impurity, and this step is hindered by the

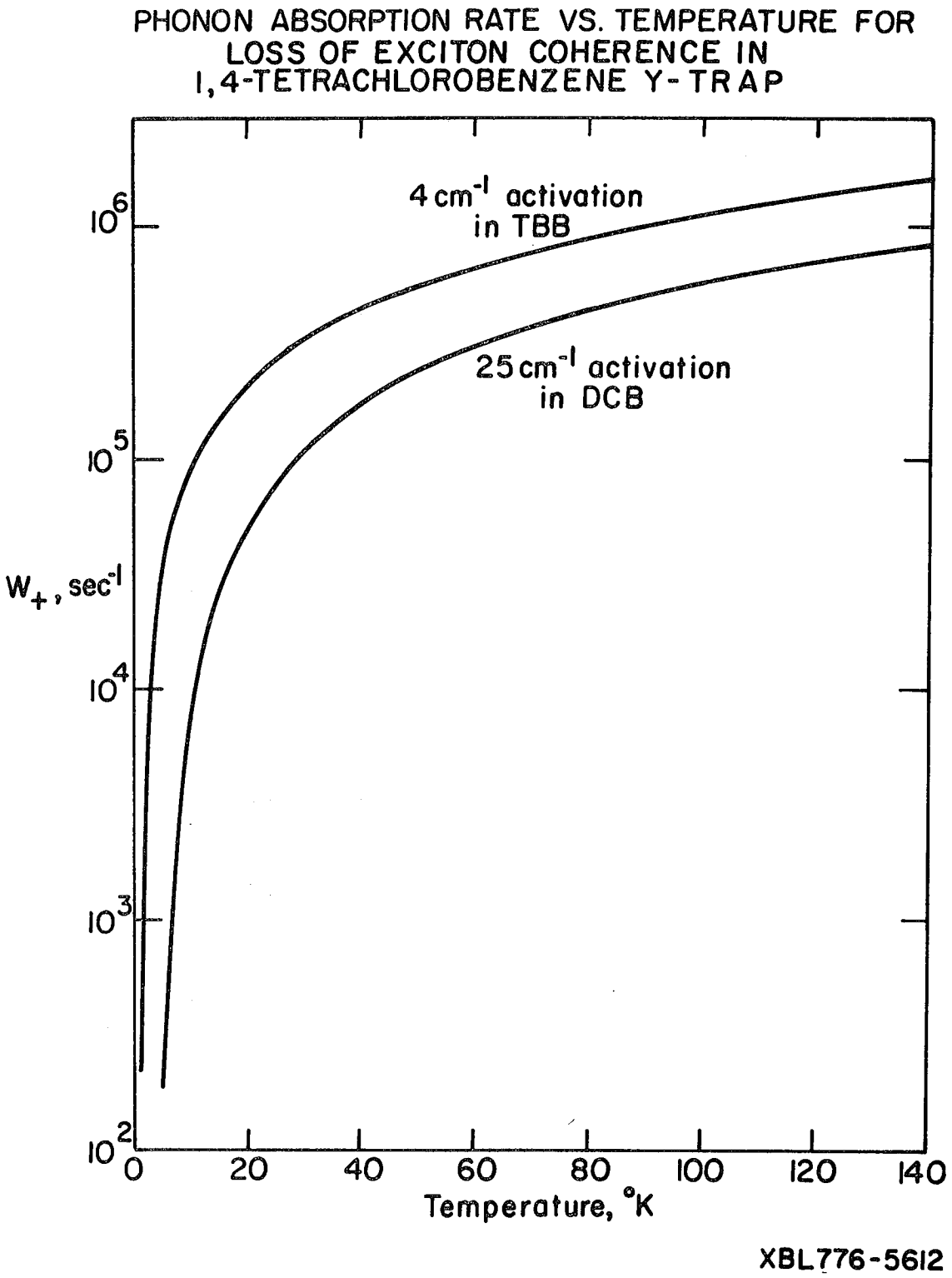

Figure 27. Phonon absorption rate as a function of temperature for a 4 cm^{-1} activation energy exchange between Y-trap and impurity in TBB/TCB and for a 25 cm^{-1} activation energy promotion to a local phonon mode in DCB and BCB/TCB.

the decoupling of lattice and local phonon modes. Alternatively, part of this difference may be due to a second dephasing mechanism caused by a differing alignment of spin axes in the trap and TBB impurity, which Brenner, Brock, and Harris[84] have shown to cause spin dephasing on transfer. This mechanism would also explain the rapid spin-lattice relaxation which eliminates the ODMR signal above 2 K.

5. Summary

We have demonstrated the usefulness of spin coherence techniques in elucidating the complex structure of chemically-induced traps. BCB/TCB and DCB/TCB Y-traps contain impurity molecules whose triplet energies lies high above the host exciton band and do not take part directly in the trap dynamics. The TBB/TCB Y-trap, though spectroscopically similar, is induced by an impurity whose triplet energy lies below the band, although above the trap. Transfer of spin population between trap and impurity is observed in the Y-trap ESR spectrum for TBB/TCB, while spin dephasing occurs in a vibrationally excited level of the DCB and BCD/TCB traps. High energy impurity "barrier" states will attenuate long-range exciton migration in the latter systems relative to the TBB/TCB system.

The dynamics of the exciton-trap interaction have been classified within the slow and intermediate exchange region. The low promotion rate and long vibrationally-excited lifetime are interpreted as a decoupling of the lattice phonons from the localized phonon levels of the trap associated with the adjacent chemical impurity.

VII. VANTAGE

The midpoint of this thesis provides a vantage from which to review the conclusions of the first half and prepare for the additional complexities of surface effects. The elegant simplicity of the exciton model has proven inadequate to describe disordered solids. Steps have been taken, theoretical and experimental, in attempting to replace it with a new model that is conceptually simple, calculationally useful, and consistent with the principles of physics and thermodynamics.

The results of random walk probability theory have been applied to energy migration under the assumption of partial localization of the energy. The effects of coherence, detrapping, and tunneling are explored in increasingly complex one-dimensional disordered chains. The goal has been to build a framework to infer microscopic details of exciton transfer from experimental measurements of energy partitioning in ternary systems. In an isotopically mixed one-dimensional exciton conductor, experimental results show that both thermal detrapping and tunneling play an important role in triplet exciton transfer. A complete theoretical model, however, must treat both mechanisms coexisting in competition in the same system as well as treating a statistical distribution of barrier widths in the chain in addition to statistical concentrations of barrier widths. In the course of experiments, it also became clear that exciton transfer in the singlet state, where isotopic components are amalgamated into a single band, is unexpectedly important in mixed crystal systems.

The deduction of macroscopic energy transfer behavior from knowledge of microscopic structure and dynamics is an equally valid approach. Using a battery of optically-detected magnetic resonance techniques, two critically different structures for an impurity-induced trap in TCB have been identified. Electron spin coherence technique demostrate that the dynamics of the Y trap are limited by the decoupling of crystal phonon modes from the local phonon modes of the impurity.

In each case, the structure of the disordered one-dimensional crystal determines the nature of energy transfer, by limiting dimensionality, by placing discontinuities in the electronic energy band, or by channeling the distribution of thermal energy. In the following chapter, structure and its influence on energy transfer will be of critical importance in the competition between the molecular crystal character of the adsorbate and the significant influence of the metallic substrate.

B. The Spectroscopy of Molecules Adsorbed on Metal Surfaces

E indi l'altrui raggio si rifonde
così come color torna per vetro
lo qual di retro a sé piombo nasconde.

-Dante

VIII. INTRODUCTION

Experimental and theoretical progress in surface science over the last fifteen years has dramatically increased our knowledge of the structure and chemistry of interfaces, as well as the recognition by the general scientific community of the importance of surface effects in electrochemistry, membrane physics, and catalysis. In this same period, many new surface-sensitive techniques have been developed or put on a quantitative basis: LEED, Auger, and photoelectron spectroscopy; thermal desorption; work function measurement; field ion or electron microscopy; ion scattering; and IR reflectance and absorption. The proliferation of techniques occasionally obscures the importance of the problems being investigated.

The questions of greatest interest to us carry over from our interests in molecular spectroscopy:

i) What is the molecular nature of adsorbed overlayers on metal surfaces?

ii) What energy transfer processes are important within the overlayer and between the overlayer and the metal?

iii) To what extent do collective processes, involving many surface atoms or admolecules, determine the physical and chemical properties of surfaces?

My personal project has been to address these questions within the context of organic adlayers on transition metal surfaces, by characterizing

the excited states in the proximity of the metal surface. In parallel with this effort, a variety of investigations in small molecule surface chemistry, the spectroscopy of chemisorbed adlayers, and anisotropic surface optical properties have been pursued. These projects have often overlapped, but this thesis will focus on optical measurements of low temperature aromatic overlayers on the nickel (111) surface. This work has been extraordinarily exciting because the behavior of molecular crystals at metal surfaces is fresh ground for exploration. As a corollary, there are no guidelines and little past experience to draw upon in interpreting the results and the few investigations made by us in a single year are only beginnings, preliminary and often inconclusive. Our discussion of the experimental results here is an attempt to organize part of our findings at this stage in the research and an attempt to point up the importance and complexity of the problems and the power of the techniques we have used to probe them.

The remainder of this chapter serves as an introduction to our present theoretical understanding of surface optical and energy transfer properties. Two experimental chapters follow on sample surface preparation and spectroscopic ellipsometry, an important optical technique. These chapters and the appendices are detailed because no description of our procedures and equipment has been published for reference. Two chapters of results and discussion follow. The first reports on the UV spectra of pyrazine, pyridine, and naphthalene adsorbed on nickel (111) as measured by spectroscopic ellipsometry. The second describes our observation of phosphorescent emission from the optically-excited triplet

state of pyrazine on nickel (111). A final chapter summarizes our surface science research and points out natural extensions of the work for further investigations.

1. The Optical Properties of Surface Adlayers

This discussion of the optical properties of surface adlayers reflects the traditional dichotomy between two perspectives on the behavior of such structures. I will review the calculation of expressions for the complex amplitude reflection coefficients based on the classical electromagnetic theory of light propagation and the macroscopic optical constants of the media involved. Then I will summarize the microscopic quantum mechanical phenomena specific to surface adlayer systems. In justification, I point out that the experiments described in this part of the thesis make use of classical optical techniques to demonstrate just such microscopic phenomena. The general considerations explored here apply to all surfaces and all wavelengths of light, but will emphasize the experimental systems of interest, dielectric overlayers on metal substrates under UV-visible light.

The reflection of light at a planar interface between two semi-infinite regions containing homogeneous, optically isotropic media is determined by the boundary conditions in the electromagnetic field.[85] The ambient and substrate are described by complex indices of refraction, $\tilde{n}_o$ and $\tilde{n}_1$, across the interface. Using the conventions of the 1968 International Conference on Ellipsometry[86]

$$\tilde{n}(\omega) = n(\omega) - ik(\omega) \qquad \text{[VIII-1]}$$

where n is the real index of refraction, k is the absorption, at frequency of light ω. By Maxwell's equations, the tangential components of the electric field E and magnetic field H are continuous across the interface, which defines several characteristics of the electromagnetic field. (1) The incident, transmitted, and reflected propagation axes lie in a single plane orthogonal to the interface. (2) The angle of incidence equals the angle of reflection. (3) The angles of incidence and transmission obey Snell's law,

$$\tilde{n}_o \sin\phi_o = \tilde{n}_1 \sin\phi_1 \qquad \text{[VIII-2]}$$

(4) Light linearly polarized parallel or perpendicular to the plane of incidence remains so upon reflection or transmission. The effect of reflection on the amplitude and phase of the light is expressed by the Fresnel expressions

$$r_p = [\tilde{n}_1^2\cos\phi - \tilde{n}_o(\tilde{n}_1^2 - \sin^2\phi)^{1/2}]/[\tilde{n}_1^2\cos\phi + \tilde{n}_o(\tilde{n}_1^2 - \sin^2\phi)^{1/2}] \qquad \text{[VIII-3a]}$$

$$r_s = [\tilde{n}_o\cos\phi - (\tilde{n}_1^2 - \sin^2\phi)^{1/2}]/[\tilde{n}_o\cos\phi + (\tilde{n}_1^2 - \sin^2\phi)^{1/2}] \qquad \text{[VIII-3b]}$$

where r_p and r_s are the Fresnel reflection coefficients for parallel and perpendicularly polarized light, respectively. An arbitrary polarization may be treated as the superposition of the two orthogonal polarizations.

For all systems involving a surface adlayer, the following model shown in Figure 28 will be used to interpret the optical properties of the system. The adlayer has plane parallel boundaries separated by the adlayer thickness d surrounded by semi-infinite ambient and substrate regions. The isotropic optical constants for the ambient, adlayer, and substrate are $\tilde{n}_o$, $\tilde{n}_1$, and $\tilde{n}_2$, respectively. If each interface is

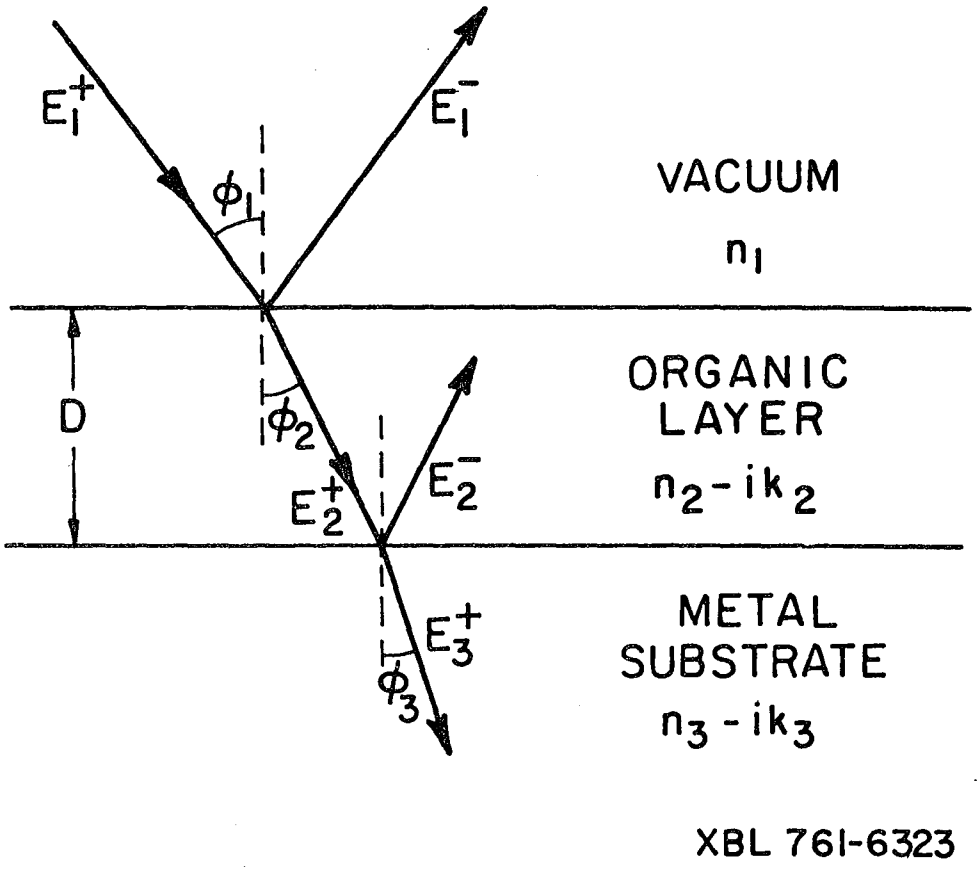

Figure 28. Three-component surface model. In text, vacuum index of refraction is called n_o, overlayer index is $n_1 - ik_1$, etc.

partially reflective, the reflected electromagnetic field is the superposition of the field which is reflected from the ambient-adlayer interface 01 and the field which undergoes one or more internal reflections between the 01 interface and the adlayer-substrate 12 interface (in absorbing substrates, such as metals below the plasmon frequency, the transmitted field is damped and can be neglected in this discussion. Likewise, in most interesting cases, the ambient is transparent, $\tilde{n}_o$ is real). Effective Fresnel coefficients[87] for the two interface system are

$$r_p = [r_{01p} + r_{12p}\, e^{-2i\beta}]/[1 + r_{01p}\, r_{12p}\, e^{-2i\beta}] \qquad \text{[VIII-4a]}$$

$$r_s = [r_{01s} + r_{12s}\, e^{-2i\beta}]/[1 + r_{01s}\, r_{12s}\, e^{-2i\beta}] \qquad \text{[VIII-4b]}$$

$$\beta = 2\pi d\, (\tilde{n}_1^{\,2} - \tilde{n}_o^{\,2} \sin^2\phi)^{1/2}/\lambda \qquad \text{[VIII-4c]}$$

where ϕ is the angle of incidence and λ is the wavelength. It has been shown that the Fresnel coefficients for three or more parallel planar interfaces take a similar form.[88]

It remains to consider the mechanism which give rise to the macroscopic absorption k and index of refraction n measured for the surface adlayer. These mechanisms or resonances reveal the microscopic chemical environment of the surface species and are intimately related to the geometry and bonding at the interface. The systems of greatest relevance to the experimental portions of this section are adlayers consisting of adsorbed or condensed organic molecules on transition metal surfaces, but a wide range of theoretical and experimental studies show that even this limited class may demonstrate optical properties ranging from molecular crystal exciton states to metallic reflection, as the

strength of adlayer-substrate coupling grows.

Molecules in a surface overlayer possess intrinsic molecular absorptions. In going from the gas phase to condensed phases, the electronic absorptions of these molecules are generally shifted by the excited state polarization energy, which reflects the relaxation of an excited molecule surrounded by polarizable neighbors. Near the overlayer-ambient interface, molecules will lack nearest and/or next nearest neighbors and it has been shown[89] that the excited state polarization energy shift is reduced for molecules near the surfaces of molecular crystals. Surface molecule resonances 78 cm^{-1} and 200 cm^{-1} above the first singlet origins of naphthalene[90] and anthracene[89] have been observed in molecular crystal absorption spectra. Although the surface structure of molecular crystals is not known, surface periodicity has been assumed in several theoretical studies of surface exciton and surface polariton collective excitations which may, in some cases, couple very strongly to an incident radiation field.[91]

The effect of metal substrate coupling to a molecular adlayer on the adlayer optical properties has received limited attention, particularly if the question of adlayer-substrate energy transfer is deferred to another chapter. The substitution of metal atoms for molecules will change the excited state polarization energy and three-dimensional exciton dispersion by an unknown extent. But the coupling of individual admolecules to the metal surface atoms will have perhaps the greatest effect on the energies and strength of molecular absorption. Several effects may be predicted.

1) Molecular orbital (MO) overlap between admolecule and metal atom(s) can lead by either charge transfer (CT) or exchange force to an external heavy-atom spin-orbit coupling effect on the admolecule, increasing the singlet-triplet absorption strength by intermixing the spin character of the state.[92]

2) In analogy to CT bands between ligand and metal atom in transition metal complexes, investigators have reported the observation of a CT band for pyridine on supported nickel catalysts in absorption.[93] They propose that this band involves transfer of nickel d electrons to an anti-bonding π^* orbital of the admolecule.

3) Given the strong bonding associated with chemisorption, the bonding orbital may be characteristic of neither the admolecule nor the metal surface. Entirely new transitions have been observed in the UV-visible spectra of H_2, O_2, and C_2H_4 chemisorbed on polycrystalline copper and are interpreted in terms of the molecular orbital diagram of the adsorbate and a small number of metal atoms.[94]

4) An ohmic or Mott-Gurney contact between adsorbate and substrate occurs if the work functions of the two materials differ. In general, the work function of the metal will be lower than that of a molecular overlayer and the metal will inject electrons into the dielectric overlayer. The space charge layer or accumulation region may be hundreds of angstroms thick in a good insulator and gives rise to a free carrier or metallic absorbance in the overlayer. This effect has been invoked to explain anomalous absorbances of thin films on gold substrates.[95]

It can be seen that the absorbance measured becomes less characteristic of the isolated admolecule and more characteristic of the admolecule-metal system as the absorption coupling increases. At some stage, the adlayer becomes merely a mechanism for coupling the radiation field to modes of the substrate itself, as has been shown by coupling of photons to surface plasmon modes by disordered surface layers in attenuated total reflection experiments.[96] These questions, however, properly belong to the subject of energy transfer across interfaces.

2. Energy Transfer Across Adlayer-Metal Interfaces

Energy transfer in condensed media is the central theme of this dissertation. The reader may have followed me through a description of optical and double resonance techniques as probes of singlet and triplet exciton dynamics in molecular crystals. Similarly, by measuring linewidths, lifetimes, energy partitioning ratios and the like, these techniques should illuminate the behavior of excited molecules near metal surfaces. A new decay channel, energy transfer to the surface, acts in concert with radiative, non-radiative, and intermolecular transfer relaxation. The experimental work reported in the following chapters is an attempt to lay the groundwork for studying these effects at well-characterized surfaces.

Interest in surface effects on excited state lifetimes has inspired great experimental and theoretical ingenuity. In particular, Drexhage and others[97-99] have investigated long-range interactions between fluorescing dye molecules and metal surfaces by application of the classic Langmuir-Blodgett technique.[100] In these experiments, a metal

surface is dipped repeatedly through a monomolecular film on a liquid surface, depositing a precisely known number of monolayers of a long-chain fatty acid on the surface. A fluorescing dye molecule is co-deposited in the final layer.

The fluorescent lifetime of the dye is measured as a function of the distance between dye and metal. At distances less than 100 Å, the lifetime exhibits a damped oscillation approaching the free molecule lifetime, with a period on the order of half the emitted wavelength.

In the remainder of this section, I will briefly describe the principal theoretical models proposed to explain these effects, the interference theory of Drexhage[98] and Kuhn[101] and the "Sommerfeld" model of Prock, Chance, and Silbey,[102-105] and others.[106] The probability of enhancement of molecule-metal energy transfer by intermolecular transfer in an ordered, homogeneous overlayer is pointed out in the final paragraph.

The interference model of Drexhage[98] and Kuhn[101] is based on the familiar concept of an image dipole generated in the metal by an excited molecule above the surface, as shown in Figure 29. Radiation from the real and image dipoles will interfere constructively or destructively in the upper half space, depending on the relative phase retardation of the two. The image or reflected field amplitude varies, for the vertical dipole, as

$$A_2 \sim \sin\theta \; r_p \; e^{-2\ell\hat{d}} \qquad \text{[VIII-5a]}$$

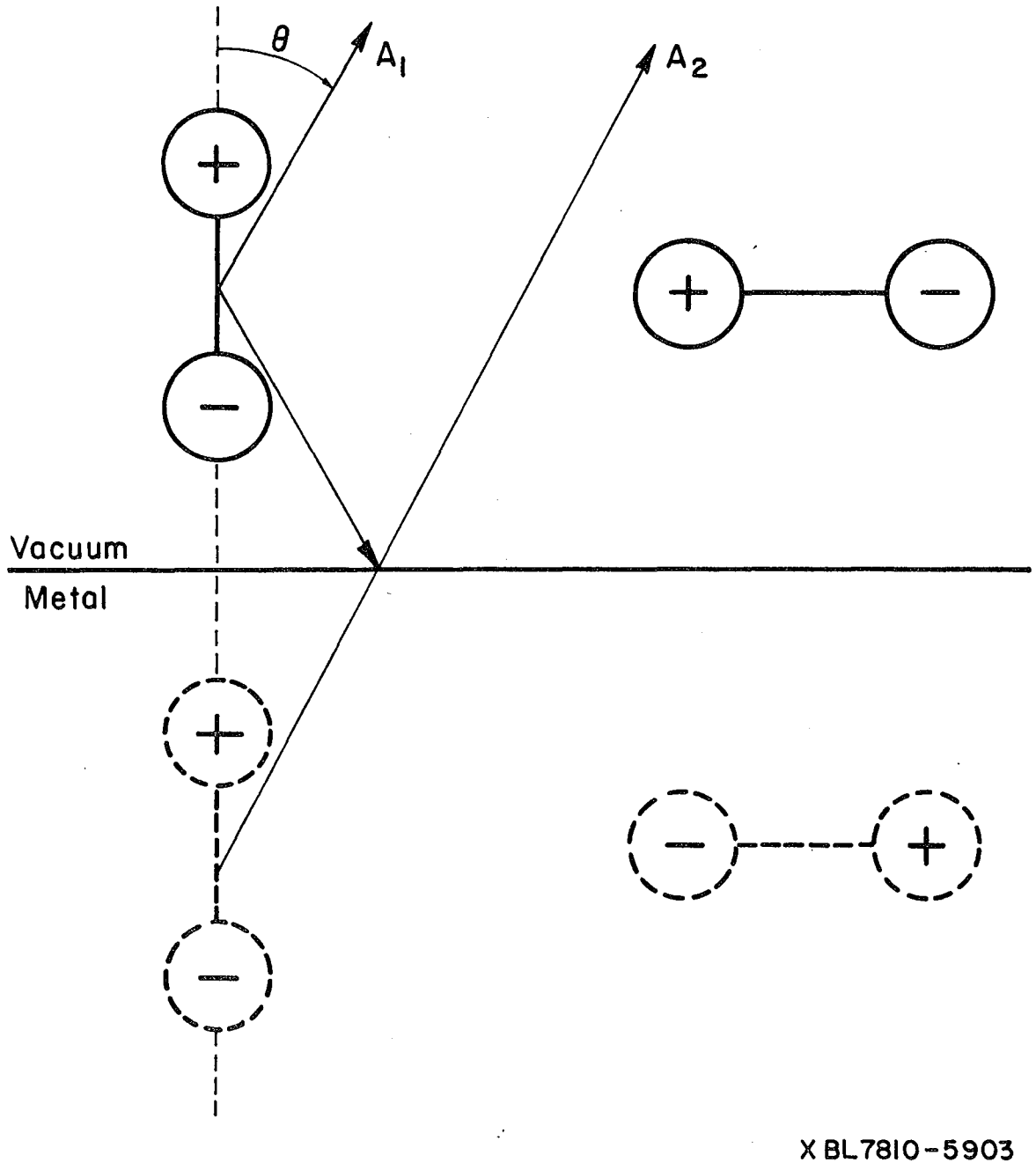

Figure 29. Image dipole model for excited molecule above a metal surface.

where r_p is the Fresnel coefficient, Eq. (3a), $\hat{d}$ is the normalized thickness

$$\hat{d} = 2\pi d / \lambda \qquad \text{[VIII-5b]}$$

and

$$\ell = - i\cos\theta \qquad \text{[VIII-5c]}$$

Adding the primary and reflected amplitudes, squaring to get the intensity, and integrating over the upper half space, the radiated flux Φ varies as

$$\Phi = 2\pi \int_o^{\pi/2} (1+|r_p|^2) \sin^3\theta \, d\theta + 2\pi \int_o^{\pi/2} 2\mathrm{Re}[r_p e^{-2\ell \hat{d}}]\sin^3\theta d\theta \qquad \text{[VIII-6]}$$

Normalizing Φ to the flux in the absence of the metal surface, the decay rate γ in the presence of the mirror is

$$\gamma = \gamma_o - \gamma_r \frac{3}{2} \int_o^1 \mathrm{Im}[r_p e^{-2\ell\hat{d}}] \frac{u^3}{\ell} du \qquad \text{[VIII-7a]}$$

where γ_o and γ_r are the total and radiative decay rates in the absence of a mirror and u equals $\sin\theta$. The equivalent result for the horizontal dipole is

$$\gamma = \gamma_o + \gamma_r \frac{3}{4} \int_o^1 \mathrm{Im}[\{r_s + (1-u^2)r_p\} e^{-2\ell\hat{d}}] \frac{u}{\ell} du \qquad \text{[VIII-7b]}$$

The second term in Eq. (7) predicts the large distance oscillation in the excited state lifetime, but not the short distance behavior.

Seeking better agreement, several researchers have adapted the analysis by Arnold Sommerfeld[107] of a radio antenna over a conducting earth to the smaller but analogous system of a radiating dipole over a

metal surface. The equation for a damped harmonic oscillator dipole driven by its own reflected field E_R

$$\ddot{\mu} + \gamma_o \dot{\mu} + \omega^2 \mu = \frac{e^2}{m} E_R \qquad \text{[VIII-8]}$$

can be solved assuming a single Fourier component in μ and E_R, $\exp[-i(\omega + \Delta\omega)t - \gamma t/2]$, to give

$$\gamma = \gamma_o + \left(\frac{e^2}{\mu_o m \omega}\right) \mathrm{Im}[E_R] \qquad \text{[VIII-9]}$$

as well as an expression for the change in the oscillator frequency. Following the Sommerfeld analysis, the reflected field at the dipole is calculated by generating the electric Hertz vectors[85] above and below the interface from superpositions of continuous cylindrically symmetric basis functions and using the continuity of electric and magnetic fields tangential to the surface as boundary conditions. Ultimately, Eq. (9) becomes

$$\gamma = \gamma_o - \frac{3}{2} \gamma_r \int_o^\infty \mathrm{Im}[r_p e^{-2\ell d}] \frac{u^3}{\ell} du \qquad \text{[VIII-10a]}$$

for the vertical dipole and

$$\gamma = \gamma_o + \frac{3}{4} \gamma_r \int_o^\infty \mathrm{Im}[\{r_s + (1-u^2) r_p\} e^{-2\ell \hat{d}}] \frac{u}{\ell} du \qquad \text{[VIII-10b]}$$

for the horizontal dipole. The integration now runs from zero to infinity rather than zero to one as in Eq. (7).

The agreement between this model and experiment is excellent.[103] For small distances and an isotropic distribution of dipoles, this new contribution to the decay rate is

$$\lim_{\hat{d}\to 0} \gamma = \gamma_r \frac{1}{4\hat{d}^3} \mathrm{Im}\left[\frac{\varepsilon_2-\varepsilon_1}{\varepsilon_2+\varepsilon_1}\right] \qquad \text{[VIII-11]}$$

where ε_1 and ε_2 are the dielectric constants for the ambient and metal.[102] As a figure of merit, the total decay rate is about 10^4 greater than the radiative rate for a molecule radiating in the near UV 10 Å from the nickel surface. The new contribution to the decay rate represents non-radiative energy transfer from the excited dipole to the metal surface, mediated by the short-range near field of the dipole which decays as R^{-2} and R^{-3}. The near field is a localized field rather than a radiation field and contains all wave-vector components, so it can couple to a surface resonance which cannot couple to a photon radiation field with simultaneous conservation of energy and wave-vector. A likely candidate for the energy acceptor is the surface plasmon mode,[108-110] whose frequency ω_{sp} is shifted from the bulk plasmon frequency ω_p by

$$\omega_{sp} = \omega_p \, (1 + \varepsilon_1)^{-1/2} \qquad \text{[VIII-12]}$$

and which has an out of surface transverse electric field component as well as an in-plane longitudinal component. Calculation for the wavelength dependence of Eq. (10) shows a great increase in the energy transfer rate between molecule and surface near the surface plasmon frequency.[104]

The Drexhage experiments give few data points in the short-range energy transfer area because of the considerable thickness of even a single fatty acid monolayer (~ 27 Å), nor do they begin with "clean" metal surfaces. Our experimental techniques for depositing thin molecular overlayers on UHV prepared surfaces overcomes these limitations, but our use

of homogenous films rather than layered assemblies opens up new mechanisms for relaxation. Short-range stochastic excitation transfer between molecules can enhance energy transfer to the surface by transferring excitation to molecules nearest the surface for which the nonradiative transfer rate to the surface is greatest. The molecular overlayer does not need to be a molecular crystal for this to take place, although intermolecular transfer is, of course, sensitive to intermolecular orientation and orbital overlap.

A simple random walk model clarifies some of these observations. Consider a surface overlayer a+1 molecules thick. τ is the jump time between adjacent layers. Considering the steep d^{-3} dependence for transfer to the metal, I will assume energy transfer to the metal is instantaneous from the first monolayer and does not occur for more distant layers. For an excitation starting in layer z, counting from the surface, the average time to reach the first layer in a random walk is

$$\tau_{a,z} = z\ (2a + 1 - z)\tau \qquad \text{[VIII-13]}$$

from the simple statistical arguments discussed in Chapter III-2. Averaging the decay rate, $\gamma_{a,z} = \tau^{-1}_{a,z}$, over all layers except the first,

$$\langle \gamma_a \rangle_z \cong \frac{1}{\tau}\ \frac{\ell n(4a^2)}{4a^2} \qquad \text{[VIII-14]}$$

Since a is proportional to d, the short range transport mechanism falls off more slowly than the direct transfer. The relative importance of

the two mechanisms will be determined largely by τ. A complete analysis of the problem has not been published, although a more sophisticated model has been applied to exciton transport and charge transfer across a metal surface.[111]

IX. SURFACE PREPARATION AND CHARACTERIZATION

1. Vacuum Chamber

The experiments to be reported in the second division of this thesis take advantage of the unique capabilities of a custom stainless steel vacuum chamber designed by A. R. Gallo. A full account of its design, use, and maintenance will be given in his thesis. In order to clarify experiments described in later chapters, a general description of the chamber diagrammed in Figure 30 will be given here.

System base pressure is in the low 10^{-11} torr range after bake-out, as measured by a nude Bayard-Alpert ionization gauge in the central chamber. Principal residual gases are CO and H_2, as determined by a UTI precision gas analyzer (Model 100C) sensitive to partial pressures of 10^{-14} torr. The cylindrical chamber is pumped by a 400 l/sec triode ion pump and titanium sublimation pump (Varian). A cylindrical cooling shield, through which liquid nitrogen, water, or other coolants may be flowed, separates the central experimental area from the walls of the chamber. A lower section of the shield provides cooled surfaces for efficient titanium gettering.

The sample is mounted for the optical experiments in a liquid helium cooled variable temperature cold tip (Air Products and Chemicals, Inc., Heli-Tran refrigerator LT-3-110) which can be regulated between 10 and 300 K by throttling the helium flow through the transfer line. Temperature is measured by a gold(Fe .07%)-alumel thermocouple with external ice bath junction (accuracy $\pm 5^{o}$K). Three fused silica

SCHEMATIC VIEW OF ULTRAHIGH VACUUM SPECTROSCOPIC ELLIPSOMETRY ARRANGEMENT

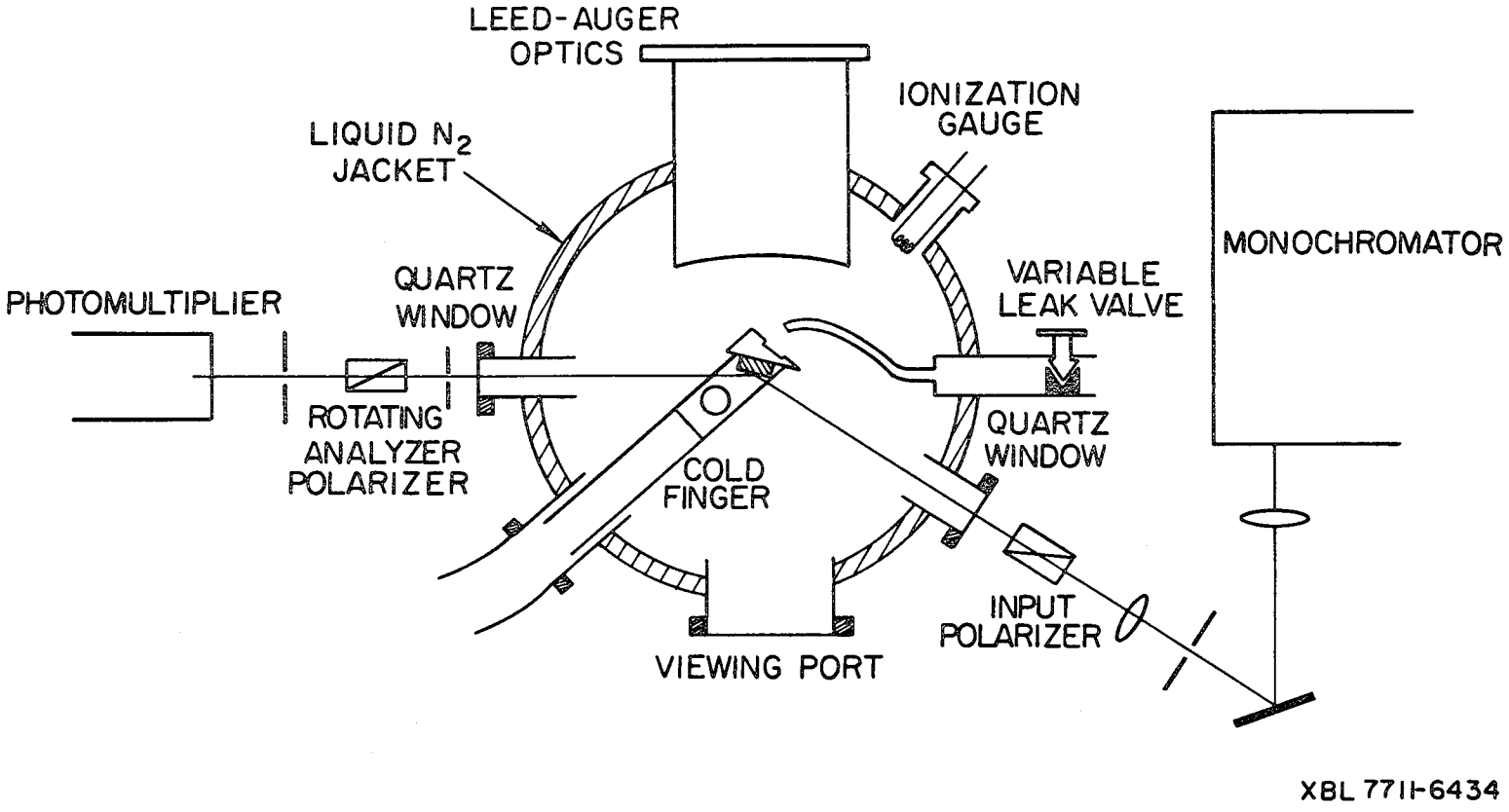

Figure 30. Diagram of ellipsometer with UHV chamber and optics.

windows have access to the crystal surface for optical experiments at angles of 67.5°, 22.5° (LEED viewport), and -67.5° from the surface normal, in the horizontal plane. Gases for cleaning or sample deposition enter the chamber from a diffusion-pump-based vacuum sample handling line through a variable leak valve, into a 4mm. i.d. stainless steel tube open at the end 3 cm from the crystal face. The crystal is transferred between experimental and cleaning stages by a magnetically coupled sample manipulator with linear and rotational motion.

2. Sample Preparation and Cleaning

All experiments in this thesis used two samples showing the nickel(111) crystal face. The samples were cut from a single crystal nickel rod (Materials Research Corp., 99.999%, lent by Prof. G. Somorjai) oriented to expose the (111) face within 2° by Laue x-ray diffraction. 2 mm thick wafers with parallel (111) faces were spark discharge cut and finished to produce crystals approximately 1 cm × 1 cm × 0.2 cm. Each crystal was electron beam welded along the edges to a machined polycrystalline nickel backing as illustrated in Figure 31. Each backing has a 4-40 threaded hole matching the threaded tip of the sample manipulator and a dovetail on the back which fit into dovetailed joint on the cold tip and cleaning stage for temporary mounting. The sample manipulator and mounting was designed by A. Gallo.

The exposed crystal (111) face was polished mechanically through 4/0 emery paper, 1 μ diamond paste on a polishing wheel, and with 0.05 μ alumina in water overnight on a Syntron vibrating bed polisher. No final

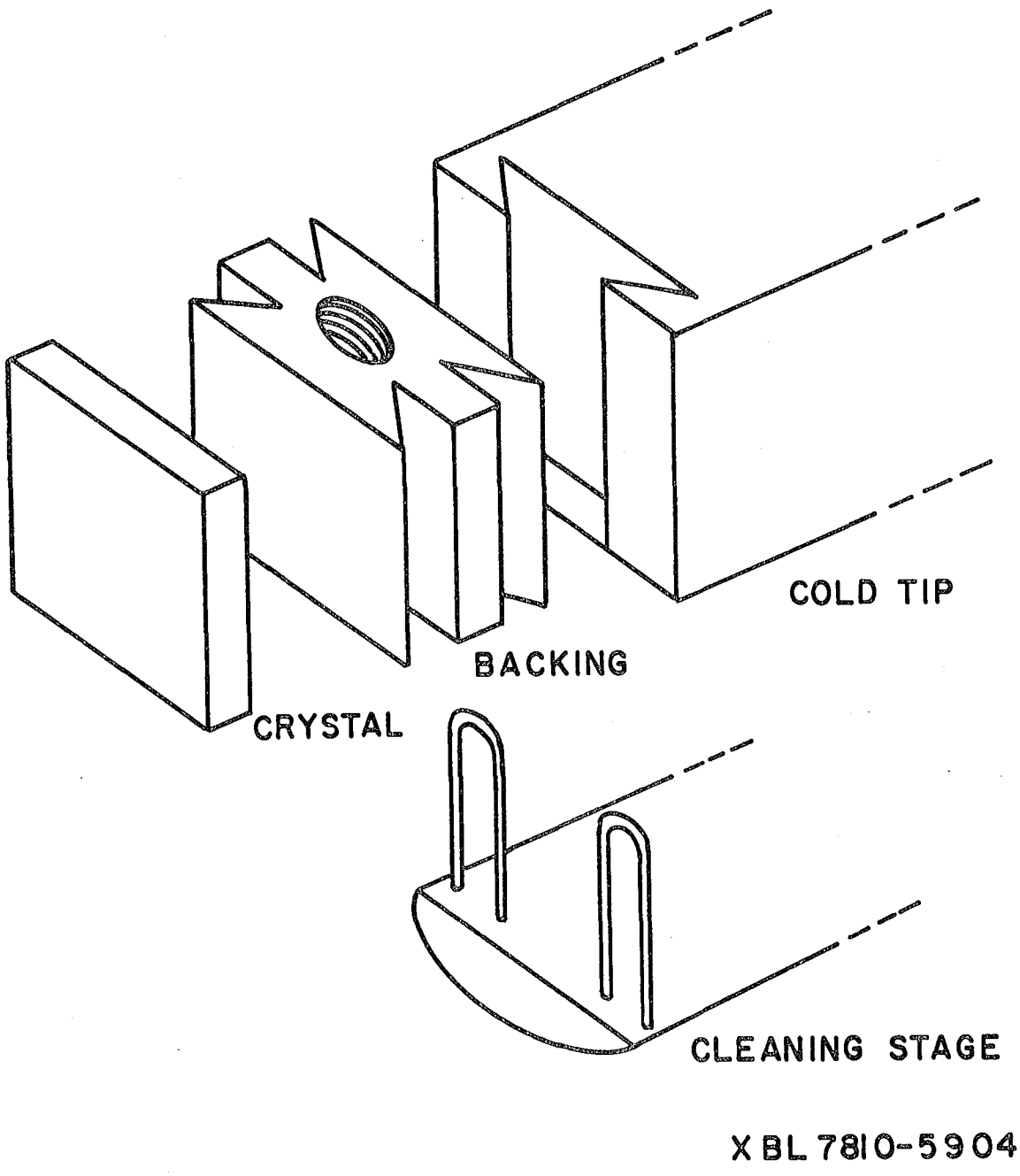

Figure 31. Exploded diagram of sample mount. Crystal is e-beam welded along edges to backing. Threaded manipulator slides backing vertically into cold tip dovetail groove (copper) or cleaning stage (molybdenum wire loops in ceramic).

chemical etch was used. Final orientation was checked with Laue diffraction.

The crystal was ordinarily cleaned in the vacuum chamber by electron bombardment heating to 1000 K in oxygen, hydrogen, and vacuum, successively. On an insulated holder in the lower half of the chamber, the crystal was biased 4.5 kV positive with respect to an adjacent tungsten coil filament. Electron currents of 5 mA across the filament-crystal gap were usually sufficient to reach cleaning temperature. Cleaning gases were Matheson research grade used without further purification, at a pressure inside the chamber of 5×10^{-7} torr. Oxygen was used to remove sulfur and carbon surface contamination and hydrogen reduced the resulting oxide overlayer. Generally twenty minutes of oxygen and forty minutes of hydrogen were sufficient to clean the surface. Alternately, argon ion sputtering and vacuum annealing could be used to sputter etch heavy sulfur or oxygen coverages. Experience showed that sulfur segregated from the bulk to the surface disappeared after several weeks use of the crystal, but carbon contamination became serious after introducing organic samples into the vacuum chamber. Heavy oxygen coverages were occasionally caused by over-vigorous heating or oxygen exposure during cleaning.

3. LEED and Auger Spectroscopy

The UHV chamber is equipped for low energy electron diffraction (LEED) and Auger electron spectroscopy. Electron energy is analyzed by a Varian 4-grid retarding field analyzer which doubles as LEED optics

(Model 981-0127) with integral electron gun centered in the grids. In LEED, this gun directs a collimated beam of monoenergetic electrons normal to the crystal face 5 cm away. The electrons are scattered back into a hemispherical grid assembly in which the second and third grids are biased to transmit elastically scattered electrons and repel inelastically scattered electrons. The first and fourth grids are grounded to shield the rest of the chamber from the retarding field and the positive 5 kV bias of the phosphor screen, which accelerates the transmitted electrons towards the screen which emits light when the electrons strike it. The size of the spots on the LEED screen are determined by the electron source bandwidth and size, and the size of ordered domains on the crystal surface. In our clean samples, the spot size appears to be limited by the lateral coherence width of the source beam. In Auger, a higher energy beam of electrons is used and the scattered electrons are captured and measured at the phosphor screen. Changes in the scattered electron current as a function of the electron energy are detected by modulating the retarding field grid potential and separating out the signal component at twice the modulation frequency with a PAR HR-8 lock-in amplifier and custom tuned pre-amp.

LEED is sensitive to the structure of surfaces of condensed phases. A monoenergetic beam of electrons directed at the sample surface obeys the Bragg diffraction conditions defined by the surface periodicity, as x-rays are diffracted by the bulk periodicity. The surface sensitivity is a result of the low inelastic mean free path for electrons with 100 eV energy. The angular distribution and intensity of the

elastically scattered electons are sharply defined by the conservation of electron wave-vector parallel to the surface within a reciprocal lattice vector of the surface. The two-dimensional pattern formed by the intersection of the diffracted electron beams and a phosphor screen is the reciprocal space image of the two-dimensional structure. The addition of an ordered overlayer to a metal single crystal surface often results in the appearance of new LEED spots whose closer spacing reflects a longer period between repeating units of the overlayer than for the metal. The final pattern can be used to determine the relative size and orientation of the overlayer and metal unit cells. LEED intensities can be used to confirm models of structure normal to the surface.

Auger electron spectroscopy is a technique for the quantitative analysis of the atomic composition of the top surface layers. A 2000 eV incident electron beam generates Auger electrons in a three step process: i) the incident electron ionizes a core-level electron in a surface atom; ii) a valence or higher core-level electron relaxes into the core-level vacancy; iii) the energy released by the relaxation ionizes a second electron, the Auger electron. The escape depth for the Auger electron is limited by the inelastic mean free path, leading to high surface sensitivity. The kinetic energies and intensities of Auger electrons are characteristic of the identity and concentration of the atomic species which produces them. Greater background on LEED[112] and Auger[113] can be found in a number of reviews of the fields.

Our principal use for LEED and Auger was establishing the cleanliness and surface order of the nickel crystal before every optical experiment. The LEED pattern for the nickel (111) surface shows sixfold

symmetry about the central zero-order beam, with a simple hexagon of points appearing for incident electron voltages between 50 and 150 eV. The nickel Auger peaks are 60 eV, 110 eV and a series of peaks between 650 and 850 eV. However, several peaks between 100 and 380 eV, ascribed to favorable diffraction conditions for secondary electron escape,[114] interfere with the sulfur, carbon, and nitrogen peaks. LEED has proven more sensitive to surface contamination than Auger because of this effect in nickel, showing the partial order spots of an ordered overlayer where no contaminants are detected by Auger. In one sample, doubling of first order LEED spots was observed after several weeks of use. Since it has been reported that vicinal faces near the (111) plane of nickel reconstruct to give multi-steps and terraces comparable to the lateral coherence width of the electron beam,[115] room temperature doubling is not readily explained. The crystal was replaced after the doubling was observed.

The chamber is not presently equipped to use LEED-Auger and optical techniques simultaneously. However, electron spectroscopies can be used on the cooled sample in separate experiments and residual overlayers at room temperature can be examined by LEED and Auger after the optical experiment. Such results will be given where relevant in the experimental sections.

X. SPECTROSCOPIC ELLIPSOMETRY

Ellipsometry is an optical technique for measuring the change in polarization of monochromatic light reflected from a linear optical element at non-normal incidence. The change in polarization is related to the surface optical parameters under some model for the surface structure chosen by the experimenters. Spectroscopic ellipsometry measures the wavelength dependence of these optical parameters and includes the field of optical spectroscopy of absorbing overlayers. As a surface-sensitive technique, ellipsometry possesses several important advantages. It is non-destructive, independent of source intensity fluctuations, sensitive to surface coverages as low as 0.01 monolayer, and compatible with a wide range of ambient or immersion media. Combined studies have shown that ellipsometry can be more sensitive to surface contamination than LEED.[116]

A review of the century-old technique of ellipsometry and its theory, instrumentation, and applications to electrochemistry, surface science, and solid-state physics is beyond the scope of this thesis. The need for such review is better filled by a recent book by Azzam and Bashara,[117] a manual by Archer,[118] and review papers by Muller[119] and Aspnes.[120] The purpose of the rest of this chapter and the appendices is a technical description of the instrument and methods used in our experiments with sufficient detail to help future workers in the field. The following section treats our model of the surface and the resulting relationships between experimental observables and surface optical parameters, with a brief discussion of the differences between the model and

real surface. The second section describes the rotating analyzer ellipsometer. The final section is somewhat more detailed and describes the hardware and software for interfacing the ellipsometer to an LSI-11 minicomputer for data acquisition and analysis. Experimental results are deferred to succeeding chapters.

1. Theory and Calculation

Plane polarized light with arbitrary polarization becomes elliptically polarized when reflected (or transmitted) by an interface. In general, ellipsometry measures two independent parameters of a single or compound interface, for example, the relative attenuation, $\tan\psi$, and relative phase shift, Δ, of light polarized parallel and perpendicular to the plane of incidence. These parameters can also be expressed by the complex ratio ρ of the Fresnel reflection coefficients.

$$\rho = \tan\psi \; e^{i\Delta} \qquad [X\text{-}1]$$
$$= r_p / r_s$$

At best, only two optical parameters of the surface can be uniquely determined from ρ, for example, the real and imaginary components of $\tilde{n}_1$ for a two phase system, or n_1 and d for a transparent overlayer. These calculations require a simplified model of the surface and, even so, may not lead to unique determination of the surface optical constants.

The calculation of ψ and Δ is addressed in section 3 of this chapter. This section focusses on the calculation of surface optical constants given ψ and Δ. First the two phase, single interface system is solved for the complex substrate dielectric constant $\tilde{\varepsilon}_1$ given known

ambient $\tilde{\varepsilon}_o$. Second, the three phase, double interface with transparent overlayer ($\tilde{\varepsilon}_1$ real) is solved for ε_1 and d given known $\tilde{\varepsilon}_o$ and $\tilde{\varepsilon}_2$ for ambient and substrate. Finally, ε_1 is calculated for an absorbing overlayer of known thickness d, given $\tilde{\varepsilon}_o$ and $\tilde{\varepsilon}_2$ in addition.

The models for two and three phase surfaces are described in Chapter VIII. In review, all media are homogeneous and isotropic; all interfaces are abrupt and (parallel-) planar. Additional assumptions are made about the real system: 1) the lateral dimensions of the overlayer must be greater than the thickness, so that the summing of multiply reflected beams can be closed analytically, 2) light collimation and bandwidth must be narrow enough to allow coherent superposition of the partial waves, and 3) no non-linear optical properties are significant.

For a two phase, single interface system, all optical properties are defined by $\tilde{\varepsilon}_o$ and $\tilde{\varepsilon}_1$, the complex dielectric constants of ambient and substrate, respectively,

$$\tilde{\varepsilon} = \tilde{n}^2 \qquad [X-2]$$

From the two phase Fresnel coefficients, Eq. (VIII-3a) and Eq. (VIII-3b) it is simple to derive

$$\rho = \left\{\sin^2\phi - \cos\phi\,[(\tilde{\varepsilon}_1/\tilde{\varepsilon}_o) - \sin^2\phi]^{1/2}\right\} / \left\{\sin^2\phi + \cos\phi\,[(\tilde{\varepsilon}_1/\tilde{\varepsilon}_o) - \sin^2\phi]^{1/2}\right\} \qquad [X-3]$$

Inverted to solve for $\tilde{\varepsilon}_1/\tilde{\varepsilon}_o$, Eq. (3) becomes

$$\tilde{\varepsilon}_1/\tilde{\varepsilon}_o = \sin^2\phi + \sin^2\phi \tan^2\phi\,[(1-\rho)/(1+\rho)]^2 \qquad [X-4]$$

The relationships become more complex for the three phase system described by dielectric constants $\tilde{\varepsilon}_o$, $\tilde{\varepsilon}_1$, and $\tilde{\varepsilon}_2$ for ambient, overlayer, and substrate, respectively, and overlayer thickness d. From the two interface effective Fresnel coefficients, Eq. (VIII-4), ρ becomes

$$\rho = \frac{r_{01p} + r_{12p}\, e^{-2i\beta}}{1 + r_{01p}\, r_{12p}\, e^{-2i\beta}} \cdot \frac{1 + r_{01s}\, r_{12s}\, e^{-2i\beta}}{r_{01s} + r_{12s}\, e^{-2i\beta}} \qquad [X\text{-}5]$$

where β is half the phase shift for internal reflection within the overlayer

$$\beta = 2\pi\left(\frac{d}{\lambda}\right)\left(\tilde{n}_1^{\,2} - \sin^2\phi\right)^{1/2} \qquad [X\text{-}6]$$

Equation (5) cannot be inverted to solve for any $\tilde{\varepsilon}$ or d analytically. Solutions for overlayer optical constants and/or thickness must be approached numerically or by approximation.

For the three phase system with transparent overlayer, computer programs give both approximate and numerical solutions for ε_1 and d. For thin films (< 100 Å), the results for both methods are generally within 10%. An approximate solution is obtained by expanding the exponentials in Eq. (5) and retaining terms linear in d.[118,120,121]

$$\varepsilon_1 = \mathrm{Im}[\tilde{\varepsilon}_2] \cdot \mathrm{Im}[A] \cdot (\mathrm{Re}[A]^{-1}) + \mathrm{Re}[\tilde{\varepsilon}_2] \qquad [X\text{-}7a]$$

$$d = (\varepsilon_1 - 1) \cdot \mathrm{Re}[A] \cdot (\varepsilon_1 \cdot \mathrm{Im}[\tilde{\varepsilon}_2])^{-1} \cdot \frac{\lambda}{4\pi \cos\phi} \qquad [X\text{-}7b]$$

where

$$A = \frac{\rho' - \rho}{\rho} \cdot \frac{(\tilde{\varepsilon}_2 - \tilde{\varepsilon}_o)(\tilde{\varepsilon}_2 \cot^2\phi - \tilde{\varepsilon}_o)}{\tilde{\varepsilon}_2} \qquad [X\text{-}7c]$$

The numerical solution of Eq. (5) for transparent overlayer is outlined by Aspnes[120] using Newton's method to iterate n_1 so as to minimize $\ln|e^{-2i\beta}|$. $\ln|e^{-2i\beta}|$ is zero for a transparent overlayer. The overlayer thickness d can be calculated from β when the minimum value of $\ln|e^{-2i\beta}|$ is achieved.

For a transparent overlayer, d cannot be uniquely determined. The thickness factor in Eq. (5), $e^{-2i\beta}$, is a periodic oscillation and values of d are separated by

$$\nu \lambda / 2(\varepsilon_1 - \sin^2\phi)^{1/2} \qquad [X-8]$$

where ν is a integer. In practice, the correct thickness must be chosen by an independent method, by multiple wavelength measurements, or by monitoring the overlayer thickness continuously during its deposition or formation on a bare substrate. Computer programs KZERO1 and KZERO2 calculate approximate and numerical solutions, respectively, for ε_1 and d; listings and annotations appear in the appendices.

Algorithms for an absorbing overlayer of known thickness in the three phase, two interface systems are similar to those for the transparent overlayer. The linear approximation, Eq. (7), can be inverted to solve for the complex $\tilde{\varepsilon}_1$ resulting in a quartic equation in $\mathrm{Re}[\tilde{\varepsilon}_1]$ and for solutions for $\tilde{\varepsilon}_1$. Two solutions, which assign complex values to $\mathrm{Re}[\tilde{\varepsilon}_1]$ can be ignored. The numerical solution for $\tilde{\varepsilon}_1$ is due to Heinz Robota and uses a Newton's method iteration of $\tilde{n}_1$ in two dimensions, minimizing the difference between the experimentally determined ρ and ρ calculated from the system optical parameters at that stage in the iteration. Two solutions for $\tilde{\varepsilon}_1$, corresponding to the two approximate solutions, can be calculated,

depending on the initial value chosen for $\tilde{\varepsilon}_1$. There is no a priori way to choose the correct value for the optical parameters of the surface. However, as a function of wavelength, the solutions fall into two distinct, continuous sets or spectral curves, one of which usually strays into physically unrealistic regions (e.g., negative $\mathrm{Re}[\tilde{n}_1]$)and can be eliminated. Computer programs LEROY and FIELDS combine both methods to solve for $\tilde{n}$ of an absorbing overlayer, using approximate solutions as starting values for the numerical iteration; listings and annotations are in appendix.

The two and three phase models just discussed are poor representations of optically rough surfaces or submonolayer films. Theoreticians have advanced several alternative models to treat these systems. Strachan[122] has shown that a submonolayer of admolecules, modeled as a two-dimensional array of dipoles, gives rise to a linear relationship between ψ, Δ, and coverage. Relative coverage can be simply measured by ellipsometry, but the calculated $\tilde{n}_1$ values have no simple relationship to bulk values for the adsorbed species. Surface roughness on a clean substrate has been modeled by Garnett[123] as a homogeneous three phase system. The disordered region is treated as a well-behaved overlayer whose thickness and index of refraction are determined by the volume fraction of substrate material in the disordered region. More recently, Dignan and Moskovits[124] have treated a disordered surface with adlayer as a homogeneous overlayer whose polarizability is that of a two-dimensional array of adsorbate-covered substrate spheres. Unfortunately, these theoretical models and their many refinements are of little use to the experimentalist attempting

to measure surface optical properties because they contain many more parameters than can be determined uniquely by the measured ψ and Δ.

These remarks serve as an introduction to a major problem in the interpretation of our experimental data. The thickness of nominally transparent overlayers varies as a function of the wavelength of light, with the calculated thickness roughly inversely proportional to the wavelength. Systems studied were argon, pyrazine, and CO on nickel(111), all of which show the same magnitude effect and all of which show bulk transparency in the visible where the measurements were made. Argon and pyrazine were condensed at low temperatures and no independent measurement of thickness was available. CO at room temperature saturates at a coverage of one-quarter monolayer. Several possible explanations for this effect have been explored.

1) Change in substrate optical parameters. The optical properties of substrates with dangling surface bonds, such as silicon, are strongly affected by any adsorbate.[125] However, incremental deposition of pyrazine on nickel gives wavelength-dependent incremental increases in thickness, although the surface properties of the metal would not be expected to change after the first few monolayers.

2) Anomalous overlayer absorbance. Argon would not be expected to interact with the nickel surface so as to have a visible resonance. Absorbance induced by a space charge layer with a plasmon-like dispersion would give an increase in thickness with increasing wavelength, opposite to that observed.

3) Surface roughness. It has been shown that surface roughness gives misleading surface overlayer optical constants.[126] Future experimental work on nickel(111) substrates polished or etched in different ways may indicate a problem of this nature.

4) Optical anisotropy. Anisotropic surface optical constants mix perpendicular and parallel components of the radiation field and invalidate the surface models. Very little experimental or theoretical work has addressed this problem.

5) Instrumental artifacts. Work is in progress to evaluate the importance of window birefringence or ellipsometer misalignment on the experimental measurements.

These wavelength dependent thickness effects are responsible for the large uncertainties in overlayer thickness given in the phosphorescence studies in Chapter XII. For a one-quarter monolayer of CO on nickel(111), the measured thickness was 2 to 4 Å, near the expected value from Van der Waals radii for CO normal to the surface. It does appear that a qualitative discussion of phosphorescence and overlayer thickness can be justified, given this near coincidence of measured and expected thickness for CO. Conclusions drawn in Chapter XI are based on resonance frequencies and relative absorbances, so these conclusions are not weakened.

2. Ellipsometer

The ellipsometer was fabricated in the College of Chemistry machine and electronics shops using the rotating analyzer design described by D. D. Aspnes of Bell Laboratories.[127-130] A schematic of the

apparatus is shown in Figure 32. This method uses a fixed input polarizer and a rotating output polarizer. Plane polarized light incident on the surface is reflected as elliptically polarized light and the rotating analyzer maps out the ellipse as an oscillating light intensity at the photoelectric detector. With respect to the conventional null ellipsometer, the rotating analyzer design has the advantages of speed, precision, the lack of wavelength-dependent optical elements such as a quarter-wave plate, and compatibility with online computer for signal averaging and analysis. Details of the computer interface and signal processing will be discussed in the next section.

The ellipsometer can be divided for description into five sections: source, polarizer, sample, analyzer, and detector. The source must provide a collimated, monochromatic light beam scannable over a wide wavelength range. It consists of a 75 W Xenon lamp in a PEK housing (Model 912-1) with condenser lens, focussed on the entrance slits of a 1 m SPEX 1700 monochromator. Output of the monochromator is collimated by two quartz lenses. The polarizer establishes linear polarization at a known angle to the plane of incidence. Two different types of polarizer have been used for both input polarizer and analyzer, air space Glan-Thompson polarizers and calcite rhomb polarizers, in attempting to minimize parallel displacement of the beam and maximize extinction of the unwanted polarization. The input polarizer was mounted at the center of a rotary stage with stepping motor (Aerotech, Model ATS-301 MR2', with translator card) for computer control of input polarization.

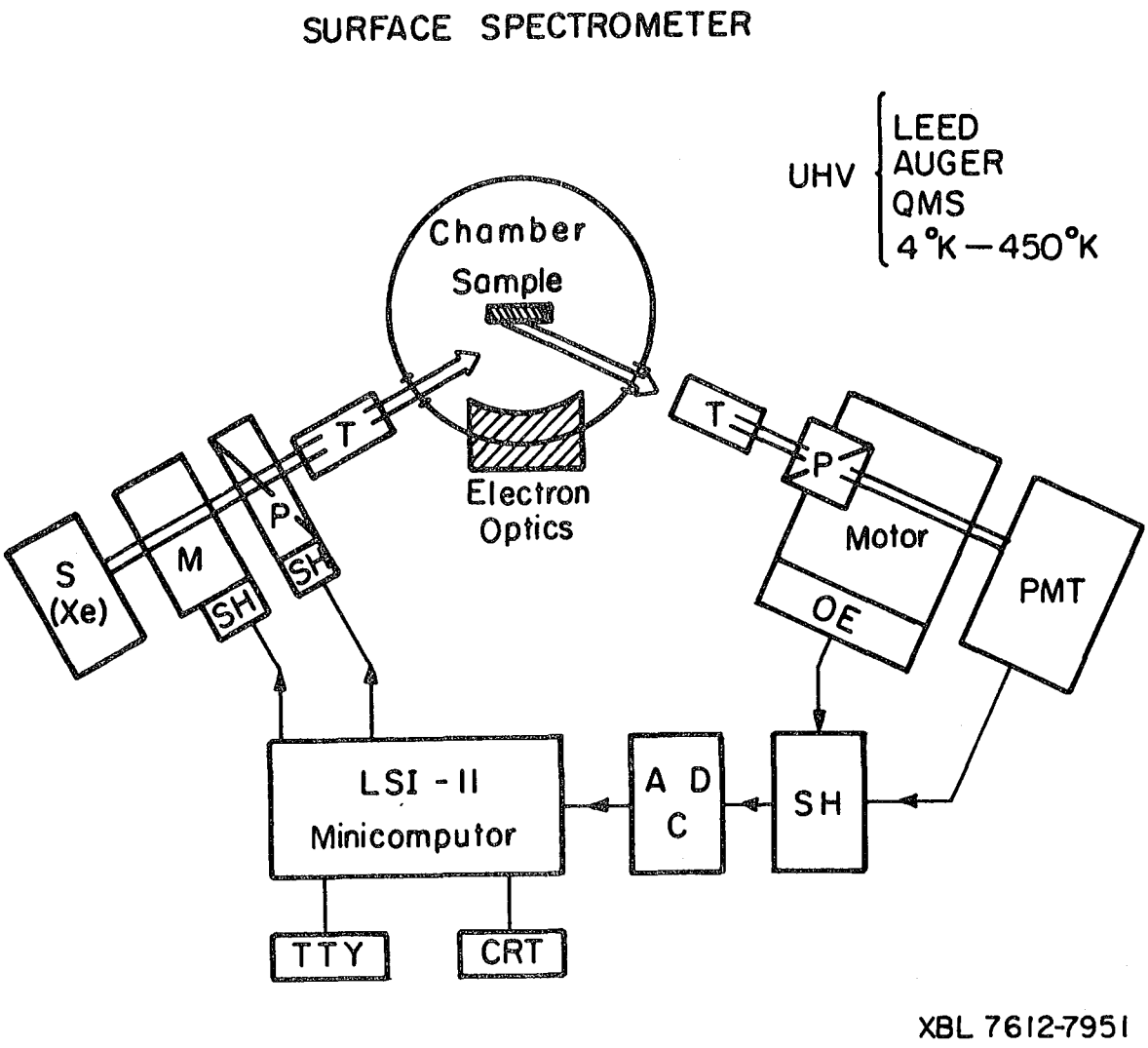

Figure 32. Block diagram of rotating analyzer, with xenon arc lamp source (S), monochromator (M) with stepping motor (SH), input polarizer (P) with stepping motor, sample, output polarizer (P) in hub of motor with optical encoders (OE), and photo-multiplier tube (PMT). Data acquisition is performed by sample-and-hold (SH), analog-to-digital converter (ADC), and LSI-11 minicomputer with teletype (TTY) and CRT graphics display. Telescopes (T) were eliminated in apparatus.

The rotating analyzer or output polarizer must rotate at a very stable frequency to minimize long-term drift and short-term fluctuation in the experimental signal. The analyzer is mounted coaxially in the hub of a 1/15 hp electric motor (Bodine El. Co.). The frequency standard is set by a 1 MHz oscillator (Vectrow Labs C011 series) with temperature-controlled oven, driving a power amplifier (Altec 9440A, 800 W mono) which drives the motor. Absolute angular displacement is measured by the passage of a gear (kanigin plated for reflectivity) mounted on the motor in front of two optional encoders (Skan-a-matic, Model S2005-3). Seventy-two gear teeth mark 5^{o} increments on the gear plate. A hole drilled in the gear plate provides a second mark once per revolution.

The detector is an EMI 9558 photomultiplier tube with end-on photocathode to minimize sensitivity to incident polarization, in a Products for Research TE200 housing. Supply voltage is provided by a Fluke high voltage power supply (415B) for constant supply voltage applications, or a programmable Kepco APH 200 supply, when it is desired to keep the PMT signal at a constant average voltage over long wavelength scans. A helium-neon laser is mounted behind the phototube for alignment purposes. Details of the alignment procedure and a more complete description of certain ellipsometer components will be given in future doctoral theses by Antonio Gallo and Heinz Robota.

3. Data Acquisition and Analysis

This section describes the computer and its interface to the experiment and the procedures for computer-controlled calibration and data taking. These procedures are due to D. D. Aspnes with minor modifications, and a fuller explanation of many of the details is given in his papers.[127,129]

The computer used was an LSI-11 V03 from the Digital Equipment Corp., a microprocessor-based mini-computer with hardwired arithmetic unit, using a 16 bit word, and having access to core memory of 28k words. Hard data storage was done on an RX 01 Floppy Disk drive unit, with two disk drives each storing 125k words. Disk access time was 0.5 seconds. Control device was an LA36 Decwriter teletype with graphics capability on a Tektronix 4006 CRT teletype and 4662 interactive digital plotter. The operating system was the DEC RT-11 system in single job mode, with Fortran capability and Tektronix TCSLIB graphics subroutine library.

The computer was interfaced to the experiment with an Adac Corp. data acquisition and control system (Model 600-LSI-11). Physically, this is a circuit board in the computer chassis with a fifteen foot cable to a panel with BNC conversion on 8 multiplexed, fully differential inputs. Conversion takes 20 microseconds, with a data sampling window of 20 nanoseconds. The Adac board has provisions for external triggering of data conversion, programmable preamplifier, and two digital-to-analog outputs (which are not used in the ellipsometry experiments). Two unused bits in the status buffer word, the fifth and fourteenth bits, are jumpered to external connectors and used to control data conversion

triggering and the rotational stage (see Appendices).

The rotational stage holding the input polarizer can be stepped by the computer through the 14 bit or manually (10,800 steps = 1 revolution); the direction of rotation is set manually. Computer control of polarizer angle is used during calibration, as discussed below, and the details of the rotational stage interface are collected in Appendix I.

The optical encoder channel A triggers data conversion and storage at 5^{o} intervals of the output analyzer rotation. The Adac board 5 bit gates the channel A pulses going into the external trigger input so that data taking begins at the same point of the analyzer rotation on each data taking cycle. The triggering circuit is described in Appendix II. The photomultiplier tube output is put through a time constant and buffer amplifier before reaching the negative input to the 0 fully differential input channel of the Adac board.

The ellipsometer must be calibrated before data taking. Calculation of the ellipsometric angles ψ and Δ requires knowledge of the angles that the polarizers make with the plane of incidence. The reference marks for the input and output polarizers are the zero of the digital counter and the angle at which the first data conversion takes place, respectively. All ellipsometric calculations can be made using angles measured relative to these references, if the angle between reference and plane of incidence can be calibrated. This is done by the computer program ATOCAL which calculates angles for each polarizer and the depolarization induced by imperfect optical elements in the beam path.

In data taking, light intensity is measured as a function of output angle, $I(\theta)$, averaged over many rotations at 31.25 Hz. The intensity fluctuates at twice that frequency, 62.5 Hz, and is analyzed as a sum of in and out of phase components (cosine and sine waves) at that frequency by a Fourier deconvolution

$$a + ib = \sum_{\theta} I(\theta)\ e^{i\theta} / \sum I(\theta) \qquad [X\text{-}9]$$

Calibration is a data taking procedure which uses the fact that light polarized in the plane of incidence is reflected still linearly polarized in that plane. With the input polarizer roughly oriented in the plane of incidence, the input polarizer is rotated by small increments through the plane of incidence by the computer, measuring the Fourier components a and b at each angle, as well as the residual R

$$R = 1 - a^2 - b^2 \qquad [X\text{-}10]$$

In an ideal system with no depolarization, linearly polarized light in the plane of incidence gives

$$a^2 + b^2 = 1 \qquad [X\text{-}11]$$

Elliptically polarized light output gives

$$a^2 + b^2 < 1 \qquad [X\text{-}12]$$

R will go through a minimum when the input polarizer axis lies in the plane of incidence, so that angle can be identified. If imperfections in the ellipsometer or sample depolarize the light, this attenuates the AC component of the signal and a depolarization parameter can be measured

from R for incident polarization in the plane of incidence. At this same input angle, the angle between the first data point and plane of incidence for the output polarizer is given by $\tan^{-1} b/a$. For example, assume that the first data point collected is in the plane of incidence. The intensity of the linearly polarized light will map out a pure cosine wave ($a = 1$, $b = 0$) and $\tan^{-1} b/a = 0$, the angle between the first data point and plane of incidence, as assumed. Alternatively, assume the first data point is 90^{o} from plane of incidence. Then intensity follows a sine wave ($a = 0$, $b = 1$) and $\tan^{-1} b/a = 90^{o}$. This calibration angle includes not only the geometrical angle in the analyzer between the marks representing the first data point and the polarizer axis, but also the angular phase lag due to the signal processing time constant.

After calibration, data taking and storage are performed by the program STORE, which calculates ψ, Δ, and several optical constants and stores them on disk. For data taking, the input polarizer is slewed manually to a position where its axis is about thirty degrees from the plane of incidence, which maximizes sensitivity to changes in Δ. The Fourier coefficients a and b are calculated, usually as a function of some variable such as wavelength or temperature. From these coefficients, the relative phase shift Δ and attenuation $\tan \psi$ of perpendicular and parallel polarized light can be calculated by the formulae given by Aspnes

$$Q = \frac{1}{2} \tan^{-1} b/a \qquad [X\text{-}13a]$$

$$\alpha = (1 - \zeta)^{1/2} / (1 + \zeta) \qquad [X\text{-}13b]$$

$$\zeta = \eta\ (a^2 + b^2)^{1/2} \qquad [X\text{-}13c]$$

$$\rho = \tan\psi\, e^{i\Delta} = [\cot(Q\text{-}A_1) - i\alpha][\tan(P - P_1)]/[1 + i\alpha \cot(Q\text{-}A_1)] \qquad [X\text{-}13d]$$

where A_1 and P_1 are calibration angles for analyzer and polarizer, η is the depolarization parameter also supplied by ATOCAL, and P is the polarizer angle measured on the digital counter during data taking. The quantities Q and α are simply the angle of the major axis of the ellipse with respect to the plane of incidence and the ratio of minor to major axis of the ellipse, respectively. Equation (13d) is the result of simple geometric relationships between the shape of the ellipse and the phase shift and attenuation, Δ and ψ, that give rise to it. Given Δ and ψ, the complex dielectric function and index of refraction of the reflecting media can be calculated by Eq. (4). For a bare surface, these represent the metal optical constants. For a multi-layer surface, these are only effective optical constants for the composite surface, with no simple physical significance.

These calculated values are stored on diskette for later analysis in blocks of sixteen data points. For each data point, 6 variables are stored, four real and two complex: data point number, time of acquisition, ψ, Δ, $\tilde{\varepsilon}$, and $\tilde{n}$. This data may be displayed graphically by the program UNSTOR, or two data files, one for the bare metal surface and

one for surface with overlayer, may be analyzed together to obtain overlayer optical constants by program LEROY or FIELDS. All programs are listed and annotated in Appendix III.

XI. UV SPECTROSCOPY OF AROMATIC MOLECULES ON NI(111)

1. Pyrazine

The spectroscopy of pyrazine has been a subject of great interest to physical chemists for many years. Added to the potential for chemistry through the two nitrogen lone pair orbitals and the two singlet electronic states within the wavelength range of our ellipsometer, this fact made pyrazine an obvious choice for study on the nickel surface. The structure and spectra of pyrazine are summarized in Figure 33. Pyrazine (Aldrich, Gold Label, 99+%) was introduced as a vapor into the UHV chamber through the variable leak valve, onto a surface prepared and characterized as described in Chapter IX. The details of obtaining the UV spectra are explained in Chapter X. This chapter will discuss our results and preliminary conclusions about the excited electronic and vibronic energy levels, molecular ordering in the adlayer, and the search for chemisorbed pyrazine.

a) Excited Electronic State Energy Levels

The lowest excited singlet states of pyrazine have been studied extensively as a simple example of interaction between lone pair orbitals.[131-133] The lowest electronic state origin occurs around 3300 Å with oscillator strength of 0.01 and has been assigned as an $n\pi^*$ transition. Two such transitions are predicted, a dipole-forbidden $n_+\pi^*$ transition where n_+ represents a symmetric superposition of the two nitrogen lone pair orbitals, and a dipole-allowed $n_-\pi^*$ transition where n_- represents an anti-symmetric combination. Surprisingly, the

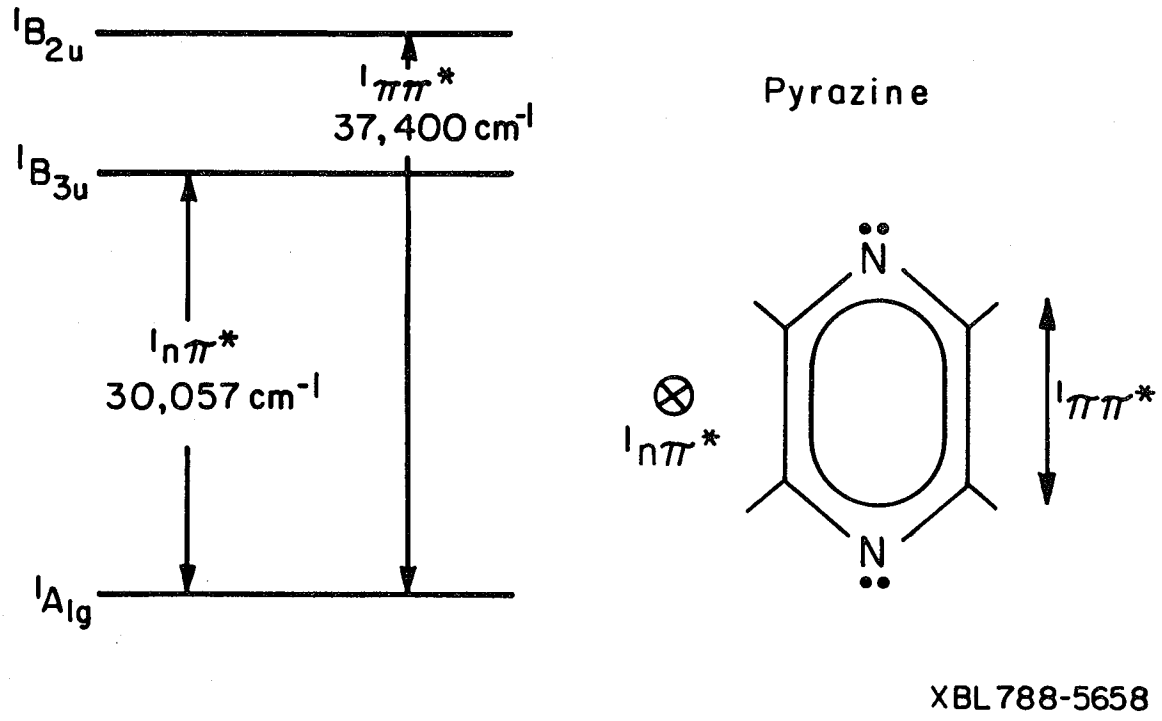

Figure 33. Structure of pyrazine ($C_4H_4N_2$) with energies and polarizations of lowest singlet states.

$n_-\pi^*$ state is expected to be much lower than the symmetric $n_+\pi^*$ state, due to interaction with the σ^* and σ orbitals, respectively, of the ring skeleton. The best theoretical and experimental estimates of the $n_+\pi^*$ state energy place it above the $\pi\pi^*$ singlet state.[132,134] Despite many attempts and some false assignments, the $n_+\pi^*$ transition has never been observed, so the lowest singlet electronic state at 3300 Å is identified as the $n_-\pi^*$, $^1B_{3u}$ state. At wavelengths below 2800 Å, strong transitions (oscillator strength 0.10 - 1.0) are identified as $\pi\pi^*$, the $^1B_{2u}$ resonance corresponding to the benzene bands at 2670 - 2270 Å.[132]

Near UV spectra of pyrazine on nickel (111), derived from spectroscopic ellipsometry, are shown in Figures 34, 35, and 36, for pyrazine overlayers between 5 and 10 Å thick. The thickness is measured by assuming that the overlayer is transparent in the region above 3300 Å using the equations given in Chapter X-3. Instrumental resolution is about 10 Å in these spectra. The pyrazine is deposited on the metal substrate at 10 K and annealed at 120 K before the spectra were taken. The effect of annealing is discussed further in Section c). The spectra are temperature independent between 10 and 160 K after annealing. The important features of the spectra are the onset of absorption at 3300 Å with partially resolved structure in the region 3300 - 3000 Å and the appearance of a stronger absorption around 2700 Å with a distinct shoulder on the rising edge. These features are reproducible from the thinnest overlayer observed (3-4 Å) to the thickest (100 Å). The energy of the lowest absorption is 3296 Å, measured at the center of the first peak. The energy of the higher energy resonance is 2717 Å, measured from the center of the resolved shoulder in Figure 35.

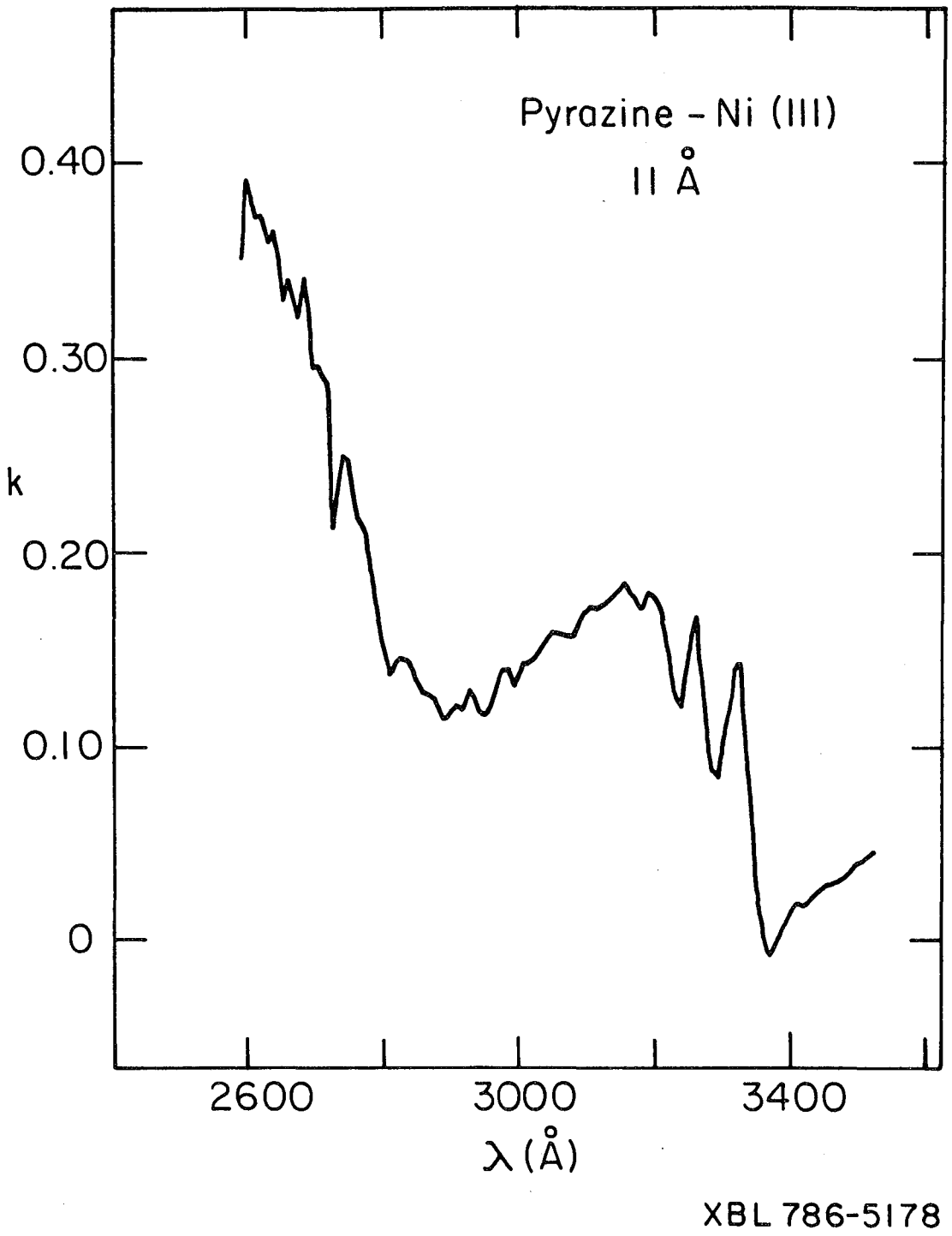

Figure 34. Absorbance spectrum of 11 Å overlayer of pyrazine on Ni(111) surface at 10 K showing $\pi\pi^*$ and $n\pi^*$ transitions. Absorbance, k, is related to molar extinction coefficient, ε, by $k = \ln(10)\,\varepsilon\, c\lambda/4\pi$ where c is concentration in moles/liter and λ is in decimeters.

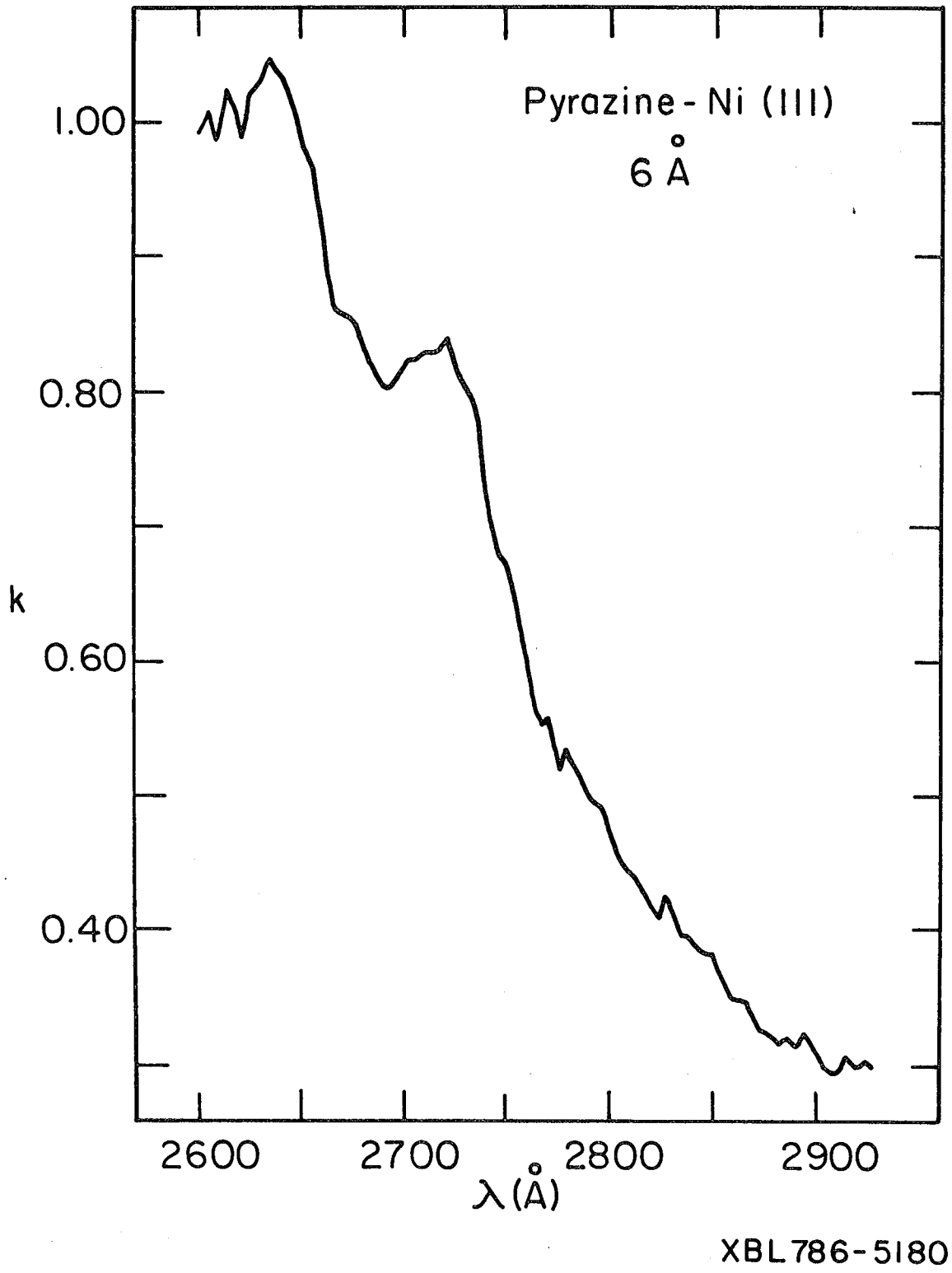

Figure 35. Absorbance spectrum of 6 Å overlayer of pyrazine on Ni(111) surface at 10 K showing $\pi\pi^*$ transition.

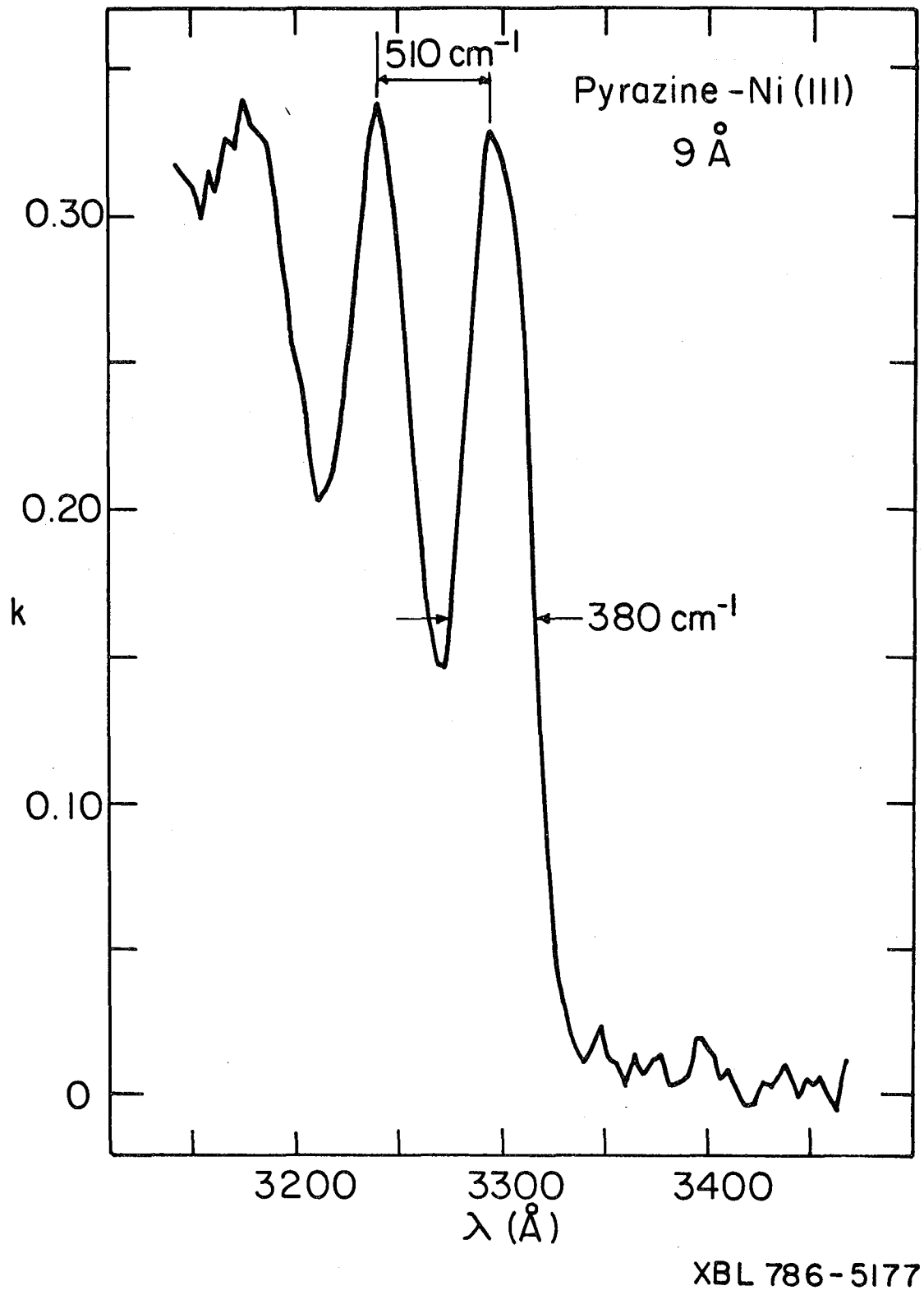

Figure 36. Absorbance spectrum of 9 Å overlayer of pyrazine on Ni(111) surface at 10 K showing nπ* transition.

The pyrazine overlayer absorptions follow closely the bulk transition energies. Table IV summarizes the relative energies of the pyrazine lowest excited singlet states for the vapor,[131] for pure crystalline pyrazine at 4.2 K,[133] and for the pyrazine overlayer on nickel (111) at 10 K. For the $n\pi^*$ state, the energies are ranked

$$E(\text{gas}) > E(\text{surface}) > E(\text{crystal}). \qquad [XI-1]$$

Energies of surface transitions seen in reflection or transmission spectra of bulk molecular crystals obey a similar ranking.[89] On going from the gas phase to the solid phase, an excited molecule undergoes a greater relaxation than a ground state molecule, because of the interaction of the excited molecule with its neighbors. This gives rise to a shift to longer wavelength of the electronic transition. A surface molecule has a smaller number of neighbors and undergoes an intermediate shift. The overlayer of 100 Å thickness does not, however, show a superposition of bulk and surface values as might be expected, indicating that the overlayer energy shifts are due to another mechanism. The $\pi\pi^*$ energies in Table IV are arranged differently.

$$E(\text{gas}) > E(\text{crystal}) > E(\text{surface}) \qquad [XI-2]$$

where the overlayer molecules show a larger relaxation shift than the bulk molecules. An interaction between overlayer and substrate, the possible nature of which is discussed in the following sections, may be responsible for the site shifts. In general, however, the overlayer and bulk transition energies agree quite closely, particularly in light of the difficulty in assigning values to the broad overlayer transitions. The good correspondence between surface and bulk indicates that

Table IV. Pyrazine Singlet Energy Levels

		$^1n\pi^*$	$^1\pi\pi^*$
Vapor	(298 K)	30875 cm^{-1}	37839 cm^{-1}
Pure Crystal	(4.2 K)	30057	37400
Adsorbed Overlayer	(10 K)	30340	36805

interaction between overlayer and metal substrate does not essentially change the molecule's identity and that the molecules observed are physisorbed on the surface, or, in the case of multiple layer deposition, condensed on the surface.

b) Excited State Vibrational Frequencies

The absorbance spectrum of the pyrazine $n\pi^*$, $^1B_{3u}$ excited state shown in Figure 36 has a vibronic progression in a ν_6 ring stretching mode, with the first three peaks sufficiently well resolved to measure the vibronic splitting. To our knowledge, this is the first direct and conclusive observation of an excited state vibrational frequency for molecules adsorbed on a metal surface. IR reflection and transmission spectroscopy and high resolution electron energy loss spectroscopy have been used extensively to measure ground state vibrational frequencies. Photoelectron spectroscopy has revealed vibrational structure of excited final states in the gas phase, but the natural photoelectron linewidth of adsorbed molecules has prevented similar resolution for surfaces.[135] Optical techniques, including spectroscopic ellipsometry, appear to be the best probe available of excited state vibrational frequencies.

Measuring excited state vibrational frequencies has advantages and disadvantages compared to measuring ground state vibrations. The body of literature on bulk vibrations for comparison is more limited for excited states. An object of great experimental interest, the vibration of small admolecules against the surface, cannot be studied

in the excited state unless the complex has an electronic state at an accessible wavelength and the vibration has the correct symmetry to couple to the electronic state. Some evidence using other optical techniques suggests this situation may not, however, be uncommon. As advantages, high resolution is more easily obtained with UV-visible photons than electrons and vibrations below 1000 cm^{-1}, which are often inaccessible to surface IR spectrometers, are easily resolved from the electronic origin in the excited state. Finally, the literature on excited vibronic levels in aromatic molecules is extensive and gives not only vibrational splittings in the bulk phase, but also describes how vibronic intensities and linewidths carry information about the symmetry of the excited state and coupling to other states.[136]

An expanded plot of the $n\pi^*$ transition of pyrazine on nickel (111) is shown in Figure 36. Neither the vibrational splitting between the low energy peak and the next maximum, nor their relative intensities, vary systematically with overlayer thickness between 4 and 100 Å. This disproves an earlier speculation that the peaks represented different adsorption environments. Instead, they represent separate vibrational levels of the same molecules. The vibrational splitting, averaged over many spectra, is 525 ± 25 cm^{-1}. The large error limits are due to the large linewidth, about 380 cm^{-1} for the origin (larger than the instrumental linewidth). Higher vibrational levels are poorly resolved, although the 525 cm^{-1} spacing does appear to continue for several additional quanta, particularly in the phosphorescence excitation spectra described in the next chapter.

The measurement of the vibrational splitting was our first significant surprise in studying adsorbed aromatics. The appearance of the ν_6 progression is additional evidence for the weak perturbation of the physisorbed molecules, because both gas and solid phase adsorption spectra show this strong progression in the $^1n\pi^*$ transitions.[133] However, the frequency of the surface vibration is significantly shifted. Figure 37 summarizes information known about the ν_6 totally symmetric vibration. Its frequency in the excited state is almost completely independent of the environment. In the gas phase, the pure crystal, and several solid solutions, the ν_6 frequency lies between 580 and 590 cm^{-1}, well outside the range of experimental error of the overlayer splitting of 525 cm^{-1}. It should be reiterated that the overlayer splitting is not appreciably shifted or broadened for overlayers as thick as 100 Å, proving that a direct nickel to pyrazine interaction is not responsible. Still, it is regrettable that high resolution UV spectra of nickel coordination compounds with pyrazine ligands have not been published, that the effect of a direct interaction might be known. It is necessary to invoke some other mechanism to explain this shift. Since it has been shown that the ν_6 mode is very sensitive to molecular distortion in combination bands with out-of-plane vibrations, a change in molecular geometry may be responsible. The possibility that pyrazine takes on an unorthodox pseudomorphic crystal structure on the nickel surface, with a resultant shift in vibrational splitting is being explored by examining thicker overlayers presently.

The absence of resolved vibronic structure in the pyrazine overlayer below 3100 Å can be accounted for by intramolecular effects

Pyrazine

Environment	ν_6 Frequency in $^1B_{3u}$ State
Vapor	584 cm^{-1}
Cyclohexane sol'n	582
Benzene sol'n	586
Pure crystal (4K)	587

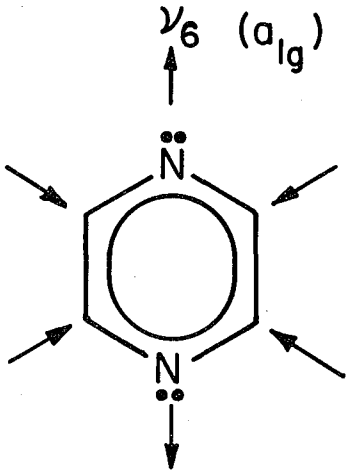

Average – Non-surface environment 585 cm^{-1}

Surface Nickel (111) 525 ± 25 cm^{-1}

XBL 788-5659

Figure 37. Summary of data on ν_6 mode in $^1n\pi^*$ state of pyrazine.

equally important in the bulk phase in combination with the broad linewidth exhibited by the overlayer $n\pi^*$ origin. Several new, strong, totally symmetric vibrations, such as the ν_1 mode at 989 cm^{-1} and the ν_9 mode at 1117 cm^{-1}, and their overtones and combination bands with ν_6 are sufficiently dense in the higher reaches of the $^1n\pi^*$ state to form a continuum.[133] The vibrational analysis of the higher $^1\pi\pi^*$ state of pyrazine is not well established in any condensed media, largely due to interactions between the $n\pi^*$ and $\pi\pi^*$ states that lead to diffuse transitions in many heteroatomic molecules.[136]

c) Annealing and Molecular Reorientation

The spectra shown in Figures 34 through 36 are for annealed overlayers. The pyrazine, deposited on the nickel surface at 10 K, is allowed to warm up to 120 - 130 K by cutting off the liquid helium flow to the sample holder. When the temperature reaches 120 K, flow is resumed and the temperature begins to drop within about 10 minutes. The entire process of annealing takes about 1½ hours. Annealing gives rise to a slight contraction (~ 10%) in adlayer thickness, the appearance of resolved vibronic structure around 3200 Å, a shift to lower energy of the $n\pi^*$ and $\pi\pi^*$ transitions, and a relative intensity change. These last three effects are seen in the spectra of Figure 38. As mentioned in an earlier chapter, the absolute thicknesses and absorbances may not be accurate. The following conclusions, however, are based on relative changes that occur reproducibly during a single experimental run.

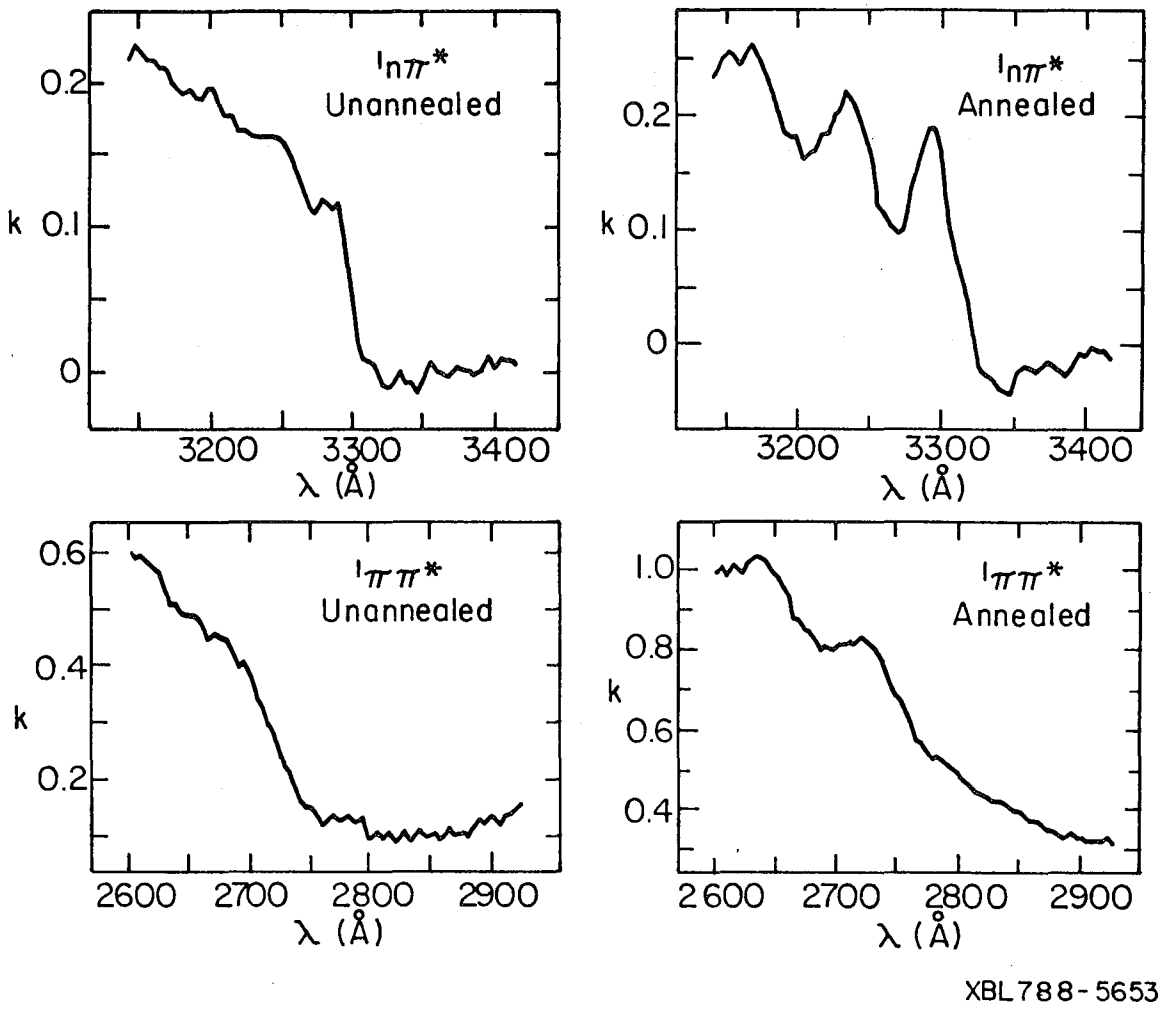

XBL788-5653

Figure 38. Absorbance spectra of $^1n\pi^*$ (top) and $^1\pi\pi^*$ (bottom) transitions of ~ 8 Å pyrazine overlayers on Ni(111) at 10 K. Left hand spectra show unannealed overlayers and right hand spectra show overlayers after annealing at 120 K.

Valuable information about molecular geometry and local environment can be deduced from the optical transition intensities. Additional selection rules are created by the presence of the metal surface. At a perfectly reflective metal surface, light forms a standing wave and has no electric field component parallel to the surface. Only transition moment dipoles with a component normal to the surface can be observed in this ideal case.

The annealing process increases the absorbance k of the $\pi\pi^*$ transition as shown in Figure 38, while the integrated intensity of the $^1n\pi^*$ transition remains approximately constant. The $\pi\pi^*$ transition dipole is polarized along the nitrogen-nitrogen (N-N) axis; the $n\pi^*$ is polarized out of plane.[131] Assuming an amorphous distribution of molecular orientations in the initially deposited layer at 10 K, a uniform reorientation upon annealing to give the N-N axis normal to the surface, as proposed for chemisorbed pyridine on Pt(111)[137] and nickel[93,138] would triple the $^1\pi\pi^*$ absorbance and eliminate the $^1n\pi^*$ transition which is then polarized entirely in the surface plane. If the plane of the ring were allowed to tip approximately thirty degrees from the surface normal, so that both N-N and out of plane polarizations have normal components, the $^1\pi\pi^*$ absorbance would double and the $^1n\pi^*$ transition intensity would remain constant. Experimentally, the $^1\pi\pi^*$ absorbance is not quite doubled and the $^1n\pi^*$ absorbance increases by 10-20%, indicating that the actual angle between the surface normal and the molecular plane may lie between 30° and 45° as indicated in Figure 39. Absorbance changes on overlayer contraction, the imperfect

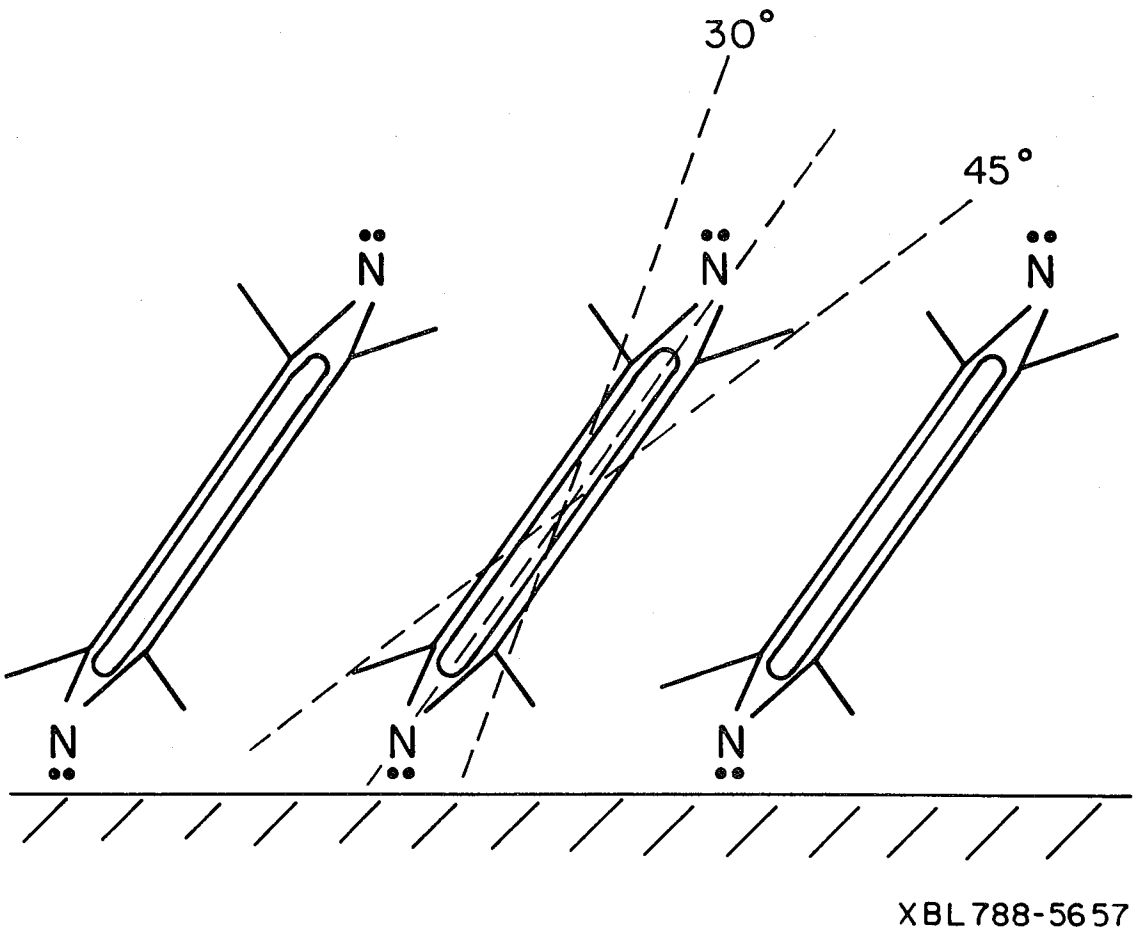

Figure 39. Proposed surface geometry of annealed pyrazine molecules on the Ni(111) surface below 160 K. Angles shown are between plane of molecule and surface.

reflectivity of nickel, and experimental accuracy preclude a more precise determination of molecular geometry.

The proposed molecular geometry does not correspond to the bulk molecular crystal structure, which contains two translationally equivalent sites per unit cell.[139] It has been shown that the crystal structure of a molecular overlayer hundreds of angstroms thick may be determined by the metal substrate structure.[140] If the pyrazine overlayer structure is affected by the metal surface as the evidence suggests, an appreciable and anisotropic coupling between the metal and physisorbed pyrazine, perhaps mediated by the nitrogen lone pair orbitals, must be as important as intermolecular interactions in deciding the crystal structure. This novel structure may also give rise to the low vibrational frequency observed in overlayers many monolayers thick.

d) Chemisorbed Pyrazine

Previous sections describe the spectra of physisorbed pyrazine. A goal of the surface science research we have undertaken is measurement of the absorbance spectrum of a chemisorbed overlayer. Pyrazine is, in some respects, a poor choice for such studies because we know of no evidence that pyrazine molecularly chemisorbs on nickel (111). UV transmission spectroscopy has been applied extensively to a closely related molecule, pyridine, on amorphous nickel films, where it demonstrates that pyridine is chemisorbed to the nickel surface through the nitrogen lone pair orbital.[93,138] A similar structure for pyridine on platinum (111) has been determined by LEED and work function

measurement.[137] In addition, chemisorbed pyridine shows a featureless charge transfer band around 3100 Å,[93] as discussed in Chapter VIII-1. In sum, the UV-visible absorbance spectra promises to hold a good deal of information about surface structure and bonding.

When the condensed pyrazine overlayers on nickel are warmed above 160 K, all traces of structure in the pyrazine absorbance spectra disappear. The ellipsometric parameters ψ and Δ change abruptly, reaching final values similar, but not equal to those of bare nickel, indicating the presence of a transparent overlayer approximately 1 Å in effective thickness on the nickel substrate. The same final state is reached by depositing pyrazine on Ni(111) at room temperature. In a separate experiment, the cooled nickel surface is covered with a pyrazine overlayer sufficiently thick to hide the Auger peaks of the underlying nickel atoms. When the crystal is warmed above 160 K, the residual pressure of pyrazine in the chamber detected by the mass spectrometer increases by two orders of magnitude and a second Auger spectrum shows that the ratio of carbon to nitrogen peak intensities remains the same as for the original condensed pyrazine overlayer, although nickel is now also clearly detectable. Neither the ellipsometric parameters nor the Auger spectrum change further as the crystal is warmed to room temperature or cooled back down to 10 K.

A residual overlayer of less than one monolayer containing carbon and nitrogen remains on the nickel surface after room temperature deposition or the sublimation of a thick condensed pyrazine overlayer. It shows no absorbance above 2600 Å. Three simple explanations appear plausible. First, the first monolayer of pyrazine at the nickel

surface may chemisorb dissociatively by either a thermal or photochemical mechanism before or at the sublimation temperature. The residue would contain some combination of carbon and nitrogen species, cyanide groups, or polymers whose atomic composition ratio is similar to that of pyrazine and whose electronic transitions are outside our accessible wavelength region. Second, the residue may be molecularly chemisorbed pyrazine, but the electronic transitions are shifted to much higher energy. In pyridine, however, the $\pi\pi^*$ transition is shifted to lower energies by 50-100 Å for pyridine chemisorbed on a nickel film and for pyridine-nickel coordination complexes.[93] The $\pi\pi^*$ transition of pyrazine should behave similarly, and pyrazine on nickel should also show the charge transfer band seen for pyrazine-nickel complexes around 4000 Å.[141] Third, the experiment may lack the sensitivity to detect a weak absorbance of a fraction of a monolayer. Calculation by A. Gallo predicts that a minimum absorbance of $k = 0.02$ for an overlayer 1 Å thick is detectable. The $n\pi^*$ transition for a 3-4 Å physisorbed overlayer is clearly detectable on our instrument. However, an extremely broad and featureless absorbance, even of comparable oscillator strength to the physisorbed species, would be difficult to detect against the changing optical constants of the nickel substrate.[142]

2. Pyridine

Our study of the UV spectrum of pyridine adsorbed on nickel (111) was motivated by our work on the similar molecule, pyrazine, and by the UV transmission spectra of pyridine adsorbed on thin polycrystalline films of nickel that have been published by Kishi and Ikeda[138] and

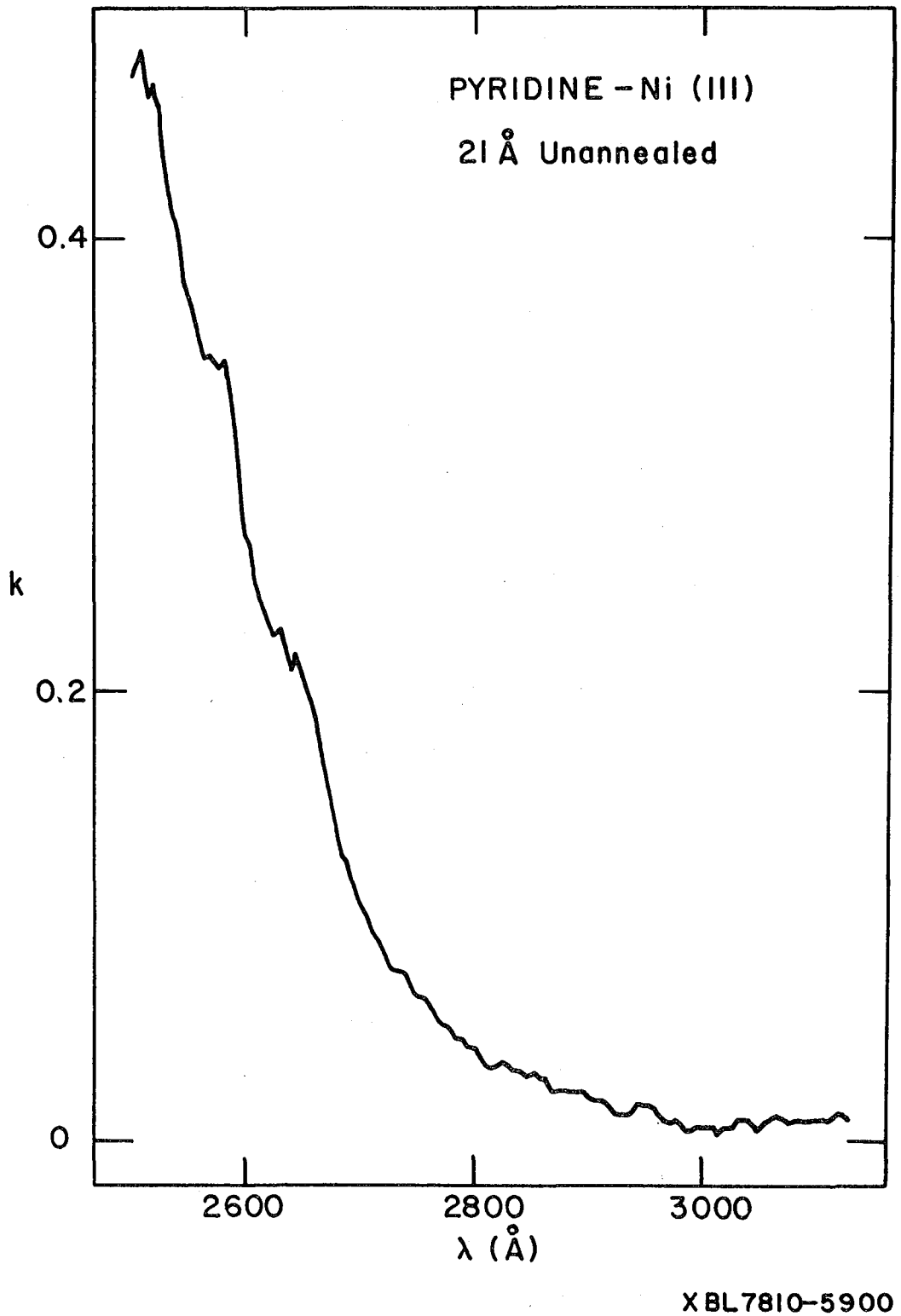

Figure 40. Absorbance spectrum of 21 Å overlayer of pyridine on Ni(111) surface at 10 K showing $\pi\pi^*$ transition, unannealed. Spectrum is stable under annealing up to 120 K.

Sheets and Hansen.[193] Our results show that the ellipsometric spectrum of pyridine on nickel resembles the chemisorbed or coordinated pyridine molecular spectrum rather than the isolated molecule spectrum, under conditions in which the spectrum of the stronger Lewis base, pyrazine, shows principally isolated molecule behavior.

The spectrum of pyridine adsorbed on nickel (111) at 60 K measured by spectroscopic ellipsometry is shown in Figure 40. The overlayer absorbs strongly below 2800 Å. The only structure evident in this transition is two weak shoulders at 2637 and 2574 Å. The pyridine (Baker, reagent grade) is degassed before use and the crystal surface is prepared as described in Chapter IX-2. This spectrum remains unchanged after annealing for 30 minutes at 120 K, 10° below the sublimation temperature. Thin film IR studies suggest that the pyridine annealing temperature may be higher than the sublimation temperature under UHV conditions.[143]

In the previous chapter, we described the pyrazine as physisorbed on nickel at low temperatures because the spectrum of the adsorbed overlayer resembled the bulk molecular spectrum. Under similar conditions, pyridine, a weaker Lewis base and less reactive, should also physisorb. There are, however, two important differences between the adsorbed pyridine spectrum and the bulk pyridine spectrum. First, the $^1n\pi^*$ transition at 2850 Å is absent in the adsorbed spectrum. In the isolated molecule, the oscillator strength of the $^1n\pi^*$ transition is approximately one-tenth that of the $^1\pi\pi^*$ for both pyridine and pyrazine.[131] The pyrazine $^1n\pi^*$ state is easily observed beside the $^1\pi\pi^*$ state in Figure 34, while the pyridine $^1n\pi^*$ state is not observed

in Figure 40. Second, the $^1\pi\pi^*$ absorbance is shifted to lower energy for adsorbed pyridine.[93] If the unresolved shoulders are identified as vibronic structure of the $^1\pi\pi^*$ transition, these peaks are shifted 40 Å to lower energy than in the vapor phase. This identification is supported by the 1000 cm^{-1} spacing between the shoulders, which matches the spacing of the ν_1 progression observed in the $^1\pi\pi^*$ state.[131]

These two discrepancies are also observed in the transmission spectra of pyridine chemisorbed on nickel films and nickel-pyridine coordination complexes, in which the nitrogen lone pair orbital is closely involved in nickel-pyridine bonding.[138] There are several strong reasons to believe, however, that our studies are of physisorbed and condensed pyridine: the physisorption of pyrazine under similar conditions, the thickness of the pyridine overlayer (as great as 21 Å), and the lack of a charge-transfer band at 3000 Å, as observed in chemisorbed and coordinated pyridine spectra.[93] I do not yet have an explanation for the discrepancies between the bulk and adsorbed molecular spectra. I point out, however, that this effect may have caused confusion in the literature. The "chemisorbed" pyridine transmission spectra of Kishi and Ikeda[138] is very similar to ours and very unlike the "chemisorbed spectrum" of Sheets and Hansen,[93] who report that pretreatment of the nickel surface with O_2 or CO is necessary to chemisorb pyridine at room temperature. Kishi and Ikeda may have observed only physisorbed pyridine, as we have. Attempts to observe a chemisorbed pyridine spectrum by warming the overlayer or by oxygen pretreatment of the nickel crystal have produced residual overlayers like those obtained in the pyrazine chemisorption experiments.

3. Naphthalene

Unlike pyrazine and pyridine, the UV spectrum of naphthalene adsorbed on nickel (111) at low temperatures exactly matches the bulk absorption spectrum for the naphthalene single crystal. It is perhaps the lack of interaction with the surface that gives rise to an ellipsometric spectrum, shown in Figure 41, sharper and more complex than any obtained for the heterocyclic systems. The near UV naphthalene spectrum includes two $\pi\pi^*$ singlet transitions, the $^1A_{1g} - {}^1B_{3u}$ transition observed between 3160 and 2970 Å and the stronger $^1A_{1g} - {}^1B_{2u}$ transition below 2970 Å.[144,145]

The procedure for spectroscopic ellipsometry of naphthalene (Mallinkrodt Purified, degassed before use) is identical to that for pyrazine. Spectra for overlayers ranging from 10 Å to 660 Å show no change in the general spectral features. The origin of the adsorbed overlayer in Figure 41 falls at 3162 Å, as compared to 3160 Å in the bulk spectrum,[145] and Table V summarizes the excellent correspondence between the $^1B_{3u}$ vibrational splittings for adsorbed and bulk systems. The $^1B_{2u}$ transition, marked by the abrupt increase in absorbance in Figure 41, is also well-behaved, showing the 510 and 1400 cm^{-1} progressions seen in the bulk. The width of the peaks (~ 100 cm^{-1} for the origin at 3162 Å) is comparable to that obtained for high resolution naphthalene single crystal studies (~ 50 cm^{-1} for the origin).[145] All traces of spectral structure disappear on warming above 200 K.

The epitaxial growth of the napthalene molecular crystal on the platinum (111) surface was studied in detail by Firment and Somorjai using LEED.[140] Below 105 K, a vapor-grown naphthalene overlayer does

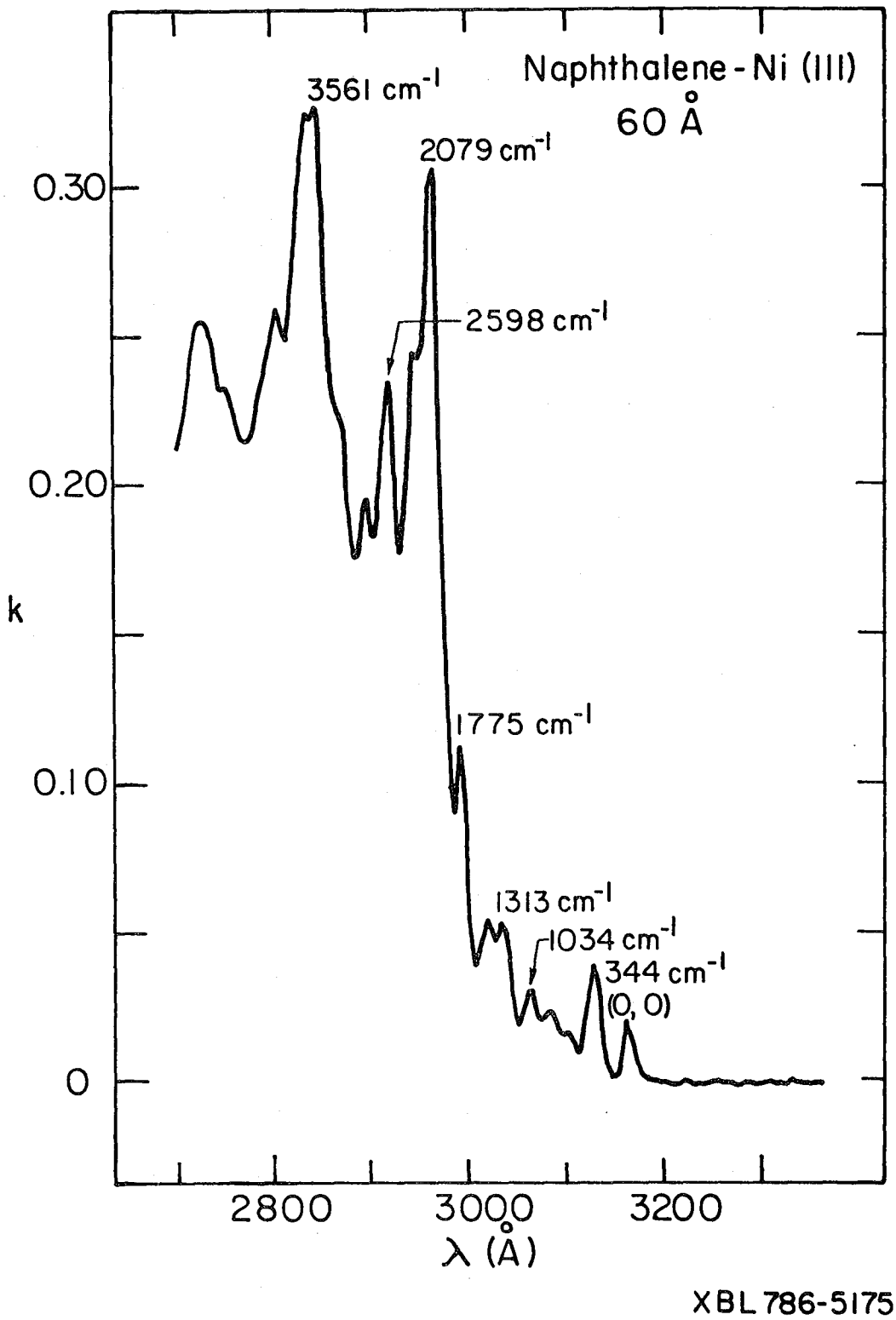

Figure 41. Absorbance spectrum of 60 Å overlayer of naphthalene on Ni(111) surface at 10 K showing first and second $\pi\pi^*$ transitions.

not order. Between 105 and 200 K, an epitaxial overlayer thousands of angstroms thick with the bulk naphthalene crystal structure can be grown on the Pt(111) surface. The ab plane is parallel to the metal surface. The resulting LEED pattern shows circular rings because the molecules are not ordered azimuthally within the layers. If the initial monolayer of naphthalene is warmed to 150°C, the admolecules are ordered azimuthally, producing a (6 × 6) LEED pattern. Epitaxially grown microcrystalline domains are oriented along the substrate lattice axes, producing separate but diffuse LEED spots.

Although we have not investigated the LEED patterns for naphthalene on nickel (111), the optical spectra are generally consistent with oriented epitaxial growth in terms of annealing, polarization, and Davydov splitting. Like pyrazine, the initially deposited overlayer at 10 K shows only broad spectral features. The sharp features in Figure 41 are the result of annealing at 130 K and the formation of an ordered overlayer. As discussed in Chapter IX-1c), transition dipoles parallel to the surface cannot absorb as strongly as dipoles oriented normal to the metal surface. Both the $^1B_{3u}$ state polarized on the short in-plane molecular axis and the $^1B_{2u}$ state polarized on the long molecular axis[144] have equal components normal to the ab plane in the bulk crystal structure,[145] so the fact that the $^1B_{3u}$ and $^1B_{2u}$ transitions have the same relative intensity in the adlayer as in the bulk indicates that the ab plane is parallel to the metal, as in the platinum system. Finally, although the extent of azimuthal ordering within the ab plane is not known from LEED, the Davydov splitting of the 3162 Å origin is

the same as in the bulk crystal. The Davydov splitting is caused by intermolecular interaction and a crystal structure with two molecules per unit cell.[29] The magnitude of the splitting is dependent on the strength of intermolecular coupling and therefore on their separation and mutual angular orientation. This splitting cannot be measured directly in the adsorbed overlayer, because the low energy Davydov component is very weak, but the splittings in Table V between the high energy Davydov component of the origin and the vibronic peaks which are not shifted prove that the Davydov splitting is the same as in the bulk crystal. This is very strong evidence that the annealed naphthalene overlayer has the bulk structure and that short-range order, over the distance reached by the intermolecular coupling that causes the Davydov effect, is very large. The size of the micro-crystalline domains cannot be estimated.

Table V. The Vibrational Splittings of the $^1B_{3u}$ State of Naphthalene

Bulk Absorption	Adlayer Absorption
0-0 (3160 Å)	0-0 (3162 Å)
334 cm^{-1}	341 cm^{-1}
633	631
711	
824	825
1048	1038
1320 1348	1323
1507	1502
1812	1784

XII. EMISSION SPECTROSCOPY OF ADSORBED OVERLAYERS

Optical emission spectroscopy confirms and complements absorption spectroscopy. Just as importantly, it is a uniquely valuable probe of the energy transfer and relaxation mechanisms available to electronically excited molecules. All the techniques applied to bulk molecular crystals in the first half of this dissertation are in principle applicable to surfaces, where new relaxation processes may come into play. The theory of energy transfer from adsorbed overlayer to metal substrate was reviewed in Chapter VIII-2. Measuring the concentration and lifetime of excited surface species not only increases our understanding of interactions between adsorbates and substrates, but it also sets limits to the potential for surface photochemical reactions. The following sections are perhaps not appropriate for a PhD. thesis in that they do not present a tidy or complete picture, but I believe their inclusion is useful because of the importance of the experiments, the surprising nature of the preliminary results, and the tying together of the energy transfer studies in the first half of this thesis and the surface spectroscopy in the second. This chapter describes the observation of low temperature phosphorescence from pyrazine adsorbed on nickel (111), done in collaboration with Dr. A. Campion and A. Gallo.

Our experiments differ radically from previous surface fluorescence and energy transfer studies using fatty acid monolayer assemblies on evaporated metal films at room temperature. We are able to prepare a clean ordered metal surface under UHV conditions and adsorb and anneal an organic adlayer at cryogenic temperatures, the overlayer thickness

measured by ellipsometry. Our homogeneous overlayers are not simply interpreted in terms of dipole-metal separation dependences as are monolayer assemblies, but their structure is physically more interesting, they are more adaptable, and they are more useful for short-range energy transfer studies. In our experiments, pyrazine is excited in the singlet and the total phosphorescence intensity is monitored. By scanning the excitation source, the singlet excitation spectrum of pyrazine is monitored. By modulating the excitation source using a fast shutter or a pulsed laser, the triplet phosphorescence lifetime can be measured.

From our preliminary results, the critical distance at which energy transfer between molecule and surface becomes important is much smaller than predicted by theory. Pyrazine phosphorescence has been observed for adlayers as thin as 3 Å, where theory[102] predicts a quantum yield five orders of magnitude below the bulk value, and slightly thicker overlayers have triplet lifetimes equal to bulk values. On the other hand, a thickness dependence on the excited state lifetime is observed, as well as a temperature dependent quenching process. Encouragingly, singlet excitation spectra match the spectroscopic ellipsometry data for pyrazine. These studies are being pursued at this writing, with extensions to phosphorescence emission spectra, fluorescence from aromatic hydrocarbon overlayers, and optically-detected magnetic resonance.

1. Experimental

The phosphorescence experiments follow ellipsometry and use the same UHV system with only external rearrangement of the optics. There

are two types of experiment, excitation spectra and lifetime measurement, and they have in common with ellipsometry the preparation of the sample as described in Chapter IX-2. The thickness of the surface overlayer is measured by ellipsometry, as described in Chapter X-1 with the included caveats, and the optics are arranged as in Figure 42.

For phosphorescence excitation spectra, the excitation source, which is the xenon arc lamp passed through the monochromator, is focussed to a 3mm spot on the surface through the front viewport, striking the surface at an angle of 22.5° from the surface normal. The viewport is masked except for the beam aperture, which is filtered to block all visible and near UV light which might interfere with phosphorescence from the overlayer (Corning 7-54). All internal light sources (Ti-ball, filaments, etc.) are turned off and all unused ports are masked. A photomultiplier tube (EMI 9558) in a dry ice cooled housing is mounted at a side port to observe phosphorescence. This port sees the crystal face at an angle of 67.5° from the surface normal, so specularly reflected excitation light does not intercept the detector. The photomultiplier tube is also filtered to eliminate scattered excitation light (Schott 375 and Corning 4-97) and carefully masked from external light sources.

The low sample concentrations and an experimental geometry that places the detector six inches from the sample result in extremely low light levels, so single photon counting detection of the phosphorescence is used. The output of the photomultiplier is fed into a Keithley 106 pulse amplifier (x100) and a differential discriminator (EG&G, Model TD101/N) which discards spurious photomultiplier noise and passes

SCHEMATIC VIEW OF UHV PHOSPHORESCENCE ARRANGEMENT

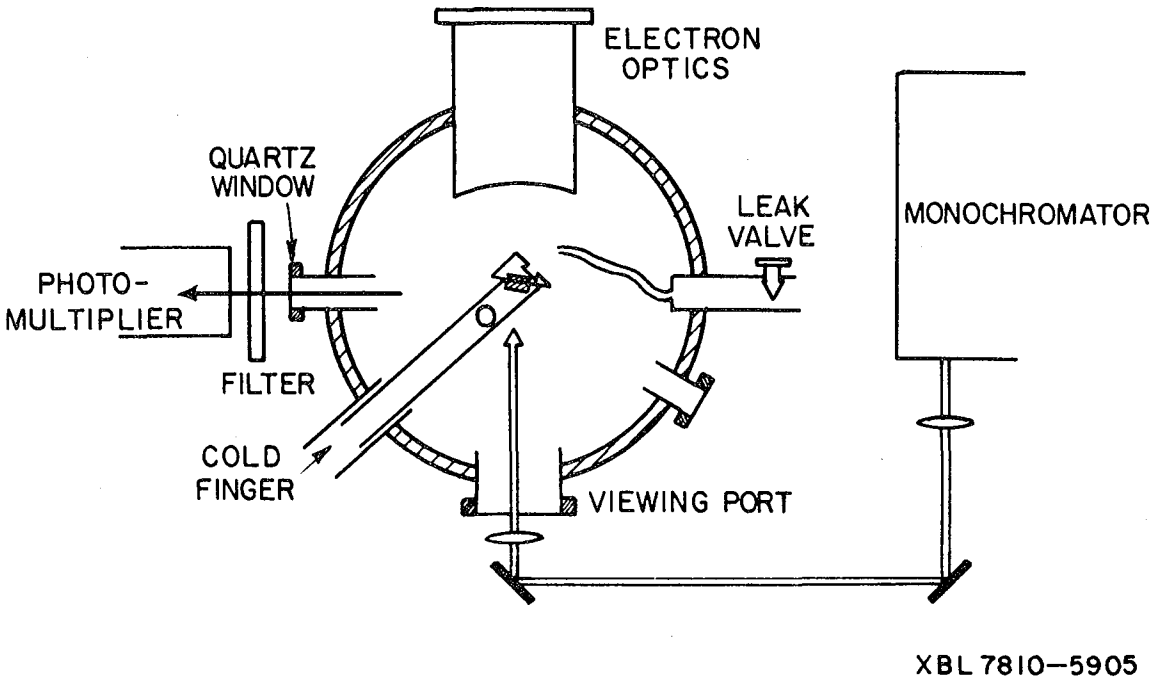

Figure 42. Diagram of surface phosphorescence experiments UHV chamber and optics.

only single photon events. Count rates for usable spectra are at least 10^3 Hz at singlet absorbance maximum, with dark current less than 10^2 Hz. Counting is done by a Hewlett Packard 5245L electronic counter or a Mech-Tronics Nuclear ratemeter. To measure the excitation spectra, the monochromator is scanned through the singlet absorbance region while the ratemeter analog output is recorded on a strip chart recorder. Wavelength references from the monochromator are recorded manually.

For triplet phosphorescence lifetime measurement, two techniques are used to modulate the excitation source. The arc lamp-monochromator combination is tuned to maximize total phosphorescence and shuttered with a 2 msec risetime electronic shutter. For measuring decay components faster than 2 msec, a pulsed dye laser (Chromatix CMX-4 with 10 μsec pulses) using Rhodamine B doubled is used to excite the overlayer phosphorescence. The photomultiplier output is fed directly into a Northern NS-575 signal averager to store and analyze the decay curve.

2. Excitation Spectra

The structure of the pyrazine singlet transitions on nickel (111) measured by excitation spectra is identical to that obtained by spectroscopic ellipsometry, providing important confirmation of those experiments. Figure 43 compares the results for the two techniques in the $^1n\pi^*$ region. The $^1\pi\pi^*$ transition is also seen in the complete excitation spectrum. However, light intensity in the excitation source, a xenon arc, falls off rapidly with decreasing wavelength in this region. The uncorrected excitation spectrum in Figure 43 shows the high energy peaks instrumentally attenuated by this effect and the $^1\pi\pi^*$ transition

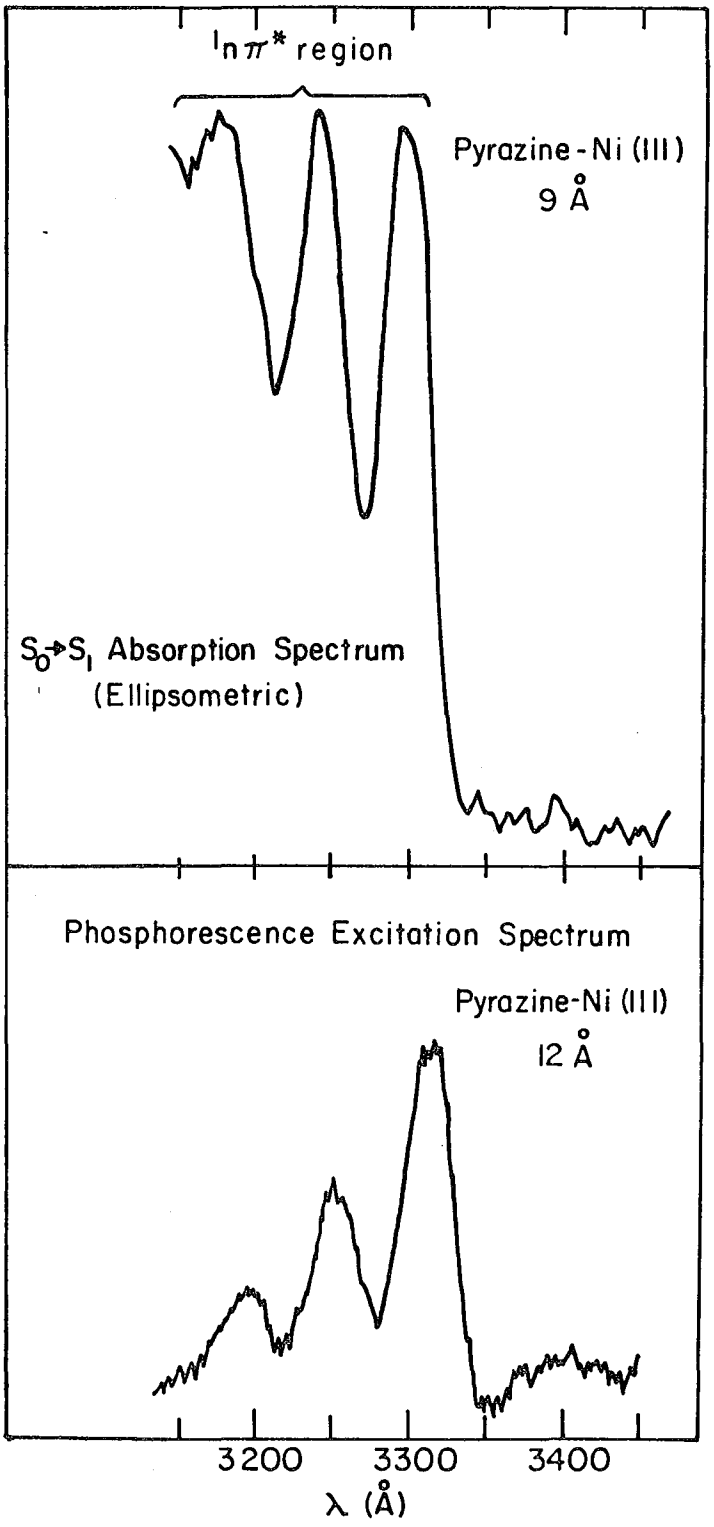

XBL788-5656

Figure 43. Comparison of phosphorescence excitation spectrum of 12 Å overlayer of pyrazine on Ni(111) at 10 K with ellipsometry spectrum from Figure 36.

is extremely weak.

3. Triplet State Lifetimes

The observation of triplet state phosphorescence for 20 Å pyrazine overlayers on nickel was unexpected. The triplet lifetimes measured, although consistent with the observation of phosphorescence, are equally at odds with the theoretical predictions for excited molecules near metal surfaces discussed in Chapter VIII-2. The interaction of the $^1\pi\pi^*$ and $^3\pi\pi^*$ states, which gives rise to the electric dipole phosphorescent emission from the lowest triplet state,[146] should also give rise to long-range non-radiative energy transfer from the triplet excited molecules to the metal plasmon modes. By the short-range energy transfer rate approximation, Eq. (VIII-11), of Prock, Chance, and Silbey,[102] the energy transfer rate should be $\sim 10^4$ times greater than the radiative rate for an excited pyrazine molecule 10 Å from the nickel surface, and $\sim 10^3$ times greater for a 20 Å separation.

For a homogeneous 20 Å pyrazine overlayer, the triplet state lifetime is almost the same as for the bulk molecular crystal. In the bulk crystal, the lifetimes of the three triplet sublevels are averaged by spin-lattice relaxation into a single exponential decay constant of 18 msec at 10 K.[146] For a 20 Å overlayer on nickel, the decay rate at 10 K is 26 msec, as shown in Figure 44. There is, however, evidence for a new decay channel for much thinner overlayers. For a 5 Å overlayer, the decay rate is 1 msec at 10 K, as shown in Figure 45.

Figure 44. Time-resolved decay of pyrazine triplet phosphorescence for 20 Å overlayer on Ni(111) at 10 K. Inset shows linear fit to exponential decay. Excitation beam was shuttered with 2 msec risetime electronic shutter.

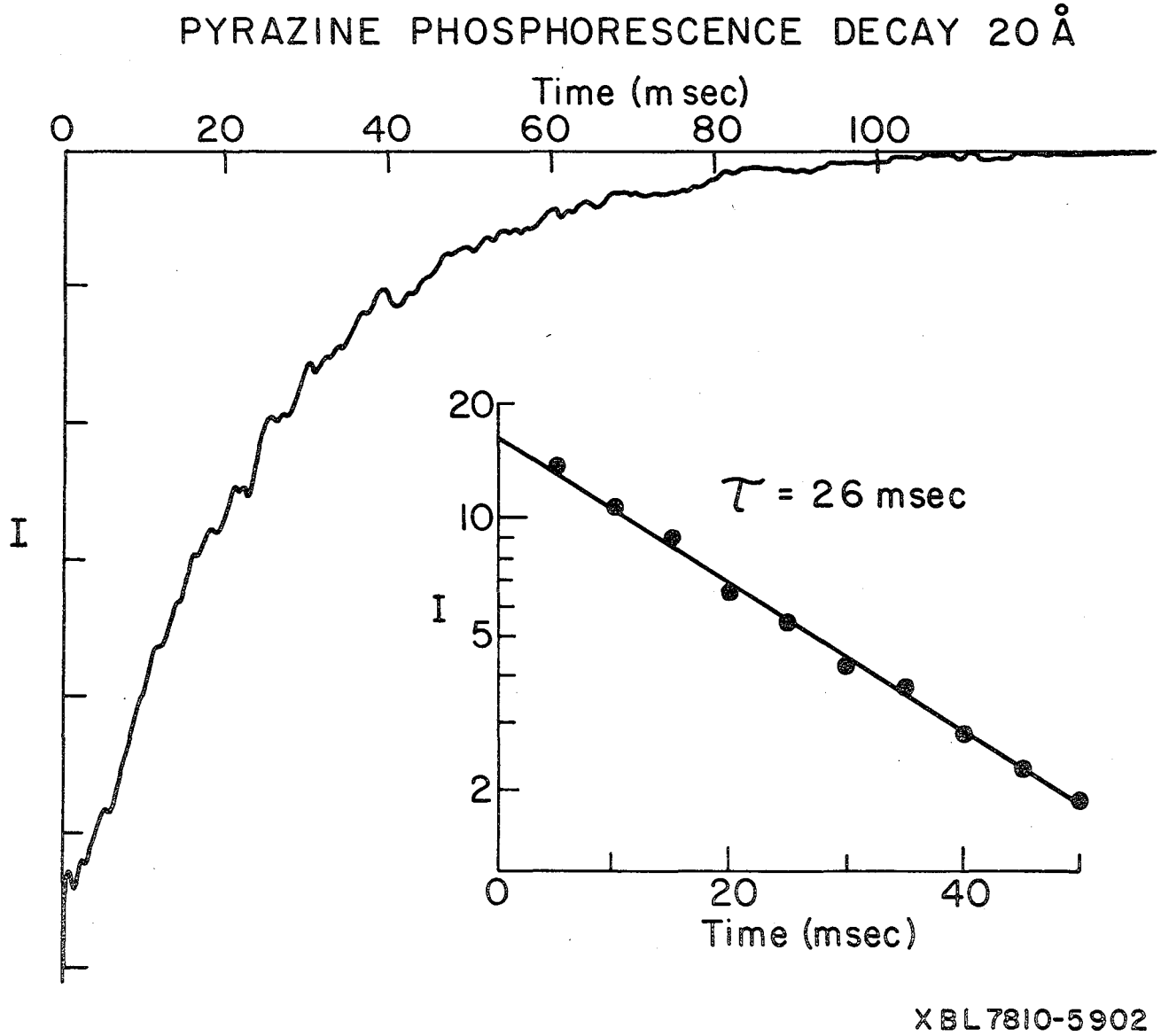
PYRAZINE PHOSPHORESCENCE DECAY 20 Å
Time (m sec)
0
20
40
60
80
100
I
20
10
5
2
I
τ = 26 msec
0
20
40
Time (msec)
XBL7810-5902

Figure 44

Figure 45. Time-resolved decay of pyrazine triplet phosphorescence for 5 Å overlayer on Ni(111) at 10 K. Inset shows linear fit to exponential decay. Excitation beam was 10 μsec pulse from Chromatix CMX-4 dye laser.

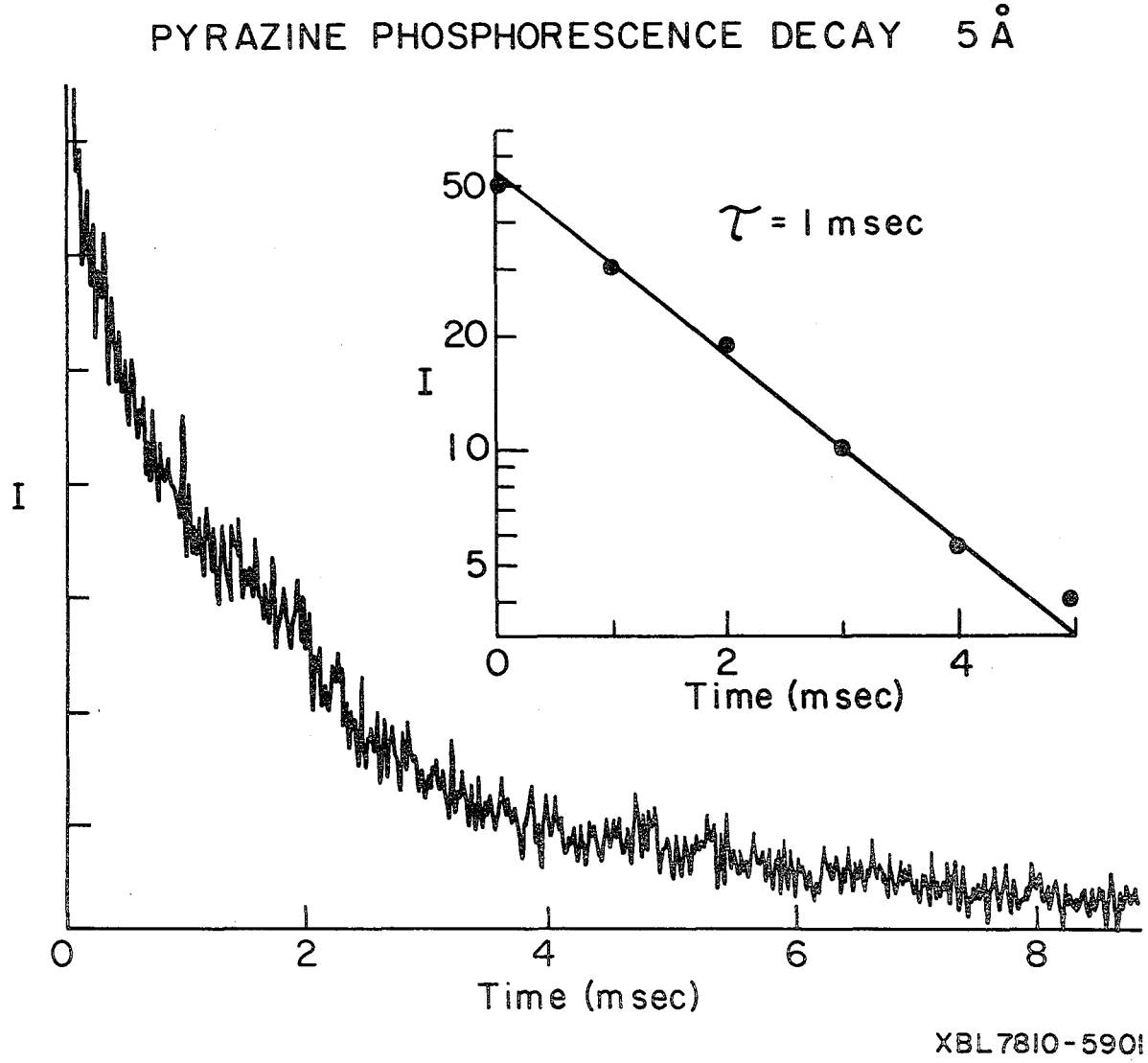
PYRAZINE PHOSPHORESCENCE DECAY 5 Å
I
0
2
4
6
8
Time (msec)
50
20
10
5
I
τ = 1 msec
0
2
4
Time (msec)
XBL7810-5901

Figure 45

The phosphorescence intensity shows a strong temperature dependence. Figure 46 shows that the total phosphorescence intensity decreases rapidly between 30 and 40 K with an apparent activation energy for quenching of ~ 250 cm^{-1}. This quenching process is completely reversible. On the other hand, a single preliminary experiment shows no effect of temperature on triplet state lifetime. For a 75 Å overlayer, the lifetime is 19 msec at 25 K and 21 msec at 55 K. This suggests that a change in the radiative or non-radiative decay rate is not responsible for the quenching. Certainly the intrinsic molecular decay rates are not expected to increase, as the pyrazine bulk quantum yield is constant ($\sim .3$) over a wide temperature range.[147] The non-radiative decay rate for resonant energy transfer to the surface contains no temperature dependence.

A possible explanation for this behavior has already been discussed in Chapter VIII-2, in which I propose a mechanism where short-range intermolecular excitation transfer to the vicinity of the surface is the principle mode of relaxation. Bulk pyrazine phosphorescence at liquid helium temperatures is from defect traps 100-200 cm^{-1} below the triplet band.[148] The existence of defects is also very probable in an annealed overlayer on a metal surface. Future studies of the emission spectrum of the pyrazine overlayer will settle that question. Triplet excitation in the overlayer will be rapidly trapped at the defect sites. Let us suppose that direct energy transfer between the defect traps and the surface is much slower than theoretically predicted, for some unexplained reason. Then the 250 cm^{-1} activation energy for quenching

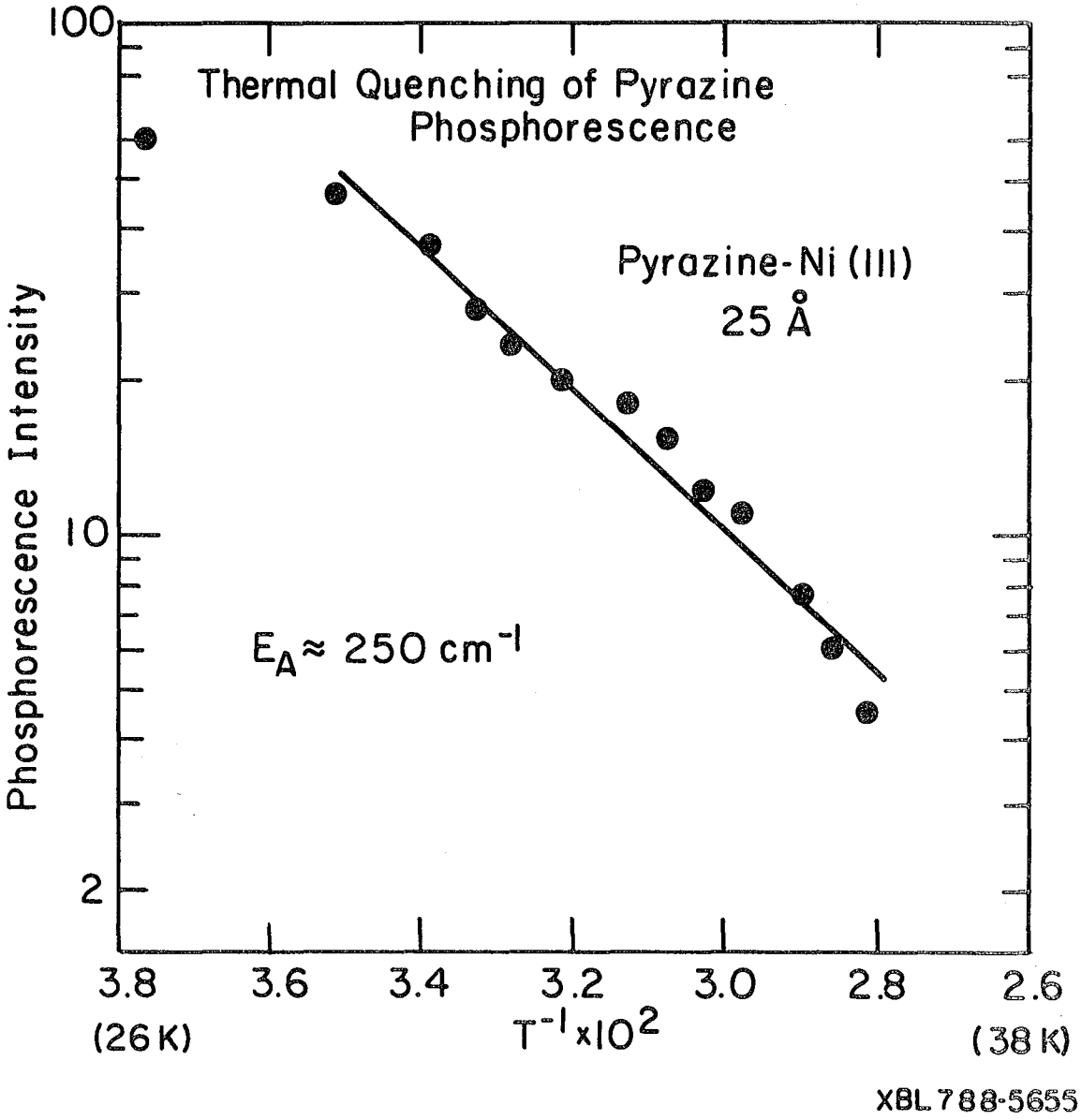

Figure 46. Thermal quenching of pyrazine triplet phosphorescence for 25 Å overlayer on Ni(111). Activation energy is ~ 250 cm^{-1}.

can easily represent the detrapping of triplet excitation from the defect states into delocalized or band states of the molecular overlayer. The excitation can migrate as an exciton to the immediate vicinity of the surface, where it relaxes into the metal. That this relaxation at very small separation occurs has been shown by the 1 msec lifetime for the the 5 Å overlayer in Figure 45. The kinetics of a two level system, where the defect and mobile states compose the two levels, are well known.[1] The decay of the defect phosphorescence will be biexponential. One decay component approaches the intrinsic decay rate, including the direct energy transfer rate to the surface. The other component approaches the detrapping rate, if the relaxation of the mobile state is comparable to the detrapping rate. This provides a satisfactory explanation for the repeated appearance of the 20 msec decay, even at temperatures where the phosphorescence is strongly quenched. The quenching process represents the second mechanism of detrapping and migration, whose decay may be too fast to observe with our equipment.

XIII. CONCLUSIONS AND CONJECTURES

This division of the thesis has reported on the UV spectrum of several aromatic molecules adsorbed on a single nickel crystal surface at low temperatures and the phosphorescence of pyrazine on nickel (111). In particular, it has focussed on the similarity between molecular crystal properties and the behavior of condensed overlayers. Due to the preliminary nature of the results, conclusions and conjectures cannot be easily separated, but the reader should appreciate the connection between the questions in the introduction and the following statements concerning long-range ordering, electronic energy levels, and energy transfer.

i) Amorphous overlayers can be annealed to form well-ordered molecular crystals on single crystal nickel surfaces for pyrazine and naphthalene. This ordering, which appears in sharp spectral structure and bulk crystal Davydov splittings, may be enhanced by the metallic substrate.

ii) The spectra observed on surfaces by ellipsometry are very similar to those for bulk molecular crystals. Certain subtle differences, however, such as the vibronic frequency shift in pyrazine and the absence of the $^1n\pi^*$ transition in pyridine, indicate the existence of some long-range surface-adlayer interaction.

iii) Phosphorescence lifetimes for pyrazine on nickel do not follow present theory for long-range non-radiative decay to the metal. Energy transfer appears much weaker than predicted and intermolecular exciton migration may be important.

Many additional experiments suggest themselves to clarify the tentative interpretations offered here. Closer examination of very thin (< 10 Å) and very thick (> 100 Å) overlayers would be useful to separate bulk and surface contributions to the spectra. The use of disordered and polycrystalline nickel surfaces would clarify the effect of ordered substrate on the ordering of adlayer during annealing. In the area of emission spectroscopy and energy transfer, much work remains. Careful thickness and temperature dependences of phosphorescence lifetime and intensity must be completed. Faster time resolution will be necessary to measure and identify the short-lived components of the decay. Intermolecular energy migration within the adlayer can be studied using mixed overlayers, with an inert gas layer separating phosphor and metal, or acting as a matrix with dilute phosphor concentration in a co-deposited film.

These specific extensions of present work are overshadowed by the myriad new directions available to the surface scientist. Entirely new classes of adsorbate and substrate, including insulators, semiconductors, and polymers, can be studied by optical techniques in conjunction with conventional electron spectroscopies or by optical techniques alone in non-UHV environments. The variety of optical techniques applied to surface science is expanding rapidly. Raman scattering, phosphorescence and fluorescence spectroscopy, and optically-detected magnetic resonance are all under development in our laboratory and elsewhere. In the coming decades, optical investigations of large molecules on surfaces promises to be one of the most active research areas in chemistry.

EPILOGUE

The scientist is a practical man and his are practical aims. He does not seek the ultimate but the proximate. He does not speak of the last analysis but rather of the next approximation. His are not those beautiful structures so delicately designed that a single flaw may cause the collapse of the whole. The scientist builds slowly and with a gross but solid kind of masonry. If dissatisfied with any of his work, even if it be near the very foundations, he can replace that part without damage to the remainder. On the whole, he is satisfied with his work, for while science may never be wholly right it certainly is never wholly wrong.

---- G. N. Lewis

ACKNOWLEDGMENTS

I would like to thank Professor Charles B. Harris for his support and encouragement during the course of this work. His breadth of interests, prodigious scientific imagination, and sense of intellectual adventure have illuminated paths I should not have seen alone. My friend Antonio Gallo has played many roles in this research; he was my first guide in the field of surface science, he designed the experimental chamber, and he collaborated on much of the surface spectroscopy. To him, special thanks. Heinz Robota also devoted much thought and effort to the surface project. Dr. Alan Campion lead the investigation of overlayer phosphorescence and Dr. Henry Brenner instigated the study of impurity-induced traps. To all members of the C. B. Harris group past and present, I thank you for lightening my darkness, questioning my complacency, and sharing so many good times.

Mrs. Vijaya Narasimhan, Mrs. Gloria Pelatowski, and members of the Technical Information Division have been invaluable in preparing sections of this manuscript, which James Chao and Paul Whitmore have been kind enough to proofread. The research itself was facilitated by Prof. Gabor Somorjai, Dr. Rolf Muller, and members of their research groups who gave freely of their expertise. The experiments would have been impossible without the superb technical support provided by the College of Chemistry machine shop and electronics shop, and facilities of the Lawrence Berkeley Laboratory.

This work was supported by the Division of Chemical Sciences, Office of Basic Energy Sciences, U. S. Department of Energy.

REFERENCES

1. R. M. Shelby, A. H. Zewail, and C. B. Harris, J. Chem. Phys. 64; 3192 (1976).
2. M. T. Lewellyn, A. H. Zewail, and C. B. Harris, J. Chem. Phys., 63; 3687 (1975).
3. R. Kopelman, E. M. Monberg, F. W. Ochs, and P. N. Prasad, Phys. Rev. Lett., 34; 1506 (1975).
4. J. Hoshen and R. Kopelman, J. Chem. Phys., 65; 2817 (1976).
5. P. Argyrakis and R. Kopelman, J. Chem. Phys., 66: 3301 (1977).
6. J. Frenkel, Phys. Rev., 37; 13, 1276 (1931).
7. R. Silbey, Ann. Rev. Phys. Chem., 27: 203 (1976).
8. C. B. Harris and M. D. Fayer, Phys. Rev. B10; 1784 (1974).
9. T. Förster, Ann. Phys. N.Y., 2; 55 (1948).
   T. Förster, in Modern Quantum Chemistry, ed. O. Sinanoglu (New York, Academic), 3; 93 (1965).
10. H. Haken and P. Reinecker, Z. Physik, 249: 253 (1972).
11. P. Reinecker and H. Haken, Z. Physik, 250: 300 (1972).
12. H. Haken and G. Strobl, in The Triplet State, ed. A. Zahlan, (Cambridge, Cambridge Univ. Press, 1968).
13. M. Grover and R. Silbey, J. Chem. Phys., 54: 4843 (1971).
14. M. Grover and R. Silbey, J. Chem. Phys., 52: 2099 (1970).
15. R. W. Munn and W. Siebrand, J. Chem. Phys., 52: 47 (1970).
16. V. Kenkre and R. Knox, Phys. Rev. B9: 5279 (1974).
17. V. Kenkre and R. Knox, Phys. Rev. Lett., 33: 803 (1974).

18. V. Kenkre, Phys. Rev. B11: 1741 (1975).

19. V. Kenkre, Phys. Rev. B12: 2150 (1975).

20. Y. Toyozawa, Prog. Theor. Phys., 20: 53 (1958).

21. Y. Toyozawa, Prog. Theor. Phys., Suppl. 12: 111 (1959).

22. Y. Onodera and Y. Toyozawa, J. Phys. Soc. Japan 24: 341 (1968).

23. Y. Toyozawa, J. Luminescence, 12: 13 (1976).

24. H. Sumi, J. Phys. Soc. Japan, 36: 770 (1974).

25. H. Sumi, J. Phys. Soc. Japan, 32: 616 (1972).

26. A. Suna, Phys. Rev., 135: A111 (1964).

27. C. B. Harris, J. Chem. Phys., 67: 5607 (1977).

28. C. B. Harris, Chem. Phys. Lett., 52: 5 (1977).

29. A. S. Davydov, Theory of Molecular Excitons (New York, Plenum, 1971).

30. E. I. Rashba, Opt. Spektrosk, 2: 568 (1957).

E. I. Rashba, Sov. Phys. - Solid State, 4: 2417 (1963).

31. E. Schwarzer and H. Haken, Opt. Comm., 6: 64 (1973).

32. M. Philpott, J. Chem. Phys. 55: 2039 (1971).

33. D. Thomas and J. Hopfield, Phys. Rev., 124: 657 (1961).

34. A. H. Francis and C. B. Harris, J. Chem. Phys., 55: 3595 (1971).

35. A. H. Francis and C. B. Harris, Chem. Phys. Lett., 9: 181 (1971).

36. A. H. Francis and C. B. Harris, Chem. Phys. Lett., 9: 188 (1971).

37. G. Gallus and H. Wolf, Phys. Stat. Sol., 16: 277 (1966).

38. R. G. Kepler and A. E. Switendick, Phys. Rev. Lett., 15: 56 (1965).

39. P. Avakian and R. Merrifield, Phys. Rev. Lett., 13: 541 (1964).

40. M. D. Fayer and C. B. Harris, Phys. Rev. B9: 748 (1974).

41. P. Soven, Phys. Rev., 156: 809 (1967).

42. V. K. Shante and S. Kirkpatrick, Adv. Phys., 20: 325 (1971).

43. J. Hoshen and J. Jortner, Chem. Phys. Lett., 5: 351 (1970).
J. Hoshen and J. Jortner, J. Chem. Phys., 56: 933 (1972).

44. E. H. Lieb and D. C. Mathis, Mathematical Physics in One Dimensions (Academic, New York, 1966).

45. R. Pearlstein, J. Chem. Phys., 56: 2431 (1972).

46. K. Lakatos-Lindenberg, R. Hemenger, and R. Pearlstein, J. Chem. Phys., 56: 4852 (1972).

47. W. L. Greer, J. Chem. Phys., 60: 744 (1974).

48. W. L. Greer, J. Chem. Phys., 65: 3510 (1976).

49. W. Feller, An Introduction to Probability Theory and its Applications, (Wiley, New York, 1968) Vol. 3, p. 93.

50. D. D. Dlott, M. D. Fayer, and R. D. Wieting, J. Chem. Phys., 67: 3808 (1977).

51. E. W. Montroll and G. H. Weiss, J. Math. Phys., 6: 167 (1965).

52. A useful discussion of correlation effects in randon walks can be found in J. R. Manning, Diffusion Kinetics for Atoms in Crystals (Van Nostrand, Princeton, 1968), Chap. 3.

53. M. D. Fayer and C. B. Harris, Chem. Phys. Lett., 25: 149 (1974).

54. H. M. McConnell, J. Chem. Phys. 35: 508 (1961).

55. G. W. Robinson and R. P. Frosch, J. Chem. Phys. 37: 1962 (1962).

56. E. W. Montroll, Proc. Symp. Appl. Math., 16: 193 (1963).

57. R. Kopelman, Excited States, Vol. 2, ed. E. C. Lim (Academic, New York, 1975).

58. H. C. Brenner, J. C. Brock, M. D. Fayer, and C. B. Harris, Chem. Phys. Lett., 33: 471 (1975).

59. M. A. El-Sayed, M. T. Wauk, and G. W. Robinson, Mol. Phys., 5: 205 (1962).

60. H. Sternlicht, G. C. Nieman, and G. W. Robinson, J. Chem. Phys., 38: 1326 (1963).

61. P. Avakian and R. Merrifield, Mol. Cryst., 5: 37 (1968).

62. R. M. Hochstrasser and J. D. Whiteman, J. Chem. Phys., 56: 5945 (1972).

63. J. Hoshen and J. Jortner, J. Chem. Phys., 56: 5550 (1972).

64. E. F. Zalewski and D. S. McClure, in Molecular Luminescence, ed. E. C. Lim (Benjamin, New York, 1969) p. 739.

65. A. H. Zewail and C. B. Harris, Phys. Rev. B11: 952 (1975).

66. F. H. Herbstein, Acta Cryst., 18: 997 (1962).

67. D. D. Dlott and M. D. Fayer, Chem. Phys., Lett. 41: 305 (1976).

68. C. A. Van't Hof and J. Schmidt, Chem. Phys. Lett., 42: 73 (1976).

69. D. P. Craig and M. R. Philpott, Proc. Roy. Soc. A290: 583, 602 (1966).

70. B. Somer and J. Jortner, J. Chem. Phys., 50: 839 (1969).

71. H. C. Wolf and K. W. Benz, Pure and Appl. Chem., 27: 439 (1971).

72. D. L. Mills, Phys. Rev., 146: 336 (1966).

73. P. G. Klemers, Phys. Rev., 125: 1795 (1962).

74. D. S. Tinti, M. A. El-Sayed, A. H. Maki, and C. B. Harris, Chem. Phys. Lett., 3: 343 (1969).

75. J. Schmidt, W. S. Yeeman, and J. H. Van der Waals, Chem. Phys. Lett., 4: 341 (1969).

D. A. Antheunis, J. Schmidt, and J. H. Van der Waals, Chem. Phys. Lett., 6: 255 (1970).

76. W. G. Breiland, Ph.D. Thesis, University of California (1975).
M. D. Fayer, Ph.D. Thesis, University of California (1974).

77. M. D. Fayer, C. B. Harris, and D. Yuen, J. Chem. Phys., 53: 4719 (1970).

78. A. H. Francis and C. B. Harris, J. Chem. Phys., 57: 1050 (1972).

79. A. P. Marchetti and D. R. Kearns, J.A.C.S., 89: 786 (1967).

80. G. A. George and G. C. Morris, Mol. Cryst. and Liq. Cryst., 11: 61 (1970).

81. C. A. Van't Hof and J. Schmidt, Chem. Phys. Lett., 36: 460 (1975).

82. P. W. Anderson, J. Phys. Soc. Japan, 9: 316 (1954).
R. Kubo, J. Phys. Soc. Japan, 9: 935 (1954).

83. A. Laubereau and W. Kaiser, Rev. Mod. Phys., 50: 607 (1978).

84. H. C. Brenner, J. C. Brock, and C. B. Harris, Chem. Phys., 31: 137 (1978).

85. M. Born and E. Wolf, Principles of Optics, 5th ed. (Pergamon, New York, 1975), Chapters I, XIII.

86. R. H. Muller, in Proceedings of the Symposium on Recent Developments in Ellipsometry, ed. N. M. Bashara, A. B. Buckman, A. C. Hall, (North Holland, Amsterdam, 1969) p. 14.

87. E. A. Stratton, Electromagnetic Theory (McGraw-Hill, New York, 1941) p. 492.

88. S. S. So, Surf. Sci., 56: 97 (1976).

89. M. R. Philpott and J.-M. Turlet, J. Chem. Phys., 64: 3852 (1976).

90. N. I. Ostapenko, M. P. Chernomorets, and M. T. Shpak, Phys. Status Solidi B72: K117 (1975).

91. F. Toigo, A. Marvin, V. Celli, and N. R. Hill, Phys. Rev. B15: 5618 (1977).

D. G. Hall and A. J. Braundmeier, Jr., Phys. Rev. B17: 3808 (1978).

92. S. P. McGlynn, T. Azumi, and M. Kinoshita, Molecular Spectroscopy of the Triplet State, (Prentice-Hall, New Jersey, 1969).

93. R. W. Sheets and R. S. Hansen, J. Phys. Chem., 76: 972 (1972).

94. M. Moskovitz and P. McBreen, J. Chem. Phys., 68: 4992 (1978).

95. E.F.I. Roberts and D. Ross, Surf. Sci., 56: 425 (1976).

96. J. Lagois and B. Fischer, Phys. Rev. Lett., 36: 680 (1976).

97. K. H. Drexhage, H. Kuhn, and F. P. Schafer, Ber. Bunsenges. Phys. Chem., 72: 329 (1968).

98. K. H. Drexhage, J. Lumin., 12: 693 (1970).

99. K. H. Drexhage, Sci. Am., 222: 108 (1970).

100. K. B. Blodgett, J.A.C.S., 57: 1007 (1935).

101. H. Kuhn, J. Chem. Phys., 53: 101 (1970).

102. R. R. Chance, A. Prock, and R. Silbey, Adv. Chem. Phys., Vol. XXVII (1978).

103. R. R. Chance, A. H. Miller, A. Prock, and R. Silbey, J. Chem. Phys., 63: 1589 (1975).

104. R. R. Chance, A. Prock, and R. Silbey, J. Chem. Phys. 62: 2245 (1975).

105. R. R. Chance, A. Prock, and R. Silbey, J. Chem. Phys., 60: 2184 (1974).

106. K. H. Tews, Ann. Phys. Leipz., 29: 97 (1973).

107. A. Sommerfeld, Partial Differential Equations in Physics, (Academic, New York, 1949) Chap. VI.

108. E. A. Stern and R. A. Ferrell, Phys. Rev., 120: 130 (1960).

109. H. Morawitz and M. R. Philpott, Phys. Rev. B10: 4863 (1974).

110. M. R. Philpott. J. Chem. Phys., 62: 1812 (1975).

111. V. M. Agranovich and A. G. Mal'shukov, Chem. Phys. Lett., 43: 221 (1976).

112. M. B. Webb and M. G. Lagally, in Solid State Physics, ed. H. Ehrenreich, F. Seitz, and D. Turnbull (Academic, New York, 1973) Vol. 28

J. B. Pendry, Low Energy Electron Diffraction, (Academic, London, 1974).

G. A. Somorjai and H. H. Farrell, Adv. Chem. Phys., Vol. XX (1971).

113. G. A. Somorjai and F. J. Szalkowski, Adv. High Temp. Chem., Vol. 4 (1971).

C. C. Chang, Surf. Sci., 25: 53 (1971).

114. G. E. Becker and H. D. Hagstrum, J. Vac. Sci. Technol., 11: 284 (1974).

115. H. V. Thapliyal and J. M. Blakely, J. Vac. Sci. Technol., 15: 600 (1978).

116. R. H. Muller, R. F. Steiger, G. A. Somorjai, and J. M. Morabito, Surf. Sci., 16: 234 (1969).

117. R. M. A. Azzam and N. M. Bashara, Ellipsometry and Polarized Light, (North-Holland, Amsterdam, 1977).

118. R. J. Archer, Manual on Ellipsometry, (Gaertner Scientific Corp., Chicago, IL).

119. R. H. Muller, in Advances in Electrochemistry and Electrochemical Engineering, Vol. 9, ed. R. H. Muller (Wiley, New York, 1973), Chap. 3.

120. D. E. Aspnes, in Optical Properties of Solids: New Developments (North-Holland, Amsterdam, 1976), Chap. 15.

121. C. E. Leberknight and B. Lustman, J. Opt. Soc. Am., 29: 59 (1939).

122. C. S. Strachan, Proc. Camb. Phil. Soc., 29: 116 (1933).

123. J. C. Maxwell Garnett, Phil. Trans., 205: 237 (1906).

124. M. J. Dignam and H. Moskovits, J. Chem. Soc. Faraday Trans., 69: 65 (1973).

125. R. J. Archer, J. Electrochem. Soc., 104: 619 (1957).

126. C. A. Fenstermaker and F. L. McCrackin, Surf. Sci., 16: 85 (1969).

127. D. E. Aspnes and A. A. Studna, Appl. Opt., 14: 220 (1975).

128. D. E. Aspnes, Opt. Commun., 8: 222 (1973).

129. D. E. Aspnes, J. Opt. Soc. Am., 64: 812 (1974).

130. D. E. Aspnes, J. Opt. Soc. Am., 64: 639 (1974).

131. K. K. Innes, J. P. Byrne, and I. G. Ross, J. Mol. Spect., 22: 125 (1967).

132. P. Esherick, P. Zinsli, and M. A. El-Sayed, Chem. Phys., 10: 415 (1975).

133. E. F. Zalewski, D. S. McClure, and D. L. Narva, J. Chem. Phys., 61: 2964 (1974).

134. W. R. Wadt and W. A. Goddard, III, J.A.C.S., 97: 2034 (1975).

135. P. R. Norton, R. L. Tapping, H. P. Broida, J. W. Gadzuk, and B. J. Waclawski, Chem. Phys. Lett., 53: 465 (1978).

136. R. M. Hochstrasser and C. Marzzacco, J. Chem. Phys., 49: 971 (1968).

137. J. L. Gland and G. A. Somorjai, Advan. Colloid Interface Sci., 5: 205 (1976).

138. K. Kishi and S. Ikeda, J. Phys. Chem., 73: 2559 (1969).

139. P. J. Wheatley, Acta Cryst., 10: 182 (1957).

140. L. Firment and G. A. Somorjai, Surf. Sci., 55: 413 (1976).

141. A. B. P. Lever, J. Lewis, and R. S. Nyholm, J. Chem. Soc., Dec: 4761 (1964).
ibid., Nov: 5042 (1963).

142. T. J. Moravec, J. C. Rife, and R. N. Dexter, Phys. Rev. B13: 3297 (1976).
A. A. Studna, Solid State Commun., 16: 1063 (1975).

143. H.-H. Perkampus and E. Baumgarten,
Ber. Bunsenges. Physik. Chem., 67: 16 (1963).

144. D. S. McClure, J. Chem. Phys. 22: 1668 (1954).

145. D. S. McClure and O. Schnepp, J. Chem. Phys.,27: 1575 (1955).

146, M. A. El-Sayed, L. Hall, A. Armstrong, and W. R. Moomaw, in Excitons, Magnons, and Phonons in Molecular Crystals, Proc. Internat. Symp., ed. A. Zahlan (Cambridge Univ. Press, 1968) p. 125.

147. B. J. Cohen and L. Goodman, J. Chem. Phys., 46: 713 (1967).

148. T. Azumi and Y. Nakano, J. Chem. Phys., 51: 2515 (1969).

APPENDIX

The technical details in this appendix are recorded as a service to future users of the UHV Chamber- Rotating Analyzer Ellipsometer. Good luck.

I. Rotary Stage Control

The control circuitry for the rotary stage holding the input polarizer is contained in a separate chassis holding the translator circuit board (TB) for the Aerotech rotary stage, the optical encoder control board (X1/X2 pulse generator), a custom control and computer interface board, and a 5 V power supply. This appendix will describe the circuitry for the control and computer interface board.

This board is diagrammed in Figure 47. It is made up of three separate circuits: slew, single step, and counter-direction, descending on the page. The front panel has one SPDT toggle switch and two push button switches to control direction, slew, and single-step movement, respectively, of the rotary stage. Each switch is buffered from the control circuitry by a two NAND gate, "no bounce" switch to suppress switching transients. The control board is connected at several points to terminal lugs on the translator board, identified as TBx-x, which are described in the rotary stage documentation. TB works on 12 V logic, so all inputs to TB are buffered by hex inverters with free-collector outputs ganged to the twelve volt power supply on the TB. All front panel BNC outputs are driven with 50 ohm drivers.

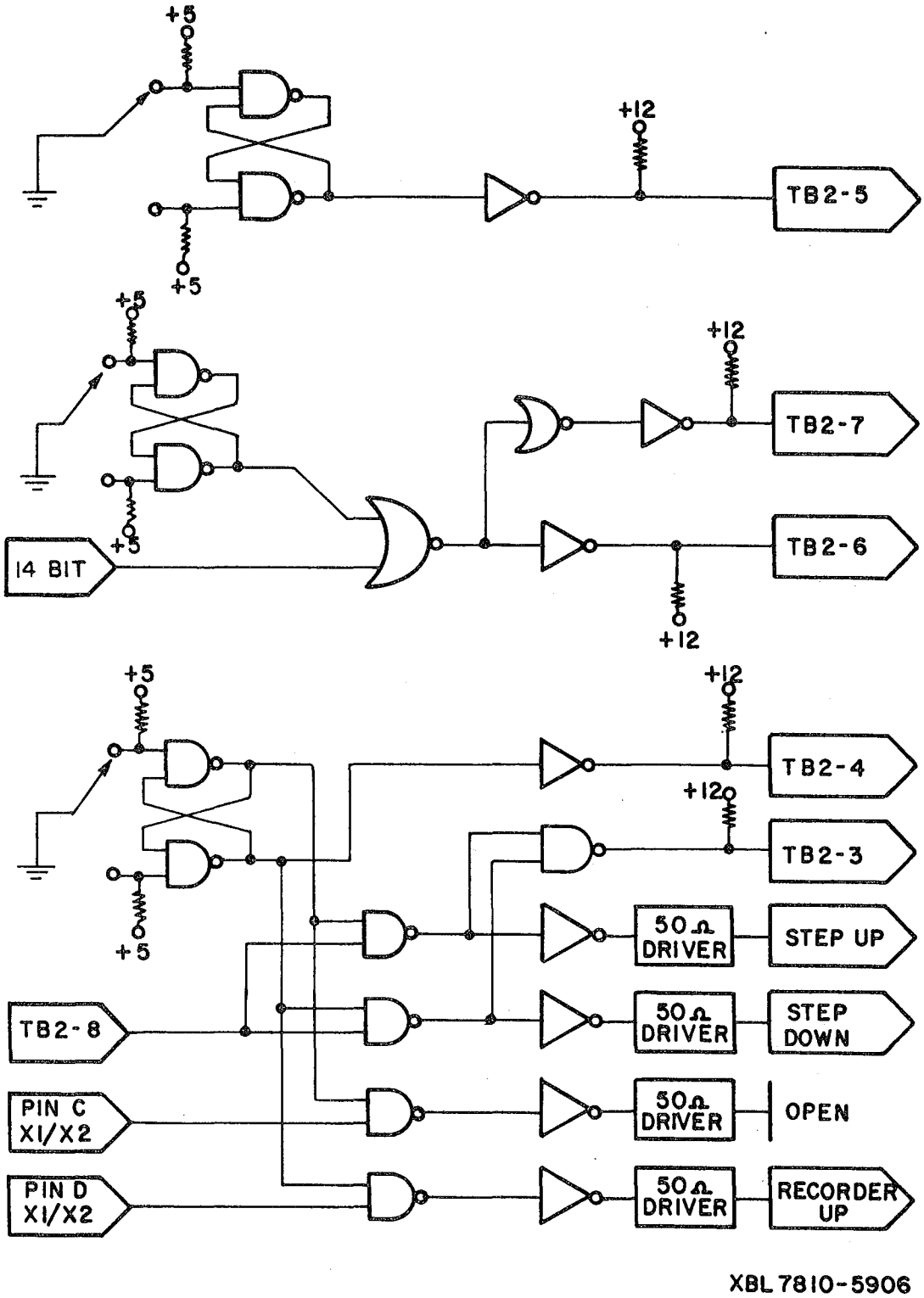

Figure 47. Rotary stage control.

a) Slew - +12 V input to the TB2-5 slews rotary stage at rate set by clock chip on TB.

b) Single-step - Rotary stage can be rotated one step (10,800 steps=1 revolution) by simultaneous high input to TB2-6 and low input to TB2-7. This transition can be initiated by a push button switch or by a TTL compatible high pulse from the 14 bit of the ADAC board status buffer.

c) Counter-Direction - A front panel toggle switch controls the direction of rotation by changing the level at TB2-4. When slew or single step motion is initiated, a clock pulse must travel between TB2-8 and TB2-3. This pulse is also transmitted to the two front panel BNC connectors (STEP UP and STEP DOWN), gated by the direction of rotation. These outputs are sent to a digital counter to display the relative angular position of the stage. Additional circuitry does the same thing for pulses from the optical encoders in the rotary stage.

Troubleshooting and Notes - The optical encoder pulses duplicated the clock pulses transmitted between TB2-8 and TB2-3 and were less reliable, so the optical encoder board was removed and the encoders disconnected electrically. A tendency for the power supply to overheat and deactivate appears to have been fixed by removal of the encoders and better ventilation. Also, a constant high or floating input to the 14 bit input will freeze rotary motion and this often happens when the computer has just been turned on.

II. Data Acquisition Trigger

Signal intensity is measured at 5° intervals of the output polarizer rotation. The computer D/A conversion is triggered by the 72 pulse/revolution from the channel A optical encoder. For each data point, data collection must start at the same point on the analyzer rotation. This is insured by the 1 pulse/revolution channel B encoder. The pulse forming circuits for the optical encoders were built and designed by the College electronics shop. I designed and built additional circuitry to suppress channel A until the computer triggered a new data taking cycle, with sufficient delay to allow the computer to prepare to accept data. The schematic of the final design is in Figure 48.

A low-to-high transition of the computer-controlled 5 bit (i) resets the clear input to flipflop, allowing flipflop output Q to change on next clock pulse, and (ii) generates a TTL compatible pulse to load counter with a value of two. The third succeeding channel B pulse into the 'count down' input of the counter generates a 'carry' pulse, which goes to the clock input of the flipflop. The flipflop output inverts and unlocks a NAND gate. All following channel A pulses are transmitted to the external trigger input of the ADAC board, until a high-low transition of the 5 bit clears the flipflop and resets the entire circuit at the end of the data taking cycle.

The time between the channel B pulse and the channel A pulses before and after it is set by the geometry of the gear and the optical encoders. If the channel B pulse is too near a channel A pulse, jitter may cause the circuit to start taking data at two different points during

EXTERNAL TRIGGER GATE

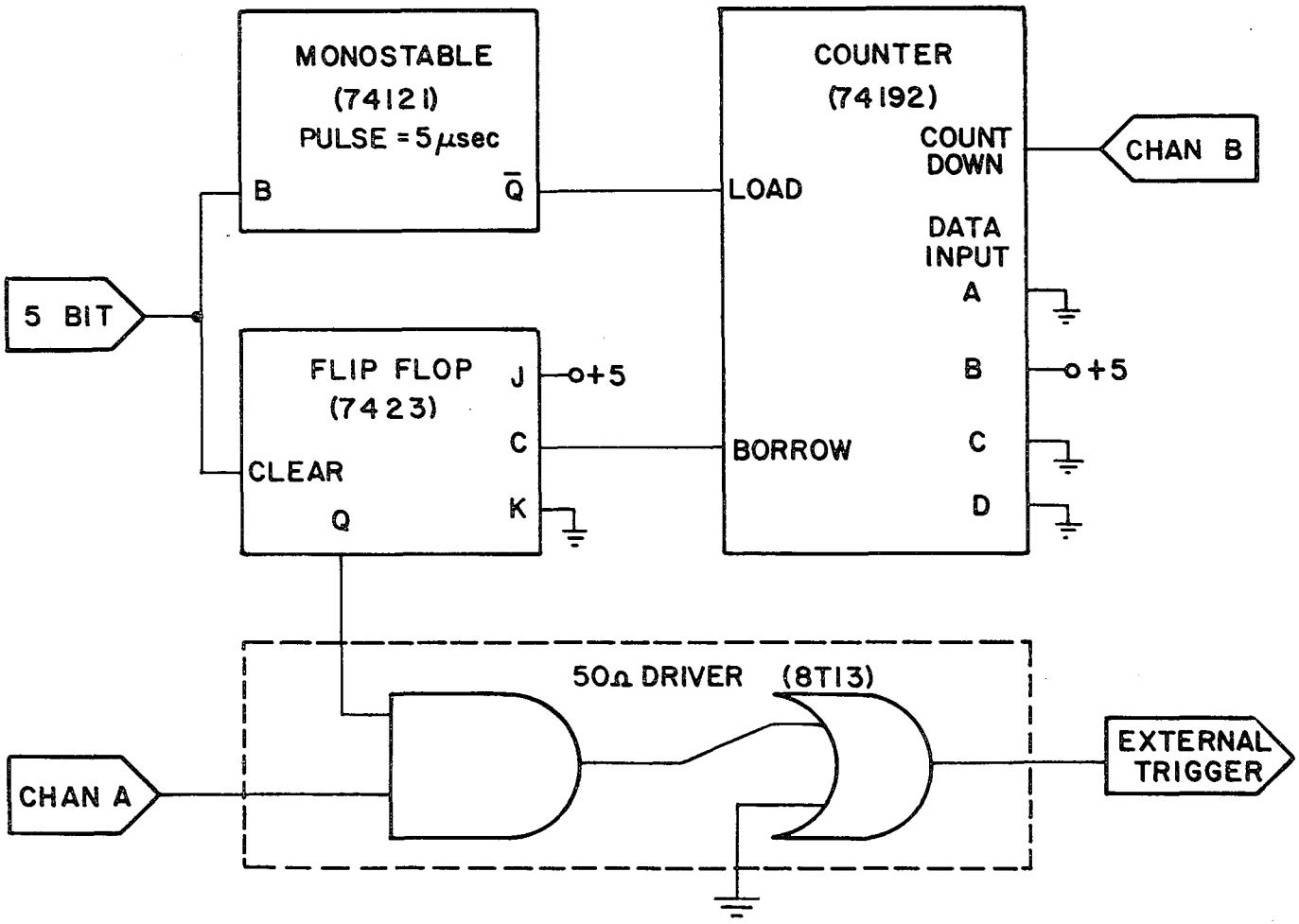

XBL 7810-5907

Figure 48. Circuit to gate external trigger pulses.

two successive cycles, producing characteristic constant magnitude glitches in the data. A channel B delay circuit was built to center the channel B pulse between two channel A pulses, consisting of two one-shots, one with a variable time constant. This is presently connected, but may be deleted by rejumpering the top of the board.

Troubleshooting and Notes - The most common problem with triggering is misalignment of the optical encoders. A second problem is the addition of spurious trigger pulses into the channel A pulse train. Both problems lie in the Electronics shop-built equipment rather than in the extra triggering circuit board in the optical encoder control chassis.

III. Computer Programs Written for Ellipsometry

General Remarks

Most of the important or commonly used programs are described in terms of purpose, procedure, data files input and output (DF), subroutines (SUB) called, and run-time parameters (RTP) input or output, which are quantities entered or printed out on the teletype at time of execution. For subroutines, the arguments of the call statement are also described. The procedure sections are sketchy; more detail is available in the comment statements in the programs themselves. Many programs written, mainly minor modifications or superceded versions, are not described. If no DF, SUB, or RTP are mentioned, none occur in the program.

Units are natural. Steps are units of the polarizer indexing head, 10,800 steps = 360°. RTP angles are in degrees, although internally angles are converted to radians. Wavelength and overlayer thickness

are in angstroms. Disk storage is in blocks of 256 words = 128 real numbers, which are stored as 16 points of 8 different quantities.

ATOCAL.FOR

Purpose: to calibrate rotating analyzer ellipsometer.

Procedure: i) RTP input, ii) zero buffer and reset done flag, iii) step input polarizer thru series of angles. At each angle, P, 200 data cycles are taken, 72 points per cycle, and the in- and out-of-phase Fourier components of the ellipse, A and B, are calculated and stored in arrays, iv) fit residuals, $R=1-A^2-B^2$, to parabola vs. polarizer angle using PARFIT, and calculate P1 and η and plot R vs. P v) fit $T = \frac{1}{2}\tan^{-1}B/A$ to straight line vs. P and calculate A1+AF.

Reference - Aspnes, Appl. Opt. 14, 220 (1975)

SUB: PARFIT, PLOTQ, IADAC, SYSLIB

RTP, input: IIP = initial polarizer angle, IFP = final polarizer angle, INT = pol. angle increment. These three quantities are in steps, as measured by external counter. KEY = flag, set for printout of P, A, B, R, and T; command, -1 for CRT display, 0 for no display, 1 for hardcopy. RTP, output: P, A, B, R, T = described in procedure, P1 = angle between plane of input polarizer and zero of external counter (radians), A1 + AF = angle between plane of output polarizer and channel B (delayed) of optical encoders, ETA = depolarization ratio. Last three calibration parameters are input unchanged into STORE.

IADAC.MAC

Purpose: to increment existing buffer contents by contents of data register on ADAC board. Macro language is used for speed.
Procedure: i) read address of subroutine argument into R2 ii) loop for completion of conversion (set bit 7, status word) iii) read data buffer contents into R0 and add R0 to double precision integer buffer iv) return. SUB ARG: (R5) = double precision integer buffer to be incremented, called KBUFF(J) in main program.

PARFIT.FOR

Purpose: to fit input array to parabola, calculating three parameters.
Procedure: least squares fitting routine, Reference Appl. Opt. 14 220 (1975). SUB ARG: N = # data points, VI = independent variable array, dim(200), VD = dependent variable array, dim(200), output A, B, C = parabolic parameters VD = A + B*VI + C*VI**2, S = RMS difference between data and calculated parabola.

PLOTQ.FOR

Purpose: to produce graphics display of R for ATOCAL.
Procedure: i) calculate minima and maxima for both arrays, ii) calculate 200 points on parabola from three parabola parameters,
iii) initialize and set virtual window, iv) if flag set, turn on and reset XY plotter, v) draw crosses at experimental points, vi) draw vertical dashed line at parabola minimum, vii) draw border around plot, viii) draw tick marks on bottom at 0.01 radian intervals,
ix) draw line through points on calculated parabola, x) turn off

plotter, kill graphics mode, and return.

SUB: TCSLIB

SUB ARG: N = # data points, P = independent variable array, dim(200), R = dependent variable array, dim(200), C0,C1, C2 = parabola parameters from PARFIT A, B, C, KEY = flag, set to activate hardcopy.

STORE.FOR

Purpose: to acquire data continuously, and to calculate and store on disk ψ, Δ, and effective optical constants of surface.

Procedure: i) input RTP, ii) initialize buffers, set external trigger, and reset done flag of ADAC status word, iii) collect RTP-set number of data points for RTP-set number of cycles per point, iv) calculate A and B Fourier components, v) calculate ρ, Δ, and ψ for surface, vi) assuming two component surface, calculate $\varepsilon_i + i\varepsilon_2$ and $n + ik$ for reflecting medium in vacuum, vii) store each 16 points as taken on diskette. Reference, Appl. Opt. 14 220 (1975)

SUB: IADAC, SYSLIB

DF, output: DX1:SPERA.DAT

RTP, input: PHID = angle of incidence, LAMBDA = wavelength (not used in program), PS = input polarizer angle in steps, PI, ETA, A1+AF = see ATOCAL, NDPT = # data points desired, which must be divisible by 16 to fill integral number of blocks, NCDP = # cycle/data point.

RTP, output: STORE(J), J = 1,8, = point number, time elapsed since first point, Δ, ψ, ε_1, ε_2, n, k

OFFSET.FOR

Purpose: to add constant to elapsed times stored in blocks on disk by STORE, so that two data files may be concatenated and displayed by UNSTOR as one file.

Procedure: i) input RTP, time increment and first and last blocks to be incremented, ii) access data file, read blocks one at a time, iii) add offset to elapsed time.

SUB: SYSLIB

DF, input and output: DX1:SPERA.DATA

RTP, input: OFFSET = increment to elapsed time in seconds, I1, I2 = first and last blocks to be changed (NB. first block in this program is called block 0).

STAGGR.FOR

Purpose: minor modification of STORE, to acquire data from ellipsometry in 8-point sets, with interrupt for manual stepping of wavelength before taking next 8 points.

DF, SUB, RTP = same as STORE.

AVG.FOR

Purpose: to calculate and print out average values of 8 point data sets stored by STAGGR

Procedure: i) access disk, DX1:SPERA.DAT, ii) read file one block at a time, iii) calculate arithmetic averages, iv) print results. Wavelength is stored in first two words of each eight point set.

SUB; SYSLIB

DF, input: DX1:SPERA.DAT

RTP, input: IBLOCK = # blocks in SPERA to average.

RTP, output: A(J), J = 1 or 65, = wavelength, C(J), J = 1, 6, = averages of Δ, ψ, ε_1, ε_2, n, k.

UNSTOR.FOR

Purpose: to produce graphics display of Δ, ψ, ε_1, ε_2, n, or k vs. elapsed time, with option of calculating and displaying smoothed, first derivative, or second derivative curves.

Procedure: i) print out instructions, ii) RTP input, iii) access disk, iv) read SPERA one block at a time, storing only elapsed time and desired output variable, v) optional smooth or differentiation of data using ZSUB1-3, vi) graphics display, with determination of maxima and minima, initialization and virtual window, border drawn, 1000 second tick marks on bottom, points drawn, vii) request hardcopy, loop to ii).

SUB: ZSUB1, ZSUB2,ZSUB3, SYSLIB, TCSLIB

DF, input: DX1:SPERA.DAT

RTP, input: IN, IF = number of initial, final data blocks to be displayed;

KEY1 = command, choice of displayed variable, 0 gives loop to data block request; KEY = command, choice of original data, smooth, or differentiation, see RT instructions; KEY = command, 0 = no copy, 1 - hardcopy, 2 = request new limits.

RTP, input and output: limits T(1), T(IDIFF),YMIN,YMAX = horizontal and vertical minima and maxima for display, may be set internally by code or externally by KEY3 = 2 and input.

ZSUB1.FOR

Purpose: to smooth data by 15 point running average.

Procedure: array B(1024) contains data to be smoothed at beginning and smoothed data at end. Array C(8) is temporary storage array for smoothed values, which slides along array B and replaces original values with smoothed values in B when original values are no longer needed to compute running average. C(8) = running 15 point average around B(N) using points B(N-7) through B(N+7) with statistical weights given in Anal. Chem. 36, 1627 (1964); Anal. Chem. 44, 1906 (1972). After C(8) is calculated, program sets B(N-7) = C(1), C(J) = C(J+1) for J = 1,7, and begins again with C(8) = weighted average around B(N+1) using points B(N-6) through B(N+8). At start, C(3) = 5 point running average around B(3), ····, C(7) = 13 point running average around B(7), and C(1) = C(2) = C(3). Equivalent shorter averages are taken for the last seven points.

SUB ARG: (in Common) B = array dim(1024); IDIFF = # points in B.

ZSUB2.FOR

Purpose: to calculate first derivative of data.

Procedure: identical to ZSUB1 with different statistical weights.

ZSUB3.FOR

Purpose: to calculate second derivative of data.

Procedure: identical to ZSUB1 with different statistical weights.

FIELDS.FOR

Purpose: to calculate overlayer optical constants n and k for overlayer of known thickness, given data files for bare and covered surfaces.

Procedure: i) RTP input, ii) access data files, iii) read data files one block at a time and read ψ and Δ for bare and covered surfaces (N.B., FIELDS assumes wavelength region for both data sets is the same), iv) calculate n and k from linear approximation formula, Reference - Aspnes, "Spectroscopic Ellipsometry of Solids" in Opt. Properties of Solids, New Developments (North Holland, Amsterdam, 1976) Eq. 3.31, v) using these values as starting values, iterate n and k alternately until real and imaginary parts of ρ = RHO or INT, are within 0.001 of experimental value (method due to HJR), vi) graphics display of results k, vii) request smooth data, hardcopy, new limits, or plot of n.

SUB: BENNY, POLRT, PLOTIT, SMOOTH, TOCK, SYSLIB, TCSLIB. (N.B., POLRT.FOR is in DEC Scientific Subroutines package; it solves for root of nth order polynomials. PLOTIT.FOR is a graphics routine written by Paul Cornelius that calls subroutines XDRAW and BORDER.)

DF, input: DX1:SPERA1.DAT = bare surface data

DX1:SPERA2.DAT = covered surface data.

RTP, input: IBLK1, IBLK2 = first and last blocks of data files to be read; PHI = angle of incidence; D = overlayer thickness; START, FINISH = initial and final wavelength covered by blocks read; IKEY = flag, set to print out wavelength, n, and k; TKX, TKY = input parameters to TOCK; KEY = command, 0 = stop, 1 = new limits,

2 = smooth, 3 = repeat, 4 = hardcopy, 5 = plot n. RTP, output: LAMBDA = wavelength; N1 = complex index of refraction.

LEROY.FOR

Purpose: minor modification of FIELDS, except SPERA1 and SPERA2 need not cover same wavelength range.

Procedure: same as FIELDS, except i) additional RTP input for SPERA1, ii) read entire file SPERA1 and store all values of ψ and Δ, iii) extrapolate ψ and Δ for bare surface for each point in SPERA2. DAT.

RTP, input: same as FIELDS, plus START1, FIN1 = initial and final wavelength for SPERA1.DAT; NOB = # blocks in SPERA1.

BENNY.FOR

Purpose: to calculate ρ for three component surface from complex indices of refraction, thickness, wavelength, angle of incidence, for interation procedure.

Procedure: calculate complex reflection coefficients using Drude's equations.

SUB ARG: N0 = real index of refraction for ambient; N1 = complex index of refraction for overlayer; N2 = complex index of refraction for substrate; LAMBDA = wavelength; PHI = angle on incidence (radians); D = overlayer thickness.

SMOOTH.FOR

Purpose: minor modification of ZSUB1, to smooth data.

Procedure: same as ZSUB1, except no common statement.

SUB ARG: B = array containing real values of independent and dependent variables at beginning, smoothed values at return, dim(2,400); IDIFF = # points in B.

TOCK.FOR

Purpose: to mark and label axes generated by PLOTIT.

Procedure: minor modification of TICK.FOR by Paul Cornelius.

SUB ARG: TK = interval between tick marks; FARRAY = LOGICAL*1 array containing format statement generated by SCOPY subroutine in main program; NAXIS = identifies axis to be labelled; NCHAR = # characters in format; NIN = scales length of tick mark.

ATOCAL.FOR

```
C       PROGRAM TO FIND CALIBRATION PARAMETERS
C       FOR ROTATING ANALYSER ELLIPSOMETER
C
      INTEGER*4 KBUFF
      DIMENSION KBUFF(72),P(200),R(200),T(200),B(200),A(200)
      WRITE(5,100)
  100 FORMAT(' CALIBRATION PROGRAM')
   10 WRITE(5,200)
  200 FORMAT(' ENTER INITIAL P IN STEPS, I5')
      N=1
      READ(5,210) IIP
  210 FORMAT(I5)
      WRITE(5,220)
  220 FORMAT(' ENTER FINAL P IN STEPS, I5')
      READ(5,210) IFP
      WRITE(5,230)
  230 FORMAT(' ENTER INTERVAL IN STEPS, I5')
      READ(5,210) INT
      K=IABS((IFP-IIP)/INT)+1
      IF(K-200) 15,15,16
   16 WRITE(5,240)
  240 FORMAT(' BUFFER SPACE EXCEEDED')
      GO TO 10
   15 WRITE(5,241)
  241 FORMAT(1H$,'TYPE 1 TO OUTPUT CALIBRATION POINTS  ')
      READ(5,242) KEY
  242 FORMAT(I2)
C
C  INITIALIZE BUFFERS AND REGISTERS
C
      MSGN=-1
      IF(IFP .GT. IIP) MSGN=1
   17 P(N)=FLOAT(IIP+MSGN*(N-1)*INT)*3.14159/5400.
      DO 20 J=1,72
   20 CALL JICVT(0,KBUFF(J))
      CALL IPOKE('176770,'72)
      KDUMMY=IPEEK('176772)
C
C  COLLECT 200 CYCLES AT THIS POL. ANGLE
C
      DO 30 I=1,200
      DO 30 J=1,72
   30 CALL IADAC(KBUFF(J))
C
C  CALCULATE A AND B AT THIS POL. ANGLE
C
      CALL IPOKE('176770,'32)
      S=0
      C=0
      D=0
      DO 40 J=1,72
      ANG=3.14159*FLOAT(1-J)/36.
      S=S+(AJFLT(KBUFF(J))*SIN(2.*ANG))
      C=C+(AJFLT(KBUFF(J))*COS(2.*ANG))
   40 D=D+AJFLT(KBUFF(J))
      A(N)=2.*C/D
      B(N)=2.*S/D
C
C  CALCULATE R AND TAN-1 AND START OVER
C
      T(N)=.5*ATAN2(B(N),A(N))
      R(N)=1.-A(N)**2-B(N)**2
      IF(KEY .EQ. 1) WRITE(5,130) N,P(N),N,A(N),
```

```
     CN,B(N),N,R(N),N,T(N)
  130 FORMAT(' P(',I3,')=',F10.6,'  A(',I3,')=',F10.6,
     C'  B(',I3,')=',F10.6,'  R(',I3,')=',F10.6,'  T(',I3,')=',F10.6)
      IF(K-N) 43,43,39
   39 CONTINUE
      DO 41 M1=1,INT
      CALL IPOKE("176770,"40032)
      DO 42 M2=1,150
   42 CONTINUE
      CALL IPOKE("176770,"32)
      DO 41 M3=1,50
   41 CONTINUE
      N=N+1
      GO TO 17
C
C CURVE FITTING
C
   43 CONTINUE
      SIGMA1=FLOAT(N)
      SIGMA2=FLOAT(N)
   45 WRITE(5,321)
  321 FORMAT(1H$,'TYPE -1 FOR CRT DISPLAY, 1 FOR HARDCOPY  ')
      READ(5,322) KEY
  322 FORMAT(I2)
      CALL PARFIT(N,P,R,C0,C1,C2,SIGMA1)
      P1=-C1/(2.*C2)
      ETA=SQRT(1./(1.-C0+((C1**2)/(4.*C2))))
      IF(KEY .NE. 0) CALL PLOTQ(N,P,R,C0,C1,C2,KEY)
      CALL PARFIT(N,P,T,C0,C1,C2,SIGMA2)
      AF1=C0+(C1*P1)+(C2*(P1**2))
      WRITE(5,150) N
  150 FORMAT(1X,I3,' RESIDUALS')
      WRITE(5,160) ETA,P1,SIGMA1
  160 FORMAT(' ETA=',F9.6,5X,'P1=',F10.6,5X,'GOODNESS
     C OF FIT=',F10.6)
      WRITE(5,170) AF1,SIGMA2
  170 FORMAT(' A1+AF=',F10.6,5X,'GOODNESS OF FIT=',F10.6)
   55 WRITE(5,500)
  500 FORMAT('$TYPE 1 TO CONTINUE')
      READ(5,510) IFIN
  510 FORMAT(I1)
      IF(IFIN) 61,61,10
   61 STOP
      END
```

IADAC.MAC

```
        .TITLE  IADAC
        .GLOBL  IADAC
        .MCALL  .REGDEF
        .REGDEF
        STATUS=176770
        DATA=176772
IADAC:  MOV     2(R5),R2            ;R2 POINTS TO KBUFF(J)
1$:     BIT     #200,@#STATUS       ;CHECK FOR ADAC READY
        BEQ     1$                  ;NO
        MOV     @#DATA,R0           ;YES, GET DATA
        ADD     R0,(R2)+            ;ADD LOWER ORDER HALVES
        ADC     (R2)                ;ADD CARRY INTO HIGHER ORDER
        RTS     PC                  ;RETURN
        .END
```

PARFIT.FOR

```
      SUBROUTINE PARFIT(N,VI,VD,A,B,C,S)
      DIMENSION VI(200),VD(200)
      VI1=0
      VI2=0
      VI3=0
      VI4=0
      VAR=0
      VD0=0
      VD1=0
      VD2=0
      DO 1 I=1,N
      VI1=VI1+VI(I)/S
      VI2=VI2+VI(I)**2/S
      VI3=VI3+VI(I)**3/S
      VI4=VI4+VI(I)**4/S
      VD0=VD0+VD(I)/S
      VD1=VD1+VD(I)*VI(I)/S
    1 VD2=VD2+VD(I)*VI(I)**2/S
      D=VI2*VI4+2.*VI1*VI2*VI3-VI2**3-VI3**2-VI1**2*VI4
      A=(VD0*(VI2*VI4-VI3**2)+VD1*(VI2*VI3-VI1*VI4)
     D+VD2*(VI1*VI3-VI2**2))/D
      B=(VD0*(VI2*VI3-VI1*VI4)+VD1*(VI4-VI2**2)
     D+VD2*(VI1*VI2-VI3))/D
      C=(VD0*(VI1*VI3-VI2**2)+VD1*(VI1*VI2-VI3)
     D+VD2*(VI2-VI1**2))/D
      DO 2 I=1,N
    2 VAR=VAR+(VD(I)-A-B*VI(I)-C*VI(I)**2)**2
      S=SQRT(VAR)
      RETURN
      END
```

PLOTQ.FOR

```
      SUBROUTINE PLOTQ(N,P,R,C0,C1,C2,KEY)
      DIMENSION NON(3),NOFF(3),NRST(3),
     CP(200),R(200),X(200),Y(200)
      DATA NON/27,65,69/NOFF/27,65,70/
      DATA NRST/27,65,78/
      P1=-C1/(2.*C2)
      YMIN=AMIN1(C0+C1*P1+C2*P1**2,R(1),R(N))
      YMAX=AMAX1(R(1),R(N),R(2))
      YMINA=YMIN-(YMAX-YMIN)/10.
      YMAXA=YMAX+(YMAX-YMIN)/10.
      XMIN=P(1)
      XMAX=P(N)
      XMINA=P(1)-(P(N)-P(1))/10.
      XMAXA=P(N)+(P(N)-P(1))/10.
      DO 40 J=1,200
      X(J)=P(1)+FLOAT(J-1)*(P(N)-P(1))/200.
   40 Y(J)=C0+C1*X(J)+C2*X(J)**2
      CALL INITT(120)
      CALL DWINDO(XMINA,XMAXA,YMINA,YMAXA)
      IF(KEY .EQ. 1) CALL TOUTST(3,NON)
      IF(KEY .EQ. 1) CALL TOUTST(3,NRST)
      DO 50 L=1,N
      CALL MOVEA(P(L),R(L))
      CALL MOVREL(-2,-2)
      CALL DRWREL(4,4)
```

```
      CALL MOVREL(0,-4)
   50 CALL DRWREL(-4,4)
      CALL MOVEA(P1,YMIN)
      CALL DASHA(P1,YMAX,3454)
      CALL MOVEA(XMINA,YMINA)
      CALL DRAWA(XMINA,YMAXA)
      CALL DRAWA(XMAXA,YMAXA)
      CALL DRAWA(XMAXA,YMINA)
      CALL DRAWA(XMINA,YMINA)
      YMINE=YMINA+.05*(YMAXA-YMINA)
      XDRA=.01*AINT(XMIN*100.)
   70 CALL MOVEA(XDRA,YMINA)
      CALL DRAWA(XDRA,YMINE)
      XDRA=XDRA+.01
      IF(XDRA .LE. XMAX) GO TO 70
      CALL MOVEA(X(1),Y(1))
      DO 80 J=2,200
   80 CALL DRAWA(X(J),Y(J))
      CALL MOVABS(0,1020)
      CALL ANMODE
      IF(KEY .EQ. 1) CALL TOUTST(3,NOFF)
      RETURN
      END


STORE.FOR

C    PROGRAM TO CALCULATE AND STORE DELTA, PSI
C   AND EFFECTIVE (TWO-PHASE) OPTICAL CONSTANTS FOR
C   SPECTROSCOPIC ELLIPSOMETRY.
C
      INTEGER*4 KBUFF
      REAL LAMBDA
      COMPLEX RHO,EPS,OCNK
      DIMENSION KBUFF(72),STORE(128),IPRGN(4)
      DATA IPRGN/3RDX1,3RSPE,3RRA ,3RDAT/
      WRITE(5,100)
  100 FORMAT(' CALCULATE AND STORE EFFECTIVE OPT. CONSTANTS')
      WRITE(5,110)
  110 FORMAT(' ENTER ANGLE OF INCIDENCE IN DEGREES,F8.3')
      READ(5,115) PHID
  115 FORMAT(F8.3)
      PHI=PHID*3.14159/180.
      WRITE(5,120)
  120 FORMAT(' ENTER LAMBDA IN ANGSTROMS, F9.2')
      READ(5,125) LAMBDA
  125 FORMAT(F9.2)
      WRITE(5,130)
  130 FORMAT('  ENTER POL. ANGLE IN STEPS, F6.0')
      READ(5,135) PS
  135 FORMAT(F6.0)
      P=PS*3.14159/5400.
      WRITE(5,140)
  140 FORMAT(' ENTER P1 IN RADIANS, F10.6')
      READ(5,145) P1
  145 FORMAT(F10.6)
      WRITE(5,150)
  150 FORMAT(' ENTER ETA', F10.6)
      READ(5,145) ETA
      WRITE(5,160)
  160 FORMAT(' ENTER A1+AF IN RADIANS, F10.6')
      READ(5,145) AF1
    4 WRITE(5,161)
  161 FORMAT(' ENTER NUMBER OF DATA POINTS TAKEN, I4')
```

```
      READ(5,162) NDPT
  162 FORMAT(I4)
      IF(NDPT .EQ. INT(FLOAT(NDPT)/16.)*16) GO TO 5
      WRITE(5,170)
  170 FORMAT(' MAKE NUMBER OF DATA POINTS A MULTIPLE OF 16')
      GO TO 4
    5 WRITE(5,163)
  163 FORMAT(' ENTER NUMBER OF CYCLES PER DATA POINT, I4')
      READ(5,162) NCDP
      WRITE(5,200)
  200 FORMAT('  DATA    TIME      DELTA       PSI
     CE1       E2       INDEX    ABSORP')
      INBLK=NDPT/16
      ICHAN=IGETC()
      IDKS=IENTER(ICHAN,IPRGN,INBLK)
      T1=SECNDS(0)
      DO 10 IDPT=1,INBLK
      DO 15 IINT=1,16
C
C  CLEAR BUFFERS
C
      DO 20 J=1,72
   20 CALL JICVT(0,KBUFF(J))
      CALL IPOKE('176770,'72)
      KDUMMY=IPEEK('176772)
C
C  COLLECT NCDP CYCLES AT THIS POL. ANGLE
C
      T=SECNDS(T1)
      DO 30 I=1,NCDP
      DO 30 J=1,72
   30 CALL IADAC(KBUFF(J))
C
C  CALCULATE A AND B AT THIS POL. ANGLE
C
      CALL IPOKE('176770,'32)
      S=0
      C=0
      D=0
      DO 40 J=1,72
      ANG=3.14159*FLOAT(1-J)/36.
      S=S+(AJFLT(KBUFF(J))*SIN(2.*ANG))
      C=C+(AJFLT(KBUFF(J))*COS(2.*ANG))
   40 D=D+AJFLT(KBUFF(J))
      A=2.*C/D
      B=2.*S/D
      SQG=ETA*SQRT(A**2+B**2)
      ALC=SQRT(1.-SQG**2)/(1.+SQG)
C
C  SET UP ARRAY FOR STORAGE ON DISK, 16 DATA POINTS (INDEXED
C  BY NO) PER BLOCK.  STORE(1) IS THE NUMBER OF THE DATA POINT
C  AND STORE(2) IS ITS TIME.
C
      NO=(IINT-1)*8
      STORE(NO+1)=FLOAT((IDPT-1)*16+IINT)
      STORE(NO+2)=T
C
C  CALCULATE OPTICAL CONSTANTS
C
      QAF=0.5*ATAN2(B,A)
      COT=COS(QAF-AF1)/SIN(QAF-AF1)
      TAN=SIN(P-P1)/COS(P-P1)
C
C  CALCULATE RHO, DELTA, AND PSI
C
```

```
      RHO=(COT-CMPLX(0,ALC))*TAN/(1.+CMPLX(0,ALC)*COT)
      DELTA=ATAN2(AIMAG(RHO),REAL(RHO))
      PSI=ATAN2(AIMAG(RHO),SIN(DELTA))
      EPS=((1.-RHO)/(1.+RHO)*SIN(PHI)**2/COS(PHI))**2+
     CSIN(PHI)**2
C
C  STORE(5) AND STORE(6) ARE REAL AND IMAGINARY COMPONENTS
C  OF EFFECTIVE DIELECTRIC CONSTANT OF SURFACE.
C
      STORE(NO+5)=REAL(EPS)
      STORE(NO+6)=AIMAG(EPS)
      OCNK=CSQRT(EPS)
C
C  STORE(7) AND STORE(8) ARE REAL AND IMAGINARY COMPONENTS
C  OF EFFECTIVE COMPLEX REFRACTIVE INDEX OF SURFACE.
C
      STORE(NO+7)=REAL(OCNK)
      STORE(NO+8)=AIMAG(OCNK)
C
C  STORE(3) AND STORE(4) ARE DELTA AND PSI IN DEGREES.
C
      STORE(NO+3)=DELTA/3.14159*180.
      STORE(NO+4)=PSI/3.14159*180.
   15 WRITE(5,210)(STORE(J),J=NO+1,NO+8)
  210 FORMAT(1X,F6.0,F8.1,2F9.3,4F9.4)
      IBLK=IDPT-1
      IDKS=IWRITW(256,STORE,IBLK,ICHAN)
   10 CONTINUE
      CALL CLOSEC(ICHAN)
      IDKS=IFREEC(ICHAN)
      STOP
      END
```

```
OFFSET.FOR

      DIMENSION IPRGN(4),A(128)
      REAL*4 OFFSET
      DATA IPRGN/3RDX1,3RSPE,3RRA ,3RDAT/
      WRITE(5,100)
  100 FORMAT('$...ENTER OFFSET (F10.0)  ')
      READ(5,120) OFFSET
  120 FORMAT(F10.0)
      WRITE(5,140)
  140 FORMAT('$...ENTER FIRST AND LAST BLOCKS (2I2)  ')
      READ(5,160) I1,I2
  160 FORMAT(2I2)
      ICHAN=IGETC()
      IDKS=LOOKUP(ICHAN,IPRGN)
      DO 10 J=I1,I2
      IDKS=IREADW(256,A,J,ICHAN)
      DO 20 K=0,15
   20 A(K*8+3)=A(K*8+2)+OFFSET
   10 IDKS=IWRITW(256,A,J,ICHAN)
      CALL CLOSEC(ICHAN)
      IDKS=IFREEC(ICHAN)
      STOP 'COMPLETED'
      END
```

STAGGR.FOR

```
C   PROGRAM TO CALCULATE AND STORE DELTA, PSI
C  AND EFFECTIVE (TWO-PHASE) OPTICAL CONSTANTS FOR
C  SPECTROSCOPIC ELLIPSOMETRY.
C
      INTEGER*4 KBUFF
      COMPLEX RHO,EPS,OCNK
      DIMENSION KBUFF(72),STORE(128),IPRGN(4)
      DATA IPRGN/3RDX1,3RSPE,3RRA ,3RDAT/
      WRITE(5,100)
  100 FORMAT(' CALCULATE AND STORE EFFECTIVE OPT. CONSTANTS')
      WRITE(5,110)
  110 FORMAT(' ENTER ANGLE OF INCIDENCE IN DEGREES,F8.3')
      READ(5,115) PHID
  115 FORMAT(F8.3)
      PHI=PHID*3.14159/180.
      WRITE(5,130)
  130 FORMAT('  ENTER POL. ANGLE IN STEPS, F6.0')
      READ(5,135) PS
  135 FORMAT(F6.0)
      P=PS*3.14159/5400.
      WRITE(5,140)
  140 FORMAT(' ENTER P1 IN RADIANS, F10.6')
      READ(5,145) P1
  145 FORMAT(F10.6)
      WRITE(5,150)
  150 FORMAT(' ENTER ETA', F10.6)
      READ(5,145) ETA
      WRITE(5,160)
  160 FORMAT(' ENTER A1+AF IN RADIANS, F10.6')
      READ(5,145) AF1
    4 WRITE(5,161)
  161 FORMAT(' ENTER NUMBER OF FREQUENCIES TO BE TAKEN, I4  ')
      READ(5,162) JFREQ
  162 FORMAT(I4)
      NDPT=8*JFREQ
      IF(NDPT .EQ. INT(FLOAT(NDPT)/16.)*16) GO TO 5
      WRITE(5,170)
  170 FORMAT(' MAKE NUMBER OF DATA POINTS A MULTIPLE OF 16')
      GO TO 4
    5 WRITE(5,163)
  163 FORMAT(' ENTER NUMBER OF CYCLES PER DATA POINT, I4')
      READ(5,162) NCDP
      WRITE(5,200)
  200 FORMAT('  DATA    TIME      DELTA        PSI
     CE1        E2       INDEX     ABSORP')
      INBLK=NDPT/16
      ICHAN=IGETC()
      IOKS=IENTER(ICHAN,IPRGN,INBLK)
      T1=SECNDS(0)
      DO 10 IDPT=1,INBLK
      DO 17 ITWI=0,1
      WRITE(5,120)
  120 FORMAT('$...ENTER LAMBDA  ')
      READ(5,125) LAMBDA
  125 FORMAT(I4)
      DO 15 IONCE=0,7
      IINT=IONCE+(ITWI*8)+1
C
C  CLEAR BUFFERS
C
      DO 20 J=1,72
   20 CALL JICVT(0,KBUFF(J))
      CALL IPOKE('176770,'72)
```

```
      KDUMMY=IPEEK('176772)
C
C   COLLECT NCOP CYCLES AT THIS POL. ANGLE
C
      T=SECNDS(T1)
      DO 30 I=1,NCOP
      DO 30 J=1,72
   30 CALL IADAC(KBUFF(J))
C
C   CALCULATE A AND B AT THIS POL. ANGLE
C
      CALL IPOKE('176770,'32)
      S=0
      C=0
      D=0
      DO 40 J=1,72
      ANG=3.14159*FLOAT(J-1)/36.
      S=S+(AJFLT(KBUFF(J))*SIN(2.*ANG))
      C=C+(AJFLT(KBUFF(J))*COS(2.*ANG))
   40 D=D+AJFLT(KBUFF(J))
      A=2.*C/D
      B=2.*S/D
      SQG=ETA*SQRT(A**2+B**2)
      ALC=SQRT(1.-SQG**2)/(1.+SQG)
C
C   SET UP ARRAY FOR STORAGE ON DISK, 16 DATA POINTS (INDEXED
C   BY NO) PER BLOCK.  STORE(1) IS THE NUMBER OF THE DATA POINT
C   AND STORE(2) IS ITS TIME.
C
      NO=(IINT-1)*8
      STORE(NO+1)=FLOAT((IDPT-1)*16+IINT)
      STORE(NO+2)=T
C
C   CALCULATE OPTICAL CONSTANTS
C
      QAF=0.5*ATAN2(B,A)
      COT=COS(QAF-AF1)/SIN(QAF-AF1)
      TAN=SIN(P-P1)/COS(P-P1)
C
C   CALCULATE RHO, DELTA, AND PSI
C
      RHO=(COT-CMPLX(0,ALC))*TAN/(1.+CMPLX(0,ALC)*COT)
      DELTA=ATAN2(AIMAG(RHO),REAL(RHO))
      PSI=ATAN2(AIMAG(RHO),SIN(DELTA))
      EPS=((1.-RHO)/(1.+RHO)*SIN(PHI)**2/COS(PHI))**2+
     CSIN(PHI)**2
C
C   STORE(5) AND STORE(6) ARE REAL AND IMAGINARY COMPONENTS
C   OF EFFECTIVE DIELECTRIC CONSTANT OF SURFACE.
C
      STORE(NO+5)=REAL(EPS)
      STORE(NO+6)=AIMAG(EPS)
      OCNK=CSQRT(EPS)
C
C   STORE(7) AND STORE(8) ARE REAL AND IMAGINARY COMPONENTS
C   OF EFFECTIVE COMPLEX REFRACTIVE INDEX OF SURFACE.
C
      STORE(NO+7)=REAL(OCNK)
      STORE(NO+8)=AIMAG(OCNK)
C
C   STORE(3) AND STORE(4) ARE DELTA AND PSI IN DEGREES.
C
      STORE(NO+3)=DELTA/3.14159*180.
      STORE(NO+4)=PSI/3.14159*180.
   15 WRITE(5,210)(STORE(J),J=NO+1,NO+8)
```

```
  210 FORMAT(1X,F6.0,F8.1,2F9.3,4F9.4)
   17 STORE(1+ITWI*64)=FLOAT(LAMBDA)
      IBLK=IDPT-1
      IDKS=IWRITW(256,STORE,IBLK,ICHAN)
   10 CONTINUE
      CALL CLOSEC(ICHAN)
      IDKS=IFREEC(ICHAN)
      STOP
      END
```

AVG.FOR

```
      DIMENSION A(128),IPRGN(4),C(12)
      DATA IPRGN/3RDX1,3RSPE,3RRA ,3RDAT/
      WRITE(5,100)
  100 FORMAT('$...ENTER NO. BLOCKS, I3  ')
      READ(5,110) IBLOCK
  110 FORMAT(I3)
      IBLOCK=IBLOCK-1
      ICHAN=IGETC()
      IDKS=LOOKUP(ICHAN,IPRGN)
      DO 10 J=0,IBLOCK
      IDKS=IREADW(256,A,J,ICHAN)
      DO 15 L=1,12
   15 C(L)=0.0
      DO 25 M=0,1
      DO 25 L=1,6
      DO 25 K=0,56,8
   25 C(L+M*6)=C(L+M*6)+A(K+L+2+M*64)/8.
      WRITE(5,120) A(1),(C(K),K=1,6)
   10 WRITE(5,120) A(65),(C(K),K=7,12)
  120 FORMAT(1X,F5.0,6F12.4)
      CALL CLOSEC(ICHAN)
      IDKS=IFREEC(ICHAN)
      STOP
      END
```

UNSTOR.FOR

```
C     THIS PROGRAM TAKES THE DATA STORED IN THE DATA FILE
C  SPERA.DAT ON DX1 BY THE PROGRAM 'STORE' AND DISPLAYS
C  EITHER THE ORIGINAL VALUES OF ANY ONE VARIABLE AGAINST THE TIME
C  OF ACQUISITION, OR, USING SUBROUTINES ZSUB1,2,3, CAN SMOOTH
C  AND TAKE DERIVATIVES OF THE DATA.  ONLY ONE VARIABLE MAY BE
C  DISPLAYED AT A TIME WITH THIS PROGRAM.
C     THE INITIAL PART OF THE PROGRAM CONSISTS OF WRITE STATEMENTS
C  WHICH EXPLAIN THE SYSTEM OF COMMANDS FOR USER INTERACTION.
C
      DIMENSION A(128),T(1024),IPRGN(4),NON(3),NOFF(3)
      COMMON B(1024),IDIFF,C(8)
      DATA IPRGN/3RDX1,3RSPE,3RRA ,3RDAT/
      DATA NON/27,65,69/NOFF/27,65,70/
      WRITE(5,100)
  100 FORMAT(' PROGRAM TO SMOOTH AND PLOT DATA IN DX1:SPERA.DAT')
      WRITE(5,110)
  110 FORMAT(' COMMAND SEQUENCE:',T20,'FIRST DIGIT',T50,'SECOND
     CDIGIT',/T20,'0=REQUEST NEW DATA BASE',/T20,'1=DELTA',T50,
     C'1=NORMAL SPECTRUM',/T20,'2=PSI',T50,'2=SMOOTHED SPECTRUM')
      WRITE(5,120)
  120 FORMAT(1X,T20,'3=REAL DIELECTRIC CONST.',T50,'3=FIRST DER
```

```
     CIVATIVE',/T20,'4=IMAG. DIELECTRIC CONST.',T50,'4=SECOND
     CDERIVATIVE',/T20,'5=INDEX OF REFRACTION',
     C/T20,'6=ABSORBTION')
C  CHOOSE THE BLOCKS TO BE READ , THE TREATMENT OF THE DATA
C  BEFORE DISPLAY, AND THE VARIABLE TO BE DISPLAYED.
C
    1 WRITE(5,150)
  150 FORMAT('$...ENTER FIRST AND LAST DATA BLOCKS,(2I3)  ')
      READ(5,200) IN,IF
  200 FORMAT(2I3)
    2 WRITE(5,210)
  210 FORMAT('$...ENTER COMMAND SEQUENCE, (2I1)  ')
      READ(5,220) KEY1,KEY2
  220 FORMAT(2I1)
      IF(KEY1 .EQ. 0) GO TO 1
C
C      THE PROGRAM OPENS A CHANNEL TO THE DISK, READS THE DATA
C  ONE BLOCK AT A TIME INTO TEMPORARY BUFFER A, AND THEN
C  PICKS OUT THE TIME AND DESIRED DISPLAY VARIABLE FROM
C  BUFFER A AND PUTS IT INTO ARRAY B, WHICH HAS SPACE FOR 1024
C  DATA POINTS.AFTER READING ALL BLOCKS IN TURN INTO A, THE DISK
C  IS CLOSED.
C
      ICHAN=IGETC()
      IDKS=LOOKUP(ICHAN,IPRGN)
      DO 3 I=IN,IF
      IUSE=I-1
      IUP=(I-IN)*16
      IDKS=IREADW(256,A,IUSE,ICHAN)
      DO 3 J=1,16
      JUP=2+(J-1)*8
      T(IUP+J)=A(JUP)
    3 B(IUP+J)=A(JUP+KEY1)
      CALL CLOSEC(ICHAN)
      IDKS=IFREEC(ICHAN)
C
C       IDIFF IS THE NUMBER OF DATA POINTS.  THE THREE SUBROUTINES
C  SMOOTH AND TAKE FIRST AND SECOND DERIVATIVES RESPECTIVELY,
C  RETURNING THE NEW VALUES IN THE ARRAY B WHICH IS
C  HELD IN COMMON.
C
      IDIFF=(IF-IN+1)*16
      IF(KEY2 .EQ. 2) CALL ZSUB1
      IF(KEY2 .EQ. 3) CALL ZSUB2
      IF(KEY2 .EQ. 4) CALL ZSUB3
C
C      THE PROGRAM CALCULATES THE MAXIMA AND MINIMA OF THE
C  ORIGINAL/MODIFIED DISPLAY VARIABLE, AS WELL AS THE INITIAL
C  AND FINAL ACQUISITION TIMES, AND PRINTS THESE
C  LIMITS OUT.
C
      YMIN=B(1)
      YMAX=B(1)
      DO 4 I=2,IDIFF
      IF(YMIN .GT. B(I)) YMIN=B(I)
    4 IF(YMAX .LT. B(I)) YMAX=B(I)
    8 WRITE(5,230) T(1),T(IDIFF),YMIN,YMAX
  230 FORMAT('+LIMITS:X ',2F12.1,'  SECS',/7X,'Y ',2F12.4)
C
C      PLOTTING SECTION
C
      KEY3=0
      XRANGE=T(IDIFF)-T(1)
      XMIN=T(1)-.1*XRANGE
      XMAX=T(IDIFF)+.1*XRANGE
```

```
      YRANGE=YMAX-YMIN
      YMIN=YMIN-.1*YRANGE
      YMAX=YMAX+.1*YRANGE
      MARK=INT(XRANGE/1000.)
C
    5 CALL INITT(120)
      CALL DWINDO(XMIN,XMAX,YMIN,YMAX)
      IF(KEY3 .EQ. 1) CALL TOUTST(3,NON)
      CALL MOVEA(XMIN,YMIN)
      CALL DRAWA(XMIN,YMAX)
      CALL DRAWA(XMAX,YMAX)
      CALL DRAWA(XMAX,YMIN)
      CALL DRAWA(XMIN,YMIN)
      DO 6 I=0,MARK
      XMARK=T(1)+FLOAT(I)*1000.
      CALL MOVEA(XMARK,YMIN)
    6 CALL DRWREL(0,40)
      CALL MOVEA(T(1),B(1))
      DO 7 I=2,IDIFF
    7 CALL DRAWA(T(I),B(I))
      IF(KEY3 .EQ. 1) CALL TOUTST(3,NOFF)
      CALL ANMODE
      IF(KEY3 .EQ. 1) GO TO 2
C
C  REQUEST HARDCOPY.
C
      WRITE(5,250)
  250 FORMAT('$...HARDCOPY? 1=YES,0=NO  ')
      READ(5,260) KEY3
  260 FORMAT(I1)
      IF(KEY3 .EQ. 0) GO TO 2
      IF(KEY3 .EQ. 2) GO TO 9
      GO TO 5
    9 WRITE(5,270)
  270 FORMAT('$...ENTER NEW LIMITS FOR X,Y  ')
      READ(5,280) T(1),T(IDIFF),YMIN,YMAX
  280 FORMAT(4F16.4)
      GO TO 8
      STOP
      END
```

ZSUB1.FOR

```
      SUBROUTINE ZSUB1
      COMMON B(1024),IDIFF,C(8)
      C(3)=(-3.*(B(1)+B(5))+12.*(B(2)+B(4))+17.*B(3))/35.
      C(1)=C(3)
      C(2)=C(3)
      C(4)=(-2.*(B(1)+B(7))+3.*(B(2)+B(6))+6.*(B(3)+B(5))
     C+7.*B(4))/21.
      C(5)=(-21.*(B(1)+B(9))+14.*(B(2)+B(8))+39.*(B(3)+B(7))
     C+54.*(B(4)+B(6))+59.*B(5))/231.
      C(6)=(-36.*(B(1)+B(11))+9.*(B(2)+B(10))+44.*(B(3)+B(9))
     C+69.*(B(4)+B(8))+84.*(B(5)+B(7))+89.*B(6))/429.
      C(7)=(-11.*(B(1)+B(13))+9.*(B(3)+B(11))+16.*(B(4)+B(10))
     C+21.*(B(5)+B(9))+24.*(B(6)+B(8))+25.*B(7))/143.
      DO 10 I=8,IDIFF-7
      C(8)=(-78.*(B(I-7)+B(I+7))-13.*(B(I-6)+B(I+6))+42.*(B(I-5)+B(I+5))
     C+87.*(B(I-4)+B(I+4))+122.*(B(I-3)+B(I+3))+147.*(B(I-2)+B(I+2))
     C+162.*(B(I-1)+B(I+1))+167.*B(I))/1105.
      B(I-7)=C(1)
```

```
      DO 10 J=1,7
   10 C(J)=C(J+1)
      J=IDIFF-13
      C(8)=(-11.*(B(J+1)+B(J+13))+9.*(B(J+3)+B(J+11))+16.*(B(J+4)+B(J+10
     C))+21.*(B(J+5)+B(J+9))+24.*(B(J+6)+B(J+8))+25.*B(J+7))/143.
      B(J)=C(1)
      DO 11 J=1,7
   11 C(J)=C(J+1)
      J=IDIFF-11
      C(8)=(-36.*(B(J+1)+B(J+11))+9.*(B(J+2)+B(J+10))+44.*(B(J+3)+B(J+9)
     C)+69.*(B(J+4)+B(J+8))+84.*(B(J+5)+B(J+7))+89.*B(J+6))/429.
      B(IDIFF-12)=C(1)
      DO 12 J=1,7
   12 C(J)=C(J+1)
      J=IDIFF-9
      C(8)=(-21.*(B(J+1)+B(J+9))+14.*(B(J+2)+B(J+8))+39.*(B(J+3)+B(J+7))
     C+54.*(B(J+4)+B(J+6))+59.*B(J+5))/231.
      B(IDIFF-11)=C(1)
      DO 13 J=1,7
   13 C(J)=C(J+1)
      J=IDIFF-7
      C(8)=(-2.*(B(J+1)+B(J+7))+3.*(B(J+2)+B(J+6))+6.*(B(J+3)+B(J+5))
     C+7.*B(J+4))/21.
      B(IDIFF-10)=C(1)
      DO 14 J=1,7
   14 C(J)=C(J+1)
      J=IDIFF-5
      C(8)=(-3.*(B(J+1)+B(J+5))+12.*(B(J+2)+B(J+4))+17.*B(J+3))/35.
      J=IDIFF-9
      DO 15 K=1,8
   15 B(J+K-1)=C(K)
      B(IDIFF-1)=C(8)
      B(IDIFF)=C(8)
      RETURN
      END
```

ZSUB2.FOR

```
      SUBROUTINE ZSUB2
      COMMON B(1024),IDIFF,C(8)
      C(3)=((B(1)-B(5))-8.*(B(2)-B(4)))/12.
      C(1)=C(3)
      C(2)=C(3)
      C(4)=(22.*(B(1)-B(7))-67.*(B(2)-B(6))
     C-58.*(B(3)-B(5)))/252.
      C(5)=(86.*(B(1)-B(9))-142.*(B(2)-B(8))-193.*(B(3)-B(7))
     C-126.*(B(4)-B(6)))/1188.
      C(6)=(300.*(B(1)-B(11))-294.*(B(2)-B(10))-532.*
     C(B(3)-B(9))-503.*(B(4)-B(8))-296.*(B(5)-B(7)))/5148.
      C(7)=(1133.*(B(1)-B(13))-660.*(B(2)-B(12))
     C-1578.*(B(3)-B(11))-1796.*(B(4)-B(10))
     C-1489.*(B(5)-B(9))-832.*(B(6)-B(8)))/24024.
      DO 10 I=8,IDIFF-7
      C(8)=(12922.*(B(I-7)-B(I+7))-4121.*(B(I-6)-B(I+6))
     C-14150.*(B(I-5)-B(I+5))-18334.*(B(I-4)-B(I+4))
     C-17842.*(B(I-3)-B(I+3))-13843.*(B(I-2)-B(I+2))
     C-7506.*(B(I-1)-B(I+1)))/334152.
      B(I-7)=C(1)
      DO 10 J=1,7
   10 C(J)=C(J+1)
      J=IDIFF-13
      C(8)=(1133.*(B(J+1)-B(J+13))-660.*(B(J+2)-B(J+12))
     C-1578.*(B(J+3)-B(J+11))-1796.*(B(J+4)-B(J+10))
     C-1489.*(B(J+5)-B(J+9))-832.*(B(J+6)-B(J+8)))/24024.
```

```
      B(J)=C(1)
      DO 11 J=1,7
   11 C(J)=C(J+1)
      J=IDIFF-11
      C(8)=(300.*(B(J+1)-B(J+11))-294.*(B(J+2)-B(J+10))-532.*
     C(B(J+3)-B(J+9))-503.*(B(J+4)-B(J+8))-296.*(B(J+5)-B(J+7)))/5148.
      J=IDIFF-12
      B(J)=C(1)
      DO 12 J=1,7
   12 C(J)=C(J+1)
      J=IDIFF-9
      C(8)=(86.*(B(J+1)-B(J+9))-142.*(B(J+2)-B(J+8))-193.*
     C(B(J+3)-B(J+7))-126.*(B(J+4)-B(J+6)))/1188.
      J=IDIFF-11
      B(J)=C(1)
      DO 13 J=1,7
   13 C(J)=C(J+1)
      J=IDIFF-7
      C(8)=(22.*(B(J+1)-B(J+7))-67.*(B(J+2)-B(J+6))
     C-58.*(B(J+3)-B(J+5)))/252.
      J=IDIFF-10
      B(J)=C(1)
      DO 14 J=1,7
   14 C(J)=C(J+1)
      J=IDIFF-5
      C(8)=((B(J+1)-B(J+5))-8.*(B(J+2)-B(J+4)))/12.
      J=IDIFF-9
      DO 15 K=1,8
   15 B(J+K-1)=C(K)
      B(IDIFF-1)=C(8)
      B(IDIFF)=C(8)
      RETURN
      END
```

ZSUB3.FOR

```
      SUBROUTINE ZSUB3
      COMMON B(1024),IDIFF,C(8)
      C(4)=(-13.*(B(1)+B(7))+67.*(B(2)+B(6))-19.*(B(3)+B(5))
     C-70.*B(4))/132.
      C(3)=C(4)
      C(1)=C(3)
      C(2)=C(3)
      C(5)=(-126.*(B(1)+B(9))+371.*(B(2)+B(8))+151.*(B(3)+B(7))
     C-211.*(B(4)+B(6))-370.*B(5))/1716.
      C(6)=(-90.*(B(1)+B(11))+174.*(B(2)+B(10))+146.*
     C(B(3)+B(9))+1.*(B(4)+B(8))
     C-136.*(B(5)+B(7))-190.*B(6))/1716.
      C(7)=(-2211.*(B(1)+B(13))+3504.*(B(3)+B(11))+1614.*(B(4)+
     CB(10))-971.*(B(5)+B(9))-3016.*(B(6)+B(8))-3780.*B(7)
     C+2970.*(B(2)+B(12)))/58344.
      DO 10 I=8,IDIFF-7
      C(8)=(-31031.*(B(I-7)+B(I+7))+29601.*(B(I-6)+B(I+6))
     C+44495.*(B(I-5)+B(I+5))+31856.*(B(I-4)+B(I+4))+
     C6579.*(B(I-3)+B(I+3))-19751.*(B(I-2)+B(I+2))
     C-38859.*(B(I-1)+B(I+1))-45780.*B(I))/1108536.
      B(I-7)=C(1)
      DO 10 J=1,7
   10 C(J)=C(J+1)
      J=IDIFF-13
      C(8)=(-2211.*(B(J+1)+B(J+13))+3504.*(B(J+3)+B(J+11))+1614.
     C*(B(J+4)+B(J+10))-971.*(B(J+5)+B(J+9))-3016.*(B(J+6)+
     CB(J+8))-3780.*B(J+7)+2970.*(B(J+2)+B(J+12)))/58344.
      B(J)=C(1)
```

```
      DO 11 J=1,7
   11 C(J)=C(J+1)
      J=IDIFF-11
      C(8)=(-90.*(B(J+1)+B(J+11))+174.*(B(J+2)+B(J+10))+146.*
     C(B(3)+B(9))
     C+1.*(B(J+4)+B(J+8))-136.*(B(J+5)+B(J+7))-190.*B(J+6))/1716.
      B(IDIFF-12)=C(1)
      DO 12 J=1,7
   12 C(J)=C(J+1)
      J=IDIFF-9
      C(8)=(-126.*(B(J+J+1)+B(J+9))+371.*(B(J+2)
     C+B(J+8))+151.*(B(J+3)+B(J+7))
     C-211.*(B(J+4)+B(J+6))-370.*B(J+5))/1716.
      B(IDIFF-11)=C(1)
      DO 13 J=1,7
   13 C(J)=C(J+1)
      J=IDIFF-7
      C(8)=(-13.*(B(J+1)+B(J+7))+67.*(B(J+2)
     C+B(J+6))-19.*(B(J+3)+B(J+5))
     C-90.*B(J+4))/132.
      B(IDIFF-10)=C(1)
      DO 14 J=1,7
   14 C(J)=C(J+1)
      J=IDIFF-5
      C(8)=(-3.*(B(J+1)+B(J+5))+48.*(B(J+2)+B(J+4))-90.*B(J+3))/3.
      J=IDIFF-9
      DO 15 K=1,8
C  IF THE PROGRAM LOGIC DOESN'T APPEAR TO MAKE SENSE AT
C  THIS POINT , IT'S BECAUSE IT DOESN'T.  IT IS PURE KLUGE.
   15 B(J+K-1)=C(K)
      B(IDIFF-2)=B(IDIFF-3)
      B(IDIFF-1)=B(IDIFF-3)
      B(IDIFF)=B(IDIFF-3)
      RETURN
      END
```

FIELDS.FOR

```
C  THIS PROGRAM CALCULATES THE OPTICAL CONSTANTS OF A
C  SURFACE OVERLAYER FROM THE PSI AND DELTA VALUES FOR
C  THE BARE AND COVERED SURFACE FOR A GIVEN OVERLAYER
C  THICKNESS, USING THE LINEAR APPROXIMATION FORMULAS
C  FROM THE ASPNES REVIEW.(3.31) SPECT. ELLIPSOMETRY OF
C  SOLIDS IN 'OPTICAL PROPERTIES OF SOLIDS: NEW
C  DEVELOPMENTS, TO PROVIDE STARTING VALUES FOR AN
C  ITERATIVE SOLUTION.
C
      DIMENSION A(5),B(5),RR(4),RI(4),IPRGN1(4),IPRGN2(4),
     0ALPHA(128),BETA(128),GAMMA(2,400),NON(3),NOFF(3),THETA(400)
      REAL*4 I1,I2,LAMBDA,NO
      COMPLEX RHO,RHOPRI,EPSIS,P,E,N1,N2,T2,INT(2),J,Y,INTA
      LOGICAL*1 FARRAY(10)
      DATA IPRGN1/3RDX1,3RSPE,3RRA1,3RDAT/
      DATA IPRGN2/3RDX1,3RSPE,3RRA2,3RDAT/
      DATA NOFF/27,65,70/NON/27,65,69/
      WRITE(5,100)
  100 FORMAT('$ENTER FIRST AND LAST BLOCKS, 2I3...')
      READ(5,110) IBLK1,IBLK2
  110 FORMAT(2I3)
      WRITE(5,120)
  120 FORMAT('$ENTER PHI, OVERLAYER THICKNESS, 2F10.3...')
      READ(5,130) PHI,D
  130 FORMAT(2F10.3)
```

```
      WRITE(5,140)
  140 FORMAT('$ENTER INITIAL AND FINAL WAVELENGTH, 2F10.1...')
      READ(5,150) START,FINISH
  150 FORMAT(2F10.1)
      WRITE(5,180)
  180 FORMAT('$TYPE 1 FOR PRINTOUT...')
      READ(5,190)IKEY
  190 FORMAT(I1)
      WRITE(5,160)
  160 FORMAT('$ENTER TICK MARK INCREMENTS, 2F12.4...')
      READ(5,170) TKX,TKY
  170 FORMAT(2F12.4)
      J=CMPLX(0.0,1.0)
      PHI=PHI*3.14159/180.
      NO=1.0
      IPT=(IBLK2-IBLK1+1)*16
C
C  THE DATA FOR THE BARE METAL IS STORED IN A FILE
C  NAMED SPERA1.DAT ON DX1.  THE COVERED METAL VALUES ARE
C  STORED IN DX1:SPERA2.DAT.  THE FOLLOWING CODE READS
C  THESE VALUES ONE BLOCK AT A TIME INTO MEMORY.
C
      ICHAN1=IGETC()
      ICHAN2=IGETC()
      I=LOOKUP(ICHAN1,IPRGN1)
      I=LOOKUP(ICHAN2,IPRGN2)
      DO 40 KBLK=IBLK1-1,IBLK2-1
      I=IREADW(256,ALPHA,KBLK,ICHAN1)
      I=IREADW(256,BETA,KBLK,ICHAN2)
C
C  BARE METAL VALUES ARE READ ONE AT A TIME AS PSI1, DELTA1
C  AND COVERED METAL VALUES AS PSI2,DELTA2.  THE COMPLEX
C  REFLECTION COEFFICIENT FOR THE BARE METAL IS RHO, AND FOR
C  COVERED SURFACES IS RHOPRI.
C
      DO 40 KPT=1,16
      P1=ALPHA((KPT-1)*8+4)
      D1=ALPHA((KPT-1)*8+3)
      P2=BETA((KPT-1)*8+4)
      D2=BETA((KPT-1)*8+3)
      PSI1=(P1+180.)*3.14159/180.
      DELTA1=-D1*3.14159/180.
      PSI2=(P2+180.)*3.14159/180.
      DELTA2=-D2*3.14159/180.
      RHO=CMPLX((SIN(PSI1)*COS(DELTA1)/COS(PSI1)),
     D(SIN(PSI1)*SIN(DELTA1)/COS(PSI1)))
      RHOPRI=CMPLX((SIN(PSI2)*COS(DELTA2)/COS(PSI2)),
     D(SIN(PSI2)*SIN(DELTA2)/COS(PSI2)))
      LAMBDA=START+((FINISH-START)/((IBLK2-IBLK1+1)*16.)
     D*((KBLK-IBLK1+1)*16.+KPT-0.5))
      EPSIS=SIN(PHI)**2*(1.+(SIN(PHI)*(1.-RHO)/(1.+RHO)/COS(PHI))**2)
      N2=CSQRT(EPSIS)
C
C  THE FOLLOWING CODES USES THE INVERTED APPROXIMATION
C  FORMULAS TO CALCULATE N AND K FOR THE OVERLAYER.  THE
C  RESULTING QUARTIC EQUATION IS SOLVED USING THE SCIEN-
C  TIFIC SUBROUTINE POLRT AND NON-PHYSICAL SOLUTIONS ARE
C  DISCARDED.
C
      P=(RHOPRI-RHO)/RHO
      E=-4.*3.14159*COS(PHI)*EPSIS*D/(LAMBDA*
     D(EPSIS-1.))*(EPSIS*(COS(PHI)/SIN(PHI))**2-1.))
      R1=REAL(EPSIS)
      I1=AIMAG(EPSIS)
      R2=REAL(EPSIS)-AIMAG(P/E)+1.
```

```
      I2=AIMAG(EPSIS)+REAL(P/E)
      A(1)=I1*I2*R2-I1**2+R1*R2**2
      A(2)=-I2**2*R2-R2**3-4.*R1*R2
      A(3)=5.*R2**2+I2**2+4.*R1
      A(4)=-8.*R2
      A(5)=4.
      CALL POLRT(A,B,4,RR,RI,IER)
C
C  RR CONTAINS THE REAL PART OF THE CALCULATED REAL
C  COMPONENT OF THE DIELECTRIC CONSTANT.  IF RI IS NON-
C  ZERO, THEN THE REAL COMPONENT HAS AN IMAGINARY PART AND
C  THAT ROOT IS NON-PHYSICAL.  ALSO, IF N, THE INDEX OF RE-
C  FRACTION OF THE OVERLAYER IS GREATER THAN 6 OR LESS THAN
C  0.8, THAT ROOT IS DISCARDED.  IT IS POSSIBLE TO OBTAIN
C  MORE THAN ONE PHYSICAL SOLUTION AND BOTH ARE
C  PRINTED OUT,
C
      DO 10 JK=1,4
      IF(ABS(RI(JK)) .GT. 0.001) GO TO 10
      EPSIL2=(RR(JK)*I2-I1)/(2.*RR(JK)-R2)
      N1=CSQRT(CMPLX(RR(JK),EPSIL2))
      IF(REAL(N1) .LT. 0.8 .OR. REAL(N1) .GT. 6.0) GO TO 10
C
C  JJ COUNTS THE NUMBER OF CYCLES FOR THE ITERATION.  THE
C  PROGRAM CRAPS OUT AFTER 100.  N AND K ARE VARIED IND-
C  EPENDENTLY ACCORDING TO NEWTON'S METHOD, USING THE
C  SUBROUTINE BENNY TO CALCULATE RHO=INT
C  FROM N1 AND N2 USING THE EXACT EQUATIONS.
C
      JJ=0
    5 JJ=JJ+1
      IF(JJ .GT. 100) GO TO 20
      DO 1 N=1,2
      CALL BENNY(NO,N1,N2,LAMBDA,PHI,D,INTA)
      INT(N)=INTA
    1 N1=N1+0.001
      Y=(RHOPRI-INT(1))*0.001/(INT(2)-INT(1))
      N1=N1+Y-0.001
      DO 2 N=1,2
      CALL BENNY(NO,N1,N2,LAMBDA,PHI,D,INTA)
      INT(N)=INTA
    2 N1=N1+0.001*J
      Y=(RHOPRI-INT(1))*0.001*J/(INT(2)-INT(1))
      N1=N1+Y-0.001*J
      AN=ABS(REAL(RHOPRI)-REAL(INT(1)))
      BN=ABS(AIMAG(RHOPRI)-AIMAG(INT(1)))
      IF(AN .GT. 0.001 .OR. BN .GT. 0.001) GO TO 5
      IF(IKEY .EQ. 1) WRITE(5,200) LAMBDA,N1
  200 FORMAT(1X,F10.1,5X,'N1=',2F10.3)
      L=(KBLK-IBLK1+1)*16+KPT
      GAMMA(1,L)=LAMBDA
      GAMMA(2,L)=-AIMAG(N1)
      THETA(L)=REAL(N1)
      GO TO 10
   20 WRITE(5,210) LAMBDA
  210 FORMAT(1X,F10.1,5X,'NO CONVERGENCE IN 100 CYCLES')
   10 CONTINUE
   40 CONTINUE
C
C  REMAINING CODE SHUTS DOWN CHANNELS TO DISK.
C
      CALL CLOSEC(ICHAN1)
      CALL CLOSEC(ICHAN2)
      I=IFREEC(ICHAN1)
      I=IFREEC(ICHAN2)
```

```
      CALL INITT(120)
      KEY=0
      ISCALE=1
   75 CALL PLOTIT(IPT,GAMMA,-1,ISCALE)
      CALL SCOPY('(F5.0)',FARRAY)
      CALL TOCK(TKX,FARRAY,3,5,1)
      CALL SCOPY('(F9.4)',FARRAY)
      CALL TOCK(TKY,FARRAY,1,9,1)
      IF(KEY .EQ. 4)CALL TOUTST(3,NOFF)
      WRITE(5,300)
  300 FORMAT(' TYPE 1 FOR NEW LIMITS, 2 FOR SMOOTH, 3 FOR REPEAT,')
      WRITE(5,305)
  305 FORMAT('$4 FOR HARD COPY, 5 TO PLOT N...')
      READ(5,310) KEY
  310 FORMAT(I1)
      IF(KEY .EQ. 2) CALL SMOOTH(GAMMA,IPT)
      IF(KEY .EQ. 4) CALL TOUTST(3,NON)
      IF(KEY .EQ. 5) GO TO 80
      IF(KEY .GE. 2) GO TO 75
      IF(KEY .EQ. 0) CALL FINITT(0,760)
      WRITE(5,400)
  400 FORMAT('$ENTER NEW LIMITS,XMIN-YMAX,4F10.3...')
      READ(5,410) XMIN,XMAX,YMIN,YMAX
  410 FORMAT(4F10.3)
      CALL DWINDO(XMIN,XMAX,YMIN,YMAX)
      ISCALE=0
      GO TO 75
   80 DO 85 L=1,IPT
   85 GAMMA(2,L)=THETA(L)
      ISCALE=1
      GO TO 75
      CALL FINITT(0,760)
      END
```

LEROY.FOR

```
C  THIS PROGRAM CALCULATES THE OPTICAL CONSTANTS OF A
C  SURFACE OVERLAYER FROM THE PSI AND DELTA VALUES FOR
C  THE BARE AND COVERED SURFACE FOR A GIVEN OVERLAYER
C  THICKNESS, USING THE LINEAR APPROXIMATION FORMULAS
C  FROM THE ASPNES REVIEW.(3.31) SPECT. ELLIPSOMETRY OF
C  SOLIDS IN 'OPTICAL PROPERTIES OF SOLIDS: NEW
C  DEVELOPMENTS, TO PROVIDE STARTING VALUES FOR AN
C  ITERATIVE SOLUTION.
C
      DIMENSION A(5),B(5),RR(4),RI(4),IPRGN1(4),IPRGN2(4),
     2ALPHA(128),BETA(128),GAMMA(2,400),NON(3),NOFF(3),THETA(400),
     3ALF(2,400)
      REAL*4 I1,I2,LAMBDA,NO
      COMPLEX RHO,RHOPRI,EPSIS,P,E,N1,N2,T2,INT(2),J,Y,INTA
      LOGICAL*1 FARRAY(10)
      DATA IPRGN1/3RDX1,3RSPE,3RRA1,3RDAT/
      DATA IPRGN2/3RDX1,3RSPE,3RRA2,3RDAT/
      DATA NOFF/27,65,70/NON/27,65,69/
      WRITE(5,100)
  100 FORMAT('$ENTER FIRST AND LAST BLOCKS, 2I3...')
      READ(5,110) IBLK1,IBLK2
  110 FORMAT(2I3)
      WRITE(5,120)
  120 FORMAT('$ENTER PHI, OVERLAYER THICKNESS, 2F10.3...')
      READ(5,130) PHI,D
  130 FORMAT(2F10.3)
      WRITE(5,140)
```

```
  140 FORMAT('$ENTER INITIAL AND FINAL WAVELENGTH, 2F10.1...')
      READ(5,150) START,FINISH
  150 FORMAT(2F10.1)
      WRITE(5,105)
  105 FORMAT('$ENTER INIT.,FINAL LAMBDA,#BLOCKS,SPERA1,2F10.3,I3..')
      READ(5,115) START1,FIN1,NOB
  115 FORMAT(2F10.3,I3)
      LNOB=16*NOB
      WRITE(5,125)
  125 FORMAT('$ENTER K1 LIMITS, 2F10.3...')
      READ(5,130) SL1,SL2
      WRITE(5,180)
  180 FORMAT('$TYPE 1 FOR PRINTOUT...')
      READ(5,190)IKEY
  190 FORMAT(I1)
      WRITE(5,160)
  160 FORMAT('$ENTER TICK MARK INCREMENTS, 2F12.4...')
      READ(5,170) TKX,TKY
  170 FORMAT(2F12.4)
      J=CMPLX(0.0,1.0)
      PHI=PHI*3.14159/180.
      NO=1.0
      IPT=0
C
C  THE DATA FOR THE BARE METAL IS STORED IN A FILE
C  NAMED SPERA1.DAT ON DX1.  THE COVERED METAL VALUES ARE
C  STORED IN DX1:SPERA2.DAT.  THE FOLLOWING CODE READS
C  THESE VALUES ONE BLOCK AT A TIME INTO MEMORY.
C
      ICHAN1=IGETC()
      ICHAN2=IGETC()
      I=LOOKUP(ICHAN1,IPRGN1)
      I=LOOKUP(ICHAN2,IPRGN2)
      DO 3 INOB=0,NOB-1
      I=IREADW(256,ALPHA,INOB,ICHAN1)
      DO 3 JNOB=0,15
      KNOB=1+JNOB+INOB*16
      ALF(1,KNOB)=ALPHA(JNOB*8+4)
    3 ALF(2,KNOB)=ALPHA(JNOB*8+3)
      DO 40 KBLK=IBLK1-1,IBLK2-1
      I=IREADW(256,BETA,KBLK,ICHAN2)
C
C  BARE METAL VALUES ARE READ ONE AT A TIME AS PSI1, DELTA1
C  AND COVERED METAL VALUES AS PSI2,DELTA2.  THE COMPLEX
C  REFLECTION COEFFICIENT FOR THE BARE METAL IS RHO, AND FOR
C  COVERED SURFACES IS RHOPRI.
C
      DO 40 KPT=1,16
      P2=BETA((KPT-1)*8+4)
      D2=BETA((KPT-1)*8+3)
      PSI2=(P2+180.)*3.14159/180.
      DELTA2=-D2*3.14159/180.
      RHOPRI=CMPLX((SIN(PSI2)*COS(DELTA2)/COS(PSI2)),
     D(SIN(PSI2)*SIN(DELTA2)/COS(PSI2)))
      LAMBDA=START+((FINISH-START)/((IBLK2-IBLK1+1)*16.)
     0*((KBLK-IBLK1+1)*16.+KPT-0.5))
      IF(FIN1 .LT. START1) GO TO 195
      IF(LAMBDA .LT. START1) GO TO 40
      IF(LAMBDA .GT. FIN1) GO TO 40
      GO TO 196
  195 IF (LAMBDA .GT. START1) GO TO 40
      IF(LAMBDA .LT. FIN1) GO TO 40
  196 CONTINUE
      IPT=IPT+1
      ANOB=(LAMBDA-START1)/(FIN1-START1)*FLOAT(LNOB-1)+1.
```

```
      NNOB=IFIX(ANOB)
      RNOB=ANOB-NNOB
      P1=(1.-RNOB)*ALF(1,NNOB)+RNOB*ALF(1,NNOB+1)
      D1=(1.-RNOB)*ALF(2,NNOB)+RNOB*ALF(2,NNOB+1)
      PSI1=(P1+180.)*3.14159/180.
      DELTA1=-D1*3.14159/180.
      RHO=CMPLX((SIN(PSI1)*COS(DELTA1)/COS(PSI1)),
     D(SIN(PSI1)*SIN(DELTA1)/COS(PSI1)))
      EPSIS=SIN(PHI)**2*(1.+(SIN(PHI)*(1.-RHO)/(1.+RHO)/COS(PHI))**2)
      N2=CSQRT(EPSIS)
C
C  THE FOLLOWING CODES USES THE INVERTED APPROXIMATION
C  FORMULAS TO CALCULATE N AND K FOR THE OVERLAYER.  THE
C  RESULTING QUARTIC EQUATION IS SOLVED USING THE SCIEN-
C  TIFIC SUBROUTINE POLRT AND NON-PHYSICAL SOLUTIONS ARE
C  DISCARDED.
C
      P=(RHOPRI-RHO)/RHO
      E=-4.*3.14159*COS(PHI)*EPSIS*D/(LAMBDA*
     D(EPSIS-1.)*(EPSIS*(COS(PHI)/SIN(PHI))**2-1.))
      R1=REAL(EPSIS)
      I1=AIMAG(EPSIS)
      R2=REAL(EPSIS)-AIMAG(P/E)+1.
      I2=AIMAG(EPSIS)+REAL(P/E)
      A(1)=I1*I2*R2-I1**2+R1*R2**2
      A(2)=-I2**2*R2-R2**3-4.*R1*R2
      A(3)=5.*R2**2+I2**2+4.*R1
      A(4)=-8.*R2
      A(5)=4.
      CALL POLRT(A,B,4,RR,RI,IER)
C
C  RR CONTAINS THE REAL PART OF THE CALCULATED REAL
C  COMPONENT OF THE DIELECTRIC CONSTANT.  IF RI IS NON-
C  ZERO, THEN THE REAL COMPONENT HAS AN IMAGINARY PART AND
C  THAT ROOT IS NON-PHYSICAL.  ALSO, IF N, THE INDEX OF RE-
C  FRACTION OF THE OVERLAYER IS GREATER THAN 6 OR LESS THAN
C  0.8, THAT ROOT IS DISCARDED.  IT IS POSSIBLE TO OBTAIN
C  MORE THAN ONE PHYSICAL SOLUTION AND BOTH ARE
C  PRINTED OUT,
C
      DO 10 JK=1,4
      IF(ABS(RI(JK)) .GT. 0.001) GO TO 10
      EPSIL2=(RR(JK)*I2-I1)/(2.*RR(JK)-R2)
      N1=CSQRT(CMPLX(RR(JK),EPSIL2))
      IF(REAL(N1) .LT. 0.8 .OR. REAL(N1) .GT. 6.0) GO TO 10
      IF(AIMAG(N1) .LT. SL1 .OR. AIMAG(N1) .GT. SL2) GO TO 10
C
C  JJ COUNTS THE NUMBER OF CYCLES FOR THE ITERATION.  THE
C  PROGRAM CRAPS OUT AFTER 100.  N AND K ARE VARIED IND-
C  EPENDENTLY ACCORDING TO NEWTON'S METHOD, USING THE
C  SUBROUTINE BENNY TO CALCULATE RHO=INT
C  FROM N1 AND N2 USING THE EXACT EQUATIONS.
C
      JJ=0
    5 JJ=JJ+1
      IF(JJ .GT. 100) GO TO 20
      DO 1 N=1,2
      CALL BENNY(N0,N1,N2,LAMBDA,PHI,D,INTA)
      INT(N)=INTA
    1 N1=N1+0.001
      Y=(RHOPRI-INT(1))*0.001/(INT(2)-INT(1))
      N1=N1+Y-0.001
      DO 2 N=1,2
      CALL BENNY(N0,N1,N2,LAMBDA,PHI,D,INTA)
      INT(N)=INTA
```

```
    2 N1=N1+0.001*J
      Y=(RHOPRI-INT(1))*0.001*J/(INT(2)-INT(1))
      N1=N1+Y-0.001*J
      AN=ABS(REAL(RHOPRI)-REAL(INT(1)))
      BN=ABS(AIMAG(RHOPRI)-AIMAG(INT(1)))
      IF(AN .GT. 0.001 .OR. BN .GT. 0.001) GO TO 5
      IF(IKEY .EQ. 1) WRITE(5,200) LAMBDA,N1
  200 FORMAT(1X,F10.1,5X,'N1=',2F10.3)
      L=(K8LK-IBLK1+1)*16+KPT
      GAMMA(1,L)=LAMBDA
      GAMMA(2,L)=-AIMAG(N1)
      THETA(L)=REAL(N1)
      GO TO 10
   20 WRITE(5,210) LAMBDA
  210 FORMAT(1X,F10.1,5X,'NO CONVERGENCE IN 100 CYCLES')
   10 CONTINUE
   40 CONTINUE
C
C  REMAINING CODE SHUTS DOWN CHANNELS TO DISK.
C
      CALL CLOSEC(ICHAN1)
      CALL CLOSEC(ICHAN2)
      I=IFREEC(ICHAN1)
      I=IFREEC(ICHAN2)
      DO 77 I=2,IPT
      IF(GAMMA(1,I) .GT.10000 .OR. GAMMA(1,I) .LT. 1500.) GO TO 78
      IF(GAMMA(2,I) .GT. -1.*SL1) GO TO 78
      IF(GAMMA(2,I) .LT. -1.*SL2) GO TO 78
      GO TO 77
   78 CONTINUE
      GAMMA(1,I)=GAMMA(1,I-1)
      GAMMA(2,I)=GAMMA(2,I-1)
      THETA(I)=THETA(I-1)
   77 CONTINUE
      CALL INITT(120)
      KEY=0
      ISCALE=1
   75 CALL PLOTIT(IPT,GAMMA,-1,ISCALE)
      CALL SCOPY('(F5.0)',FARRAY)
      CALL TOCK(TKX,FARRAY,3,5,1)
      CALL SCOPY('(F9.4)',FARRAY)
      CALL TOCK(TKY,FARRAY,1,9,1)
      IF(KEY .EQ. 4)CALL TOUTST(3,NOFF)
      WRITE(5,300)
  300 FORMAT(' TYPE 1 FOR NEW LIMITS, 2 FOR SMOOTH, 3 FOR REPEAT,')
      WRITE(5,305)
  305 FORMAT('$4 FOR HARD COPY, 5 TO PLOT N...')
      READ(5,310) KEY
  310 FORMAT(I1)
      IF(KEY .EQ. 2) CALL SMOOTH(GAMMA,IPT)
      IF(KEY .EQ. 4) CALL TOUTST(3,NON)
      IF(KEY .EQ. 5) GO TO 80
      IF(KEY .GE. 2) GO TO 75
      IF(KEY .EQ. 0) CALL FINITT(0,760)
      WRITE(5,400)
  400 FORMAT('$ENTER NEW LIMITS,XMIN-YMAX,4F10.3...')
      READ(5,410) XMIN,XMAX,YMIN,YMAX
  410 FORMAT(4F10.3)
      CALL DWINDO(XMIN,XMAX,YMIN,YMAX)
      ISCALE=0
      GO TO 75
   80 DO 85 L=1,IPT
   85 GAMMA(2,L)=THETA(L)
      ISCALE=1
      GO TO 75
```

```
      CALL FINITT(0,760)
      END
```

BENNY.FOR

```
      SUBROUTINE BENNY(N0,N1,N2,LAMBDA,PHI,D,INT)
      COMPLEX N1,N2,RP1,RP2,RS1,RS2,G,INT,J,T1,T2,T3,T4,T5
      REAL N0,LAMBDA,PHI,D
      J=CMPLX(0.0,1.0)
      T1=N1**2
      T2=N0**2
      T3=CSQRT(T1-T2*SIN(PHI)**2)
      T4=N2**2
      T5=CSQRT(T4-T2*SIN(PHI)**2)
      T6=COS(PHI)
      RP1=(T1*T6-N0*T3)/(T1*T6+N0*T3)
      RP2=(T4*T3-T1*T5)/(T4*T3+T1*T5)
      RS1=(N0*T6-T3)/(N0*T6+T3)
      RS2=(T3-T5)/(T3+T5)
      G=J*(4.*3.14159*D/LAMBDA)*T3
      INT=((RP1+RP2*CEXP(-G))/(1.+RP1*RP2*CEXP(-G)))*
     D((1.+RS1*RS2*CEXP(-G))/(RS1+RS2*CEXP(-G)))
      RETURN
      END
```

SMOOTH.FOR

```
      SUBROUTINE SMOOTH(B,IDIFF)
      DIMENSION B(2,400),C(8)
      C(3)=(-3.*(B(2,1)+B(2,5))+12.*(B(2
     C,2)+B(2,4))+17.*B(2,3))/35.
      C(1)=C(3)
      C(2)=C(3)
      C(4)=(-2.*(B(2,1)+B(2,7))+3.*(B(2,
     C2)+B(2,6))+6.*(B(2,3)+B(2,5))
     C+7.*B(2,4))/21.
      C(5)=(-21.*(B(2,1)+B(2,9))+14.*(B(
     C2,2)+B(2,8))+39.*(B(2,3)+B(2,7))
     C+54.*(B(2,4)+B(2,6))+59.*B(2,5))/231.
      C(6)=(-36.*(B(2,1)+B(2,11))+9.*(B(
     C2,2)+B(2,10))+44.*(B(2,3)+B(2,9))
     C+69.*(B(2,4)+B(2,8))+84.*(B(2,5)+B(2,7))+89.*B(2,6))/429.
      C(7)=(-11.*(B(2,1)+B(2,13))+9.*(B(
     C2,3)+B(2,11))+16.*(B(2,4)+B(2,10))
     C+21.*(B(2,5)+B(2,9))+24.*(B(2,6)+B(2,8))+25.*B(2,7))/143.
      DO 10 I=8,IDIFF-7
      C(8)=(-78.*(B(2,I-7)+B(2,I+7))-13.
     C*(B(2,I-6)+B(2,I+6))+42.*(B(2,I-5)+B(2,I+5))
     C+87.*(B(2,I-4)+B(2,I+4))+122.*(B(2
     C,I-3)+B(2,I+3))+147.*(B(2,I-2)+B(2,I+2))
     C+162.*(B(2,I-1)+B(2,I+1))+167.*B(2,I))/1105.
      B(2,I-7)=C(1)
      DO 10 J=1,7
   10 C(J)=C(J+1)
      J=IDIFF-13
      C(8)=(-11.*(B(2,J+1)+B(2,J+13))+9.
     C*(B(2,J+3)+B(2,J+11))+16.*(B(2,J+4)+B(2,J+10
     C))+21.*(B(2,J+5)+B(2,J+9))+24.*(B(
     C2,J+6)+B(2,J+8))+25.*B(2,J+7))/143.
      B(2,J)=C(1)
      DO 11 K=1,7
```

```
   11 C(K)=C(K+1)
      J=IDIFF-12
      C(8)=(-36.*(B(2,J+1)+B(2,J+11))+9.*(B(2,J+2
     C)+B(2,J+10))+44.*(B(2,J+3)+B(2,J+9)
     C)+69.*(B(2,J+4)+B(2,J+8))+84.*(B(2
     C,J+5)+B(2,J+7))+89.*B(2,J+6))/429.
      B(2,J)=C(1)
      DO 12 K=1,7
   12 C(K)=C(K+1)
      J=IDIFF-11
      C(8)=(-21.*(B(2,J+1)+B(2,J+9))+14.
     C*(B(2,J+2)+B(2,J+8))+39.*(B(2,J+3)+B(2,J+7))
     C+54.*(B(2,J+4)+B(2,J+6))+59.*B(2,J+5))/231.
      B(2,J)=C(1)
      DO 13 K=1,7
   13 C(K)=C(K+1)
      J=IDIFF-10
      C(8)=(-2.*(B(2,J+1)+B(2,J+7))+3.*(
     CB(2,J+2)+B(2,J+6))+6.*(B(2,J+3)+B(2,J+5))
     C+7.*B(2,J+4))/21.
      B(2,J)=C(1)
      DO 14 K=1,7
   14 C(K)=C(K+1)
      J=IDIFF-9
      C(8)=(-3.*(B(2,J+1)+B(2,J+5))+12.*
     C(B(2,J+2)+B(2,J+4))+17.*B(2,J+3))/35.
      DO 15 K=1,8
   15 B(2,J+K-1)=C(K)
      B(2,IDIFF-1)=C(8)
      B(2,IDIFF)=C(8)
      RETURN
      END
```

TOCK.FOR

```
      SUBROUTINE TOCK(TK,FARRAY,NAXIS,NCHAR,NIN)
      DIMENSION Z(4),NDRAW(2,4)
      LOGICAL*1 FARRAY(2),STRING(10)
      DATA NDRAW/10,0,-10,0,0,10,0,-10/
      CALL SEEDW(Z(1),Z(2),Z(3),Z(4))
      K=((4-NAXIS)/2)*2+1
      AN=(Z(K+1)-Z(K))/TK+0.5
      IF(AN .GT. 100.) RETURN
      N=IFIX(AN)
      DO 1 I=1,N
      ZZ=IFIX(Z(K)/TK+I)*TK
      IF (NAXIS .LE. 2) CALL MOVEA (Z(NAXIS),ZZ)
      IF (NAXIS .GE. 3) CALL MOVEA (ZZ,Z(NAXIS))
      CALL DRWREL(NDRAW(1,NAXIS)*NIN,NDRAW(2,NAXIS)*NIN)
      IF(NAXIS .NE. 1) CALL MOVREL(-LINWDT(NCHAR/2),0)
      ENCODE (NCHAR,FARRAY,STRING) ZZ
      CALL RECOVR
      CALL AOUTST(NCHAR,STRING)
    1 CONTINUE
      RETURN
      END
```

☆ U.S. GOVERNMENT PRINTING OFFICE: 1978-689-058/(F)40

TECHNICAL INFORMATION DEPARTMENT
LAWRENCE BERKELEY LABORATORY
UNIVERSITY OF CALIFORNIA
BERKELEY, CALIFORNIA 94720